How does O$^+$ outflow vary with solar wind conditions?

Audrey Schillings

Atmospheric Science

LULEÅ
UNIVERSITY
OF TECHNOLOGY

Doctoral thesis

How does O$^+$ outflow vary with solar wind conditions?

Audrey Schillings

Swedish Institute of Space Physics
Kiruna, Sweden

Division of Space Technology
Department of Computer Science, Electrical and Space Engineering
Luleå University of Technology
Kiruna, Sweden

Supervisors:

Hans Nilsson
Rikard Slapak
Lars-Göran Westerberg

The Moon taught me it's okay to go through phases. The Sun taught me that no matter how many times I go down, keep on rising.
Leticia Rae

Most people say that it is the intellect which makes a great scientist. They are wrong: it is character.
Albert Einstein

Abstract

The entire solar system including Earth is enveloped in a region of space where the Sun's magnetic field dominates, this region is called the heliosphere. Due to this position in the heliosphere, a strong coupling exists between the Sun and our planet. The Sun continuously ejects particles, the solar wind, which is composed mainly of protons, electrons as well as some helium and heavier elements. These high energetic particles then hit the Earth and are partly deflected by the Earth's magnetosphere (the region around Earth governed by the geomagnetic field). Depending on the strength of the solar wind hitting our planet, the magnetosphere is disturbed and perturbations can be seen down to the lower atmosphere.

The upper atmosphere is affected by short wave-length solar radiation that ionise the neutral atoms, this region is referred to as the ionosphere. In the ionosphere, some of the heavier ion populations, such as O^+, are heated and accelerated through several processes and flow upward. In the polar regions (polar cap, cusp and plasma mantle) these mechanisms are particularly efficient and when the ions have enough energy to escape the Earth's gravity, they move outward along open magnetic field lines. These outflowing ions may be lost into interplanetary space.

Another aspect that influences O^+ ions are disturbed magnetospheric conditions. They correlate with solar active periods, such as coronal holes or the development of solar active regions. From these regions, strong ejections emerge, called coronal mass ejections (CMEs). When these CMEs interact with Earth, they produce a compression of the magnetosphere as well as reconnection between the terrestrial magnetic field lines and the interplanetary magnetic field (IMF) lines, which very often leads to geomagnetic storms. The energy in the solar wind as well as the coupling to the magnetosphere increase during geomagnetic storms and therefore the energy input to the ionosphere. This in turn increases the O^+ outflow. In addition, solar wind parameter variations such as the dynamic pressure or the IMF also influence the outflowing ions.

Our observations are made with the Cluster mission, a constellation of 4 satellites flying around Earth in the key magnetospheric regions where we usually observe ion outflow. In this thesis, we estimated O^+ outflow for different solar wind parameters (IMF, solar wind dynamic pressure) and extreme ultraviolet radiations (EUV) as well as for extreme geomagnetic storms. We found that O^+ outflow increases exponentially with enhanced geomagnetic activity (Kp index) and about 2 orders of magnitude during extreme geomagnetic storms compared to quiet conditions. Furthermore, our investigations on solar wind parameters showed that O^+ outflow increases for high

dynamic pressure and southward IMF, as well as with EUV radiations. Finally, the fate of O^+ ions from the plasma mantle were studied based on Cluster observations and simulations. These results confirm that ions observed in the plasma mantle have sufficient energy to be lost in the solar wind.

Sammanfattning

Den del av rymden som domineras av solens magnetfält kallas heliosfären. Heliosfären omfattar hela solsystemet inklusive jorden, vilket gör att det finns en stark koppling mellan solen och jorden. Solen sänder oavbrutet ut laddade partiklar, den så kallade solvinden, och när dessa träffar jorden påverkas magnetosfären, som är det område kring jorden där det geomagnetiska fältet dominerar. När solvinden är starkare än vanligt uppstår störningar som kan observeras ner till den lägre atmosfären.

Den övre atmosfären utsätts för strålning från solen som joniserar atomer och molekyler, och formar det område som kallas jonosfären. Några av de tyngre jonpopulationerna i jonosfären, som till exempel syrejoner, kan hettas upp och accelereras genom flera olika processer. Detta gör att de flödar uppåt i atmosfären. I polarområdena är dessa mekanismer särskilt effektiva och om tillräckligt med energi tillförs jonerna kan gravitationen övervinnas, vilket gör att jonerna flödar upp längs öppna magnetfältlinjer och kan gå förlorade ut i den interplanetära rymden.

En annen aspekt som påverkar syrejoner är störda magnetosfäriska förhållanden som korrelerar med solens aktivitet, som till exempel under utvecklingen av aktiva solområden. Från dessa områden härstammar koronamassautkastningar. När dessa extrema händelser når jorden komprimeras magnetosfären och det geomagnetiska och interplanetära magnetiska fältet sammankopplas, vilket ofta leder till geomagnetiska stormar. Under dessa tillförs stora mängder av solvindspartiklar och energi till magnetosfären, och ett högre syrejonsutflöde observeras också. Dessutom påverkar solvindsparametrar som dynamiskt tryck och det interplanetära magnetfältet de utströmmande jonerna.

I denna avhandling har data från Clustersatelliterna använts; dessa utgörs av fyra satelliter i formation i omloppsbana kring jorden. Plasmaområdena där satelliterna befinner sig är där jonutflödet vanligtvis observeras. Denna avhandling behandlar syrejonutflöde för olika solvindparametrar (solvindens dynamiska tryck, IMF) och olika extrem ultraviolett strålning samt för extrema geomagnetiska stormar. Det visas att syrejonutflödet som förloras till solvinden ökar exponentiellt med den geomagnetiskta aktiviteten (Kp-index) och ökar med upp till 2 storleksordningar under extrema geomagnetiska stormar jämfört med lugna förhållanden. Det visas också att syrejonutflödet ökar för högt dynamiskt tryck i solvinden, IMF-riktning söderut, och vid högre extrem ultraviolett strålning (EUV). Slutligen studerades ödet för O^+ joner från plasmamanteln med Clustersatelliterna och simuleringar. Dessa resultat bekräftar att joner som observerats i plasmamanteln har tillräckligt med energi för att gå förlorade i solvinden.

Appended papers

This thesis includes a Summary and the following appended papers:

Paper I
Slapak, R., **Schillings, A.**, Nilsson, H., Yamauchi, M., Westerberg, L. G., and Dandouras I.. Atmospheric loss from the dayside open polar region and its dependence on geomagnetic activity: implications for atmospheric escape on evolutionary timescales. *Annales Geophysicae, Volume 35, 721-731, 2017*
Note that this paper has a corrigendum.

Paper II
Schillings, A., Nilsson, H., Slapak, R., Yamauchi, M., and Westerberg, L. G.. Relative outflow enhancements during major geomagnetic storms - Cluster observations. *Annales Geophysicae, Volume 35, 1341-1352, 2017*

Paper III
Schillings, A., Nilsson, H., Slapak, R., Wintoft, P., Yamauchi, M., Wik, M., Dandouras, I., and Carr C. M.. O^+ escape during the extreme space weather event of September 4–10, 2017. *Space Weather, 16, 1363-1376, 2018*

Paper IV
Schillings, A., Slapak, R., Nilsson, H., Yamauchi, M., Dandouras, I., and Westerberg, L. G.. Earth atmospheric loss through the plasma mantle and its dependence on solar wind parameters. *Earth, Planets and Space, 71:70, 2019*

Paper V
Schillings, A., Gunell, H., Nilsson, H., De Spiegeleer, A., Ebihara, Y., Westerberg, L.-G., Yamauchi, M. and Slapak, R.. The fate of O^+ ions observed in the plasma mantle and cusp: particle tracing modelling and Cluster observations. *Submitted to Annales Geophysicae, October 2019*

x

Other papers

During my PhD, I also contributed to the following papers:

Nilsson, H., Hamrin, M., Pitkänen, T., Karlsson, T., Slapak, R., Andersson, L., Gunell, H., **Schillings, A.**, Vaivads, A.. Oxygen ion response to proton bursty bulk flows. *Journal of Geophysical Research Space Physics, 121, 7535-7546, 2016*

Slapak, R., Hamrin, M., Pitkänen, T., Yamauchi, M., Nilsson, H., Karlsson, T., and **Schillings, A.**. Quantification of the total ion transport in the near-Earth plasma sheet. *Annales Geophysicae, 35, 869-877, 2017*

Yamauchi, M., Sergienko, T., Enell, C. F., **Schillings, A.**, Slapak, R., Johnsen, M. G., Tjulin, A., and Nilsson, H.. Ionospheric response observed by EISCAT during the 6-8 September 2017 space weather event: Overview. *Space Weather, 16, 1437-1450, 2018*

Krcelic, P., Haaland, S., Maes, L., Slapak, R., **Schillings, A.**. Estimating the fate of oxygen ion outflow from the high altitude cusp. *Submitted to Annales Geophysicae, August 2019*

CONTENTS

Acknowledgements

you baked.

Finally, my parents, my siblings and my daily sun, who will recognise himself, have my greatest gratitude for supporting me at any time, listen to me, comfort me and for your ability to "blow the storm away", thank you so much.

Introduction

Atmospheric loss is an important phenomenon in connection to space weather but also to understand the atmospheric evolution on geological timescales. It is also needed to understand the conditions that lead to habitable planets. Several current missions in the solar system are investigating the environment of planets and moons to judge their past and current habitability. About billion years ago, the young Sun is believed to have been more active than nowadays, so that today's geomagnetic storms correspond to undisturbed magnetic conditions of the past (Güdel, 2007; Ribas et al., 2005; Krauss et al., 2012). Thus, investigations of ionospheric O^+ outflow during geomagnetic storms and disturbed solar wind conditions is one approach to expand our knowledge on the atmospheric evolution.

On daily basis, the Earth's atmosphere is losing neutrals and ions (~ 2.2 kg/s). At an altitude of approximately 500 km, there is a transition region between the collisional and collisionless medium, called the exobase. Above the exobase, some upward moving particles will have enough velocity to escape the Earth's gravity. This escape velocity is about 11 km/s and the particles moving upward are called outflow, whereas particles moving upward but with velocities below the escape velocity are defined as upflow. Upflow is usually observed at lower altitudes than outflow. The terrestrial outflowing flux mainly consists of neutral hydrogen and hydrogen- and oxygen ions (H^+, O^+) over a wide energy range. The neutral hydrogen escapes through thermal escape (Jeans escape), while ion outflow needs ionisation and further acceleration in order to escape the magnetosphere. Thus, these ions experience heating and acceleration along their trajectories in the polar regions; the polar cap, the cusp and the plasma mantle. Depending on the location, ion outflow signatures and their associated mechanisms might be different. The heating and acceleration mechanisms are fairly well understood, since we can explain the observed temperatures and velocities using simple theory of the dominating acceleration mechanisms at high-altitudes (Nilsson et al., 2008; Waara et al., 2011; Slapak et al., 2011), see also Section 4.4. After being heated and accelerated, the ions have sufficient velocity and energy to escape the Earth's gravity and eventually be lost into the solar wind.

O^+ outflow under disturbed magnetospheric conditions including major geomagnetic storms is the interest of this thesis. We first give a background with a description of the solar-terrestrial environment. Solar features such as coronal mass ejections and solar wind are discussed, followed by a short review of the Earth's magnetosphere. Chapter 3 is an introduction to the basic plasma physics and describes the theory related to this thesis. In chapter 4, we present the main topic, ion outflow and escape. This chapter gives a short history of ion outflow as well as the signatures and their associated mechanisms that lead to ion outflow. Finally, chapter 6 summarises the results and concludes this thesis, while chapter 7 gives a short description of the appended papers.

The solar-terrestrial environment

Our solar system is composed of different celestial objects such as planets, dwarf planets, comets, asteroids and the most important body, the Sun. The Earth, the third planet starting from the Sun, is located at an average distance of 1 AU or 1.5×10^8 km and fulfills a rotation around our star in one year. The Earth is surrounded by a stream of particles continuously ejected from the Sun, called the solar wind. Depending on its strength, the solar wind creates disturbances in the Earth's environment. In addition, both the Sun and Earth have intrinsic magnetic fields and when the two magnetic fields interact, it leads to perturbations in the terrestrial environment. This chapter gives a general description of the solar-terrestrial environment and what phenomena cause disturbances at Earth.

2.1   The Sun

The Sun rotates around its axis in approximately 27 days (25 days near the equator and 31 at the poles) and its rotation axis is tilted about 7° compared to the axis of Earth. The Earth rotates around the Sun with an elliptical orbit with small eccentricity (close to circular) where the Sun is located in one of the focal points. The solar cycle is usually defined according to the number of sunspots R[1], which quantifies the solar activity. The typical maximum value of R is between 100 and 120 and its minimum velue between 10 and 20. One solar cycle is about 11 years (it can vary between 9 and 14 years) and we are currently in solar cycle 24, however, approximately every 11 years the Sun's polarity is inverted, thus one solar cycle could also be seen as ~ 22 years.

The Sun's interior is composed of a core where the generated energy diffuses through the radiative zone mostly in the form of X-rays and gamma-rays as well as

---

[1]A sunspot is a solar feature seen as a dark area in white light, tending to occur in group in the solar latitudes of 5° to 30°. The number of sunspots is given by the *Wolf sunspot number* $R = k(f + 10g)$ where f is the total of spots seen, g number of disturbed regions and k is an observatory constant.

through the convection zone by convective fluid flows (NASA). Between the radiative and convective zone, the solar magnetic field is generated in a thin layer called the tachocline (NASA).

The Sun has also an atmosphere, which is divided into three regions. Starting from the closest region to the surface, the photosphere is a layer with a density of 10^{23} particles per cubic metre and the region where most of the Sun light is emitted (Kamide and Maltsev, 2007). Different structures can be observed; granules that are cellular features covering the entire solar surface, and areas with intense magnetic fields called bright faculae and dark sunspots. The second region of the solar atmosphere is the chromosphere with a lower density of 10^{17} part/m^3 and thus more transparent. The chromosphere can be observed with a Hα filter that enables to perceive brighter regions around sunspots, also known as active regions (AR)(Kamide and Maltsev, 2007). The rapid evolution of these active regions leads occasionally to solar flares. Finally, the corona is the third atmospheric region of the Sun with 10^{15} part/m^3 and its brightness is very faint compared to the others.

2.1.1 Solar flares

Solar flares are observed near solar AR mostly in Hα, C$_a$(II) lines or at radio wavelengths in the chromosphere and corona. This localised phenomena is a release of a huge amount of energy, about 10^{25} J, from the solar atmosphere and a total power of 10^{20} W - 10^{22} W in a very short time (approximately 10 minutes) (Prölss, 2004). Solar flares play a key role in the solar-terrestrial coupling because they may provoke measurable disturbances in the upper atmosphere. Their signatures are electromagnetic radiations that may reach Earth (depending on where on the Sun they occur) and thus are detectable at several wavelengths such as Hα, γ-rays, extreme ultraviolet (EUV) or X-rays. Depending on their emission, solar flares are classified with their apparent solar area on a scale from 1 to 4 and relative brilliance of Hα with the characters F (faint), N (normal), and B (bright). For example, a flare classified as 3N is rather large but with a normal brilliance. Another and more common classification is the classes (A, B, C, M, and X) according to the order of magnitude of their intensity in X-ray flux (see Tab. 2.1, Koskinen (2011)). The intensity is given in decimals between 1 and 9.9 within each class except in the X-class where it goes up to 100. For example, a flare C3.5 implies a flux peak of 3.5×10^{-6} W/m^2.

Within the electromagnetic emission, the increase of EUV and X-rays are important for the upper atmosphere disturbances. During large flares, the intensity of EUV can be twice than usual (it goes up to ~ 10 mW/m^2) and about 4 orders of magnitude higher for soft X-rays (up to 1 mW/m^2) (Prölss, 2004). Additionally, solar flares also release energetic particles, mainly electrons and protons.

The physics behind solar flares is not well understood yet, especially the source of the huge amount of energy released from the solar active regions. Simulations and models have tried to investigate this complex phenomena. So, a coronal loop (of magnetic field) reconnects on its top and sometimes forms an ejecta of magnetic field, also called a coronal mass ejection or CME (see Section 2.1.2). Note that flares do not

Table 2.1: Classes of solar X-ray emission for flares (Koskinen, 2011).

Classe	Intensity
A	10^{-8} W/m^2
B	10^{-7} W/m^2
C	10^{-6} W/m^2
M	10^{-5} W/m^2
X	$\geq 10^{-4}$ W/m^2

necessary have an associated CME (Toriumi and Wang, 2019). The magnetic energy is converted into kinetic energy, which accelerates the charged particles. These accelerated charged particles are injected into the solar chromosphere and the electrons emit electromagnetic radiation (see Fig. 2.1).
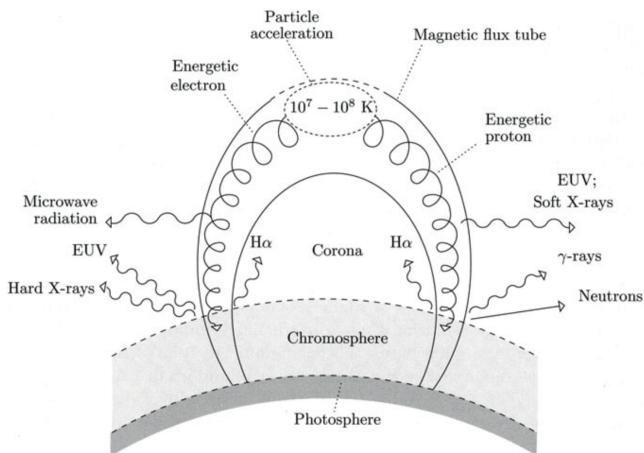
Figure 2.1: Solar flare model and the associated emissions. Credits: Prölss (2004).

In solar cycle 23, the strongest solar flares were an X28.0 on November 4, 2004; an X20.0 on April 2, 2001 and an X17.2 on October 28, 2003. The first and third flares were associated with CMEs that reached Earth and subsequently extreme geomagnetic storms were observed (see also Section 2.3). For these both storms, we investigated the ion ouflow in Paper II. During solar cycle 24, the strongest flares occurred in September 2017, on the 6th and the 10th, classified as X9.3 and X8.2 respectively. The third strongest one was recorded on August 9, 2011 and was classified as X6.9 (SpaceWeatherLive). The two strongest flares of solar cycle 24 also induced a

major geomagnetic storm, which was investigated in Paper III from the solar aspects to the ion outflow. Fig. 2.2 shows the intensity of the X-ray flux evolution during September 4-7, 2017, where two X-flares (green line and dashed circle) were detected on September 6.
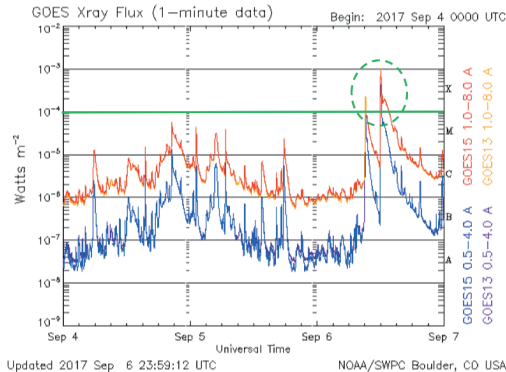
Figure 2.2: Intensity of the X-ray flux during September 4-7, 2017. The right y-axis gives the flares classes (A-X). Credits: Adapted from NOAA/SWPC Boulder, CO USA.

2.1.2 Coronal mass ejections

Despite its name, the coronal mass ejections (CMEs) do not come from the corona but originates in the lower solar atmosphere, nevertheless they are observed in the corona. CMEs are huge ejections of plasma and magnetic energy from the Sun. They are produced by a reconnection of magnetic field lines on the Sun, and may originate from a flare, however, different theories exist (Toriumi and Wang, 2019). Characteristic CMEs have masses of about 5×10^{12} - 10^{13} kg, move outward from the Sun with speeds between 200 km/s and 3000 km/s and have kinetic energies of the same order of magnitude as solar flares, 10^{24} - 10^{25} J (Koskinen, 2011). When these solar structures are observed in the interplanetary space, they become interplanetary CMEs (ICMEs). An ICME hitting Earth disturbs its surroundings and has several effects from the magnetic field down to the lower atmosphere.

For extreme events such as those we studied in Papers II and III, the solar wind easily reaches 1000 km/s and strong disturbances are seen in the magnetosphere[2]. In Paper III, during September 4-10, 2017, we detected two CMEs and their associated shock arrivals at Earth. Fig. 2.3 shows the geomagnetic field (top panel) and the

---

[2]The magnetosphere is defined as the region where the Earth's magnetic (or geomagnetic) field is dominating.

interplanetary magnetic field (IMF, bottom panel)[3] for September 5-11, 2017. The green dashed line displays the second CMEs, which occurred at the Sun on September 6, 12:12 UT, whereas no geomagnetic data were available for the first CMEs, which occurred on September 4. The associated shocks of the first and the second ICMEs were observed at Earth at the early morning and late evening of September 7, respectively (see the green and blue dotted lines in Fig. 2.3). In the geomagnetic field, we observed small perturbations associated with the first shock and a significant drop of the Bz component as a response to the second one.
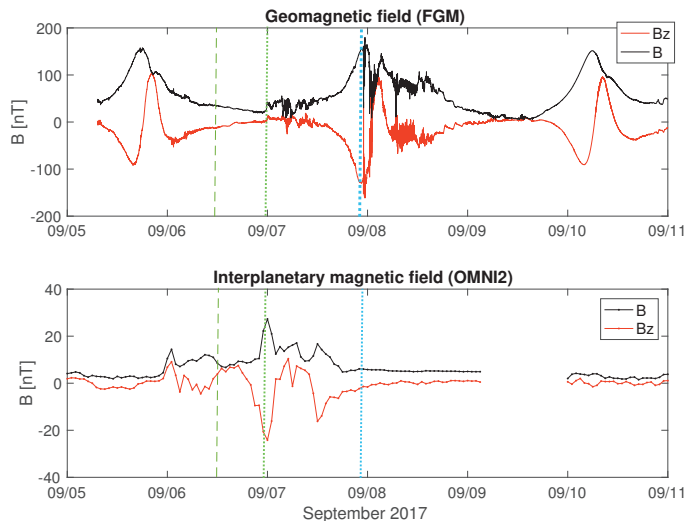
Figure 2.3: Geomagnetic field (FGM-Cluster) and IMF (OMNI2) for September 5 to 11, 2017.

2.1.3 Solar wind

The Sun continuously ejects a stream of particles called the solar wind. In 1958, Parker deduced the solar wind velocity from a theoretical approach based on the hydrodynamic expansion of the solar corona. Considering that the outflow from the Sun (solar wind) is spherically symmetric, isothermal, steady and with a constant rate of mass loss, Parker found an equation derived from the momentum equation (Kamide and Maltsev, 2007)

---

[3]See Section 2.1.3

$$\left(\frac{v}{v_c}\right)^2 - \ln\left(\frac{v}{v_c}\right)^2 = 4\ln\left(\frac{r}{r_c}\right)^2 + 4\frac{r_c}{r} + C. \tag{2.1}$$

where C stands for constant and subscript c for *critical point*. The critical point occurs when $dv/dr \to 0$ and $v_c = \sqrt{RT/\mu}$ and $r_c = GM_s/2v_c^2$ where R is the gas constant, T the coronal temperature (typically 10^6 K), μ the mean atomic weight, G the gravitational constant and M_s the mass of the Sun. In Eq. 2.1, v is the expansion velocity, v_c and r_c are velocity and radius (r_c is typically 6 R_s) at the *critical point* respectively, and r is the expansion radius. This equation has several solutions but only one is the solar wind solution (and was confirmed later on). The valid and physical solution is the one passing through the critical point for $r = r_c$ and $v = v_c$. Fig. 2.4 illustrates the different solutions, the line numbered V indicates the solar wind solution (Kamide and Maltsev, 2007). Solutions I and II are unphysical, whereas III is supersonic and IV is subsonic.
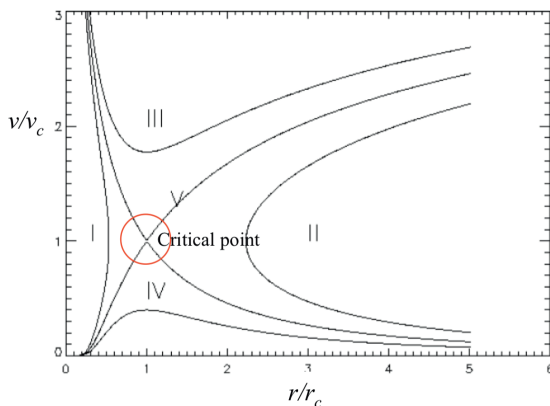
Figure 2.4: Illustration of the solutions given by Eq. 2.1. The solar wind solution defined by Parker is the fifth (V) one passing through the critical point. Credits: Illustration taken from *www.tcd.ie*, lecture from Peter Gallagher, Feb 2006.

Parker deduced the solar wind velocity to be between 260 km/s and 1160 km/s at Earth distance (Hargreaves, 1992), whereas the current observed average value is ~ 470 km/s. This theory of outflowing particles from the solar surface inspired the scientists working with plasma flow at Earth. Thus, the polar wind (see Section 4.3.1) was derived from the solar wind theory developed by Parker.

The solar wind is mainly composed of protons (H^+) with 5% - 10%, He^{2+} (or α-particles) and some heavier ions (0.5%). At 1 AU, its temperature is typically 10 eV and the ion number density is 5 cm^{-3} (Russell et al., 2016). Besides that the solar

wind fills the interplanetary space in the Earth's vicinity, it has a crucial role in the solar-terrestrial coupling by carrying a weak magnetic field called the interplanetary magnetic field (IMF). Since the plasma is highly conductive, the IMF is frozen-in[4] to the plasma and the solar wind has a kinetic energy (left hand side of Eq. 2.2) 8 times bigger than the energy density of the magnetic field (right hand side of Eq. 2.2) (Hargreaves, 1992):

$$\frac{nmv^2}{2} > \frac{B_s^2}{2\mu_0}$$
(2.2)

where n is the particle density, m the particle mass, v the solar wind velocity, B_s the magnetic flux strength and the permeability constant $\mu_0 = 4\pi \times 10^{-7}$ Vs/Am.

2.2 The Earth's magnetosphere

The Earth is immersed in the solar wind and IMF, and it has a dipole-like magnetic field which deflects part of the solar wind and forms the magnetosphere. Outside the magnetosphere, at the Earth's orbit, the solar wind is supersonic but becomes subsonic, compressed and heated by flowing through a wave shock called *bow shock*. The bow shock is formed about 2-3 R_e (Earth radius or 6371 km) upstream at the nose of the magnetosphere, so approximately 12 R_e to 13 R_e from the Earth's centre (see Fig. 2.5). After the bow shock, the shocked solar wind plasma occupies a turbulent region, *the magnetosheath*. In the magnetosheath, the plasma is heated through the conversion of the kinetic energy into thermal energy to approximately 5 to 10 times the solar wind temperature (Kallenrode, 1998). The transition region between the magnetosheath and the outer border of the magnetosphere is *the magnetopause*, where (as first approximation) the magnetic pressure of the geomagnetic field (left hand side of Eq. 2.3) is balanced by the dynamic pressure of the solar wind (right hand side of Eq. 2.3):

$$\frac{B_M^2}{2\mu_0} \simeq \rho_{sw} V_{sw}^2$$
(2.3)

where sw and M stand for solar wind and magnetosphere, ρ_{sw} is the plasma mass density, V_{sw} the velocity, B_M the geomagnetic field strength and μ_0 the permeability constant (Koskinen, 2011). From Eq. 2.3, we see that the magnetopause depends strongly on solar wind conditions and therefore is not stationary. Under strong solar wind conditions the magnetopause is pushed toward Earth whereas it extends outward for lower solar wind velocities. The typical location of the magnetopause is at around 10 R_e (subsolar point), while it has been observed around 6 R_e under extreme conditions such as the Halloween event in October 2003 (Rosenqvist et al., 2005).

The transition region's solar wind - magnetosheath and magnetosheath - magnetosphere are mainly derived by the pressure gradients. In an ideal spherical case

---

[4]In a medium of infinite conductivity, the magnetic field is frozen-in to the plasma and carried away by the matter as if glued to it (Kamide and Maltsev, 2007).

being steady state ($\partial/\partial t = 0$) and irrotational ($\nabla \times \mathbf{u} = 0$), the pressure balance is given by (Schunk and Nagy, 2009)

$$\rho u^2 + p + \frac{B^2}{2\mu_0} = constant \tag{2.4}$$

where ρu^2 is the *dynamic pressure*, p is the *kinetic/thermal pressure* and $B^2/2\mu_0$ the *magnetic pressure*. In the first transition region - bow shock, the dynamic pressure dominates in the solar wind, whereas the kinetic pressure dominates in the magnetosheath. As the sum of the three types of pressure is constant, for the second transition region - magnetopause, the stand off distance of the magnetopause is derived by equaling the dynamic pressure with the magnetic pressure (Eq. 2.3), despite the fact that the kinetic pressure in the magnetosheath is significant. All the regions mentioned above are displayed in Fig. 2.5, a schematic view of the Earth's magnetosphere and its environment.
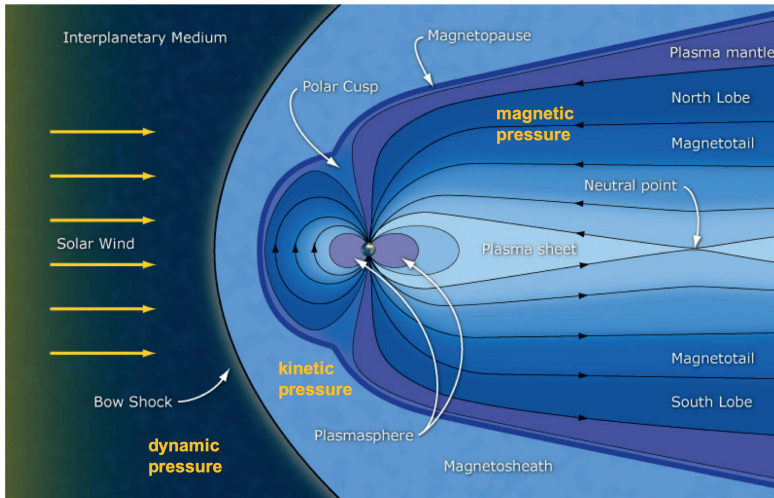
Figure 2.5: Earth's magnetosphere. Credits: ESA/C. T. Russel retrieved from NASA website *https://www.nasa.gov/*.

In the dayside the magnetopause is compressed by the solar wind, while, in the nightside the magnetosphere extends beyond the Moon's orbit ($X \simeq 60$ R$_e$) resulting in the so-called *magnetotail*. The further it extends, the bigger its radius is with a width of approximately 25 to 30 R$_e$ near $X \simeq 200$ R$_e$ (Prölss, 2004). Going back to Eq. 2.4, in the magnetotail the dynamic pressure of the solar wind is much lower and therefore the pressure balance is obtained by the local plasma and the kinetic pressure of the magnetosheath that balance the magnetic pressure from the tail.

The magnetotail is a general term; it contains the *plasma sheet* around the tail midplane. The plasma sheet is a concentrated region of magnetotail plasma near the current sheet that forms between oppositely directed magnetic fields of the two hemispheres. It extends along the field lines to the high-latitude ionosphere near from Earth and the outer parts of the magnetotail (surrounding the plasma sheet) are known as the *lobes*. The lobes map to the central polar cap in the ionosphere.

Under undisturbed magnetospheric conditions, a funnel exists around 78° latitude in the dayside, where magnetosheath plasma enters the magnetosphere along the open magnetic field lines (field lines that are simultaneously magnetically connected to southward IMF and Earth's ionosphere). With one in each hemisphere, these regions are *the cusps*, they separate the closed magnetic field lines from the dayside with the open field lines in the nightside (see Fig. 2.5) and are the main regions where solar wind can penetrate and interact with the Earth's atmosphere. At latitudes higher than typically $\pm$ 78°, the magnetic field lines are open and sweep to the nightside. The footprint of all those open field lines gives the *polar cap*, which is bounded by the auroral oval (Kallenrode, 1998). Fig. 2.6 shows a top view of the high latitudes regions, including the footprint of the cusp (dashed region) and the polar cap (middle circle). The polar cap size and shape vary with solar wind conditions, especially IMF. Under extreme conditions, the polar cap (and cusp) extends to lower latitudes (see Section 4.5 for more details).
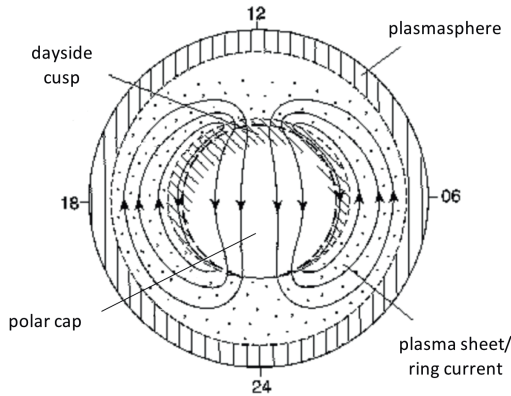
Figure 2.6: Top view of the high latitude regions with the footprint of the magnetosphere. Credits: Adapted from Hutchinson et al. (2011).

Finally, tailward of the cusp, the open magnetic filed lines form the *plasma mantle*, a region with plasma coming from the ionosphere mixed with magnetosheath plasma. The plasma mantle consists of magnetosheath particles reflected in the low-altitude cusp and sufficiently heated through the cusp on their way up to follow open magnetic field line into the nightside (Rosenbauer et al., 1975). The plasma mantle, part of the magnetotail, is characterised by lower density (~ 0.1 cm^{-3} - 1 cm^{-3}) and similar temperatures as in the magnetosheath ($\sim$0.05 keV - 0.2 keV) (Wang et al., 2014).

Magnetospheric regions can be distinguished partly through the plasma beta parameter (β). If we assume a stationary plasma ($\mathbf{u} = 0$) inside the magnetosphere, we see from Eq. 2.4 that the magnetic pressure should be opposite to the kinetic pressure in order to keep the pressure balance. So in magnetospheric regions of strong magnetic field, the density should be lower and vice versa (Schunk and Nagy, 2009). A convenient way to describe such regions, is to use the plasma beta given by the ratio of the thermal pressure and the magnetic pressure,

$$\beta = \frac{p}{B^2/2\mu_0} = \frac{nk_B T}{B^2/2\mu_0}. \tag{2.5}$$

2.3   Geomagnetic storms

Several phenomena can strongly disturb the magnetosphere such as solar flares and CMEs (see Sections 2.1.1 and 2.1.2). When an ICME hits the Earth, depending on the magnetic field orientation it carries, a reconnection process takes place between the geomagnetic field and the IMF. The reconnection process consists of two magnetic field lines with opposite direction that connects together changing the magnetic connectivity. At the dayside magnetopause, this leads to open magnetic field lines. Fig. 2.7 shows the so-called closed magnetosphere where no reconnection happens (top panel) and the open magnetosphere where dayside reconnection happens (bottom panel). The dayside reconnection occurs when IMF is directed southward, whereas lobe/plasma mantle reconnection happens for northward IMF. A third reconnection site is identified in the magnetotail, the neutral line or X-line. This type of reconnection occurs between two geomagnetic field lines one from the north and one from the south lobe respectively. The X-line is usually identified at X $\simeq 100$ R$_e$ and the magnetotail plasma trapped by the newly closed field lines is transported back toward Earth.

Reconnection increases the incoming solar particles entering the magnetosphere as well as magnetic energy that will be stored in the magnetotail. Thus, magnetospheric perturbations due to reconnection may lead to a geomagnetic storm. A characteristic signature of a geomagnetic storm is a depression in the horizontal (H) component of the magnetic field due to an enhanced electric current encircling Earth, the ring current.

A geomagnetic storm is described by three phases, the initial phase, the main phase and the recovery phase, identified from the behaviour of the Dst index (see
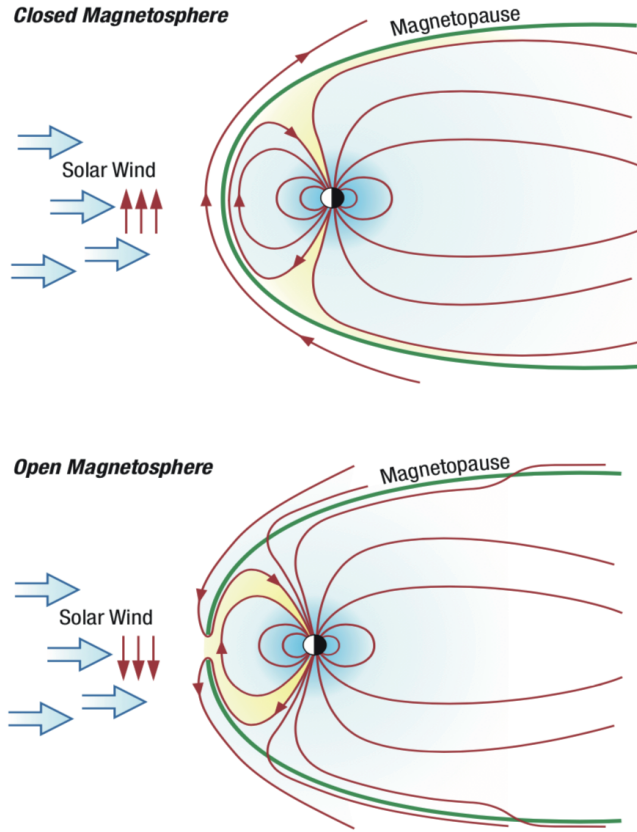
Figure 2.7: Top panel: closed Earth's magnetosphere (without reconnection). Bottom panel: open Earth's magnetosphere (dayside reconnection). Credits: J. A. Eddy, The Sun, the Earth, and Near-Earth Space: A Guide to the Sun-Earth System - Chapter 6, Kindle Editions, 2013.

Section 5.4). Before the initial phase, a storm sudden commencement (SSC) may be observed. It is defined as a sudden positive increase in the H component of the magnetic field created by the compression of the geomagnetic field due to a solar wind discontinuity (shocks, CMEs), but it is not always present. When an SSC occurs, the initial phase is identified by northward IMF and quiet geomagnetic field period following the SSC. The structure of the solar driver determines its length and is therefore highly variable. Without SSC, the initial phase might not be present and the geomagnetic storm is directly initiated with a significant development of the ring current which leads to the main phase (Kamide and Maltsev, 2007).

The main phase is characterised by a drastical drop of the H component and lasts between 2 h and 10 h. The drop is due to significant energisation of the ring current and increased currents in the inner magnetosphere by the input of solar wind energy (Koskinen, 2011). When the input solar wind energy decreases so that the excess energy of the ring current decreases as well, the geomagnetic field returns to a quiet level and the recovery phase has started. Its length varies from a few hours to a few days. Fig. 2.8 shows the behaviour of Dst index for a severe geomagnetic storm that occurred in September 2017 (Paper III). The orange curve displays the Dst index calculated by IRF, Sweden and the blue curve the Dst index estimated by Kyoto, Japan. The vertical blue and red lines represents the ICMEs (solid lines) and the ICMEs-shocks (dashed lines). The numbers indicate the initial phase (1), the main phase (2) and the recovery phase (3). An SSC was also observed in this case.
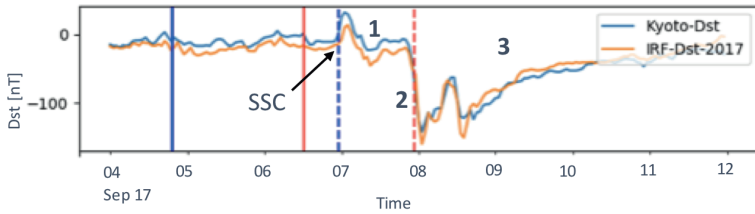
Figure 2.8: Behaviour of the Dst index during the geomagnetic storm of September 4-12, 2017. Credits: A. Schillings et al. (2018), Paper III.

Chapter 3

Plasma Physics

Numerous textbooks discuss (space) plasma physics, thus this chapter aims to describe the physics and the phenomena associated with this thesis work. The information provided in this chapter are mainly taken from Goldston and Rutherford (1995); Kallenrode (1998); Prölss (2004); Schunk and Nagy (2009); Russell et al. (2016).

3.1 Plasma properties

Space is dominated by an ionised gas that is called *plasma*. This 'fourth' state of matter happens when a gas is heated enough that the constituents become ionised, split into free electrons and ions. As an example, hydrogen (gas) consists of one proton and one electron orbiting around the proton. If electromagnetic radiations with sufficient energy are applied, the electron is separated from the proton and hydrogen gas becomes a hydrogen plasma. A plasma can be weakly or fully ionised; for the former, Coulomb collisions are neglected and the electron and ion collisions with neutrals dominate. It is usually found at lower altitude in the ionosphere. Whereas for the latter, Coulomb collision should be considered.

In a plasma, the number of positive and negative charged particles remain nearly equal, consequently the plasma is *quasi-neutral* and appears to be electrically neutral from outside. Thus, the electron and ion density are roughly equal ($n_e \simeq n_i \simeq n$). However, the density is directly related to another plasma parameter, the *Debye length*. The Debye length is defined as the spatial space where electrostatic forces are applied on the charged particles (Kallenrode, 1998). In other words, it is a potential shielding around a charged body. Its expression is given by

$$\lambda_D = \sqrt{\frac{\epsilon_0 k T_e}{q_e^2 n}} \tag{3.1}$$

where ϵ_0 is the permittivity constant, k the Boltzmann constant, T_e the electron temperature, q_e the electron charge and n the plasma density. The Debye length is

proportional to $\sqrt{T_e}$ or $1/\sqrt{n}$, so that an increase of the thermal motion of the plasma or a lighter plasma makes the shielding weaker. This plasma parameter is important when cold ions (low-energised ions) start to be considered around a spacecraft.

3.2 Motion of a charged particle in the geomagnetic field

The Earth magnetic field is approximated as a geocentric dipole, which is tilted by about 11.5° from the Earth's rotation axis. The dipole axis intercepts the Earth's surface in the northern hemisphere at 78°N, 291°E and in the southern hemisphere at 78.5°S, 111°E (geographic coordinates)[1]. This geomagnetic field influences the motion of charged particles. Let's first assume that the magnetic field is homogeneous (**B** uniform) and that the parallel velocity of the particles (along the direction of the magnetic field) is zero: the magnetic field accelerates the particles perpendicularly to their motion as

$$\mathbf{F}_B = m\dot{\mathbf{v}}_\perp = q\mathbf{v}_\perp \times \mathbf{B} \tag{3.2}$$

where m is the mass, $\mathbf{v}_\perp$ the perpendicular velocity, q the charge of the particle and **B** the magnetic field. The magnetic force F_B induces a spiral motion that increases in curvature, however, this motion is opposed to the centrifugal force F_c and results in an equilibrium. This balance between the two forces gives a circular motion to the charged particles, with the radius of this orbit given by

$$F_B = F_c \quad \Rightarrow \quad |q|v_\perp B = \frac{mv_\perp^2}{r} \quad \Rightarrow \quad r = \frac{mv_\perp}{|q|B}. \tag{3.3}$$

This radius is called the *gyroradius* or *Larmor radius*. As seen in Eq. 3.3, the direction of the motion depends on the particle charge, therefore ions and electrons gyrate in opposite direction. The orbital period τ [s] and gyrofrequency ω [rad/s] of the particle are

$$\tau = \frac{2\pi r}{v_\perp} = 2\pi \frac{m}{|q|B} \quad \text{and} \quad \omega = \frac{2\pi}{\tau} = \frac{|q|B}{m} \tag{3.4}$$

respectively. Note that these two parameters are independent from the velocity of the particle. Considering an O$^+$ ion of mass $m_{H+} = 16m_{O+} = 2.68 \times 10^{-26}$ kg with a velocity of 80 km/s at an altitude of 8 R$_e$ (B = 500 nT), its gyroradius is 26.8 km. Thus, in approximation at high altitude (8 R$_e$ - 10 R$_e$), the magnetic field and the O$^+$ gyroradius varies between 500 nT - 50 nT and 27 km - 270 km respectively. The O$^+$ ion at 8 R$_e$ takes 2.1 sec to complete its orbit. This theory is not longer valid

---

[1]These dipole axis interceptions are taken from Schunk and Nagy (2009), however the magnetic pole axis is drifting relatively fast, so that the dipole axis in the model has changed recently (Witze, 2019).

for phenomena which are much smaller than the Larmor radius, in this case particles are insensitive to the magnetic field and equations of unmagnetised plasma should be applied.

If we extend this analysis by including a parallel velocity along the magnetic field, the particle's trajectory becomes helical (along B). The helical trajectory is shown in Fig. 3.1a, left panel. The angle between the magnetic field line and the particle trajectory is called the *pitch angle* (see Fig. 3.1a, right panel), which is defined by

$$\frac{v \sin \alpha}{v \cos \alpha} = \tan \alpha = \frac{v_\perp}{v_\parallel} \quad \Rightarrow \quad \alpha = \arctan \frac{v_\perp}{v_\parallel}. \tag{3.5}$$

(a) Left panel: Particle trajectory in an homogeneous magnetic field. Right panel: Schematic of the pitch angle.

(b) Illustration of Earth's dipole and pitch angle direction according to the hemisphere.
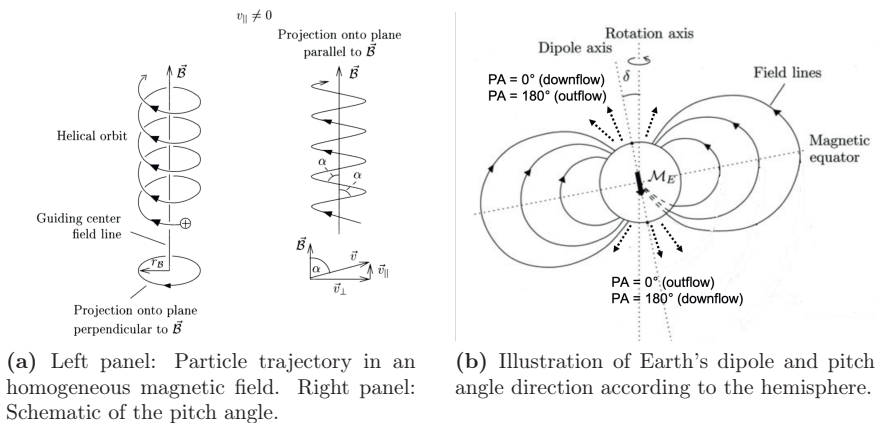
Figure 3.1: Illustrations of the pitch angle. Credits: Prölss (2004)

This parameter is useful to identify ion outflow in the data. In the northern hemisphere (NH) the magnetic field lines are directed toward Earth whereas in the southern hemisphere (SH) they are directed away from Earth. Due to this magnetic configuration, a pitch angle of 180° (opposite direction to the magnetic field line) in the northern hemisphere corresponds to outflowing ions (see Fig. 3.1b). In a similar way, a 0° pitch angle corresponds to downflowing ions (toward Earth). Given that the magnetic field line configuration is reversed in the southern hemisphere, a pitch angle of 0° corresponds to outflowing ions. Fig. 3.2 shows the pitch angle distribution for O^+ (top and middle panels) and H^+ (bottom panel) during a geomagnetic storm (Cluster - CODIF data, see chapter 5). The dashed black boxes illustrate the southern (on the left) and northern (on the right) hemispheres during one Cluster orbit. Additionally, the solid and dashed white line display a pitch angle of 180° (in NH) and 0° (in SH) respectively, corresponding to outflowing O^+ ions.
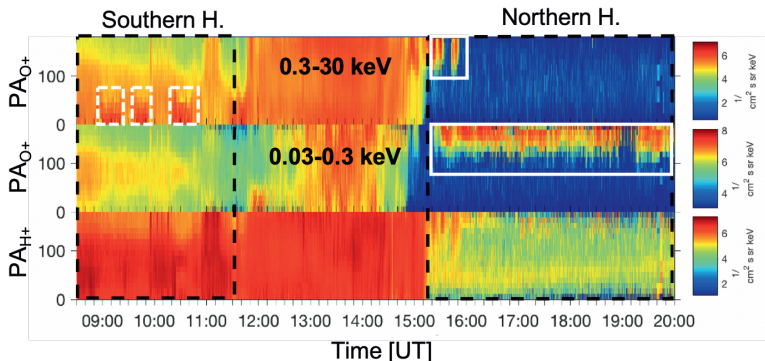
Figure 3.2: Pitch angle (PA) distribution (in degrees) during a geomagnetic storm (Halloween - 29 Oct 2003) - Cluster observations. The top and middle panels show the pitch angle for O^+ ions for different energy ranges, whereas the bottom panel displays the pitch angle for protons. The time is given in UT and the colour bar represents the differential particle flux. Credits: Schillings et al. (2017), Paper II.

3.3 Charged particle in an electromagnetic field

Now, let's add a uniform electric field to our system (in addition to the uniform magnetic field). The two fields are assumed to be time-independent. In this configuration, the perpendicular component of the electric field[2] accelerates (increase the Larmor radius) and decelerates (decrease the Larmor radius) the particle alternatively, depending on whether they move with or against the electric field, which results in the $\boldsymbol{E} \times \boldsymbol{B}$ *drift*. The $\mathbf{E} \times \mathbf{B}$ drift is defined by

$$\mathbf{v}_D = \frac{\mathbf{E}_\perp \times \mathbf{B}}{B^2} \tag{3.6}$$

where $\mathbf{E}_\perp$ is the perpendicular electric field and $\mathbf{B}$ is the magnetic field. Note that neither the mass, neither the charge, nor the velocity influence the particle motion. Therefore, electrons and ions move in the same direction and with the same velocity.

In addition to the $\mathbf{E} \times \mathbf{B}$ drift, the centrifugal force and a non-uniform magnetic field produce curvature and gradient drifts respectively. The curvature drift has an important contribution as it forces the particles to drift along the curvature of the magnetic field lines whereas the gradient drift is derived from a perpendicular gradient to the magnetic field lines. Due to this gradient, the gyroradius increases with decreasing field strength as $r \sim 1/B$, so that the particle's motion is perpendicular

---

[2]The electric field is assumed to be perpendicular to the magnetic field because the parallel electric field creates an ambipolar electric field due to charge separation that roughly cancels its own parallel component.

to the magnetic field and the gradient (see Fig. 3.3). The curvature ($\mathbf{v}_c$) and the gradient drift ($\mathbf{v}_{\nabla \mathbf{B}}$) are defined by

$$\mathbf{v}_c = \frac{mv_{\parallel}^2}{qB^3}\mathbf{B} \times \nabla_{\perp}\mathbf{B},$$

$$\mathbf{v}_{\nabla \mathbf{B}} = \pm\frac{v_{\perp}r}{2B^2}\mathbf{B} \times \nabla\mathbf{B} \tag{3.7}$$

respectively. All parameters in Eq. 3.7 are already defined in the previous sections. Together, these two drifts reinforce and superpose each others, so that they create a westward ring current around Earth.
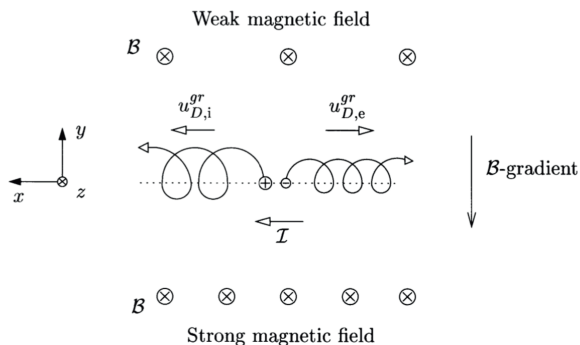
Figure 3.3: Illustration of the gradient drift. Credits: Prölss (2004).

3.4 The three adiabatic invariants

The invariants in the particle's motion are based on the hypothesis that fields are changing slowly compared to the gyroperiod or that scale lengths are much greater than the gyroradius, therefore some parameters are considered invariant. This section is based on Kallenrode (1998).

3.4.1 Magnetic moment

The first adiabatic invariant is the magnetic moment of the particle. In an inhomogeneous magnetic field, the force on a magnetic dipole is defined as

$$\mathbf{F} = \mu \cdot \nabla\mathbf{B} \qquad \text{with} \qquad \mu = \frac{mv_{\perp}^2}{2B} \tag{3.8}$$

19

where μ is the magnetic moment. An application of the first adiabatic moment is the magnetic mirror. This phenomenon is explained by a gradient in the magnetic field and no electric field, thus the kinetic energy of the particle is conserved and written as

$$\frac{mv^2}{2} = \frac{1}{2}m(v_\parallel^2 + v_\perp^2) = \frac{1}{2}mv_\parallel^2 + \mu B = constant. \tag{3.9}$$

Considering that the magnetic moment is invariant, if B increases, $v_\parallel$ decreases accordingly. When the parallel velocity reach zero, $v_{tot} = v_\perp$ and the entire drift energy is transformed into gyration energy (μB). This point is called the *mirror point* and is the location where the particle is reflected back toward the diverging magnetic field. The location of the mirror point is given by the pitch angle of the particle (see Section 3.2), which increases with the magnetic field strength. For an initial pitch angle of 0°, $\mu = 0$ and the particle is not affected by the mirror, whereas if the initial pitch angle is 90° then the particle will only have gyration energy and the particle is stuck at the mirror point. Furthermore, for a pitch angle between 0° and 90°, the particle is (a) either transmitted or (b) reflected back. In the first case (a) the gradient is too weak to convert the drift energy into gyration energy, while in the second case (b) the gradient is sufficient and the particle is reflected at the mirror point. The condition defining if the particle is reflected or transmitted is

$$\mu = \frac{mv_{\perp 1}^2}{2B_1} = \frac{mv_{\perp 2}^2}{2B_2}$$

so that $\quad \dfrac{v_1^2 \sin^2 \alpha_1}{B_1} = \dfrac{v_2^2 \sin^2 \alpha_2}{B_2}$ $\tag{3.10}$

where 1, 2 denoted two points in the magnetic field. The relation comes from the constancy of μ that indicates a constancy in the ratio of the gyration energy and the magnetic field strength. Additionally, the velocity can then be rewritten using the pitch angle. In Eq. 3.10, $v_1 = v_2$ because the kinetic energy is constant, therefore we obtain

$$\frac{2\mu}{mv^2} = \frac{\sin^2 \alpha_{1,2}}{B_{1,2}}$$

that becomes $\quad \alpha_{1,2} = \arcsin \sqrt{\dfrac{B_{1,2}}{B_{mp}}}$ $\tag{3.11}$

where B_{mp} is the magnetic field strength at the mirror point. At B_{mp}, the particles with an initial pitch angle $\alpha_{1,2}$ will be reflected, particles with a larger α are reflected earlier whereas particles with a smaller α will pass through. So, Eq. 3.11 determines the limit of the *loss cone*, a cone in which particles will pass without being reflected (so transmitted). Two magnetic mirrors give a *magnetic bottle*, where particles are trapped between two mirror points.

3.4.2 Bounce invariant

The second adiabatic invariant is directly related to the magnetic bottle. Considering a stable magnetic field, the integral over the distance between the two mirror points is constant. The relation is written as

$$J = \int_{s_1}^{s_2} mv_\parallel ds = \int_{s_1}^{s_2} m\sqrt{v^2 - \frac{2\mu B}{m}} ds \qquad (3.12)$$

where s is the distance along the field line and $v_\parallel$ is derived from Eq. 3.9. In the magnetosphere, the particles bounce between two magnetic mirrors (see Fig. 3.4a). However, the curvature of the magnetic field lines should be taken into account, so that the particles additionally to the bouncing motion also drift around Earth due to the dipole field. The electron drift to the west whereas ions drift to the east, which form the ring current (see also Section 3.3).

| (a) Bounce motion. | (b) Three adiabatic invariants. |
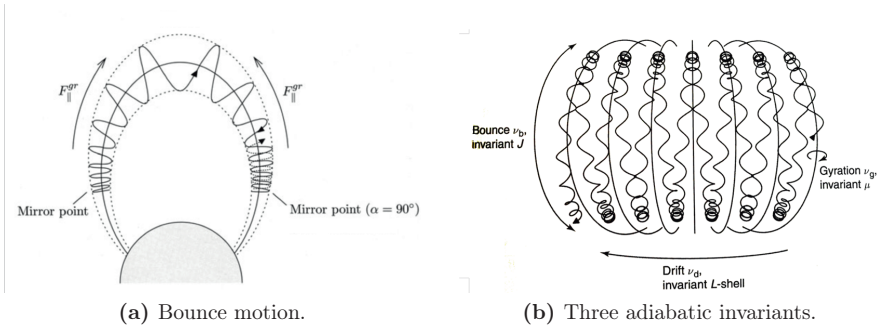
Figure 3.4: Illustrations of adiabatic invariants. Credits: Prölss (2004) (on the left), Russell et al. (2016) (on the right).

3.4.3 L-shell

The third adiabatic invariant is the conservation of the magnetic flux encircled by the drift orbit of the particle. The variations of the magnetic field create an adjustment of the surface where the particle moves so that the magnetic flux enclosed by this surface stays constant. This invariant is based on the distance between the two mirror points, therefore the *shell parameter L* can be introduced. The L-shell is defined as "*the geocentric distance of a magnetic field line in the geomagnetic equatorial plane*" (Prölss, 2004). Subsequently, the invariant is also called L-shell invariant.

3.5   Particle's motion in the Earth's magnetosphere

The presence of magnetic and electric fields lead to drift in the particle's motion. The most important have been introduced in this chapter; the $\mathbf{E} \times \mathbf{B}$ drift (or electric drift) in Eq. 3.6, the gradient and curvature drifts in Eq. 3.7. As already mentioned in the previous sections, these drifts require length and spatial scales to be larger than the Larmor radius and gyroperiod, respectively. Finally, the three invariants described in Section 3.4 gives a good idea of the particle's motion in the Earth's environment (see Fig. 3.4b).

An application of this theory is directly used in our forward tracing code of O^+ ions observed the plasma mantle (see Paper V). A magnetic field (Tsyganenko T96) and an ionospheric potential (Weimer 2001) models are employed to represent the magnetosphere, while the ions are traced with the Lorentz force $md\mathbf{v}/dt = q(\mathbf{E} + \mathbf{v} \times \mathbf{B})$. Therefore, to initiate the motion of O^+, the total velocity utilised in the Lorentz force is given by

$$v_{tot} = v_{\parallel} \frac{\mathbf{B}}{B} + v_{E \times B} + v_{\perp} \frac{\mathbf{E}}{E}. \tag{3.13}$$

where $v_{\parallel}$ is the parallel velocity along the magnetic field line, $v_{E \times B}$ is the $\mathbf{E} \times \mathbf{B}$ drift and $v_{\perp}$ is the perpendicular velocity along the electric field. Figure 3.5 shows an example of an O^+ ion from the plasma mantle traced forward in time using Tsyganenko T96 model for the magnetic field (Tsyganenko, 1995) and Weimer 2001 model for the electric field (Weimer, 2001). The ion is represented in XZ and XY planes. The initial position, in the plasma mantle (the cross in Fig. 3.5), is taken from Cluster observation on 21$^{\text{st}}$ of December 2002 between 14.34 UT - 14.47 UT (see Tab. 3.1). Additionally, the ion initial parallel and perpendicular velocities (referred to in Eq. 3.13) are also given by Cluster observations (see Tab. 3.1).

In Fig. 3.5 the trajectory of the oxygen ion clearly shows two mirror points as well as the bouncing phenomenon. To summarise, the ion starts in the plasma mantle (SH) with a perpendicular velocity that is about twice the parallel one. The ion eventually interacts with the plasma sheet in the equatorial plane at around -55 R_e in X direction, then drifts back toward Earth and is trapped for some time in the mirror bottle. The final destination of the sample ion is at high altitude (about 8 R_e) and in the dusk side at around 9 R_e, where it leaves the simulation box and is lost from the magnetosphere. The time between the starting and ending points is approximately 256 minutes. This trajectory simulation based on data observations shows the different phenomena describe in this chapter.

Table 3.1: Parameters corresponding to the tracing of one O^+ ion in the plasma mantle. Date: 21.12.2002 and trajectory nb 30. Pos = position.

Start Pos (x,y,z) $[R_e]$	Final Pos (x,y,z) $[R_e]$	v_{perp} [km/s]	v_{par} [km/s]	Time [min]
(4.12, 2.01, -8.28)	(-7.74, 9.72, 8.09)	48.14	29.36	256.25
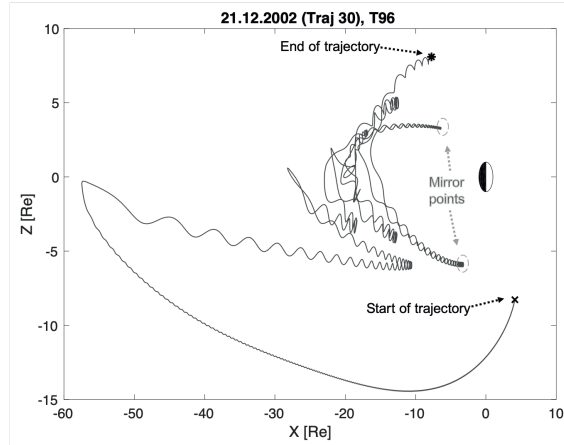
(a) XZ plane.
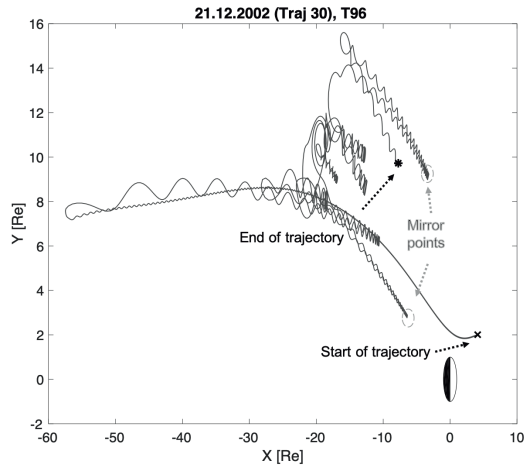
(b) XY plane.

Figure 3.5: One O^+ ion from the plasma mantle traced forward in time using Tsyganenko T96 and Weimer 2001 models (21.12.2002).

Ion outflow and escape

In the past - 4 billion of years ago - the Sun was more active than today, namely more flares were produced and more extreme ultraviolet radiation emitted. These past conditions could be similar to the nowadays geomagnetic storm conditions. In addition to the fact that the upper atmosphere is constantly losing ions, in particular oxygen ions (O^+), the ion outflow and escape during geomagnetic storms becomes fundamental in order to understand the evolution of the terrestrial atmosphere on evolutionary timescales. This field of study started with observations of ion flux moving upward, called **upflow**, but still gravitationally bound. Later on, with new space technologies, the observed upward flow becomes observations of **outflow** and in some cases **escape**. Outflow is our term for ions with enough energy to escape the Earth's gravity, however outflowing ions may stay in the magnetosphere, whereas escaping ions are lost into the solar wind (outside the magnetosphere). This chapter describes first the general terrestrial escape mechanisms, then the history of ion outflow observations followed by the current knowledge about the ion outflow processes and finally the terrestrial matter balance.

4.1   Terrestrial escape mechanisms

The gravity binds the neutral atmosphere to the planet, except for a few particles with enough energy to escape gravitation. At the same time atmospheric composition and temperatures are altitude dependent. With increasing altitude, collisions between neutrals become less frequent until the transition region between the collisional and collisionless regions, called the *exobase* (Schunk and Nagy, 2009). The exobase at Earth is located around 500 km and has a typical temperature of 1000 K (Shizgal and Arkos, 1996). The region above the exobase, the *exosphere*, is dominated by atomic oxygen and as minor species, hydrogen and helium (Shizgal and Arkos, 1996). These particles follow ballistic trajectories because their mean-free-path is long enough. In this region, some particles have sufficient large velocity to escape Earth's gravity,

thus part of the upward flux becomes outflow (see Section 4.2). This *escape velocity* is defined as *"the kinetic energy adequate to liberate a particle from the potential barrier of the planet's gravitational field"* (Salby, 1996) and is then given by

$$v_{esc} = \sqrt{\frac{2GM_E}{r}} \tag{4.1}$$

where G is the gravitational constant, M_E is the mass of the Earth and r the radial distance from the Earth's centre to the exobase (6371 km + 500 km). At Earth, the escape velocity is approximately 11 km/s and the corresponding energies can be easily calculated from $E_{esc} = 0.5mv_{esc}^2$, which gives 0.61 eV for hydrogen, 2.4 eV for helium and 9.7 eV for oxygen. The particles with exceeding energy or velocity overcome gravity and become outflow.

Several escape mechanisms exist and according to the type of celestial body some mechanism might be more important than others. In this section, only the mechanisms relevant to Earth are presented and discussed.

4.1.1 Thermal escape

Thermal escape includes Jeans escape and hydrodynamic escape. The former quantifies the flux that evaporates from the atmosphere while the latter is an expansion of the atmosphere driven by bulk velocity of light gas that induces an upward pressure gradient force (Hunten, 1973). Hydrodynamic escape is believed to have played a major role in the early phase of the solar system, 4 billion of years ago, when solar EUV radiation was much stronger than nowadays[1].

Jeans escape flux occurs where the atmosphere is approximately collisionless, so in the vicinity of the exobase. Thus, the Jeans escape flux is dependent on the temperature and density of the particles and is defined as (Shizgal and Arkos, 1996; Hunten, 1973)

$$\phi_J = \frac{n_{exo}}{2} \sqrt{\frac{2k_B T_{exo}}{m\pi}} (1 + \lambda_{exo}) \exp\left(-\lambda_{exo}\right)$$

$$\text{with} \quad \lambda_{exo} = \frac{E_{esc}}{k_B T_{exo}} \tag{4.2}$$

where n_{exo}, T_{exo} and λ_{exo} are density, temperature and escape parameter of the escaping species respectively, k_B is the Boltzmann constant and m the mass of the particle. If we calculate the escape parameter for oxygen and hydrogen atoms in vicinity of the exobase (T = 1000 K), we obtain $\lambda_{exo}(\text{O}) \simeq 2.7 \times 10^{-51}$ and $\lambda_{exo}(\text{H}) \simeq 6.9 \times 10^{-4}$ respectively. Subsequently, the Jeans escape flux for oxygen is negligible compare to hydrogen, which is expected due to the low hydrogen mass (see Fig. 4.1). The average thermal velocity for hydrogen will then be 4 km/s which is well below the escape

---

[1]Hydrodynamic escape will not be discussed in this thesis because it is not a major escape mechanism, for more detail see Hunten (1973).

velocity. However, a significant proportion of hydrogen reach a higher velocity than the escape velocity and escape the atmosphere (see Fig. 4.1 end of the distribution). This escape flux is determined by $\phi_{esc} = 0.5 \ \phi_J$ (Salby, 1996). Consequently, very few hydrogen are found in the atmosphere, even though hydrogen has a significant production due to photodissociation of H_2O (Salby, 1996).
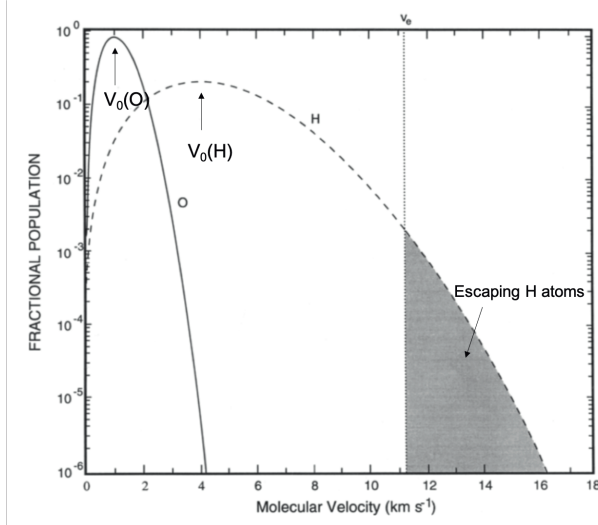
Figure 4.1: Maxwellian distribution of velocity for atomic O and H. $V_0(O)$ and $V_0(H)$ represents the most probable velocity for O and H in the distribution, whereas V_e is the velocity escape defined in Eq. 4.1. Credits: Salby (1996).

4.1.2   Nonthermal (suprathermal) escape

One of the main nonthermal escape mechanisms for neutrals on Earth is charge exchange. During this reaction, a charged particle such as O^+ or H^+, collides with a neutral atom (or molecule) that gives an electron to the initially charged particle. This particle becomes neutral, however, very little energy is transferred between the initially charged particle and the neutral atom. As a result, the initially charged particle becomes an energetic neutral atom that is not constrained by electric and magnetic fields and have enough energy to escape the atmosphere. Its path becomes a straight line from the location of the collision. The remaining ion is trapped by the magnetic field. The charge exchange for energetic (hot) hydrogen is given by (Schunk and Nagy, 2009)

$$H^+_{hot} + H \rightarrow H^+ + H_{hot}$$
$$H^+_{hot} + O \rightarrow O^+ + H_{hot}$$
$$(4.3)$$
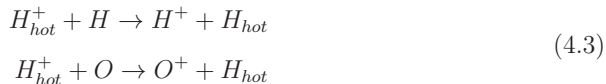
According to the escape energy determined in the introduction of Section 4.1, if the hydrogen ion (H^+_{hot}) has an energy greater than 0.61 eV and moving upward, the newborn energetic neutral H_{hot} will escape the atmosphere. With an increase of the exospheric temperature, the charge exchange hydrogen flux decreases while the Jeans escape flux (for hydrogen) increases, so that the sum of the two fluxes remains constant for a temperature range of 1000 K - 1400 K (Bertaux, 1975).

The main nonthermal escape mechanism for ionised particles is ion outflow, which is the main topic of this thesis. Thus, the following sections discuss this mechanism in detail.

4.2   Introduction to ion outflow

The idea that particles could flow up or even escape the upper ionosphere along open magnetic field lines grew in the 1960s. Dessler and Michel (1966) describe a model of how plasma from the polar cap flow into the magnetotail. The authors argue that the plasma density above the polar cap is limited by the protons and electrons fluxes flowing out from the ionosphere. These ions flowing out are then replaced by new solar wind ionisation of the neutral atmosphere. Axford (1968) studied mainly the helium (He^+) escape and suggested that heavier ions such as O^+ in the open magnetic field line regions also flow out into interplanetary space. Similarly to the flow of the solar wind, the author named this phenomenon *polar wind* (Axford, 1968). The polar wind (ions and photoelectrons) is a thermal plasma, originating in the polar ionosphere accelerated by ambipolar diffusion[2], that escapes the Earth's gravitation and therefore flows outward along open magnetic field lines.

Banks and Holzer (1968) showed that along open magnetic field lines a large scale hydrodynamic expansion of the plasma causes H^+ and He^+ supersonic flow. Almost simultaneously, in-situ observations from the Explorer 31 satellite, confirmed an upward flow of H^+ from the polar ionosphere with a velocity of 10 to 15 km/s in the open magnetic field lines region and an O^+ dominance at 2800 km altitude (Hoffman, 1968). Additionally at higher altitudes (5000 km to 8000 km), observations of accelerated O^+ and H^+ along and across magnetic field lines have been reported by Shelley et al. (1976) and Sharp et al. (1977). Afterward, several observations of polar

---

[2]Ambipolar diffusion is the motion of ions and electrons together in an electrostatic field. This field is created by the polarisation electrostatic field due to charge separation along a magnetic field line. Indeed, electrons are more mobile than ions because they are lighter. Therefore, they move faster along the magnetic field line, create a charge separation (ions move slower) which leads to an electrical potential. This electrical potential will act on the ions (accelerates them) to maintain the charge neutrality. So the ions "are dragged" by the electrons.

wind ions were made such as with Dynamic Explorer 1 satellite (Nagai et al., 1984; Green and Waite, 1985; Chandler et al., 1991). Some years later, Abe et al. (1993) made a statistical analysis related to the altitude, invariant latitude and magnetic local time of the polar wind (low energy, few eV, O^+, H^+, He^+ and electrons). The authors observed O^+ velocities of 4 km/s and an O^+ outflow of 10^6 cm^{-2} s^{-1} around 1.6 R_e (10 000 km). Through the in-situ observations and many studies, e.g. Shelley et al. (1982); Green and Waite (1985); Chappell et al. (1987) and references therein, it became clear that the ionosphere was the main source of the polar wind. The polar wind signatures and mechanisms were reviewed by Yau et al. (2007).

At higher altitude, we currently do not refer to the polar wind anymore because it is difficult to distinguish the ionospheric H^+ from the solar wind H^+, therefore ion outflow studies are generally reduced to ionospheric O^+ outflow only. In addition, ion outflow is nowadays divided into cold ion outflow and (hot) ion outflow, which means ions with higher energies (up to few keV). Shelley et al. (1982) already observed energetic (up to few hundred eV) O^+ flowing upward and pointed out that these energetic ions were not consistent with the definition of the polar wind (composed of low energy ions). The authors suggested that these ions observed in the tail lobe flow outward with an energy range of approximately 10 eV to 100 eV and due to their higher energy enter the plasma sheet at great distances but still represent a significant source to maintain it. This discovery of energetic O^+ reevaluated the belief that the solar wind was the source of the hot magnetospheric plasma. Chappell et al. (1987) said that *"the ionosphere alone was capable of supplying the density of plasma that is measured in all regions of the Earth's magnetosphere"*.

4.3   Ion outflow signatures

This section describes the different signatures of ion upflow/outflow in the polar regions. However, a strict limit between these signatures does not exist and therefore an ion outflow might be associated to a signature at a certain altitude, but to another signature for another given altitude or location.

The ion outflow signature can be divided into bulk ion (up)flow and energetic ion outflow (Yau and André, 1997; André and Yau, 1997). The first category includes the ions that gain bulk flow energy up to a few eV along (parallel to) the geomagnetic field, like (1) the polar wind and (2) the auroral bulk O^+ upflow, whereas the second one contains energetic ions (few eV to several keV) such as (3) ion beams/conics and (4) upwelling ions. Fig. 4.2 illustrates the different sources and mechanisms of the ionospheric plasma outflow. The observed signatures (written in blue) for ionospheric outflow are the polar wind, ion conics/beams and "ion fountain" (also known as cleft/cusp ion fountain or CIF). Whereas the mechanisms (written in red) are wave heating, centrifugal acceleration, ambipolar diffusion and Joule heating. Each category has a prevalent energisation mechanism, however, several mechanisms can contribute to the same signature and the total ion outflow is a combination of different signatures. Consequently, polar wind can be accelerated into energetic ion

outflow such as upwelling ions and transported over the polar cap. Additionally, convection may bring ions from one region to another, mixing this ideal signatures. Part of the cusp population with low parallel velocity, will drift into the polar cap and form first the CIF and may later be added to the polar wind (Yau et al., 2007).
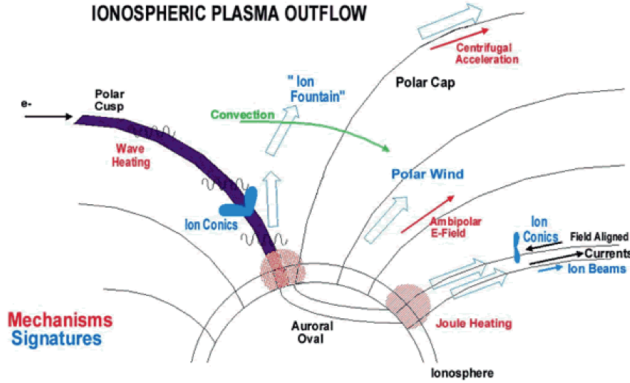
Figure 4.2: Schematic view of sources and outflow mechanisms. Credits: Max Planck Institute - Cluster Ion Spectrometer (CIS).

4.3.1 Polar wind

As already mentioned in Section 4.2, the polar wind is composed of electrons and thermal low-energy (< 10 eV) ions, namely O^+, He^+, H^+. Its composition results from charge exchange between an atomic hydrogen and an oxygen ion for H^+, from the ionospheric F-region, where O^+ is dominant, and finally from photoionisation of atmospheric helium for He^+. These ions are mainly accelerated through ambipolar diffusion. The resulting polarised electric field is larger in the dayside than in the nightside and therefore leads, at a given altitude, to higher velocities (all species) in the dayside. Thus, the ion velocities usually increase with altitude (Hultqvist et al., 1999) and reach 1 km/s near 2000 km, 3000 km and 6000 km for H^+, He^+ and O^+ respectively (André and Yau, 1997). This bulk outflow occurs over the polar cap on open magnetic field lines and has been observed from 500 km to more than 10000 km. In-situ observations of polar wind were made with ISIS-2 in the 1970's, DE-1 in the 1980's and Akebono as well as POLAR satellites in the 1990's[3] (Yau et al., 2007). These observations cover almost three solar cycles during various periods. Furthermore, Yau et al. (2007) review all the polar wind models developed in the end of last century in order to explain polar wind behaviour.

---

[3]For further details about all these observations, we refer the reader to Yau et al. (2007).

4.3.2 Auroral bulk upflow

Auroral bulk upflow, as its name indicates, is still gravitationally bound. It contains mainly O^+ but sometimes also NO^+ and is observed in the topside auroral ionosphere, ~ 500 km (Yau and André, 1997) at velocities from 100 to 1000 m/s (Hultqvist et al., 1999). For upflows higher than 100 m/s, the occurrence peak is shifted equatorward and increases with geomagnetic activity (Kp index). Furthermore, in the polar cap, the upflow has been estimated to be several times larger for northward IMF compared to southward IMF (Yau et al., 2011). Highly time- and location-dependent and generally observed in a latitudinal narrow region, the ions are locally energised by electron heating from the precipitating auroral electrons. They are accelerated by either an increase in the ion temperature, which increases the ion scale height[4] and lifts the ions at higher altitude, or an increase of the electron scale height, which enhances the ambipolar diffusion and accelerates the ions (Zhang and Paxton, 2016). In the cusp, additional energy from the solar wind may be added through particle precipitation or electromagnetic fields (Strangeway et al., 2005) and has partially been studied with radars observations (Nilsson et al., 1996; Ogawa et al., 2009). This additional energy could also enhance the ambipolar diffusion, heat the heavier ions and possibly give them enough energy to become outflow and escape. In the auroral zone and at electron and ion temperatures higher than 4000 K and 3500 K respectively, the averaged auroral bulk upflow increases to roughly 2×10^9 cm^{-2} s^{-1} (Kamide and Maltsev, 2007).

4.3.3 Upwelling ions

The upwelling ions are observed almost uniformly in the dayside (morning sector) and at lower latitude in the polar cap (Pollock et al., 1990). In the dayside auroral region, the ion upflow occurs in regions of large ion convection velocities and are transported tailward. This convection pattern combined with the upflow results in the "cleft ion fountain" (see Fig. 4.2) (Lockwood et al., 1985). Upwelling ions are energised from 1 to 10 eV mainly through perpendicular energisation (wave-particle interactions) and a small fraction through the parallel component of the electric field (Yau and André, 1997). The ions have an upward velocity between 1 and 10 km/s (André and Yau, 1997) and O^+ is the dominant specie (Pollock et al., 1990). According to Lockwood et al. (1985), their occurrence probability is 60% between 75° and 80° latitudes.

---

[4]The scale height is the distance over which density or pressure falls to $1/e$, and may vary in an atmosphere if the temperature is not constant. It is defined by $H = \frac{k_B T}{mg}$ where k_B is the Boltzmann constant, T the temperature, m the mass and g the acceleration due to gravity.

4.3.4 Ion conics and ion beams

The ion beams are upflowing ions usually observed above 5000 km altitude but can be seen down to 2000 km during disturbed conditions, and have their peak flux along magnetic field lines. This is in contrast to the ion conics that have their peak flux with an angle to the magnetic field direction and have been observed at altitudes down to approximately 1000 km (Yau and André, 1997). The occurrence probability of ion beams increases with altitude whereas it decreases (above $\sim 10\,000$ km) for ion conics. The ion conics category includes the transversely accelerated ions (also TAI) that have a pitch-angle (PA, see Section 3.2 for the definition) of approximately 90°. They have been observed in the dayside and nightside at different altitudes. The distinction between ion conics and upwelling ions is complex, especially that the heating mechanism might be similar with the only difference that for upwelling ions the heating is observed at lower energy (André and Yau, 1997). Ion beams, conics and TAI are dominated by H^+ and O^+ with energy between 10 eV to a few keV (Hultqvist et al., 1999), however, ion conics dominate in the cusp regions, whereas ion beams dominate in the prenoon and postnoon sectors outside the cusp (Øieroset et al., 1999).

Fig. 4.3 shows an example of ion beams and ion conics in the auroral zone taken by the FAST satellite in February 1997. The ion beam marked in yellow consists of ions flowing upward along the magnetic field line with a pitch-angle of 180°, similarly the ion conic marked in light blue is ions flowing upward (also along the magnetic field) but with an angle to the magnetic field line. In the velocity space, ion beams only have a parallel component, while ion conics are folded due to an additional perpendicular component.
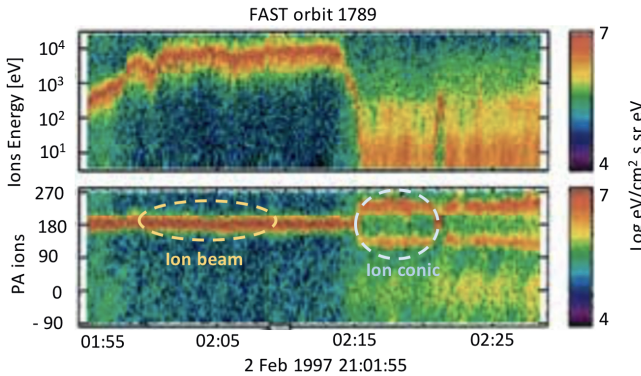

Figure 4.3: Ion beams and conics observed by FAST satellite during pre-midnight auroral zone crossing. Credits: Adapted from Carlson et al. (2001), *Space Science Review*.

4.4 Ion energisation mechanisms

As already mentioned for the ion signatures, several ionisation mechanisms can contribute to the same ion signature or one mechanism can contribute to different signatures. Polar wind, auroral bulk flow and upwelling ions are originally still gravitationally bound, their energy and velocity is below the escape energy/velocity described in Section 4.1. In order to become outflow or to escape into interplanetary space, they should be enough energised along the upflow/outflow path of the particles. The main escaping path is the regions of open magnetic field lines, which include the polar cap, the cusp and the plasma mantle (Nilsson et al., 2012).

At lower altitudes, polar wind and auroral bulk upflow are heated mainly through ambipolar diffusion. The ion upflow is moving upward due to the polarised electric field (that we already discussed partly in Sections 4.2 and 4.3.1). Photoionisation produces hot electrons, which in turn produce an enhanced electron temperature and creates a polarisation electric field. An alternative way that leads to enhanced ionospheric electron temperature is precipitation of low-energised electrons (~ 100 eV). Consequently, ions are accelerated upward.

Nilsson (2011) describes three forms of ion energisation at higher altitudes; field-aligned electric field that gives field-aligned acceleration, perpendicular heating by waves combined with the mirror force, and centrifugal acceleration. In the auroral zone at altitudes from a few thousand km to roughly 3 R_e (Zhang and Paxton, 2016), a quasi-static electric field parallel to the auroral magnetic field lines may form (see Fig. 4.4). The existence of field-aligned electric fields is well known but theoretical models remain challenging and the associated quasi-static acceleration is also intensely investigated. Nevertheless, similar quasi-static acceleration structures have been observed by Cluster in the polar cap under prolonged northward IMF (Maggiolo et al., 2006). Thus, when the ions, accelerated by a quasi-static parallel electric field, reach thermal energies of a few hundred eV, an energy exchange is produced between ions species and the heavier ions, such as O^+, become more energetic. Maggiolo et al. (2006) suggested that the cusp is a continuous source of energetic plasma whereas the polar cap is just an intermittent source region. Fig. 4.4 illustrates the field-aligned acceleration mechanism. On the left side, the ionosphere inside the U-shaped electric potential is negatively charged therefore the parallel electric field is directed upward and subsequently electrons precipitate and form an aurora, whereas ions are accelerated upward. On the right side, the opposite scenario is shown, the ion precipitation causes a "black" aurora and electrons are moving upward.

In the cusp, the perpendicular heating is mainly due to wave-particle interactions (Norqvist et al., 1996; Norqvist et al., 1998; Bouhram et al., 2005; Strangeway et al., 2005; Slapak et al., 2011; Waara et al., 2011) that effectively energise the O^+. This perpendicular energy (from the perpendicular heating) is then converted into parallel energy, in weaker geomagnetic field regions, by the mirror force and subsequently the ions are accelerated along the magnetic field lines. Slapak et al. (2011) studied different events with wave-activity in the cusp and plasma mantle and observed that
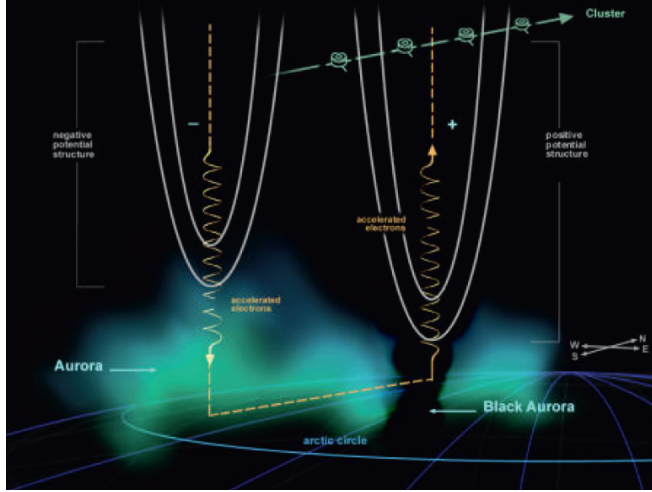
Figure 4.4: Illustration of the fiel-aligned acceleration mechanism in the low altitude cusp. Credits: ESA.

25% to 45% of the observed wave spectral density at the gyrofrequency can explain the observed enhanced perpendicular temperature. The O^+ perpendicular temperature increases with altitude from approximately 10 eV at an altitude corresponding to a magnetic field strength of 150 nT to a few keV at 50 nT despite the effect of the mirror force (Nilsson et al., 2006). It was also shown that the perpendicular heating of high-altitude O^+ with high temperature takes place a few R_e from their observation location.

The last mechanism discussed in this thesis, is the centrifugal acceleration that is observed when a convection electric field is present, while ions move along bending magnetic field lines. This convection electric field provides the energy to accelerate the ions in a changing magnetic field curvature. The ions moves with an $\mathbf{E} \times \mathbf{B}$ drift, which is curved due to the shape of the magnetic field. This curvature leads to a centrifugal acceleration (Nilsson et al., 2008; Nilsson, 2011). Nilsson et al. (2008) found that the centrifugal acceleration is about 10 m/s^2 but often reaches 100 m/s^2 near the magnetopause and consequently the ions gain energy up to several 100 eV. This mechanism has a significant impact on the ions in the high-altitude cusp as well as the plasma mantle (Nilsson, 2011) and explains the observations of O^+ field-aligned velocities in the high-altitude polar cap (Nilsson et al., 2008).

4.5 Ion outflow under disturbed magnetospheric conditions

It is well known that the ion outflow rate increases during disturbed geomagnetic conditions. Kistler et al. (2006) discussed the enhanced O^+ density and pressure observed in the plasma sheet during disturbed conditions. They found that during storm conditions, the O^+ density and pressure is a factor of 5 higher than during non-storm conditions. In a similar way, during geomagnetic storms, Kistler et al. (2010) estimated an enhancement by a factor 10 of the O^+ density in the cusp. Coming from the cusp, these O^+ are accelerated via an enhanced $\mathbf{E} \times \mathbf{B}$ velocity under the influence of the geomagnetic activity (Liao et al., 2015). Disturbed magnetospheric conditions influence also the motion of the cusp and plasma mantle that move equatorward (Newell et al., 1989) as well as the polar cap area, which is extended 2 to 3 times more than during undisturbed conditions (Li et al., 2012). These features have been observed during the September 2017 storm (Schillings et al. (2018), Paper III). Besides energetic ion outflow, cold ions have also been investigated during disturbed magnetospheric conditions. Cold ion outflow increases during disturbed conditions (Haaland et al., 2012; Li et al., 2012), however depending on the storm intensity, their density and bulk velocity vary (Haaland et al., 2015). Haaland et al. (2015) found that the density increases by a factor of 4 and bulk velocity is typically doubled between quiet and disturbed times. They suggested that the increase in the bulk velocity is due to enhanced convection in the polar cap.
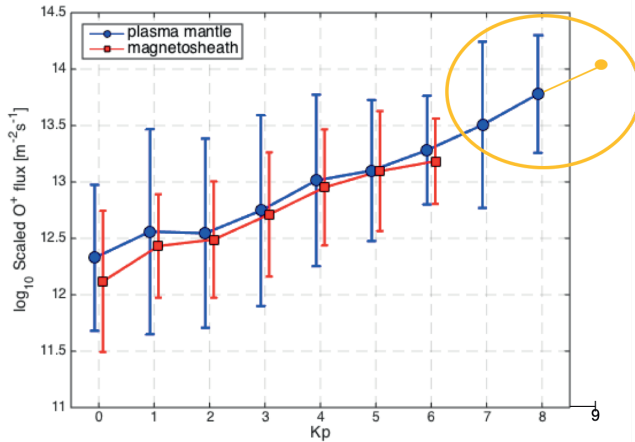

Figure 4.5: Scaled O^+ flux from the plasma mantle and magnetosheath as a function of geomagnetic activity (Kp). Credits: Adapted from Slapak et al. 2017.

This general outflow enhancement is associated with various parameters such as variations in IMF or the geomagnetic activity (Dst or Kp index, see Section 5.4 for more details). Yau et al. (1988) showed that the variations in the geomagnetic activity (quantified by Kp index) is exponentially correlated with the upflow, at an altitude range of 1.3 R_e to 2 R_e. Indeed, the O^+ upflow increases by a factor 20 for a Kp increase of 0 to 6. We did a similar study (Paper I) on the Kp dependence based on high altitude O^+ from the plasma mantle and magnetosheath. We estimated the O^+ escape rate from the plasma mantle as $8.2 \times 10^{24} \exp(0.45\text{Kp})$ s^{-1}. Due to the poor statistics at high Kp index (Kp=8 or 9), our second study (Paper II) estimated the O^+ outflow for six extreme geomagnetic storms between 2001 and 2004. We found an enhancement of 1 to 2 orders of magnitude compared to the normal conditions (Kp $\simeq$ 3) but could not confirm that the ions were escaping. The upper limit of the scaled O^+ flux, defined as the flux scaled to an ionospheric altitude to compensate for altitude dependencies and magnetospheric compressions, is 10^{14} m^{-2}s^{-1} that confirms the exponential increase of the total O^+ flux as a function of Kp (see Fig. 4.5). Fig. 4.5 shows the statistics of the scaled O^+ flux in logarithmic scale as a function of the Kp index calculated by Slapak et al. (2017) (Paper I) and the additional result for extreme geomagnetic storm (Kp=8 or 9) of Schillings et al. (2017, 2018) (Paper II and III).

This result was strengthened in our third study (Paper III), that investigated the September 4–10, 2017 storm. The scaled O^+ flux in the northern polar cap during the main phase of the storm was $\sim 10^{13}$ m^{-2}s^{-1} and the temperatures and velocities suggested a partial escape of the ions. While the data for the full year (2017) were not available (when the paper was written), we compared the scaled O^+ flux before and after the second ICME-shock (see Fig. 2.8) that hit the Earth on September 7, around 23:00 UT. The enhancement in the polar cap was small (factor of 3) and the upper limit was 6.3×10^{13} m^{-2}s^{-1}. We suggested that the enhancement was weak due to the preheating of the atmosphere by the earlier X-flares (see also Yamauchi et al. (2018)).

Disturbed magnetospheric conditions are induced by variations in different solar wind parameters such as IMF and dynamic pressure as well as solar radiations (EUV). Kistler and Mouikis (2016) showed that the O^+ density and temperature increase with the solar radio flux F10.7,[5] whereas Cully et al. (2003); Engwall et al. (2009); André et al. (2015); Li et al. (2017) showed an increased of low-energy ion outflow for increased F10.7.

Despite our careful investigations for EUV in Paper IV, we did not find a correlation between EUV and O^+ escape rate in the plasma mantle. We even found a plausible explanation for this behaviour; EUV radiations ionise atomic oxygen into O^+ ions at low altitude range (80 and 600 km). Thus, we suggested that O^+ ions observed in the plasma mantle did not depend on ion production by EUV at lower altitude but rather by cusp precipitation, so that the high altitude flux was limited by energisation mechanisms rather than source production rate. However, after discovering that our

---

[5]F10.7 is the radio solar flux at 10.7 cm (2800 MHz) and is used as a proxy for EUV radiations.

(a) Total O$^+$ escape rate for different EUV irradiances in the polar cap.

(b) Total O$^+$ escape rate for different EUV irradiances in the plasma mantle.
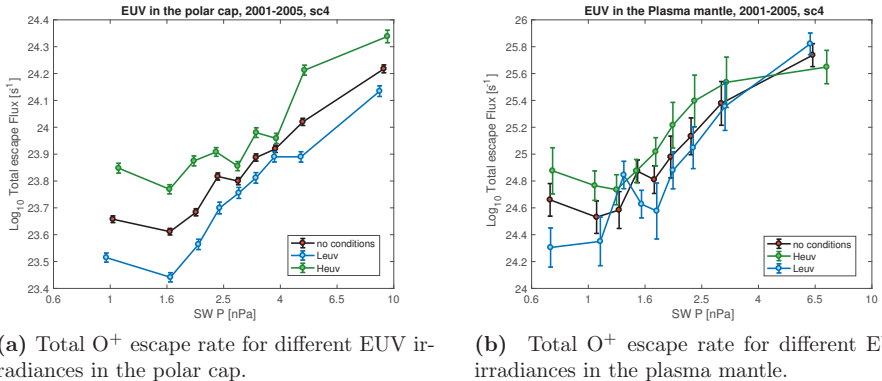
Figure 4.6: Variations of EUV irradiance in polar cap and plasma mantle with Cluster-CODIF data, 2001 - 2005, sc4. Note the difference in the scale of the O$^+$ escape rate (y axis).

initial cross-talk values was only valid for Cluster data until approximately 2003 (see Section 5.1.4), we investigated once more the EUV dependency published in Paper IV. We then found that EUV does have some influence on O$^+$ escape rate in the plasma mantle, similarly to the dependency in the polar cap. These updated results are presented in Fig. 4.6[6]. Fig. 4.6a displays the total O$^+$ escape rate as a function of solar wind dynamic pressure for high and low EUV[7] in the polar cap. We do see a higher outflow for high EUV irradiance in comparison with Fig. 4.6b that illustrates exactly the same for observations of O$^+$ in the plasma mantle.

Additionally, we investigated a combination of the dynamic pressure, the geomagnetic activity (Kp) and the EUV flux[8] and their effect on ion outflow. We found that high dynamic pressure does not necessarily causes an enhancement in geomagnetic disturbances, while EUV does not have any influence on geomagnetic perturbations. In Fig. 4.7, the left panel shows the solar wind dynamic pressure as a function of EUV flux for different Kp values (colour bar). The right panel shows the statistics of Kp index in our O$^+$ observations in the plasma mantle.

---

[6]Note that a corrigendum will be submitted in order to update the results and explain the reasons of our mistake.

[7]The high and low EUV limit is defined by the mean of the whole spectrum, in this case high EUV > 3 mW/m^2 and low EUV $\leq$ 3 mW/m^2.

[8]The EUV flux is defined as EUV irradiance divided by the photon energy.
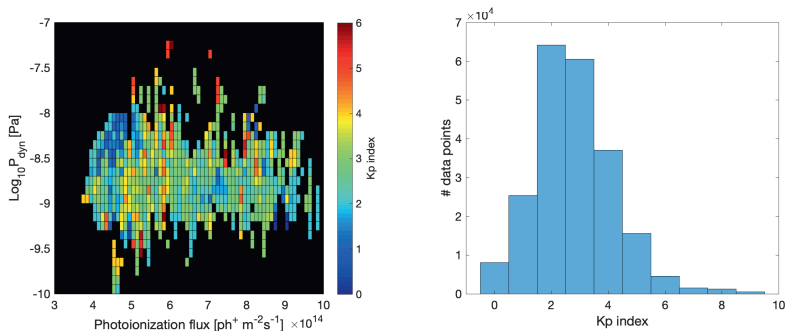
Figure 4.7: Distribution of Kp index (colour bar) for O^+ observations in the plasma mantle as a function of solar wind dynamic pressure and EUV flux. Supplement material of Paper IV.

4.6 Fate of O^+ ions observed at high altitudes

Depending on how effectively the ions are heated and accelerated, three main paths can be considered for the outflow (1) low-energised ion populations will be transported to the plasma sheet (Kistler et al., 2010; Mouikis et al., 2010; Haaland et al., 2012; Maggiolo and Kistler, 2014; Liao et al., 2015), (2) high-energised ions will be transported to the plasma mantle with sufficient velocity to pass the X-line and therefore escape in the far tail (Nilsson, 2011), and (3) high-energised ions that will escape directly from the cusp into the solar wind through the dayside magnetosheath (Slapak et al., 2012, 2013).

In our last study (Paper V), we investigated the fate of O^+ ions observed in the plasma mantle, O^+ ions following the second and third routes. We found that 96% of the ions will eventually escape the magnetosphere and be lost into the solar wind, while only 3.5% feed the plasma sheet. However, the fate of these 3.5% is not known and they might be lost anyway through charge exchange with the neutral atmosphere (see Section 4.1.2).

4.7 Terrestrial balance

In the previous sections, we presented the escape signatures and mechanisms for neutrals and ions in the Earth's atmosphere. We saw that Earth loses hydrogen and O^+ through different processes, however, the Earth also accretes matter through celestial bodies. Therefore, this section[9] aims to establish a matter assessment for Earth as a whole system (Earth and its atmosphere).

---

[9]Note that this section is greatly inspired from Engwall's thesis, chapter 4 (Engwall, 2009).

4.7.1 Accretion

Earth daily accumulates dust, micrometeorite particles, or even bigger objects coming from the solar system. On a short time scale, the most important influx comes from meteoritic material, namely particles smaller than 1 mm in size (Love and Brownlee, 1993), whereas on long time scales big impacts dominate (Ceplecha, 1992). Big impacts are typically stony and carbonaceous bodies with masses between 10^{12} kg to 10^{15} kg and small inactive comets with masses between 10^4 kg to 10^7 kg (Ceplecha, 1992). However, such impacts do not occur very often, and therefore their contribution could be removed from the total estimation. Indeed, a 10^{15} kg body represents a mass accretion of ~ 2.5 kg/s itself and happens one every 30 million years (Kyte and Wasson, 1986). Subsequently, celestial bodies impacts with a mass higher than 10^{12} kg represent about 80% of the total accretion mass. Smaller objects such as meteors and meteorite fireballs with a mass of 10^3 kg or less represent an incoming flux of 0.51 kg/s (Hughes, 1997). For Meteorites in the range of 10^{-6} kg to 10^3 kg, figure 4 of Kyte and Wasson (1986) gives a mass accretion of 0.1 kg/s. The micrometeorites and dust have a mass in a range of 10^{-10} kg to 10^{-6} kg at Earth. An estimate with simulations by Cremonese et al. (2012) showed that the accretion mass is about 0.23 kg/s for asteroidal dust and about 0.13 kg/s for dust coming from the Jupiter comets family.

In Table 4.1, we use the total mass range of 10^{-21} kg - 10^{15} kg and an accretion on Earth of ~ 5.4 kg/s given by Ceplecha (1992). As discussed above, if we remove the 80% of big impacts that happen very seldom, we obtain an average of ~ 1.1 kg/s.

4.7.2 Losses

The losses are roughly approximated from the literature and for average magnetospheric conditions. Thus, Table 4.1 gives the total escape in s^{-1} and the total loss in kg/s from Earth's average conditions of today. The oxygen budget is controlled by ion outflow, the value 4.1×10^{25} s^{-1} in the table comes from Hultqvist et al. (1999). The value is taken for high-energy data (10 eV to 17 keV) and for solar max with Kp = 2. The escape of neutral oxygen (Jeans and charge exchange) is negligible as we discussed in Section 4.1. The hydrogen value for ion outflow comes from Yamauchi and Wahlund (2007) for outflowing H^+ and for average conditions. Their values are between 0.2 to 0.8×10^{26} s^{-1} for quiet and active time respectively, we choose a middle value of 0.5×10^{26} s^{-1}. The Jeans and charge exchange mechanisms for hydrogen play a major role in the total escape of the atmosphere. The Jeans flux was determined to be 3×10^{26} s^{-1} for quiet solar conditions (Hunten and Strobel, 1974) and charge exchange is about the same range therefore we employed that value in our estimation. Finally, the helium values for ion outflow (1.5×10^{24} s^{-1}), Jeans escape (3.8×10^{22} s^{-1}) and charge exchange (1.7×10^{23} s^{-1}) were found in studies made by Su et al. (1998); MacDonald (1964); Lie-Svendsen et al. (1992) respectively. Helium charge exchange process has 3 main ions that produce He neutral, O_2, O and N_2, however the most efficient one is He^+ + O reaction. Subsequently, we took the

39

escape flux corresponding to that reaction.

From Table 4.1, we conclude that the global assessment of Earth's loss is equally driven by ion outflow for O^+ and Jeans escape for H^+, while helium is not of great importance. The total mass loss is estimated to ~ 2.2 kg/s. However, if we do the same estimations for disturbed magnetic conditions, the O^+ outflow plays the major role in escape and total mass loss because of its high mass compared to hydrogen and helium. During strong solar wind conditions, the O^+ outflow goes up to 1.5×10^{26} s^{-1} (Hultqvist et al., 1999) which increases the mass loss of oxygen to 4.11 kg/s and the total mass loss to ~ 5.3 kg/s.

4.7.3   Total mass assessment

Table 4.1 summarises the different estimations of accretion mass and losses for the Earth system. If we take into account the big impacts in the accretion estimation, the total mass is positive with ~ 3.2 kg/s remaining matter (from accretion). However, if we remove the big impacts as discussed in Section 4.7.1, we obtain a negative total mass of $\sim$ -1.1 kg/s (1.1 kg/s accretion - 2.2 kg/s escape mass), therefore Earth is losing mass through atmospheric escape. Another scenario including big impacts (5.4 kg/s) and nowadays geomagnetic storms (5.3 kg/s), gives a total assessment of almost 0 kg/s. Finally, Fig. 4.8 illustrates the different processes discussed in this section as well as summarises the numbers in Table 4.1.

Table 4.1: Global estimation of the accretion and loss processes at Earth. A remaining of ~ 3.2 kg/s of accretion matter subsists after the escaping of the particles. Accr = accretion.

interplanetary body and dust	Mass range [kg]			Mass accr [kg/s]
	10^{-21} - 10^{15}			~ 5.4
	Escape [s^{-1}]			Mass loss [kg/s]
	O or O^+	H or H^+	He or He^+	
Ion outflow	4.1×10^{25}	0.5×10^{26}	1.5×10^{24}	-1.2
Jeans	-	3×10^{26}	3.8×10^{22}	-0.5
Charge exchange	-	3×10^{26}	1.7×10^{23}	-0.5
Total escape [s^{-1}]	4.1×10^{25}	6.5×10^{26}	1.71×10^{24}	-
Total mass [kg/s]	1.1	1.1	0.03	~ 3.2
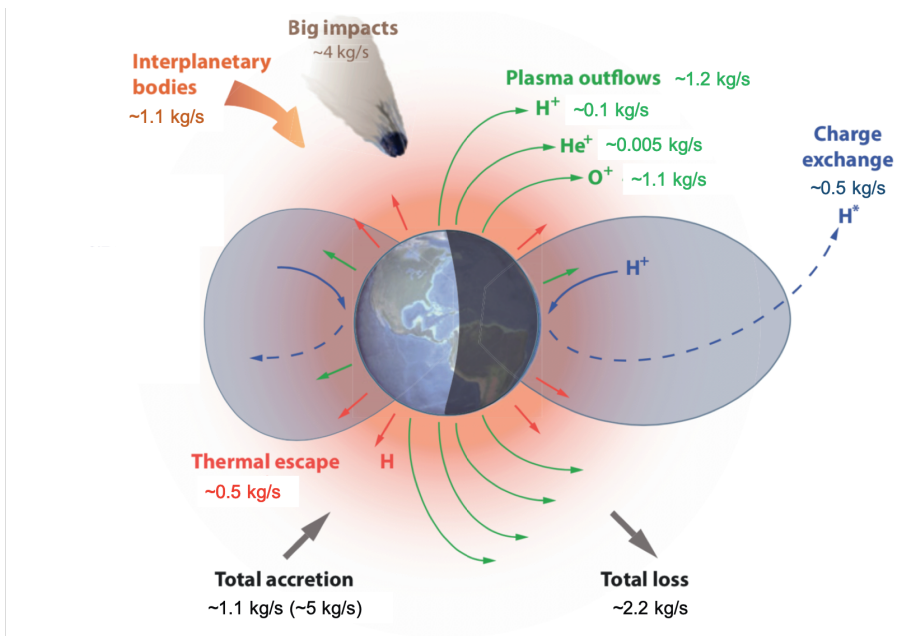
Figure 4.8: Illustration of the terrestrial balance with the numbers shown in Table 4.1. Credits: Adapted from Engwall's thesis (Engwall, 2009).

Instrumentation and data

The previous chapters describe the physics and observations of O^+ outflow and escape under different geomagnetic conditions, however, this work was only possible with the available solar wind data and ion observations as well as magnetic data from Cluster satellites. Therefore, we hereby describe the instruments and data used in this project.

5.1 The Cluster mission

Nowadays in-situ measurements in space are very common, especially around Earth. However, a few decades ago, data were collected mainly with remote sensing techniques and direct measurements in space were an achievement that added a new dimension to data analysis. Space plasma science has benefitted from this breakthrough, which raised the opportunity to study micro and macro-scale phenomena in the space environment and at different positions. The Cluster mission, composed of 4 satellites flying in tetrahedral formation, was a new possibility of analysing the data by distinguishing spatial and temporal phenomena and therefore having a three-dimensional analysis of the physical structure. Following the foot steps of Cluster, MMS and THEMIS missions have similar scientific goals but with higher resolution. Thus, Cluster mission was pioneer in the multi-satellites measurements. This was another breakthrough in space science.

5.1.1 Brief history

The Cluster mission was designed by the European Space Agency (ESA) in the 1980s and was composed of 4 satellites to collect data on small-scale magnetospheric phenomena in Earth's surroundings. The spacecraft were ready to fly in 1996 and were launched onboard the newly designed Ariane-5 booster, on 4 June 1996 from Kourou in French Guiana (Escoubet et al., 1997). Unfortunately, the 4 satellites were destroyed due to a failed launch. Afterward, while the science objectives could only be met with a satellite constellation, ESA decided to rebuild the Cluster spacecraft,

which were called the Cluster II mission. The 4 new satellites were launched 2 by 2 in July and August 2000 by Soyuz rockets from Baikonur in Kazakhstan. The mission was initially planned for 5 years, but has been extended several times and the current end is 31 December 2020.

The scientific objectives of the Cluster II mission (Escoubet et al., 2001) are multiple and various, but can be summarised as studying the interaction between the magnetosphere and the solar wind in key plasma regions such as the magnetotail, the magnetospheric cusps, the auroral zone, the bow shock, and the magnetopause. To fulfill these objectives, the spacecraft are flying in tetrahedral formation on an elliptical polar orbit around Earth with a period of 57 hours, with an initial perigee and apogee around 3 and 19 Earth radii (6371 km), respectively. However, over the years the orbit slightly changed. This orbit configuration allows to collect data in the magnetotail and in the Earth's dayside magnetosphere during northern summer as well as in the solar wind and in the near-Earth plasma sheet during northern winter. In addition, the tetrahedral formation of the four spacecraft allows for three-dimensional analysis of the physical structures and the possibility to distinguish between spatial and temporal phenomena.

5.1.2 Instrumentation onboard Cluster II

The 4 spacecraft are identical and carry 11 different instruments, presented and numbered in Tab. 5.1 and partially shown in Fig. 5.1a. These instruments measure different plasma parameters, the electric and magnetic fields. We analysed data from two instruments; ion distributions from the Cluster Ion Spectrometry (2) and magnetic fields from the FluxGate Magnetometer (4).

5.1.2.1 CIS - Cluster Ion Spectrometry experiment

The CIS instrument contains 2 ion detectors (see Fig. 5.1b), the Composition and Distribution Function Analyser (CODIF) and the Hot Ion Analyser (HIA), both able to produce a 3D distribution function with a time resolution of approximately 4 seconds (spin of the spacecraft). While we studied ion outflow, CODIF is more suitable for our analysis and therefore HIA is not described here (for more detail about HIA see Rème et al. (2001)).

We used mainly O^+ data due to their atmospheric origin while the observed H^+ can have an atmospheric or a solar wind origin. Thus, CODIF (Rème et al., 2001) is utilised because it enables to distinguish ion species. The instrument has an electrostatic analyser (ESA) followed by a time-of-flight (TOF) section (see Fig. 5.2, bottom illustration, cross-sectional view). The entrance of the ESA is divided into two 180° sections which defines the high and low sensitivity modes. Only one side of the entrance or one mode can be used at the time. The TOF technique enables to resolve different ion species, namely H^+, He^{2+}, He^+ and O^+. CODIF's detector has a field-of-view of 360° (180° used for each mode) orthogonal to the spin plane, divided into 16 sectors of 22.5° each, and the angular resolution is likewise 22.5° in the spin plane

Table 5.1: Instruments onboard each Cluster satellite (Escoubet et al., 1997).

Abbreviation	Instrument
(1) ASPOC	Active Spacecraft Potential Control experiment
(2) CIS	Cluster Ion Spectrometry experiment
(3) EDI	Electron Drift Instrument
(4) FGM	FluxGate Magnetometer
(5) PEACE	Plasma Electron And Current Experiment
(6) RAPID	Research with Adaptive Particle Imaging Detectors
STAFF	Spatio-Temporal Analysis of Field Fluctuation experiment
EFW	Electric Field and Wave experiment
DWP	Digital Wave Processing experiment
WHISPER	Waves of High frequency and Sounder for Probing of Electron density by Relaxation experiment
WBD	Wide Band Data instrument
WEC	Wave Experiment Consortium (DWP, EFW, STAFF, WBD, and WHISPER)
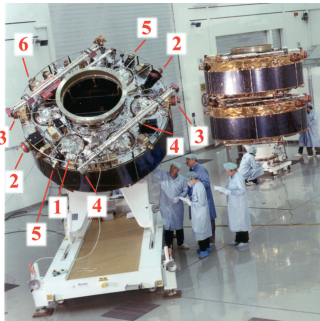
(a) Picture of one of Cluster spacecraft with CIS in (2) and FGM in (4). Credits: Escoubet et al. (2001)

(b) Cluster Ion Spectrometer with CODIF on the left and HIA on the right. Credits: Max-Planck Institute.

Figure 5.1: The Cluster mission.

(see Fig. 5.2, top view). Depending on the modes of interest, the energy coverage is from 15 eV/q (per charge) up to 38 keV/q divided in 32 logarithmically spaced steps with an energy resolution ($\Delta E/E$) of ~0.16.

In Fig. 5.2, the top illustration shows a top view of the instrument with the direction of the spin axis pointing northward, which is also shown on the right side of the CODIF picture, and some samples of incoming ion paths. The elevation counts

8 sectors and the azimuth plane is traced out by the spin, which is divided into 32 energy sweeps. In the bottom illustration, a cross-sectional view displays the ion trajectory inside the instrument. The ions will first go through the electrostatic analyser which provides the energy-per-charge measurements (E/Q), afterwards they are accelerated by a voltage, U_{acc} = 15 keV, in the post-acceleration section. Before entering the TOF section, the ions pass a carbon foil that emits a start signal. They fly through the TOF section and when they reach the microchannel plate (MCP), secondary electrons are emitted and serve as a stop signal. A valid count to get a time-of-flight requires both start and stop signals. The ion velocities ($v = d/\tau$) are measured by the distance the ions flew (d) and the time (τ) they took to reach the stop plate. Thus, the ion mass per charge can be deduced (Rème et al., 2001)

$$\frac{M}{Q} = 2\alpha \frac{E/Q + eU_{acc}}{(d/\tau)^2} \tag{5.1}$$

where e is the elementary charge and α represents the effect of energy loss in the 3 μg/cm^{-2} carbon foil at the entry of the TOF section and depends on the incident energy and particle species.
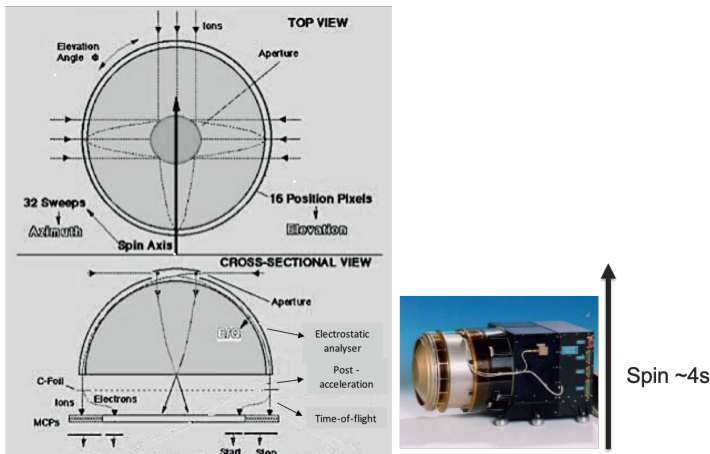

Figure 5.2: CODIF instrument with a top view in the top panel and cross-sectional view in the bottom panel. On the right side, CODIF instrument is shown with its spin axis pointing to the north. Credits: Adapted from Max-Planck Institute.

5.1.2.2 FGM - FluxGate Magnetometer

Together with O^+ data, we also need magnetic field data provided by FGM (Balogh et al., 2001), which has a sample frequency of 22.4 Hz in the normal mode. FGM is composed of an electronic unit for onboard data processing and 2 triaxial fluxgate magnetic field sensors, one located at the end of a 5 m radial boom which is working as primary source of the data in normal operation, and the second at 1.5 m from the end. For different magnetic field intensities, the magnetometers have several operative ranges going from a few tens of nT to several thousand of nT (Balogh et al., 2001). We work with the magnetic field data averaged over the spacecraft spin period of $\sim$4 s, and refer to it as the background magnetic field, even though sometimes low frequency waves can be seen. These magnetic data are used to confirm the different regions observed with the ion data and to estimate a scaled O^+ flux. In the case study of the September 2017 storm (Paper III), we used the geomagnetic field data to calculate the pitch angle and confirm the different storm phases observed in the Dst index (see Section 5.4).

5.1.3 Calibration of the data

Cluster has been in space for more than 15 years, therefore the instruments deteriorate and the initial calibrations have changed over time. CODIF has been recalibrated (Kistler et al., 2013), with the last calibration in the end of 2017. Those new calibrations have been used to estimate the scaled O^+ outflow during the September 2017 storm (Paper III). In the same way, the third paper used preliminary calibration files for the magnetic field data, while the official calibrated data were not available at the submission of the paper. These preliminary calibrations were used and do not significantly affect our results.

5.1.4 Contamination of the data - Cross-talk

Ion outflow is usually observed in the cusp, plasma mantle and polar cap regions, however the cusp and plasma mantle often contain magnetosheath origin plasma (see Chapter 2, Fig. 2.5). Therefore, in the cusp and plasma mantle CODIF O^+ data might be contaminated by intense proton (H^+) flux from the magnetosheath. This contamination is produced by chance start-stop coincidences in the TOF section. These chance coincidences may cause significant background counts (false O^+ counts). This phenomena is called cross-talk. To avoid such data, Nilsson et al. (2006) used a method based on the $\mathbf{E} \times \mathbf{B}$ drift. The $\mathbf{E} \times \mathbf{B}$ drift should be the dominant perpendicular drift and should be the same for O^+ and H^+ because it is nor mass neither charge dependent. When H^+ counts are interpreted as O^+ counts at some given energy channel, O^+ velocity moments are underestimated compared to H^+, whereas the counts are overestimated. This can be explained with the perpendicular component of the kinetic energy

$$E_\perp = \frac{1}{2} m_{O^+} v_{\perp(O^+)} = \frac{1}{2} m_{H^+} v_{\perp(H^+)}$$

$$\sqrt{\frac{m_{O^+}}{m_{H^+}}} = \frac{v_{\perp(H^+)}}{v_{\perp(O^+)}} = 4$$

(5.2)

where m_{O^+}, m_{H^+} are the mass of O^+ and H^+ respectively and $v_{\perp(O^+)}$, $v_{\perp(H^+)}$ are the perpendicular velocity for O^+ and H^+. This relation shows that the O^+ perpendicular velocity for purely false counts is $1/4$ of the H^+ perpendicular velocity, as the false counts follow the energy distribution of the H^+ counts. Those false O^+ counts are avoided in our data sets by removing data where the O^+ perpendicular velocity is close to $1/4$ of the H^+ perpendicular velocity, indicating a similar shape of the energy spectra (Eq. 5.2).

In the beginning of the Cluster mission, Nilsson et al. (2006) removed the cross-talk by demanding that

$$\frac{v_{\perp(O^+)}}{v_{\perp(H^+)}} < 0.2 \qquad \frac{v_{\perp(O^+)}}{v_{\perp(H^+)}} > 0.35 \qquad \frac{N_{O^+}}{N_{H^+}} > 0.063.$$

(5.3)

Later, we found out that the values in Eq. 5.3 were only valid until roughly 2004, afterward since the data quality has decreased, the limit values to avoid cross-talk changed. Fig. 5.3 shows the new distribution of O^+/H^+ velocity ratio for each interval of O^+/H^+ density ratio from 2001 to 2007. The colour bar gives the percentage in each bin. In comparison with Waara's figure 5.2 in his thesis (Waara, 2011), we see that the cross-talk (solid red box) has evolved during the years. We defined the new values (2001- 2007) with the total velocity instead of the perpendicular velocity to broaden the interval and be certain to avoid magnetosheath data. The new limits for acceptance are

$$\frac{v_{tot(O^+)}}{v_{tot(H^+)}} < 0.2 \qquad \frac{v_{tot(O^+)}}{v_{tot(H^+)}} > 0.5 \qquad \frac{N_{O^+}}{N_{H^+}} > 0.25.$$

(5.4)

5.1.5 Data sets

Our studies used data from the polar regions for studying ion outflow and escape. The data sets therefore consists of the polar cap (Papers II and III), the cusp (Papers III and V), the plasma mantle (Papers I, IV and V) and outside the magnetosphere, the magnetosheath (Paper I). The magnetosheath data set was prepared by Slapak R. and is described in his thesis (Slapak, 2013). Since the first and second papers were case studies about geomagnetic storms, the data were taken accordingly to the time of the storms in the suitable region (see Fig. 1 in Paper II and III).

For the ion outflow escape studies in Paper IV and V, we built an automatic routine to detect plasma mantle/cusp data. Firstly, the magnetosheath data and cross-talk are removed using Eq. 5.4. Afterward, to distinguish the plasma mantle
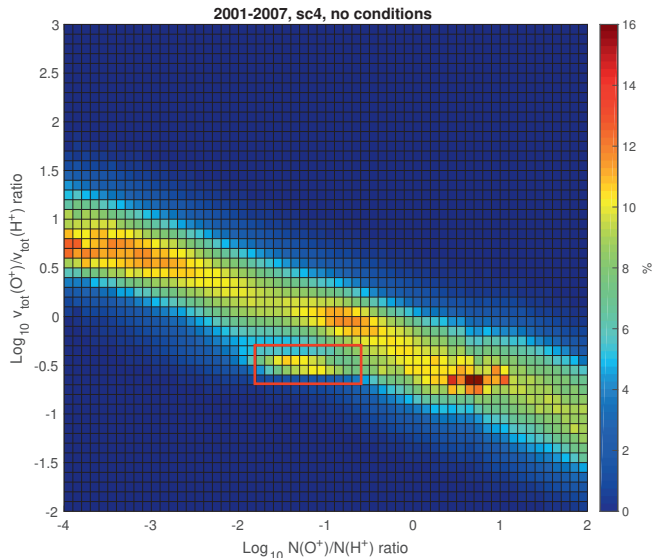
Figure 5.3: Distribution of O^+/H^+ velocity ratio for each interval of O^+/H^+ density ratio. Each column is normalised such that the sum of the data in one column equals 100% and the colour bar is in percent.

from the polar cap, the plasma beta parameter[1] should be set as $\beta > 0.1$ to remove polar cap data. In the polar cap, the plasma beta is approximately 0.05 (Liao et al., 2010, 2015). Moreover, the plasma beta restriction is not sufficient to avoid plasma sheet data. Indeed, the plasma mantle and plasma sheet may have a similar β. Thus, the distinction between this two regions is done using the perpendicular temperature of the protons, $T_\perp(H^+) < 1750$ eV in the plasma mantle (Kistler et al., 2006; Slapak et al., 2017). Cusp data are avoided with $v_\parallel(H^+) > 0$ km/s. More precisely, we used $\text{sign}(v_\parallel)$ since the outward flux is negative in the northern hemisphere and positive in southern hemisphere due to the magnetic configuration. See also explanation of the pitch angle in Section 3.2. We remove the inner magnetosphere by defining a spatial coverage as -5 $R_e <$ X < 8 R_e and R = $\sqrt{Y^2 + Z^2} > 6$ R_e. Finally, for reliable bulk velocity estimations, we also constrain the densities as 10^{-3} cm$^{-3} <$ n(O^+) < 2 cm^{-3} and n(H^+) $> 10^{-3}$ cm^{-3}. The upper limit of O^+ was introduced as it further removed some O^+ data contaminated by cross-talk. In all our data sets, we pick out only outward O^+ flux using a positive parallel velocity $v_\parallel(O^+) > 0$ km/s.

---

[1]The plasma beta β is defined as the ratio between the thermal pressure and the magnetic pressure, see Section 2.2.
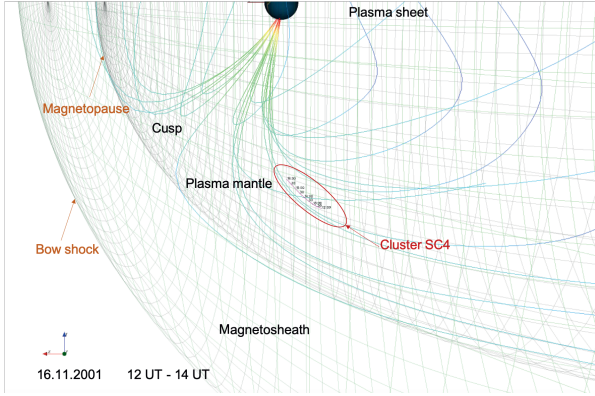
Figure 5.4: Example of one plasma mantle detection with our automatic routine described in the main text. This event occurred on Nov 16, 2001 between 12 UT and 14 UT. Credits: ovt.irfu.se

Fig. 5.4 and Fig. 5.5 show one example of automatically detected plasma mantle data. Fig. 5.4 gives the position of Cluster spacecraft 4 in the southern hemisphere during the plasma mantle crossing on Nov 16, 2001 between 12 UT and 14 UT. The first boundary in the left represents the bow shock, whereas the second represents the magnetopause. The magnetic field lines are shown in multicolour, the half sphere on the top is Earth. Cluster satellite 4 is located in a region between the open magnetic field lines of the plasma mantle and closed field lines. Our routine detects 3 plasma mantle events[2] that fit all required conditions, see Fig. 5.5. These events are highlighted with turquoise boxes. In Fig. 5.5, the two first panels give the mode and sensitivity used respectively (see Section 5.1.2.1 for more details). The third panel displays the counts per second of O^+ ions in all directions and for all energy levels. The three last panels represent the O^+ density, the velocity and temperature components (from CODIF) respectively.

5.2 Solar data

The solar wind data can be found on the free online database OMNIWeb (`https://omniweb.gsfc.nasa.gov`). This database provided by NOAA/SWPC is a compilation of several satellites collecting data from the Sun. These data are cross compared, for some of the parameters cross-normalised and time-shifted to magnetosphere-arrival time for low resolution (1h), or to the bow shock nose for high resolution (1 or 5 min).

---

[2]One event is defined as more than 60 data points in a row, approximately 4 minutes, that fit the requirements.
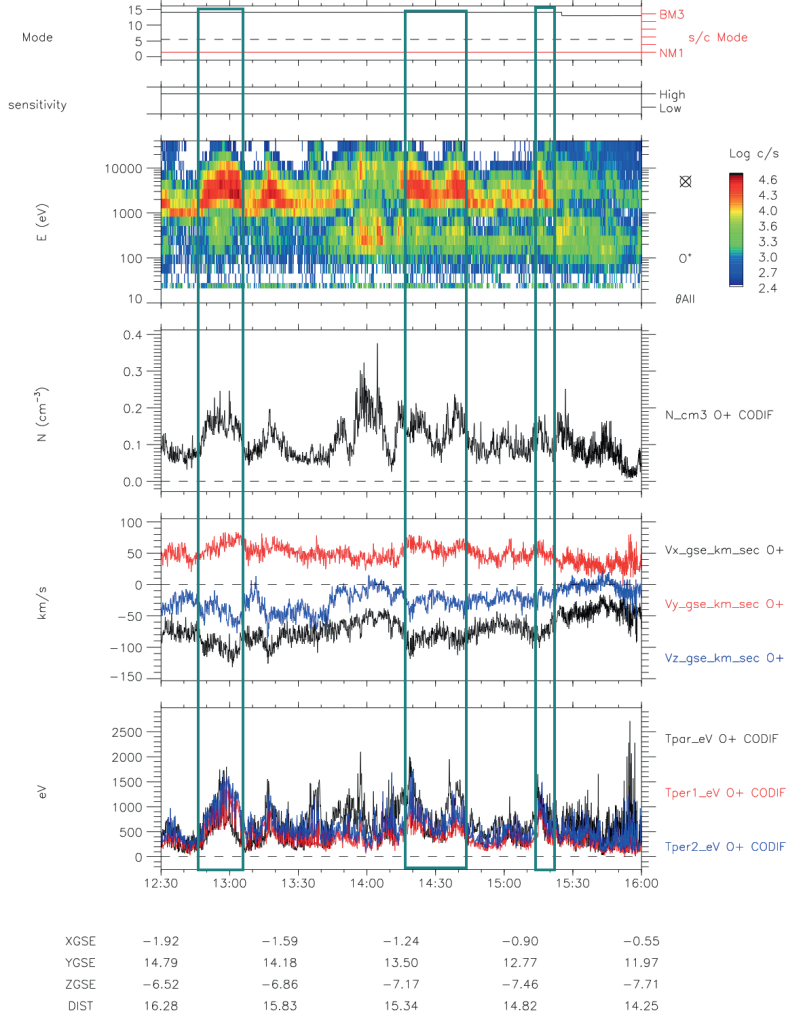
Figure 5.5: Cluster - CODIF data for plasma mantle data (turquoise boxes) detected by our automatic routine. The two first panels give the mode and the sensitivity of CODIF respectively. The third panel shows the counts per seconds for O^+ ions in all directions. The fourth, fifth, and sixth panels display the O^+ density, the velocity and temperature components respectively. Credits: clweb.irap.omp.eu

For high resolution, the solar wind magnetic field and the plasma parameters are coming from IMP 8, Wind, Geotail and ACE or since 2016 DSCOVR spacecraft. In our ion outflow studies (Papers III and IV), we used the high resolution solar wind data, namely the IMF, the velocity, the density and the dynamic pressure. We interpolated these parameters to Cluster resolution ($\sim$4s) to compare them with the O^+ data from CODIF.

In Paper III, we also utilised solar data, we analysed high resolution images from the photosphere and photospheric magnetic fields taken by Solar Dynamic Observatory (SDO) (Pesnell et al., 2012). In addition, we looked at the solar active regions (ARs) daily collected by NOAA/SWPC as well as the full-disk X-ray observations from the GOES spacecraft. Finally, the coronal mass ejections were observed by Solar and Heliospheric Observatory (SOHO) and Solar Terrestrial Relations Observatory (STEREO).

In Paper V, solar wind data are employed in the Tsyganenko and Weimer models. The high resolution solar wind dynamic pressure, velocity and IMF components are retrieved automatically once a plasma mantle/cusp event is detected. Note that there is no interpolation to Cluster data for this study.

5.3 Extreme Ultraviolet data

In Paper IV, we utilised extreme ultraviolet (EUV) data from Solar EUV Experiment (SEE) instrument on board TIMED satellite[3]. Launched in December 2001 and currently still active, TIMED has a 74.1° tilted circular orbit, which is completed in 97 min. The satellite carries four sensors including SEE (Woods et al., 2000). The SEE is a set a photometers and a spectrometer that measures solar ultraviolet radiations, such as soft X-ray, solar far ultraviolet (FUV) and EUV irradiance, in the mesosphere, lower thermosphere and ionosphere (MLTI) system. The solar ultraviolet radiations are observed with a spectral resolution of 0.5 nm and a wavelength range from 1 nm to 195 nm. Due to the orbit of TIMED, the instrument observes the Sun 14 to 15 times per day for approximately 3 min.

Fig. 5.6 shows the EUV intensity in cylindrical coordinates for O^+ observations in the plasma mantle. This means that for all O^+ observations by Cluster in the plasma mantle, the corresponding EUV data is taken in the TIMED data set. The subsets represent EUV irradiance for different years; from 2002 to 2007. The colour bar displays the EUV intensity in [W/m^2]. Fig. 5.6 clearly demonstrates that EUV intensity is dependent of the solar cycle. Indeed near the solar maximum (first subset - year 2002), the EUV intensity is a factor 3 higher than near from solar minimum (last subset - year 2007).

---

[3]TIMED satellite stands for Thermosphere, Ionosphere, Mesosphere Energetics and Dynamics (Kusnierkiewicz, 2003).
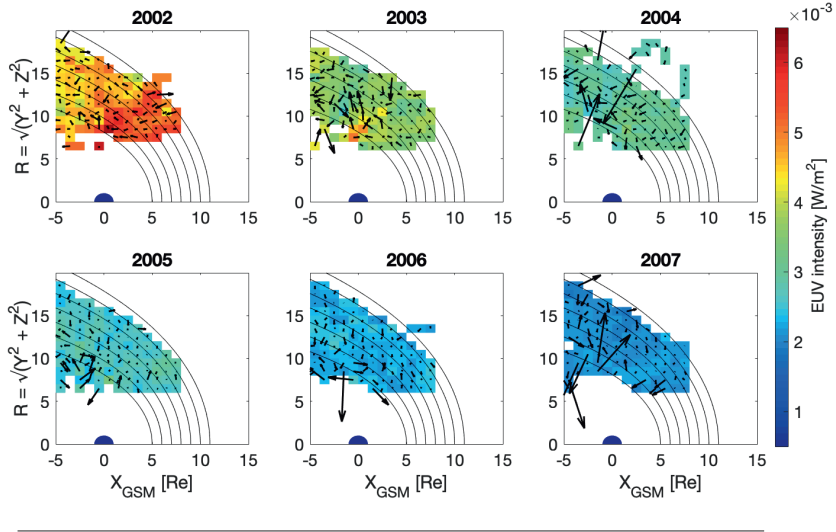
Figure 5.6: Extreme Ultraviolet intensity [W/m^2] for O$^+$ observations in the plasma mantle from 2002 to 2007. The colour bar represents the intensity.

5.4 Magnetic indices

Magnetic indices are measurements of the geomagnetic activity in different magneto-spheric regions at Earth. The most common indices are Dst, SYM-H, Kp and AE, which have different resolution and are calculated at different latitudes. Dst (1 h) and SYM-H (1 min) describe the perturbations of the horizontal component of the Earth's magnetic field measured with low-latitude magnetometer stations. Fig. 5.7a shows Dst index for October 2003 and the different colours represent the status of disturbances. The Halloween event (28 - 30 Oct) was classified as a super storm. In Paper V, we used this geomagnetic index as an input in the Tsyganenko model. The auroral electrojet index or AE (1 min) measures the strength of the auroral electrojet with 10 to 13 magnetometer stations located in the northern auroral zone. Finally, the Kp index estimates the geomagnetic activity over a global scale and is a 3 hours average of the K index (see Fig. 5.7b). The K index is measurement of local disturbances in the horizontal magnetic field component from 13 stations between |44°| and |60°| latitude. In Fig. 5.7b, the red colour means a geomagnetic storm happened whereas yellow represents active auroral display with possible substorms. The relation between the magnetic Kp index and the O$^+$ outflow/escape has been studied by Slapak et al. (2017) (Paper I) and Schillings et al. (2019) (Paper IV).

(a) Estimated Dst index for October 2003. Credits: http://www.aer.com/.

(b) Estimated planetary K index for the Halloween event, October 29, 2003. Credits: GFZ Postdam, Germany.
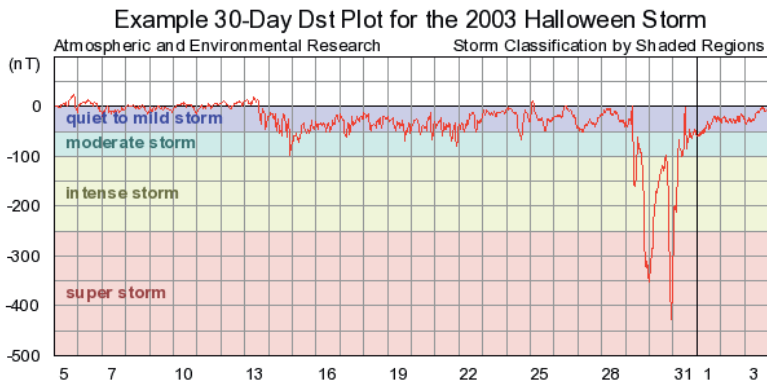
Figure 5.7: Magnetic indices.

CHAPTER 6

Summary and Outlook

Atmospheric loss is of great interest in order to extend our knowledge about planetary atmospheric evolution on long time scales. Thus, we know that Earth's is constantly losing mass through neutral and ion escape. The neutral escape is mainly due to Jeans escape and concerns hydrogen, whereas the ion escape mainly concerns H^+ and O^+ ions. Moreover, once these ions have reached the escape velocity and are not gravitationally bound to Earth anym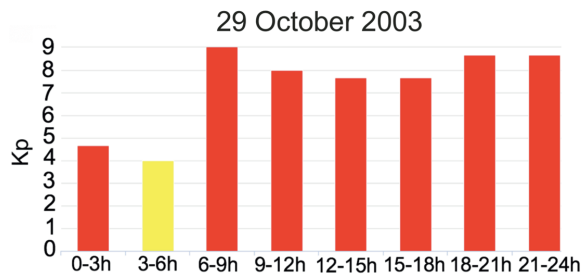ore, they do not necessarily escape the magnetosphere. This phenomenon is called ion outflow; the ions are observed in regions of open magnetic field lines such as the polar cap, the cusp and/or the plasma mantle. This outflow has different signatures associated to specific energisation and acceleration mechanisms. Depending on their energisation, the ions might be trapped again on closed magnetic field lines due to tail reconnection and end up in the plasma sheet. Part of those O^+ ions may be lost anyway due to charge exchange. Otherwise, ions with sufficient energies and accelerations eventually escape the magnetosphere and are lost into the solar wind. This escape happens in the dayside or in the distant magnetotail.

In this thesis work, we investigated several parameters that contribute to the O^+ outflow and escape. We establish or confirm correlations/anti-correlations between solar wind parameters and geomagnetic activity for O^+ in high-altitude polar regions. The observations were made with the CODIF instrument on board Cluster satellites, which can resolve O^+ within an energy range of 40 eV to 40 keV. The following sections discuss and summarise our findings.

1. Influence of the geomagnetic activity on O^+ outflow

The geomagnetic activity, measured as Kp index, has an influence on the O^+ outflow observed in the plasma mantle and the magnetosheath. We found that O^+ outflow increases exponentially with Kp index, such that during quiet Kp conditions (Kp $\sim$ 0-2) the outflow is 1.5 order of magnitude lower than during storm time, Kp > 6. The upper limit of the O^+ escape rate [s^{-1}] for Kp $\sim$ 7 is approximately 3×10^{26} ions/s, while the lowest limit is roughly one order of magnitude lower. These findings

confirm an exponential correlation between the outflow and the geomagnetic activity. The statistics were made for about 5 years of data. Finally, we estimated the total mass loss during four billion years with a typical Kp = 10 (corresponding to the Kp index four billions years ago) but exponentially decreasing until today. We found that the total O^+ loss is about 5×10^{17} kg, which indicates that the mass lost in four billion years equals to the atmospheric oxygen present in today's atmosphere.

2. O^+ outflow and escape during major geomagnetic storms

Our second study is complementary to the first one because we estimated the O^+ outflow exclusively for high Kp index, for which the statistics were fairly poor for the most extreme conditions. Thus, between 2001 and 2004 and using Cluster data, we analysed six major geomagnetic storms. A major geomagnetic storm is defined with geomagnetic indices Kp $\geq$ 7+ and Dst $<$ -100 nT. The main result is in agreement with our previous statistical study and 1.5 to 2 order(s) of magnitude O^+ outflow enhancement was observed for major storm considered to average conditions (Kp $\sim$ 2-3). However, the O^+ outflow for these storms was observed in the polar cap, so we were not able to confirm that the O^+ ions are escaping the magnetosphere.

Additionally, we got the opportunity to investigate a seventh major storm during this thesis work, the 4-10 September 2017 storm. Basically, the same study was done as for the six chosen between 2001 and 2004 with the difference that we analysed the whole evolution of the storm, from the Sun down to the ionosphere. The storm was produced by two ICMEs from the same active region on the Sun. The first ICME provoked already an enhancement in the ionosphere and triggered a storm sudden commencement (northward IMF) and positive Dst index. When the second ICME reached Earth, strong perturbations were recorded in the geomagnetic field. We determined the O^+ scaled flux before and after the second ICME arrival and we observed a flapping motion between the polar cap and cusp during the storm time. Our result agrees with the fact that O^+ outflow is enhanced during major geomagnetic storm. Furthermore, the O^+ ions we observed in the cusp had enough velocity and energy to escape the magnetosphere. So our hypothesis that ions were escaping during major storm was confirmed.

3. Solar wind dynamic pressure, IMF, EUV dependency on O^+ outflow

How does O^+ outflow depend on solar wind parameters? This is the question we tried to answer in the fourth study by making statistics using solar wind parameters. To answer this question, we used solar wind dynamic pressure, IMF, EUV and the coupling functions (Akasofu parameter and Vasyliunas at al. formula). The coupling functions define the solar wind power transferred into the magnetosphere. This study was made exclusively in the plasma mantle to determine if the ions observed in this region are escaping or not. We found that the O^+ escape rate increases for higher dynamic pressure and southward IMF, while we observe a slight increase with EUV radiation. The higher O^+ escape rate is 1.4×10^{26} ions/s, and the solar wind power transferred into the magnetosphere reaches 10^{12} W. However, a certain amount of

energy should be transferred before the O^+ escape rate increases significantly. This threshold was found to be around 10^{10-11} W. Fig. 6.1 illustrates the result of the study, on the left panel solar wind and O^+ escape rate are shown for quiet solar wind conditions. The right panel shows disturbed solar wind conditions and a southward IMF, an increase of the O^+ escape rate from the plasma mantle as well as stronger solar power input.
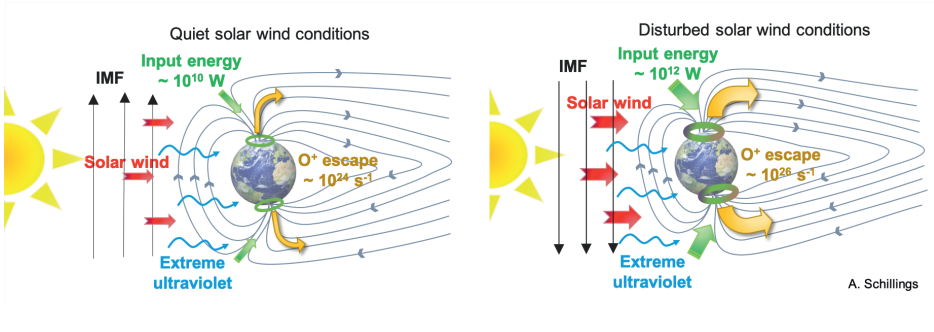
Figure 6.1: Illustration of quiet and disturbed solar wind conditions in term of EUV, IMF, solar wind dynamic pressure and solar power input into the magnetosphere. Credits: Schillings et al. (2019), graphical abstract.

4. Fate of plasma mantle O^+ outflow

Finally, we wanted to confirm with simulations that O^+ ions observed in the plasma mantle are actually escaping. Therefore, we used a forward tracing code to launch O^+ ions observed by Cluster in the plasma mantle. About 25000 ions were launched and we analysed their ending positions in the magnetosphere. Considering that if the final positions of the ions are after a geocentric radius $R = \sqrt{X_{fin}^2 + Y_{fin}^2 + Z_{fin}^2} = 10$ R_e the ions are escaping, we found that 96% of O^+ ions escape directly through the dayside, through the flank or in the distant tail. The statistics shows that the higher in the plasma mantle the ions are launched, the quicker they will escape. Furthermore, our statistics includes moderate disturbed conditions (lowest Dst = -76 nT), as well as northward and southward IMF, and shows that for R (O^+) $\leq$ 10 R_e IMF is usually northward and Dst positive. We also found that 93% of the O^+ ions observed in the plasma mantle have an initial parallel velocity about twice the perpendicular velocity, showing that the convection has a weak influence on the ions. In future studies, this forward tracing code could be applied specifically to geomagnetic storms.

CHAPTER 7

Paper summary

Paper I

Slapak, R., Schillings, A., Nilsson, H., Yamauchi, M., Westerberg, L. G., and Dandouras I. **Atmospheric loss from the dayside open polar region and its dependence on geomagnetic activity: implications for atmospheric escape on evolutionary timescales.** *Annales Geophysicae, Volume 35, 721-731, 2017*

Two different paths of escaping ions from the magnetosphere into the solar wind have been investigated for different geomagnetic activity levels (Kp index): via the plasma mantle and directly into the high-latitude dayside magnetosheath. The time-averaged O^+ flux from the plasma mantle with sufficient energy to escape in the distant tail beyond the X-line is 6 times larger than the ions escaping directly into the dayside magnetosheath. We estimated the total O^+ escape rate from the plasma mantle to be $\sim 8.2 \times 10^{24} \exp(0.45\ \mathrm{Kp})\ \mathrm{s}^{-1}$, and the O^+ escape rate during extreme geomagnetic conditions can by extrapolation be estimated to be $5.5 \times 10^{26}\ \mathrm{s}^{-1}$ (see *corrigendum*). Finally, considering that the EUV flux was higher in the past, the average O^+ escape could have reached $10^{27-28}\ \mathrm{s}^{-1}$ a few billion years ago.

Slapak, R., Schillings, A., Nilsson, H., Yamauchi, M., Westerberg, L. G., and Dandouras I. ***Corrigendum to* Atmospheric loss from the dayside open polar region and its dependence on geomagnetic activity: implications for atmospheric escape on evolutionary timescales.** *Annales Geophysicae, Volume 35, 721-731, 2017*

This paper has a short *corrigendum*, as we discovered an error in the calculation of the O^+ escape rate via the plasma mantle ($\Phi_{O^+}^{pm}$) about a factor 2 too small, whereas the O^+ escape rate from the cusp is correct. This error does not affect the general trend found between the total O^+ escape as a function of the Kp index.

Paper II

Ion outflow during geomagnetic storms have already been studied, however, the upper limit of the ion outflow during extreme geomagnetic storms is not well constrained due to poor spatial coverage during storm events. Between 2001 and 2004, the ion outflow in the polar cap during six extreme geomagnetic storms has been investigated using Cluster - CODIF data. In this paper, an extreme geomagnetic storm is defined by the criteria of minimum Dst < -100 nT or Kp $> 7+$. We estimated the upward O^+ flux scaled to an ionospheric reference altitude for each storm individually in a spatial box based on the plasma beta values and ion characteristics. The calculated O^+ scaled flux for the storm was compared to the full year O^+ scaled flux in the same spatial box which gives the relative enhancement between the storm and average conditions during the year. We found that the outflow for an extreme geomagnetic storm was 1 to 2 orders of magnitudes higher than during average conditions and the largest relative scaled outflow enhancement was 83 and the highest scaled O^+ outflow observed was 2×10^{14} m^{-2}s^{-1}.

Paper III

A severe geomagnetic storm was observed with several satellites in early September 2017. During this event several X-flares and coronal mass ejections (CMEs) were detected, while two CME–shocks hit the Earth late on September 6 and 7. The first shock produced a storm sudden commencement that initiated a geomagnetic storm, during which we analysed the upward O^+ flux scaled to an ionospheric reference altitude. Using Cluster - CODIF data, we estimated the upward O^+ flux in the polar cap before and after the second shock passage to be 10^{13} m^{-2}s^{-1}, which corresponds to an enhancement of a factor 3. This high value of ionospheric O^+ outflow is probably due to a preheating of the ionosphere by the multiple previous X-flares. Finally, we briefly discuss the space weather consequences on the magnetosphere as a whole and the enhanced O^+ outflow in connection with enhanced satellite drag.

Paper IV

Schillings, A., Slapak, R., Nilsson, H., Yamauchi, M., Dandouras, I., and Westerberg, L. G.. **Earth atmospheric loss through the plasma mantle and its dependence on solar wind parameters.** *Earth, Planets and Space, 71:70, 2019*

Under strong solar wind conditions, the magnetic field configuration of Earth is disturbed and allows more solar wind to penetrate into the magnetosphere, via the cusp. Ions in the cusp are reflected and mirrored to form a downstream region, the plasma mantle. We suggested in previous studies that O^+ ions observed in the plasma mantle escape the magnetosphere. Therefore, we investigated the dependency of the O^+ escape rate for several solar wind parameters, namely solar wind dynamic pressure, IMF and EUV. Using statistics over 5 years (2001-2005) of Cluster - CODIF data, we observed an enhancement of O^+ escape rate for high solar wind dynamic pressure as well as southward IMF, whereas we only found a slight increase with EUV irradiance. Furthermore, the solar wind power transferred into the magnetosphere is non-linear. Thus, we estimated a O^+ escape rate of $\sim 9 \times 10^{25}$ s^{-1} for a solar transferred power of roughly 10^{10} W or lower. However, higher solar transferred power leads to an exponential increase of the O^+ escape rate up to 10^{26} s^{-1}. These results show that under disturbed magnetospheric conditions more O^+ ions are escaping the magnetosphere.

Paper V

Schillings, A., Gunell, H., Nilsson, H., De Spiegeleer, A., Ebihara, Y., Westerberg, L.-G., Yamauchi, M. and Slapak, R.. **The fate of O^+ ions observed in the plasma mantle and cusp: particle tracing modelling and Cluster observations.** *Submitted to Annales Geophysicae, October 2019*

In the previous papers, we suggested that O^+ ions observed by Cluster satellites in the high-altitude cusp and in the plasma mantle had enough energy to be lost into the solar wind. To confirm this hypothesis, we analysed 136 events located in the plasma mantle and the cusp during 2001 and 2007 employing a forward tracing code. This code consists of the Tsyganenko T96 model for the representation of the magnetosphere and the Weimer 2001 model for the ionospheric potential. About 25000 O^+ ions are then traced using the Lorentz's force. We found that 96% of the traced ions are escaping the magnetosphere through the flank, in the distant tail or in the dayside. These simulations confirm the hypothesis that we suggested from Cluster observations, O^+ ions that reach high enough altitudes are escaping the magnetosphere and will be lost into the solar wind.

Bibliography

Abe, T., Whalen, B. A., Yau, A. W., Horita, R. E., Watanabe, S., and Sagawa, E.: EXOS D (Akebono) suprathermal mass spectrometer observations of the polar wind, Journal of Geophysical Research: Space Physics, 98, 11 191–11 203, doi:10.1029/92JA01971, 1993.

André, M. and Yau, A.: Theories and Observations of Ion Energization and Outflow in the High Latitude Magnetosphere, Space Science Reviews, 80, 27–48, doi:10.1023/A:1004921619885, 1997.

André, M., Li, K., and Eriksson, A. I.: Outflow of low-energy ions and the solar cycle, Journal of Geophysical Research: Space Physics, 120, 1072–1085, doi:10.1002/2014JA020714, 2015.

Axford, W. I.: The polar wind and the terrestrial helium budget, J. Geophys. Res., 73, 6855–6859, doi:10.1029/JA073i021p06855, 1968.

Balogh, A., Carr, C. M., Acuña, M. H., Dunlop, M. W., Beek, T. J., Brown, P., Fornaçon, K.-H., Georgescu, E., Glassmeier, K.-H., Harris, J., Musmann, G., Oddy, T., and Schwingenschuh, K.: The Cluster Magnetic Field Investigation: overview of in-flight performance and initial results, Annales Geophysicae, 19, 1207–1217, doi:10.5194/angeo-19-1207-2001, 2001.

Banks, P. M. and Holzer, T. E.: High-latitude plasma transport: The polar wind, Journal of Geophysical Research, 74, 6317–6332, doi:10.1029/JA074i026p06317, 1968.

Bertaux, J. L.: Observed variations of the exospheric hydrogen density with the exospheric temperature, Journal of Geophysical Research (1896-1977), 80, 639–642, doi:10.1029/JA080i004p00639, 1975.

Bouhram, M., Klecker, B., Paschmann, G., Haaland, S., Hasegawa, H., Blagau, A., Rème, H., Sauvaud, J.-A., Kistler, L. M., and Balogh, A.: Survey of energetic O^+ ions near the dayside mid-latitude magnetopause with Cluster, Annales Geophysicae, 23, 1281–1294, doi:10.5194/angeo-23-1281-2005, 2005.

Ceplecha, Z.: Influx of interplanetary bodies onto earth, Astronomy and Astrophysics, 263, 361–366, 1992.

Chandler, M. O., Waite, J. H., and Moore, T. E.: Observations of polar ion outflows, Journal of Geophysical Research: Space Physics, 96, 1421–1428, doi:10.1029/90JA02180, 1991.

Chappell, C. R., Moore, T. E., and Waite, Jr., J. H.: The ionosphere as a fully adequate source of plasma for the earth's magnetosphere, J. Geophys. Res., 92, 5896–5910, doi:10.1029/JA092iA06p05896, 1987.

Cremonese, G., Borin, P., Martellato, E., Marzari, F., and Bruno, M.: New calibration of the micrometeoroid flux on Earth, The Astrophysical Journal, 749, L40, doi: 10.1088/2041-8205/749/2/l40, 2012.

Cully, C. M., Donovan, E. F., Yau, A. W., and Arkos, G. G.: Akebono/Suprathermal Mass Spectrometer observations of low-energy ion outflow: Dependence on magnetic activity and solar wind conditions, Journal of Geophysical Research (Space Physics), 108, 1093, doi:10.1029/2001JA009200, 2003.

Dessler, A. J. and Michel, F. C.: Plasma in the geomagnetic tail, Journal of Geophysical Research, 71, 1421–1426, doi:10.1029/JZ071i005p01421, 1966.

Engwall, E.: Low-Energy Ion Escape from the Terrestrial Polar Regions, Ph.D. thesis, Uppsala University, Department of Physics and Astronomy, 2009.

Engwall, E., Eriksson, A. I., Cully, C. M., André, M., Puhl-Quinn, P. A., Vaith, H., and Torbert, R.: Survey of cold ionospheric outflows in the magnetotail, Annales Geophysicae, 27, 3185–3201, doi:10.5194/angeo-27-3185-2009, 2009.

Escoubet, C. P., Schmidt, R., and Goldstein, M. L.: Cluster - Science and Mission Overview, pp. 11–32, Springer Netherlands, Dordrecht, doi:10.1007/978-94-011-5666-0_1, 1997.

Escoubet, C. P., Fehringer, M., and Goldstein, M.: Introduction The Cluster mission, Annales Geophysicae, 19, 1197–1200, doi:10.5194/angeo-19-1197-2001, 2001.

Goldston, R. and Rutherford, P.: Introduction to Plasma Physics, CRC Press, 1995.

Green, J. L. and Waite, Jr., J. H.: On the origin of polar ion streams, Geophys. Res. Lett., 12, 149–152, doi:10.1029/GL012i003p00149, 1985.

Güdel, M.: The Sun in Time: Activity and Environment, Living Reviews in Solar Physics, 4, 3, doi:10.12942/lrsp-2007-3, 2007.

Haaland, S., Eriksson, A., Engwall, E., Lybekk, B., Nilsson, H., Pedersen, A., Svenes, K., André, M., Förster, M., Li, K., Johnsen, C., and Østgaard, N.: Estimating the capture and loss of cold plasma from ionospheric outflow, Journal of Geophysical Research (Space Physics), 117, A07311, doi:10.1029/2012JA017679, 2012.

Haaland, S., Eriksson, A., André, M., Maes, L., Baddeley, L., Barakat, A., Chappell, R., Eccles, V., Johnsen, C., Lybekk, B., Li, K., Pedersen, A., Schunk, R., and Welling, D.: Estimation of cold plasma outflow during geomagnetic storms, Journal of Geophysical Research (Space Physics), 120, 10, doi:10.1002/2015JA021810, 2015.

Hargreaves, J. K.: The Solar-Terrestrial Environment: An Introduction to Geospace - the Science of the Terrestrial Upper Atmosphere, Ionosphere, and Magnetosphere, Cambridge Atmospheric and Space Science Series, Cambridge University Press, doi:10.1017/CBO9780511628924, 1992.

Hoffman, J. H.: Ion composition measurements in the polar region from the Explorer 31 satellite, Trans. Am. Geophys. Union, 49, 1968.

Hughes, D. W.: Meteors and cosmic dust, Endeavour, 21, 31 – 35, doi:10.1016/S0160-9327(96)10030-2, 1997.

Hultqvist, B., Øieroset, M., Paschmann, G., and Treumann, R., eds.: Magnetospheric Plasma Sources and Losses, vol. 6 of *Space Sciences Series of ISSI*, Springer Netherlands, 1999.

Hunten, D. M.: The Escape of Light Gases from Planetary Atmospheres, Journal of the Atmospheric Sciences, 30, 1481–1494, doi:10.1175/1520-0469(1973)030<1481:TEOLGF>2.0.CO;2, 1973.

Hunten, D. M. and Strobel, D. F.: Production and Escape of Terrestrial Hydrogen, Journal of the Atmospheric Sciences, 31, 305–317, doi:10.1175/1520-0469(1974)031<0305:PAEOTH>2.0.CO;2, 1974.

Kallenrode, M.-B.: Space Physics. An introduction to plasma and particles in the heliosphere and magnetospheres, Springer-Verlag, 1998.

Kamide, Y. and Maltsev, Y. P.: Handbook of the Solar-Terrestrial Environment, Springer-Verlag Berlin Heidelberg, 2007.

Kistler, L. M. and Mouikis, C. G.: The inner magnetosphere ion composition and local time distribution over a solar cycle, Journal of Geophysical Research: Space Physics, 121, 2009–2032, doi:10.1002/2015JA021883, 2016.

Kistler, L. M., Mouikis, C. G., Cao, X., Frey, H., Klecker, B., Dandouras, I., Korth, A., Marcucci, M. F., Lundin, R., McCarthy, M., Friedel, R., and Lucek, E.: Ion composition and pressure changes in storm time and nonstorm substorms in the vicinity of the near-Earth neutral line, Journal of Geophysical Research (Space Physics), 111, A11222, doi:10.1029/2006JA011939, 2006.

Kistler, L. M., Mouikis, C. G., Klecker, B., and Dandouras, I.: Cusp as a source for oxygen in the plasma sheet during geomagnetic storms, Journal of Geophysical Research (Space Physics), 115, A03209, doi:10.1029/2009JA014838, 2010.

Kistler, L. M., Mouikis, C. G., and Genestreti, K. J.: In-flight calibration of the Cluster/CODIF sensor, Geoscientific Instrumentation, Methods and Data Systems, 2, 225–235, doi:10.5194/gi-2-225-2013, 2013.

Koskinen, H. E. J.: Physics of Space Storms. From the Solar Surface to the Earth., Springer Verlag, Praxis Publishing, 2011.

Krauss, S., Fichtinger, B., Lammer, H., Hausleitner, W., Kulikov, Y. N., Ribas, I. I., Shematovich, V. I., Bisikalo, D., Lichtenegger, H. I. M., Zaqarashvili, T. V., Khodachenko, M. L., and Hanslmeier, A.: Solar flares as proxy for the young Sun:

satellite observed thermosphere response to an X17.2 flare of Earth's upper atmosphere, Annales Geophysicae, 30, 1129–1141, doi:10.5194/angeo-30-1129-2012, 2012.

Kusnierkiewicz, D. Y.: An Overview of the TIMED Spacecraft, Tech. Rep. 24, No. 2, JHU/APL Technical Digest, 2003.

Kyte, F. T. and Wasson, J. T.: Accretion Rate of Extraterrestrial Matter: Iridium Deposited 33 to 67 Million Years Ago, Science, 232, 1225–1229, doi:10.1126/science.232.4755.1225, 1986.

Li, K., Haaland, S., Eriksson, A., André, M., Engwall, E., Wei, Y., Kronberg, E. A., Fränz, M., Daly, P. W., Zhao, H., and Ren, Q. Y.: On the ionospheric source region of cold ion outflow, Geophys. Res. Lett., 39, L18102, doi:10.1029/2012GL053297, 2012.

Li, K., Wei, Y., André, M., Eriksson, A., Haaland, S., Kronberg, E. A., Nilsson, H., Maes, L., Rong, Z. J., and Wan, W. X.: Cold Ion Outflow Modulated by the Solar Wind Energy Input and Tilt of the Geomagnetic Dipole, Journal of Geophysical Research: Space Physics, 122, 10,658–10,668, doi:10.1002/2017JA024642, 2017.

Liao, J., Kistler, L. M., Mouikis, C. G., Klecker, B., Dandouras, I., and Zhang, J.-C.: Statistical study of O^+ transport from the cusp to the lobes with Cluster CODIF data, Journal of Geophysical Research (Space Physics), 115, A00J15, doi:10.1029/2010JA015613, 2010.

Liao, J., Kistler, L. M., Mouikis, C. G., Klecker, B., and Dandouras, I.: Acceleration of O^+ from the cusp to the plasma sheet, Journal of Geophysical Research (Space Physics), 120, 1022–1034, doi:10.1002/2014JA020341, 2015.

Lie-Svendsen, Ø., Rees, M., and Stamnes, K.: Helium escape from the Earth's atmosphere: The charge exchange mechanism revisited, Planetary and Space Science, 40, 1639 – 1662, doi:/10.1016/0032-0633(92)90123-6, 1992.

Lockwood, M., Chandler, M. O., Horwitz, J. L., Waite, J. H., Moore, T. E., and Chappell, C. R.: The cleft ion fountain, Journal of Geophysical Research: Space Physics, 90, 9736–9748, doi:10.1029/JA090iA10p09736, 1985.

Love, S. G. and Brownlee, D. E.: A Direct Measurement of the Terrestrial Mass Accretion Rate of Cosmic Dust, Science, 262, 550–553, doi:10.1126/science.262.5133.550, 1993.

MacDonald, G. J. F.: The Escape of Helium from the Earth's Atmosphere, in: The Origin and Evolution of Atmospheres and Oceans, edited by Brancazio, P. J. and Cameron, A. G. W., p. 127, 1964.

Maggiolo, R. and Kistler, L. M.: Spatial variation in the plasma sheet composition: Dependence on geomagnetic and solar activity, Journal of Geophysical Research (Space Physics), 119, 2836–2857, doi:10.1002/2013JA019517, 2014.

Maggiolo, R., Sauvaud, J.-A., Fontaine, D., Teste, A., Grigorenko, E., Balogh, A., Fazakerley, A., Paschmann, G., Delcourt, D., and Rème, H.: A multi-satellite study of accelerated ion beams above the polar cap, Annales Geophysicae, 24, 1665–1684, doi:10.5194/angeo-24-1665-2006, 2006.

Mouikis, C. G., Kistler, L. M., Liu, Y. H., Klecker, B., Korth, A., and Dandouras, I.: H^+ and O^+ content of the plasma sheet at 15-19 Re as a function of geomagnetic and solar activity, Journal of Geophysical Research (Space Physics), 115, A00J16, doi:10.1029/2010JA015978, 2010.

Nagai, T., Waite, J. H., Green, J. L., Chappell, C. R., Olsen, R. C., and Comfort, R. H.: First measurements of supersonic polar wind in the polar magnetosphere, Geophysical Research Letters, 11, 669–672, doi:10.1029/GL011i007p00669, 1984.

NASA: Solar Physics. The Solar Interior., URL https://solarscience.msfc.nasa.gov/interior.shtml.

Newell, P. T., Meng, C.-I., Sibeck, D. G., and Lepping, R.: Some low-altitude cusp dependencies on the interplanetary magnetic field, Journal of Geophysical Research (Space Physics), 94, 8921–8927, doi:10.1029/JA094iA07p08921, 1989.

Nilsson, H.: Heavy Ion Energization, Transport, and Loss in the Earth's Magnetosphere, pp. 315–327, Springer Netherlands, Dordrecht, doi:10.1007/978-94-007-0501-2_17, 2011.

Nilsson, H., Kirkwood, S., and Bjørnå, N.: Bistatic measurements of incoherent scatter plasma lines, Journal of Atmospheric and Terrestrial Physics, 58, 175 – 187, doi:https://doi.org/10.1016/0021-9169(95)00028-3, selected papers from the sixth international Eiscat Workshop, 1996.

Nilsson, H., Waara, M., Arvelius, S., Marghitu, O., Bouhram, M., Hobara, Y., Yamauchi, M., Lundin, R., Rème, H., Sauvaud, J.-A., Dandouras, I., Balogh, A., Kistler, L. M., Klecker, B., Carlson, C. W., Bavassano-Cattaneo, M. B., and Korth, A.: Characteristics of high altitude oxygen ion energization and outflow as observed by Cluster: a statistical study, Annales Geophysicae, 24, 1099–1112, doi:10.5194/angeo-24-1099-2006, 2006.

Nilsson, H., Waara, M., Marghitu, O., Yamauchi, M., Lundin, R., Rème, H., Sauvaud, J.-A., Dandouras, I., Lucek, E., Kistler, L. M., Klecker, B., Carlson, C. W., Bavassano-Cattaneo, M. B., and Korth, A.: An assessment of the role of the centrifugal acceleration mechanism in high altitude polar cap oxygen ion outflow, Annales Geophysicae, 26, 145–157, doi:10.5194/angeo-26-145-2008, 2008.

Nilsson, H., Barghouthi, I. A., Slapak, R., Eriksson, A. I., and André, M.: Hot and cold ion outflow: Spatial distribution of ion heating, Journal of Geophysical Research (Space Physics), 117, A11201, doi:10.1029/2012JA017974, 2012.

Norqvist, P., André, M., Eliasson, L., Eriksson, A. I., Blomberg, L., Lühr, H., and Clemmons, J. H.: Ion cyclotron heating in the dayside magnetosphere, Journal of Geophysical Research, 101, 13 179–13 194, doi:10.1029/95JA03596, 1996.

Norqvist, P., André, M., and Tyrland, M.: A statistical study of ion energization mechanisms in the auroral region, Journal of Geophysical Research: Space Physics, 103, 23 459–23 473, doi:10.1029/98JA02076, 1998.

Ogawa, Y., Buchert, S. C., Fujii, R., Nozawa, S., and van Eyken, A. P.: Characteristics of ion upflow and downflow observed with the European Incoherent Scatter Svalbard radar, Journal of Geophysical Research: Space Physics, 114, doi: 10.1029/2008JA013817, 2009.

Øieroset, M., Yamauchi, M., Liszka, L., and Hultqvist, B.: Energetic ion outflow from the dayside ionosphere: Categorization, classification, and statistical study, Journal of Geophysical Research: Space Physics, 104, 24 915–24 927, doi:10.1029/ 1999JA900248, 1999.

Pesnell, W. D., Thompson, B. J., and Chamberlin, P. C.: The Solar Dynamics Observatory (SDO), Solar Physics, 275, 3–15, doi:10.1007/s11207-011-9841-3, 2012.

Pollock, C. J., Chandler, M. O., Moore, T. E., Waite, J. H., Chappell, C. R., and Gurnett, D. A.: A survey of upwelling ion event characteristics, Journal of Geophysical Research: Space Physics, 95, 18 969–18 980, doi:10.1029/JA095iA11p18969, 1990.

Prölss, G.: Physics of the Earth's Space Environment. An introduction, Springer-Verlag Berlin Heidelberg, 1 edn., 2004.

Rème, H., Aoustin, C., Bosqued, J. M., Dandouras, I., Lavraud, B., Sauvaud, J. A., Barthe, A., Bouyssou, J., Camus, T., Coeur-Joly, O., Cros, A., Cuvilo, J., Ducay, F., Garbarowitz, Y., Medale, J. L., Penou, E., Perrier, H., Romefort, D., Rouzaud, J., Vallat, C., Alcaydé, D., Jacquey, C., Mazelle, C., D'Uston, C., Möbius, E., Kistler, L. M., Crocker, K., Granoff, M., Mouikis, C., Popecki, M., Vosbury, M., Klecker, B., Hovestadt, D., Kucharek, H., Kuenneth, E., Paschmann, G., Scholer, M., Sckopke, N., Seidenschwang, E., Carlson, C. W., Curtis, D. W., Ingraham, C., Lin, R. P., McFadden, J. P., Parks, G. K., Phan, T., Formisano, V., Amata, E., Bavassano-Cattaneo, M. B., Baldetti, P., Bruno, R., Chionchio, G., di Lellis, A., Marcucci, M. F., Pallocchia, G., Korth, A., Daly, P. W., Graeve, B., Rosenbauer, H., Vasyliunas, V., McCarthy, M., Wilber, M., Eliasson, L., Lundin, R., Olsen, S., Shelley, E. G., Fuselier, S., Ghielmetti, A. G., Lennartsson, W., Escoubet, C. P., Balsiger, H., Friedel, R., Cao, J.-B., Kovrazhkin, R. A., Papamastorakis, I., Pellat, R., Scudder, J., and Sonnerup, B.: First multispacecraft ion measurements in and

near the Earth's magnetosphere with the identical Cluster ion spectrometry (CIS) experiment, Annales Geophysicae, 19, 1303–1354, doi:10.5194/angeo-19-1303-2001, 2001.

Ribas, I., Guinan, E. F., Güdel, M., and Audard, M.: Evolution of the Solar Activity over Time and Effects on Planetary Atmospheres. I. High-Energy Irradiances (1-1700 Å), Astrophys. J., 622, 680–694, doi:10.1086/427977, 2005.

Rosenbauer, H., Grünwaldt, H., Montgomery, M. D., Paschmann, G., and Sckopke, N.: Heos 2 plasma observations in the distant polar magnetosphere: The plasma mantle, Journal of Geophysical Research (1896-1977), 80, 2723–2737, doi:10.1029/JA080i019p02723, 1975.

Rosenqvist, L., Opgenoorth, H., Buchert, S., McCrea, I., Amm, O., and Lathuillere, C.: Extreme solar-terrestrial events of October 2003: High-latitude and Cluster observations of the large geomagnetic disturbances on 30 October, Journal of Geophysical Research (Space Physics), 110, A09S23, doi:10.1029/2004JA010927, 2005.

Russell, C., Luhmann, J., and Strangeway, R.: Space Physics: An Introduction, Cambridge University Press, 2016.

Salby, M. L.: Fundamentals of Atmospheric Physics., no. v. 61 in International Geophysics Series, Academic Press, 1996.

Schillings, A., Nilsson, H., Slapak, R., Yamauchi, M., and Westerberg, L.-G.: Relative outflow enhancements during major geomagnetic storms – Cluster observations, Annales Geophysicae, 35, 1341–1352, doi:10.5194/angeo-35-1341-2017, 2017.

Schillings, A., Nilsson, H., Slapak, R., Wintoft, P., Yamauchi, M., Wik, M., Dandouras, I., and Carr, C. M.: O+ Escape During the Extreme Space Weather Event of 4-10 September 2017, Space Weather, 16, 1363–1376, doi:10.1029/2018SW001881, 2018.

Schillings, A., Slapak, R., Nilsson, H., Yamauchi, M., Dandouras, I., and Westerberg, L.-G.: Earth atmospheric loss through the plasma mantle and its dependence on solar wind parameters, Earth, Planets and Space, 71, 70, doi:10.1186/s40623-019-1048-0, 2019.

Schunk, R. and Nagy, A.: Ionospheres: Physics, Plasma Physics, and Chemistry, Cambridge Atmospheric and Space Science Series, Cambridge University Press, 2 edn., doi:10.1017/CBO9780511635342, 2009.

Sharp, R. D., Johnson, R. G., and Shelley, E. G.: Observation of an ionospheric acceleration mechanism producing energetic (keV) ions primarily normal to the geomagnetic field direction, Journal of Geophysical Research (1896-1977), 82, 3324–3328, doi:10.1029/JA082i022p03324, 1977.

Shelley, E. G., Sharp, R. D., and Johnson, R. G.: Satellite observations of an iono-spheric acceleration mechanism, Geophysical Research Letters, 3, 654–656, doi:10.1029/GL003i011p00654, 1976.

Shelley, E. G., Peterson, W. K., Ghielmetti, A. G., and Geiss, J.: The polar iono-sphere as a source of energetic magnetospheric plasma, Geophys. Res. Lett., 9, 941–944, doi:10.1029/GL009i009p00941, 1982.

Shizgal, B. D. and Arkos, G. G.: Nonthermal escape of the atmospheres of Venus, Earth, and Mars, Reviews of Geophysics, 34, 483–505, doi:10.1029/96RG02213, 1996.

Slapak, R.: O^+ heating, outflow and escape in the high altitude cusp and mantle, Ph.D. thesis, Swedish Institute of Space Physics, 2013.

Slapak, R., Nilsson, H., Waara, M., André, M., Stenberg, G., and Barghouthi, I. A.: O^+ heating associated with strong wave activity in the high altitude cusp and mantle, Annales Geophysicae, 29, 931–944, doi:10.5194/angeo-29-931-2011, 2011.

Slapak, R., Nilsson, H., Westerberg, L. G., and Eriksson, A.: Observations of oxygen ions in the dayside magnetosheath associated with southward IMF, Journal of Geophysical Research (Space Physics), 117, A07218, doi:10.1029/2012JA017754, 2012.

Slapak, R., Nilsson, H., and Westerberg, L. G.: A statistical study on O^+ flux in the dayside magnetosheath, Annales Geophysicae, 31, 1005–1010, doi:10.5194/angeo-31-1005-2013, 2013.

Slapak, R., Schillings, A., Nilsson, H., Yamauchi, M., Westerberg, L.-G., and Dan-douras, I.: Atmospheric loss from the dayside open polar region and its depen-dence on geomagnetic activity: implications for atmospheric escape on evolutionary timescales, Annales Geophysicae, 35, 721–731, 2017.

SpaceWeatherLive: Solar Cycle 24 - Top 50 solar flares, URL `https://spaceweatherlive.com/`.

Strangeway, R. J., Ergun, R. E., Su, Y., Carlson, C. W., and Elphic, R. C.: Factors controlling ionospheric outflows as observed at intermediate altitudes, Journal of Geophysical Research: Space Physics, 110, doi:10.1029/2004JA010829, 2005.

Su, Y.-J., Horwitz, J. L., Moore, T. E., Giles, B. L., Chandler, M. O., Craven, P. D., Hirahara, M., and Pollock, C. J.: Polar wind survey with the Thermal Ion Dynamics Experiment/Plasma Source Instrument suite aboard POLAR, Journal of Geophysical Research: Space Physics, 103, 29 305–29 337, doi:10.1029/98JA02662, 1998.

Toriumi, S. and Wang, H.: Flare-productive active regions, Living Reviews in Solar Physics, 16, 3, doi:10.1007/s41116-019-0019-7, 2019.

Tsyganenko, N. A.: Modeling the Earth's magnetospheric magnetic field confined within a realistic magnetopause, Journal of Geophysical Research: Space Physics, 100, 5599–5612, doi:10.1029/94JA03193, 1995.

Waara, M.: High altitude ion heating observed by Cluster spacecraft, Ph.D. thesis, Swedish Institute of Space Physics, 2011.

Waara, M., Slapak, R., Nilsson, H., Stenberg, G., André, M., and Barghouthi, I. A.: Statistical evidence for O^+ energization and outflow caused by wave-particle interaction in the high altitude cusp and mantle, Annales Geophysicae, 29, 945–954, doi:10.5194/angeo-29-945-2011, 2011.

Wang, C., Lyons, L. R., and Angelopoulos, V.: Properties of low–latitude mantle plasma in the Earth's magnetotail: ARTEMIS observations and global MHD predictions, Journal of Geophysical Research: Space Physics, 119, 7264–7280, doi: 10.1002/2014JA020060, 2014.

Weimer, D. R.: An improved model of ionospheric electric potentials including substorm perturbations and application to the Geospace Environment Modeling November 24, 1996, event, Journal of Geophysical Research: Space Physics, 106, 407–416, doi:10.1029/2000JA000604, 2001.

Witze, A.: Earth's magnetic field is acting up and geologists don't know why, Nature, 565, 143–144, doi:10.1038/d41586-019-00007-1, 2019.

Woods, T., Bailey, S., Eparvier, F., Lawrence, G., Lean, J., McClintock, B., Roble, R., Rottman, G., Solomon, S., Tobiska, W., and White, O.: TIMED Solar EUV experiment, Physics and Chemistry of the Earth, Part C: Solar, Terrestrial and Planetary Science, 25, 393 – 396, doi:10.1016/S1464-1917(00)00040-4, 2000.

Yamauchi, M. and Wahlund, J.-E.: Role of the Ionosphere for the Atmospheric Evolution of Planets, Astrobiology, 7, 783–800, doi:10.1089/ast.2007.0140, 2007.

Yamauchi, M., Sergienko, T., Enell, C.-F., Schillings, A., Slapak, R., Johnsen, M. G., Tjulin, A., and Nilsson, H.: Ionospheric Response Observed by EISCAT During the 6–8 September 2017 Space Weather Event: Overview, Space Weather, 16, 1437–1450, doi:10.1029/2018SW001937, 2018.

Yau, A. W. and André, M.: Sources of Ion Outflow in the High Latitude Ionosphere, Space Sci. Rev., 80, 1–25, doi:10.1023/A:1004947203046, 1997.

Yau, A. W., Peterson, W. K., and Shelley, E. G.: Quantitative parametrization of energetic ionospheric ion outflow, Washington DC American Geophysical Union Geophysical Monograph Series, 44, 211–217, doi:10.1029/GM044p0211, 1988.

Yau, A. W., Abe, T., and Peterson, W.: The polar wind: Recent observations, Journal of Atmospheric and Solar-Terrestrial Physics, 69, 1936 – 1983, doi:10.1016/j.jastp.2007.08.010, recent Advances in the Polar Wind Theories and Observations, 2007.

Yau, A. W., Peterson, W., and Abe, T.: Influences of the Ionosphere, Thermosphere and Magnetosphere on Ion Outflows, pp. 283–314, Springer Netherlands, Dordrecht, doi:10.1007/978-94-007-0501-2_16, 2011.

Zhang, Y. and Paxton, L. J., eds.: Auroral Dynamics and Space Weather, AGU/Wiley, 2016.

Paper I

Atmospheric loss from the dayside open polar region and its dependence on geomagnetic activity: implications for atmospheric escape on evolutionary timescales

Authors:
R. Slapak, A. Schillings, H. Nilsson, M. Yamauchi, L.-G. Westerberg and I. Dandouras

Annales
Geophysicae

Atmospheric loss from the dayside open polar region and its dependence on geomagnetic activity: implications for atmospheric escape on evolutionary timescales

Rikard Slapak[1], Audrey Schillings[1,2], Hans Nilsson[1,2], Masatoshi Yamauchi[2], Lars-Göran Westerberg[3], and Iannis Dandouras[4,5]

[1]Division of Space Technology, Luleå University of Technology, Kiruna, Sweden
[2]Swedish Institute of Space Physics, Kiruna, Sweden
[3]Division of Fluid and Experimental Mechanics, Luleå University of Technology, Luleå, Sweden
[4]CNRS, Institut de Recherche en Astrophysique et Planétologie, Toulouse, France
[5]University of Toulouse, UPS-OMP, IRAP, Toulouse, France

Correspondence to: Rikard Slapak (rikard.slapak@ltu.se)

Abstract. We have investigated the total O^+ escape rate from the dayside open polar region and its dependence on geomagnetic activity, specifically Kp. Two different escape routes of magnetospheric plasma into the solar wind, the plasma mantle, and the high-latitude dayside magnetosheath have been investigated separately. The flux of O^+ in the plasma mantle is sufficiently fast to subsequently escape further down the magnetotail passing the neutral point, and it is nearly 3 times larger than that in the dayside magnetosheath. The contribution from the plasma mantle route is estimated as $\sim 3.9 \times 10^{24} \exp(0.45\,\mathrm{Kp})$ [s^{-1}] with a 1 to 2 order of magnitude range for a given geomagnetic activity condition. The extrapolation of this result, including escape via the dayside magnetosheath, indicates an average O^+ escape of $3 \times 10^{26}\,\mathrm{s}^{-1}$ for the most extreme geomagnetic storms. Assuming that the range is mainly caused by the solar EUV level, which was also larger in the past, the average O^+ escape could have reached $10^{27-28}\,\mathrm{s}^{-1}$ a few billion years ago. Integration over time suggests a total oxygen escape from ancient times until the present roughly equal to the atmospheric oxygen content today.

Keywords. Magnetospheric physics (magnetosheath; solar wind and magnetosphere interactions; storms and substorms)

1 Introduction

Investigations of terrestrial ion outflow and escape and its dependence on geomagnetic activity are important in order to obtain an increased understanding of magnetospheric dynamics, but also from an atmospheric evolution point of view. In the young solar system, the Sun is believed to have been more active (e.g. Ribas et al., 2005; Güdel, 2007) with a higher EUV flux, higher solar wind dynamic pressure, and a more intense and active magnetic field (solar dynamo) due to faster rotation (Wood, 2006; Airapetian and Usmanov, 2016). This indicates that the young Earth experienced more intense geomagnetic activity compared to the present time (Krauss et al., 2012) and hence high escaping fluxes of ionospheric ions (Moore et al., 1999; Cully et al., 2003; Peterson et al., 2008).

Ionospheric outflows typically originate at high latitudes, either along the closed field lines of the auroral region, directly feeding the plasma sheet, or along the open magnetic field lines of the polar cap and cusp. A review of high-latitude ionospheric outflow is given by Yau and André (1997). Outflow along open field lines will generally be put on trajectories leading tailward, and its fate is to a high degree determined by the energisation along the path. Cold ($< 1\,\mathrm{eV}$) H^+ and O^+ outflows can thus dominate in both flux and density in the distant magnetotail lobes (Engwall et al., 2009). The cusps are regions which enable direct interaction between the magnetosheath and the ionosphere, leading to increased elec-

tron temperatures and higher ion upflows as a consequence in the cusp ionosphere (Nilsson et al., 1996; Ogawa et al., 2003; Kistler et al., 2010). Ionospheric upflow is still gravitationally bound and needs further energisation in order to reach the magnetosphere. The act of the mirror force converts perpendicular energy into parallel energy for upflowing ions moving into regions of weaker magnetic field, and thus the perpendicular heating of plasma indirectly leads to acceleration along the field lines. Several studies have investigated this and shown that wave–particle interaction is effective in ion transverse heating over the whole range of altitudes in the cusps (André et al., 1990; Norqvist et al., 1996; Bouhram et al., 2003; Waara et al., 2011; Slapak et al., 2011), and the fate of the cusp ion outflow depends on the energisation of the ions along its path.

One can consider the cusp O$^+$ outflow to take one of three different main paths (corresponding to the yellow illustrative trajectories in Fig. 1) depending on how effectively it is accelerated: (1) low-energised ion populations will convect anti-sunward across the polar cap and further downtail and towards the plasma sheet, where they end up on closed field lines (Kistler et al., 2010; Liao et al., 2015); (2) sufficiently energised ions will reach the plasma mantle with typical velocities high enough to pass the tail X-line and consequently escape in the distant tail (Nilsson, 2011); (3) highly energised ions may escape into the dayside magnetosheath directly from the cusps (Slapak et al., 2012, 2013). Heavy (e.g. O$^+$) energetic ions can also escape to the dayside magnetosheath through magnetopause shadowing (Marcucci et al., 2004). Escaping ions during a strong northward interplanetary magnetic field may be brought back into the magnetosphere if dual-lobe reconnection takes place (Song and Russell, 1992). The fraction that might be brought back is, however, a low percentage and its effect on the total escape along route 3 is negligible (Slapak et al., 2015).

It is well known that the ion outflow rates are enhanced during geomagnetically active times. For example, Yau et al. (1988) parameterised the ionospheric ion outflow and found that the O$^+$ outflow rate increased exponentially with Kp as $\exp(0.5\,\mathrm{Kp})$. Other studies that have shown a clear correlation between O$^+$ and geomagnetic activity are Peterson et al. (2001), Cully et al. (2003), and Kistler and Mouikis (2016). The O$^+$ density close to the mid-latitude magnetopause was shown by Bouhram et al. (2005) to also increase exponentially with Kp. A consequence of increased ion outflow is an enhancement of the plasma feed into the plasma sheet during geomagnetic storms (Nose et al., 2005; Kistler et al., 2010; Haaland et al., 2012). The plasma sheet in turn feeds the ring current and its relative O$^+$ content and energy density increases significantly with geomagnetic activity. For example, Young et al. (1982) showed that the O$^+$ / H$^+$ density ratio increases exponentially with Kp ($\sim \exp(0.17\,\mathrm{Kp})$).

We will investigate and quantify the O$^+$ escape rate and its dependence on geomagnetic activity in two regions associated with ion escape: the plasma mantle and the high-
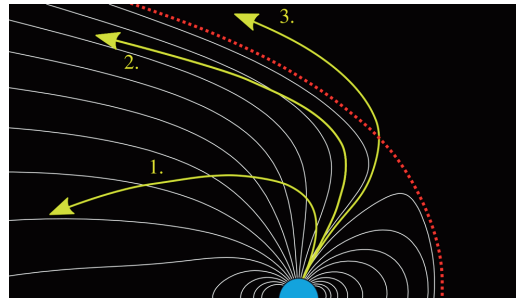

Figure 1. An illustration of possible magnetospheric ion outflow trajectories: (1) low-energy ion transport to the plasma sheet; (2) high-energy ion flows in the plasma mantle leading to escape downstream in the tail; (3) high-energy ion escape directly from the cusp into the high-latitude dayside magnetosheath. The red dashed line illustrates the magnetopause.

latitude magnetosheath. For the strongest geomagnetic conditions, the statistics become sparse and we need to extrapolate our results in order to say something about atmospheric loss during such events. Specific cases of O$^+$ outflow and escape during major geomagnetic storms need to be investigated in the future as a complement.

2 Instruments and data criteria

In this section, we first describe the instruments that provide us with the necessary data for our study, followed by descriptions of and criteria for the data sets corresponding to the plasma mantle and the high-latitude magnetosheath respectively.

2.1 Instruments

The study presented in this paper uses data obtained by instruments on-board two spacecraft (SC1 and SC4) of the Cluster mission (Escoubet et al., 2001), which consists in total of four spacecraft flying in formation with an identical set of instruments on-board. The composition distribution function (CODIF) spectrometer, described in detail by Rème et al. (2001), has mass resolution and provides ion distributions for different species (for particle energies up to $38\,\mathrm{keV}\,\mathrm{q}^{-1}$) from which the ion moments have been calculated. The magnetic field data are provided by the fluxgate magnetometer (FGM) (Balogh et al., 2001), which in normal mode has a sample frequency of 22.4 Hz. We are interested in the background magnetic field and therefore use field data averaged over the spacecraft spin period of 4 s, as is the ion moment data. The data set used for the plasma mantle statistics was obtained by SC4 and covers 2001–2005. For the high-latitude magnetosheath we use the data set compiled by Slapak et al.

(2013), in which times of high-energy O$^+$ were visually determined for 2001–2003 for SC1.

2.2 Plasma mantle

In order to study O$^+$ flows in the plasma mantle, the corresponding data need to be separated from polar cap and magnetosheath data. Figure 2 shows a high-latitude dayside passage of Cluster 1 from the magnetosheath across the magnetopause at around 09:18 UT and into the plasma mantle followed by a gradual decrease in ion flux intensity as it moves into the polar cap. The top and middle panel show the energy spectrograms for H$^+$ and O$^+$ respectively, and the bottom panel shows the magnetic field strength and its components. The magnetosheath is often characterised as a more fluctuant magnetic field compared to the field inside the magnetosphere. More importantly, it is also characterised by very strong H$^+$ fluxes. These intense fluxes cause contamination in the O$^+$ mass channel, yielding false counts; this contamination can be tracked and removed as described by Nilsson et al. (2006). The polar cap is a region associated with a low-energy ion environment in comparison with the plasma mantle, which is filled with denser energetic mirrored solar wind plasma. As a consequence, the plasma β number, defined as the thermal plasma pressure over magnetic pressure, is typically significantly higher in the plasma mantle. However, there is a gradual transition between the two regions and no distinct β value that will separate them. In statistical studies of the polar cap, data with the constraint that β is less than 0.01 are used (e.g. Liao et al., 2010, 2015). Therefore, a constraint of $\beta > 0.1$ in the dayside magnetosphere will exclude typical polar cap data. Using a somewhat lower or higher limit for β does not affect the results of this study, and therefore a $\beta > 0.1$ constraint is adopted. A blue rectangle in Fig. 2 marks the interval at which the criteria for the plasma mantle data associated with this particular magnetopause crossing are fulfilled.

We also put regional constraints on the data set by removing the inner magnetosphere ($R_{GSM} = (Y_{GSM}^2 + Z_{GSM}^2)^{1/2} > 6\,R_E$). We also consider data within a range of $-5 < X_{GSM} < 8\,R_E$. This allows for good spatial coverage in the dusk–dawn extent as well as sufficient data during the highest geomagnetic activities (high Kp). The results and conclusions of the study presented in this paper are not very sensitive to these exact limits, but they can be slightly altered.

However, the β and regional constraints are not sufficient. In Fig. 3, the H$^+$ (blue bars) and O$^+$ (red) perpendicular temperatures and number densities for $\beta > 0.1$ are presented. Panels (a) and (d) (top panels) show the distribution for all $\beta > 0.1$ data. In the H$^+$ data there are two clearly distinct peaks: around a few hundred eV and a few thousand eV for the temperature, and around 0.3 and 10 cm^{-3} for the density, suggesting two distinct plasma populations within our data set. We investigate this by separating the data into two subsets of $T_\perp(\mathrm{H}^+) < T_{cut}$ and $T_\perp(\mathrm{H}^+) > T_{cut}$

with $T_{cut} = 1750\,\mathrm{eV}$, marked in panel (a) as a vertical black dot-dashed line. The data corresponding to H$^+$ perpendicular temperatures larger than T_{cut} are shown in panels (b) and (e) (middle panels), and the data corresponding to the lower H$^+$ perpendicular temperatures are shown in panels (c) and (f) (bottom panels). It becomes clear that the data separation with respect to temperature also separates the density data, such that the lower density population relates to the high temperature population and the higher densities to the lower temperature population. This indeed confirms that there are two distinct populations with clear differences in the H$^+$ characteristics represented in the data set.

The H$^+$ population with high temperatures and low densities is consistent with the average characteristics of the plasma sheet presented by e.g. Baumjohann et al. (1989) and Kistler et al. (2006), whereas the population of lower temperatures but higher densities is what we expect to observe in the plasma mantle (e.g. Nilsson et al., 2006). The corresponding O$^+$ data also reveal differences in the characteristics between the two regions. For the plasma-sheet-like population, the O$^+$ temperatures are about the same as the H$^+$ temperatures, and the O$^+$ density is typically 1 order of magnitude lower than the H$^+$ density; this is consistent with plasma sheet measurements presented by Kistler et al. (2006). In the plasma mantle, however, the O$^+$ temperature spans a large range, from a few tens of eV up to 10 keV, but is in general considerably lower than for the plasma-sheet-like population. The O$^+$ density in the plasma mantle is higher than the plasma sheet O$^+$ densities, but still 1 to 2 orders of magnitude smaller than the corresponding H$^+$ densities, which is consistent with plasma mantle observations (Nilsson et al., 2012).

For the purpose of investigating O$^+$ fluxes in the plasma mantle, we constrict the data with the condition $T_\perp(\mathrm{H}^+) < 1750\,\mathrm{eV}$ in order to exclude the plasma-sheet-like population. The number of data points corresponding to the plasma mantle is just over 382 000, and the distribution as a function of Kp is shown as blue bars in Fig. 4. Moderate geomagnetic activity is most common, but some data for the highest values of Kp are also available. The number of data points for periods of Kp = 9 is below 100; this is too low to be visible in the chart due to the linear scale, and we leave it out of the statistical analysis.

2.3 The high-latitude magnetosheath

O$^+$ data in the high-latitude dayside magnetosheath covering 2001 to 2003 were identified by Slapak et al. (2013) through the visual inspection of O$^+$ energy spectrograms for ion energies larger than 3 keV in order to avoid false counts due to the intense H$^+$ fluxes in the magnetosheath (Nilsson et al., 2006). The middle panel of Fig. 2 shows such typical magnetosheath high-energy O$^+$ populations (marked with red rectangles) in the interval up to the magnetopause crossing at $\sim$09:18. Studies of such populations were presented by Slapak et al. (2012), who reported that the pop-
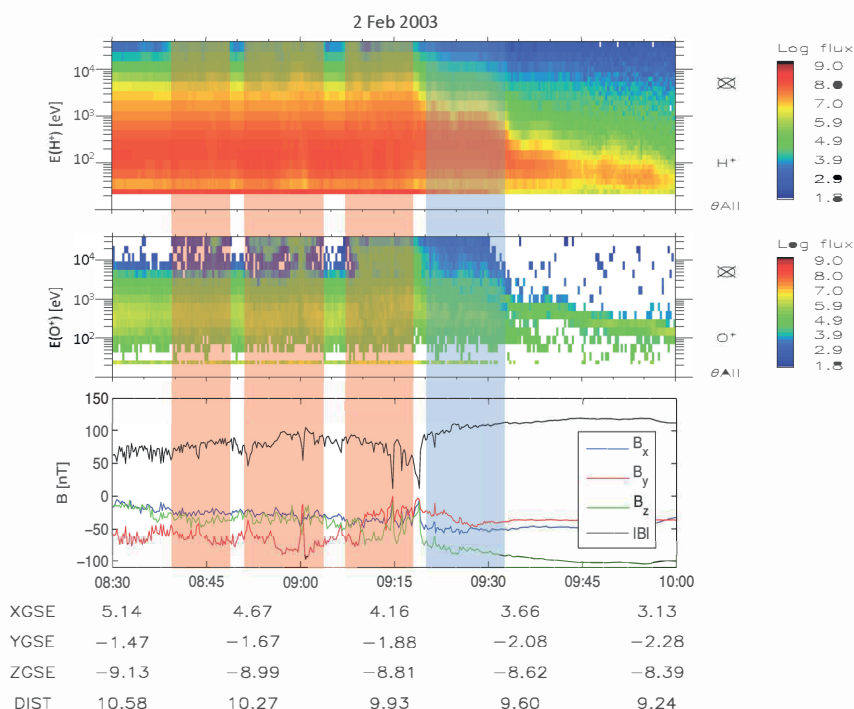
Figure 2. An example of a magnetopause crossing ($\sim$ 09:18 UT) in the southern high-latitude dayside hemisphere with Cluster 1, travelling from the magnetosheath into the plasma mantle and then the polar cap. The first and second panels show the H$^+$ and O$^+$ energy spectrograms respectively. The third panel shows the magnetic field strength and its components. The time intervals of the plasma mantle and magnetosheath data included in this study (for this particular time interval) are marked with blue and red rectangles respectively.

ulations had D-shaped velocity distributions, indicating that they had passed through a rotational discontinuity at the magnetopause, which is consistent with escape along open field lines. Only the months January to June were considered when picking out these types of magnetosheath O$^+$ populations as this period corresponds to a Cluster apogee in the dayside, allowing for regular passages through the high-latitude dayside magnetosheath. This data set allowed Slapak et al. (2013) to estimate an average total anti-sunward O$^+$ flux of 0.7×10^{25} s^{-1}, corresponding to direct escape from the cusps. In this study, we will use the same data set to study how the total escape from the cusps depends on the geomagnetic activity. The distribution of the O$^+$ observations in response to geomagnetic activity is shown in Fig. 4, where the magnetosheath data (roughly 92 000 data points) are binned (red bars) according to the simultaneously measured Kp values. Unfortunately, no magnetosheath data for conditions of Kp $\geq$ 7 are present in the data set. For Kp $=$ 6 we have very few data points, such that the O$^+$ data are not visible in the figure due to the choice of a linear scale.

3 Observations

Based on the data of the plasma mantle and magnetosheath described in Sect. 2, average fluxes scaled to ionospheric altitudes in order to cancel any altitude dependencies are calculated as a function of Kp. If the total particle flux is assumed to be conserved along a magnetic flux tube, the local particle flux F can be scaled to an ionospheric altitude as $F_I = F B_I / B$, where B_I is the ionospheric magnetic field strength set to 50 000 nT and B is the locally measured field strength. The result is shown in Fig. 5 and reveals a clear increase in flux with increased geomagnetic activity for both the plasma mantle (blue) and the high-latitude dayside magnetosheath (red). The error bars represent the standard deviations and are slightly shifted in the figure for visibility. Note that results are obtained only for Kp $\leq$ 8 and $\leq$ 6 for the plasma mantle regime and the magnetosheath respectively. The fluxes in the plasma mantle typically increase by 1.5 orders of magnitude between quiet times and times of the most extreme geomagnetic conditions. The scaled O$^+$ flux in the
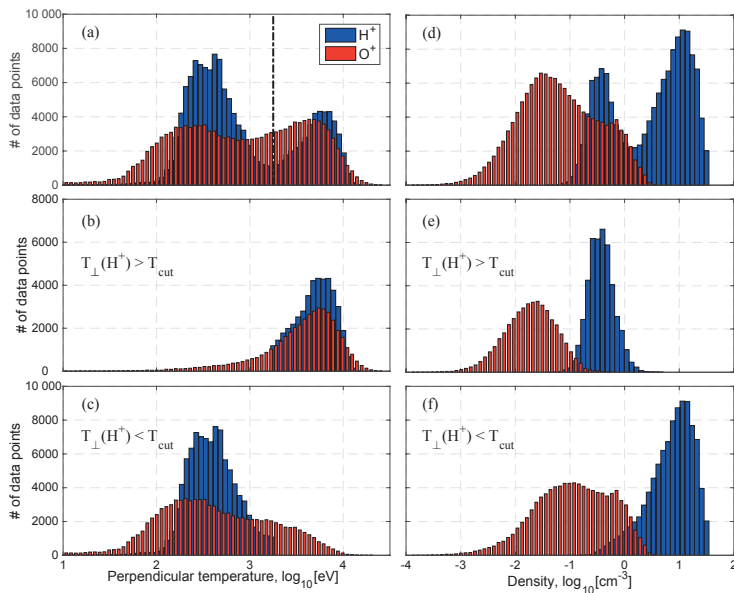
Figure 3. Distributions of $\beta > 0.1$ data in the dayside magnetosphere, covering 2001–2005. The left and right panels represent H$^+$ and O$^+$ temperatures and number densities respectively. The top panels **(a, d)** show all data, whereas the middle panels **(b, e)** show the data subset corresponding to H$^+$ $T_\perp$ higher than $T_{cut} = 1750$ eV, marked with a vertical line in **(a)**. The lower panels show the data subset corresponding to H$^+$ $T_\perp$ lower than T_{cut}.

magnetosheath is in principle the same as in the plasma mantle, at least up to Kp = 6.

We will estimate the total O$^+$ flux in the plasma mantle and magnetosheath separately as functions of Kp using the method implemented by Slapak et al. (2013) when calculating the average O$^+$ escape flux from the cusp into the high-latitude magnetosheath. They divided the data into spatial segments aligned with the magnetosheath high-latitude flow, yielding an escape cross section when also considering an effective outflow region with a dusk–dawn extent of 106° at the highest latitudes. The flow is typically tangential to the magnetopause, and therefore a magnetopause shape model, introduced by Shue et al. (1997), was used to define the stream-aligned segments in which O$^+$ occurrence rates and average fluxes were used to calculate the total O$^+$ escape rate. A much more detailed description of the method is given by Slapak et al. (2013). We note that the most significant plasma mantle outflows are at high latitudes as one would expect, and it turns out that the same dusk–dawn extent as observed for the magnetosheath is suitable for the plasma mantle calculations.

The plasma mantle bulk flow is similar to the magnetosheath flow in terms of the magnetopause-aligned flux. The method requires, however, good spatial coverage with significant data points. The most common are times with Kp = 3,

followed by Kp = 2 and 4 and then Kp = 1 and 5 (Fig. 4), and the method works fine for data corresponding to these Kp indices individually. However, the amounts of data for Kp = 0, 6, 7, and 8 are too small. We therefore combine the data for Kp = 0 and 1 and let the corresponding escape rate correspond to the average Kp value for this subset. For the highest geomagnetic activity conditions (Kp = (6, 7, 8)), the combined number of data points is even lower. This can be seen in Fig. 6, where the spatial coverage of the plasma mantle O$^+$ data is shown for different Kp values. However, the spatial coverage for this high geomagnetic activity subset is still decent and the same method can be applied. In the figure, the data are divided into bins of $1 R_E \times 1 R_E$ for which average O$^+$ fluxes (defined by the colour bar) and bulk velocities (arrows) are determined in order to visualise the spatial coverage and bulk flow. An arrow for reference is in the upper right corner in the first plot (Kp = (0, 1)) and has a length corresponding to 100 km s^{-1}. For clarity, we note that for the estimate of the total escape, we consider the average within each magnetopause tangential segment rather than the averages of the bins.

For the magnetosheath we use the same data set as Slapak et al. (2013). The data cover, as already mentioned, a smaller range of geomagnetic activity and we calculate the O$^+$ escape rate for Kp = (0, 1), Kp = 2, Kp = 3, and Kp = (4, 5, 6).
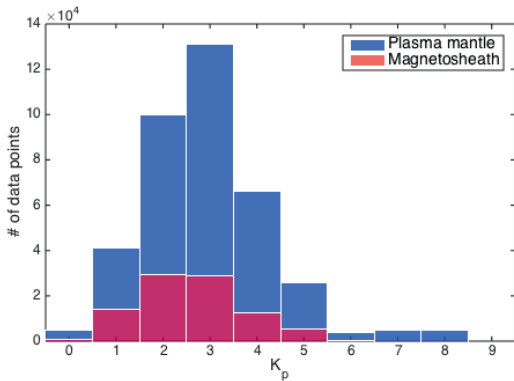
Figure 4. Distribution of O$^+$ observations over Kp for the plasma mantle (blue) and dayside magnetosheath (red) respectively.

The average O$^+$ escape rates are shown in Fig. 7 as blue (plasma mantle) and red (magnetosheath) solid lines with circles and squares respectively. As expected, the O$^+$ escape flux increases with higher geomagnetic activity for both escape paths, but with plasma mantle total O$^+$ flux typically a factor of 3 higher than in the magnetosheath. The black dashed line is the least-squares fit to the plasma mantle data, and its formula will be presented and discussed in Sect. 4. For quiet times (Kp $\approx$ 1), the total O$^+$ escape rate (considering the plasma mantle route) is $\sim 6 \times 10^{25}$ s^{-1}, whereas for the highest geomagnetic activity conditions (average Kp $\approx$ 7) the rate is $\sim 10^{26}$ s^{-1}.

As seen in Fig. 5, there are large variations in the measured scaled fluxes for a given Kp value. Therefore, the estimated values given above, for which the whole range of flux values were considered, can be seen as average O$^+$ escape rates. To get an estimate of how high (and low) the escape rate may be for a given geomagnetic condition, we instead only consider the flux data over the 80th (below the 20th) percentile within each segment. The results give an upper and lower estimate of the range of escape rates for a given geomagnetic condition, also shown in Fig. 7 as coloured areas; light blue is the plasma mantle route and light red is the dayside magnetosheath route. The upper and lower estimates typically have the same dependence on Kp as the average escape rates, but are significantly higher or lower, which is consistent with the large standard deviations observed in the scaled fluxes (Fig. 5)
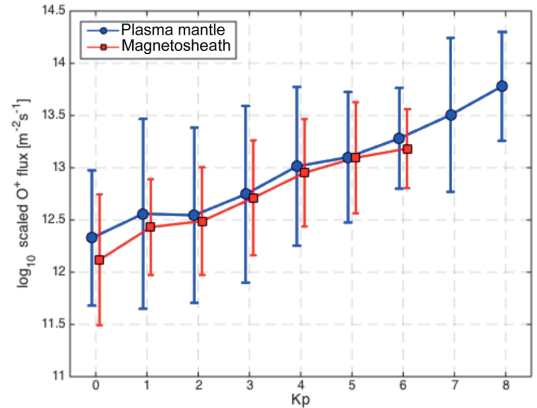

Figure 5. The average O$^+$ flux measured for the plasma mantle (blue circles) and in the magnetosheath (red squares), scaled to an ionospheric reference altitude as a function of Kp with error bars representing the standard deviations.

4 Discussion

4.1 Kp dependence

The total O$^+$ escape from the terrestrial magnetosphere as a function of geomagnetic activity for two different escape routes (via the plasma mantle and subsequent escape in the far tail and via open magnetic field lines directly from the cusp into the high-latitude magnetosheath) has been statistically investigated and quantified. As expected, there is a clear increase in the O$^+$ escape with increased Kp index for both escape routes, as shown in Fig. 7. In the same figure, the least-squares fit of O$^+$ escape via the plasma mantle (superscript pm) as a function of Kp is an exponential function given by

$$\Phi_{O^+}^{pm}(Kp) = 3.9 \times 10^{24} \exp(0.45 \, Kp), \quad [s^{-1}]. \quad (1)$$

The O$^+$ escape directly from the cusp into the high-latitude magnetosheath (superscript ms) is typically a factor of 3 smaller than the escape via the plasma mantle for a given geomagnetic activity condition, such that $\Phi_{O^+}^{ms} \approx \Phi_{O^+}^{pm}/3$. These expressions can be extrapolated to predict average escape fluxes for the very strongest geomagnetic storms: $\Phi_{O^+}^{pm}(Kp = 9) = 2.25 \times 10^{26}$ s^{-1} and a total escape of 3×10^{26} s^{-1}, if also considering the escape directly from the cusp into the dayside magnetosheath. Note that this value is an average including both hemispheres, i.e. the summer and winter hemispheres, because the Cluster trajectory with a 90° inclination was nearly north–south symmetric during 2001–2005.

The exponential dependence of O$^+$ escape on Kp ($\Phi \propto \exp(0.45 \, Kp)$) is similar and consistent with an O$^+$ outflow
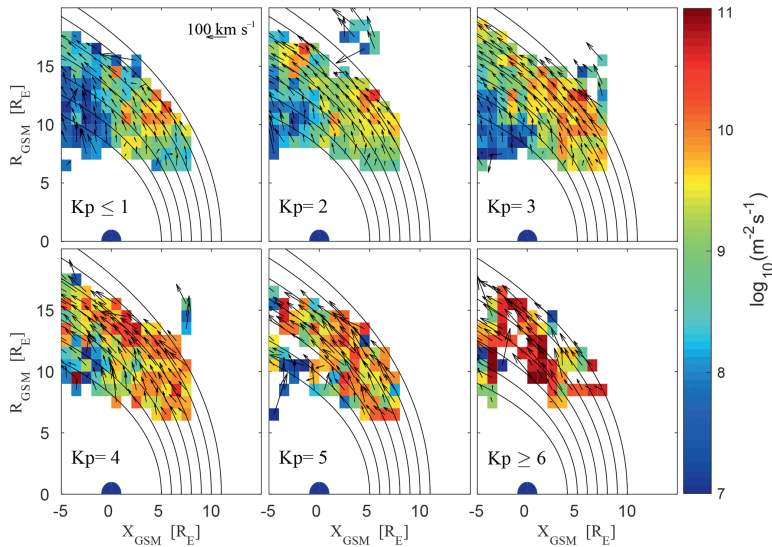
Figure 6. The spatial distribution of plasma mantle O$^+$ flux in cylindrical coordinates, (X_{gse}, $R_{gse} = (Y_{gse}^2 + Z_{gse}^2)^{1/2}$), for periods of different geomagnetic conditions: Kp = (0, 1), Kp = 2, Kp = 3, Kp = 4, Kp = 5, and Kp = (6, 7, 8). The colour bar defines the average flux intensity, and the arrows represent the average O$^+$ bulk velocity.

study by Yau et al. (1988), who mapped and integrated high-invariant latitude ($> 56°$) O$^+$ outflows using data obtained by Dynamics Explorer 1 (DE1) for an O$^+$ energy range of 0.01–17 keV. They found an $\propto \exp(0.50 \text{Kp})$ relation for a Kp range from 0 to 6. The total O$^+$ flux in their study was about a factor of 2.3 larger than the results presented in our study, given a certain condition on the geomagnetic activity. It makes no real sense to further compare our results with those of Yau et al. (1988), since the lower limit of the invariant latitude of 56° includes the whole polar cap, cusp, and auroral region. Pollock et al. (1990) calculated the total O$^+$ outflow for the cusp region specifically, also using data provided by instruments on-board DE1, and obtained a flux rate of 2×10^{25} s^{-1} without investigating any dependence on geomagnetic activity. This outflow is similar to the escape rates that we present in this study for average geomagnetic conditions, suggesting that a significant part of the O$^+$ cusp outflow will eventually escape, in principle via route 2 or 3 (Fig. 1).

4.2 EUV and seasonal effects

According to Cully et al. (2003), Peterson et al. (2008), and Maes et al. (2015), EUV flux is another leading factor that controls the escape flux, with much higher EUV flux associated with the summer hemisphere than the winter hemisphere. Figure 7 shows a wide range of escaping flux for a given Kp value, with 1 to 2 orders of magnitude difference

between the lower (below the 20th percentile) and the upper (over the 80th percentile) values. This is largely influenced by the influx of the solar EUV to the ionosphere (Moore et al., 1999; Cully et al., 2003; Peterson et al., 2006).

A solid estimate including the EUV dependence must include an estimation of the EUV influx to the ionosphere and the solar zenith angle, but such a formulation is model-dependent since we need to assume an effective latitude. Instead, we use the upper value in Fig. 7 as an estimate of the escape rate from the summer hemisphere.

4.3 Escape rate in the past

By considering the highest 20 % of the values instead of all data points, the O$^+$ loss rate from the cusp and plasma mantle becomes as high as 10^{27} s^{-1} for Kp = 9. This O$^+$ escape rate is 2 orders of magnitude larger than observed for typical average conditions (Nilsson, 2011; Slapak et al., 2013). Considering the evolution of G-type stars (or all main sequence stars), the young Sun was much more active than it is today in terms of higher emission of EUV radiation, faster solar wind, and a faster rotation, with more active sunspots and stronger IMF as a consequence due to a more effective solar dynamo (e.g. Ribas et al., 2005; Wood, 2006). Conditions during major geomagnetic storms are currently sometimes considered as a proxy for normal conditions in the ancient solar system (Krauss et al., 2012), and therefore Eq. (1) and the corresponding expression for the high-latitude mag-
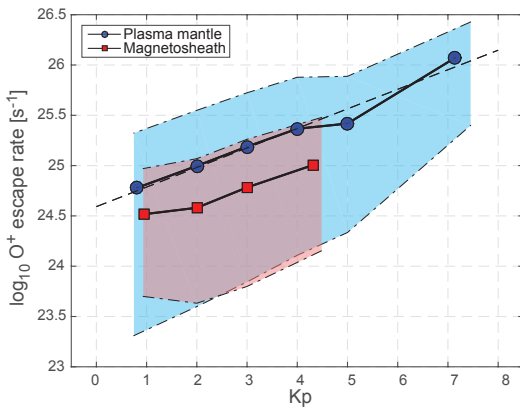
Figure 7. The average O$^+$ escape rates for the plasma mantle (solid blue line and circles) and the dayside magnetosheath (solid red line and squares) as a function of Kp. The dashed black line is a least-squares fit to the average escape rates for the plasma mantle. The thin dot-dashed lines correspond to estimated upper and lower O$^+$ escape rates in the plasma mantle (blue area) and the magnetosheath (red) based on the highest and lowest flux values observed under the different geomagnetic conditions.

netosheath can be used to estimate atmospheric loss during ancient epochs. However, a possible issue is that the relative abundance of oxygen in the atmosphere has changed considerably over time (e.g. Holland, 2006; Lyons et al., 2014), and consequently the question arises of how this change affects the O$^+$ outflow and escape over time. Measurements at Mars and Venus, which have CO_2-dominant atmospheres, show oxygen-dominated upper ionospheres and outflows (Lundin, 2011, and references therein). This indicates that the relative abundance of oxygen and even the composition of the atmosphere as a whole will not significantly affect the upper ionosphere. Therefore the upper ionosphere of the ancient Earth was most probably O$^+$-dominated independent of the oxygen abundance in the atmosphere, allowing us to extrapolate our result for present Earth to ancient times.

If Kp(t) is the average geomagnetic activity as a function of time, then the total loss L of O$^+$ from a time t_0 until the present day t_n can be expressed as

$$L = \int_{t_0}^{t_n} \Phi(Kp(t)) \mathrm{d}t, \qquad (2)$$

with Φ given by Eq. (1). We do not know how the average Kp has changed explicitly over time, but we can make rough estimates of the total O$^+$ escape. Assuming that Kp = 10 four billion years ago and decreasing linearly with time (exponential decay in terms of geomagnetic deviation in nT), the total O$^+$ loss becomes $\sim 4.8 \times 10^{17}$ kg, corresponding to 40 % of today's total oxygen mass in the atmosphere. Krauss

et al. (2012) investigated an X17.2 flare on 28 October 2003 during the "Halloween period" (Rosenqvist et al., 2005) and concluded that the conditions served as a proxy for the Sun at the age of 2.3 billion years. Using this as a reference time and Kp = 9 as associated with the Halloween events and integrating over four billion years, we get a total O$^+$ loss that is 1.3 times the total oxygen mass in the atmosphere today. Both estimates give a total O$^+$ loss of the same order as atmospheric oxygen content at the present time. These estimates assume that all ions detected in the O$^+$ mass channel of the CODIF spectrometer are indeed O$^+$. However, given the finite mass resolution of the instrument ($m/\Delta m \sim 5-7$), N$^+$ ions could also be part of the population. N$^+$ ions have been observed to take substantial proportions in the outflow during very active periods (Hamilton et al., 1988; Christon et al., 2002). A better understanding of and insight into the solar and geomagnetic conditions on geological timescales is needed in order to further investigate this matter and is left for future consideration. A systematic survey of the outflows using high mass-resolution instrumentation, as with the recently proposed ESA ESCAPE mission, would allow a detailed investigation, a separation of the O$^+$ and N$^+$ escape rates, and a study of their links to the solar and magnetospheric activity.

5 Conclusions

We have estimated the typical O$^+$ escape in high-latitude and high-altitude regions via the plasma mantle and dayside magnetosheath and found that it increases exponentially as $\exp(0.45\,\mathrm{Kp})$; this is consistent with earlier observed O$^+$ outflow dependences on Kp at lower altitudes (Yau et al., 1988). The dominant escape route is via the plasma mantle and is quantitatively given by $\Phi_{\mathrm{O}^+}^{\mathrm{pm}}(\mathrm{Kp}) = 3.9 \times 10^{24} \exp(0.45\,\mathrm{Kp})$ [s^{-1}]. Escape directly from the cusp into the dayside magnetosheath is smaller (by about a factor of 3) but significant. An extrapolation of the result suggests an average oxygen ion escape of 3×10^{26} s^{-1} for conditions when Kp = 9. Estimates of the total O$^+$ escape [kg] since the Earth was young until today indicate that it is roughly equal to the amount of the present atmospheric oxygen content.

References

Airapetian, V. S. and Usmanov, A. V.: Reconstructing the solar wind from its early history to current epoch, Astrophys. J. Lett., 817, L24, https://doi.org/10.3847/2041-8205/817/2/L24, 2016.

André, M., Crew, G. B., Peterson, W. K., Persoon, A. M., Pollock, C. J., and Engebretson, M. J.: Ion heating by broadband low-frequency waves in the cusp/cleft, J. Geophys. Res., 95, 20809–20823, https://doi.org/10.1029/JA095iA12p20809, 1990.

Balogh, A., Carr, C. M., Acuña, M. H., Dunlop, M. W., Beek, T. J., Brown, P., Fornacon, K.-H., Georgescu, E., Glassmeier, K.-H., Harris, J., Musmann, G., Oddy, T., and Schwingenschuh, K.: The Cluster Magnetic Field Investigation: overview of in-flight performance and initial results, Ann. Geophys., 19, 1207–1217, https://doi.org/10.5194/angeo-19-1207-2001, 2001.

Baumjohann, W., Paschmann, G., and Cattell, C. A.: Average plasma properties in the central plasma sheet, J. Geophys. Res., 94, 6597–6606, https://doi.org/10.1029/JA094iA06p06597, 1989.

Bouhram, M., Malingre, M., Jasperse, J. R., Dubouloz, N., and Sauvaud, J.-A.: Modeling transverse heating and outflow of ionospheric ions from the dayside cusp/cleft. 2 Applications, Ann. Geophys., 21, 1773–1791, https://doi.org/10.5194/angeo-21-1773-2003, 2003.

Bouhram, M., Klecker, B., Paschmann, G., Haaland, S., Hasegawa, H., Blagau, A., Rème, H., Sauvaud, J.-A., Kistler, L. M., and Balogh, A.: Survey of energetic O$^+$ ions near the dayside mid-latitude magnetopause with Cluster, Ann. Geophys., 23, 1281–1294, https://doi.org/10.5194/angeo-23-1281-2005, 2005.

Christon, S. P., Mall, U., Eastman, T. E., Gloeckler, G., Lui, A. T. Y., McEntire, R. W., and Roelof, E. C.: Solar cycle and geomagnetic N^{+1}/O^{+1} variation in outer dayside magnetosphere: Possible relation to topside ionosphere, Geophys. Res. Lett., 29, 1058, https://doi.org/10.1029/2001GL013988, 2002.

Cully, C. M., Donovan, E. F., Yau, A. W., and Arkos, G. G.: Akebono/Suprathermal Mass Spectrometer observations of low-energy ion outflow: Dependence on magnetic activity and solar wind conditions, J. Geophys. Res.-Space, 108, 1093, https://doi.org/10.1029/2001JA009200, 2003.

Engwall, E., Eriksson, A. I., Cully, C. M., André, M., Torbert, R., and Vaith, H.: Earth's ionospheric outflow dominated by hidden cold plasma, Nat. Geosci., 2, 24–27, https://doi.org/10.1038/ngeo387, 2009.

Escoubet, C. P., Fehringer, M., and Goldstein, M.: *Introduction* The Cluster mission, Ann. Geophys., 19, 1197–1200, https://doi.org/10.5194/angeo-19-1197-2001, 2001.

Güdel, M.: The Sun in time: activity and environment, Living Rev. Sol. Phys., 4, 1–137, https://doi.org/10.12942/lrsp-2007-3, 2007.

Haaland, S., Eriksson, A. I., Engwall, E., Lybekk, B., Nilsson, H., Pedersen, A., Svenes, K., Förster, M., Li, K., Johnsen, C., and Østgaard, N.: Estimating the capture and loss of cold plasma from ionospheric outflow, J. Geophys. Res., 117, A07311, https://doi.org/10.1029/2012JA017679, 2012.

Hamilton, D. C., Gloeckler, G., Ipavich, F. M., Wilken, B., and Stuedemann, W.: Ring current development during the great geomagnetic storm of February 1986, J. Geophys. Res., 93, 14343–14355, https://doi.org/10.1029/JA093iA12p14343, 1988.

Holland, H. D.: The oxygenation of the atmosphere and oceans, Phil. Trans. R. Soc. B, 361, 903–915, https://doi.org/10.1098/rstb.2006.1838, 2006.

Kistler, L. M. and Mouikis, C. G.: The inner magnetosphere ion composition and local time distribution over a solar cycle, J. Geophys. Res., 121, 2009–2032, https://doi.org/10.1002/2015JA021883, 2016.

Kistler, L. M., Mouikis, C. G., Cao, X., Frey, H., Klecker, B., Dandouras, I., Korth, A., Marcucci, M. F., Lundin, R., McCarthy, M., Friedel, R., and Lucek, E.: Ion composition and pressure changes in storm time and nonstorm substorms in the vicinity of the near-Earth neutral line, J. Geophys. Res., 111, A11222, https://doi.org/10.1029/2006JA011939, 2006.

Kistler, L. M., Mouikis, C. G., Klecker, B., and Dandouras, I.: Cusp as a source for oxygen in the plasma sheet during geomagnetic storms, J. Geophys. Res., 115, A03209, https://doi.org/10.1029/2009JA014838, 2010.

Krauss, S., Fichtinger, B., Lammer, H., Hausleitner, W., Kulikov, Yu. N., Ribas, I., Shematovich, V. I., Bisikalo, D., Lichtenegger, H. I. M., Zaqarashvili, T. V., Khodachenko, M. L., and Hanslmeier, A.: Solar flares as proxy for the young Sun: satellite observed thermosphere response to an X17.2 flare of Earth's upper atmosphere, Ann. Geophys., 30, 1129–1141, https://doi.org/10.5194/angeo-30-1129-2012, 2012.

Liao, J., Kistler, L. M., Mouikis, C. G., Klecker, B., Dandouras, I., and Zhang, J.-C.: Statistical study of O$^+$ transport from the cusp to the lobes with Cluster CODIF data, J. Geophys. Res., 115, A00J15, https://doi.org/10.1029/2010JA015613, 2010.

Liao, J., Kistler, L. M., Mouikis, C. G., Klecker, B., and Dandouras, I.: Acceleration of O$^+$ from the cusp to the plasma sheet, J. Geophys. Res.-Space, 120, 1022–1034, https://doi.org/10.1002/2014JA020341, 2015.

Lundin, R.: Ion acceleration and outflow from Mars and Venus: An overview, Space Sci. Rev., 162, 309–334, https://doi.org/10.1007/s11214-011-9811-y, 2011.

Lyons, T. W., Reinhard, C. T., and Planavsky, N. J.: The rise of oxygen in Earth's early ocean and atmosphere, Nature, 506, 307–315, https://doi.org/10.1038/nature13068, 2014.

Maes, L., Maggiolo, R., De Keyser, J., Dandouras, I., Fear, R. C., Fontaine, D., and Haaland, S.: Solar illumination control of ionospheric outflow above polar cap arcs, Geophys. Res. Lett., 42, 1304–1311, https://doi.org/10.1002/2014GL062972, 2015.

Marcucci, M. F., Bavassano Cattaneo, M. B., Pallocchia, M., Amata, E., Bruno, R., Di Lellis, A. M., Formisano, V., Rème, H., Bosqued, J. M., Dandouras, I., Sauvoud, J. A., Kistler, L. M., Moebius, E., Klecker, B., Carlson, C. W., Parks, G. K., McCarthy, M., Korth, A., Lundin, R., and Balogh, A.: Energetic magnetospheric oxygen in the magnetosheath and its response to IMF orientation: Cluster observations, J. Geophys. Res., 109, A07203, https://doi.org/10.1029/2003JA010312, 2004.

Moore, T. E., Lundin, R., Alcayde, D., André, M., Ganguli, S. B., Temerin, M., and Yau, A.: Source processes in the high-latitude ionosphere, Space Sci. Rev., 88, 7–84, https://doi.org/10.1023/A:1005299616446, 1999.

Nilsson, H.: Heavy ion energization, transport, and loss in the Earth's magnetosphere, in: The Dynamic Magnetosphere, edited by: Liu, W. and Fujimoto, M., https://doi.org/10.1007/978-94-007-0501-2_17, IAGA, Springer, 2011.

Nilsson, H., Yamauchi, M., Eliasson, L., Norberg, O., and Clemmons, J.: Ionospheric signature of the cusp as seen by incoherent scatter radar, J. Geophys. Res., 101, 10947–10963, https://doi.org/10.1029/95JA03341, 1996.

Nilsson, H., Waara, M., Arvelius, S., Marghitu, O., Bouhram, M., Hobara, Y., Yamauchi, M., Lundin, R., Rème, H., Sauvaud, J.-A., Dandouras, I., Balogh, A., Kistler, L. M., Klecker, B., Carlson, C. W., Bavassano-Cattaneo, M. B., and Korth, A.: Characteristics of high altitude oxygen ion energization and outflow as observed by Cluster: a statistical study, Ann. Geophys., 24, 1099–1112, https://doi.org/10.5194/angeo-24-1099-2006, 2006.

Nilsson, H., Barghouthi, I. A., Slapak, R., Eriksson, A., and André, M.: Hot and cold ion outflow: spatial distribution of ion heating, J. Geophys. Res., 117, A11201, https://doi.org/10.1029/2012JA017974, 2012.

Norqvist, P., André, M., Eliasson, L., Eriksson, A. I., Blomberg, L., Lühr, H., and Clemmons, J. H.: Ion cyclotron heating in the dayside magnetosphere, J. Geophys. Res., 101, 13179–13194, https://doi.org/10.1029/95JA03596, 1996.

Nose, M., Taguchi, S., Hosokawa, K., Christon, S. P., McEntire, R. W., Moore, T. E., and Collier, M. R.: Overwhelming O$^+$ contribution to the plasma sheet energy density during the October 2003 superstorm: Geotail/EPIC and IMAGE/LENA observations, J. Geophys. Res., 110, A09S24, https://doi.org/10.1029/2004JA010930, 2005.

Ogawa, Y., Fujii, R., Buchert, S. C., Nozawa, S., and Ohtani, S.: Simultaneous EISCAT Svalbard radar and DMSP observations of ion upflow in the dayside polar ionosphere, J. Geophys. Res., 108, 1101, https://doi.org/10.1029/2002JA009590, 2003.

Peterson, W. K., Collin, H. L., Yau, A. W., and Lennartsson, O. W.: Polar/Toroidal Imaging Mass-Angle Spectrograph observations of suprathermal ion outflow during solar minimum conditions, J. Geophys. Res., 106, 6059–6066, https://doi.org/10.1029/2000JA003006, 2001.

Peterson, W. K., Collin, H. L., Lennartsson, O. W., and Yau, A. W.: Quiet time solar illumination effects on the fluxes and characteristic energies of ionospheric outflows, J. Geophys. Res., 111, A11S05, https://doi.org/10.1029/2005JA011596, 2006.

Peterson, W. K., Andersson, L., Callahan, B. C., Collin, H. L., Scudder, J. D., and Yau, A. W.: Solar-minimum quiet time ion energization and outflow in dynamic boundary related coordinates, J. Geophys. Res., 113, A07222, https://doi.org/10.1029/2008JA013059, 2008.

Pollock, C. J., Chandler, M. O., Moore, T. E., Waite Jr., J. H., Chappell, C. R., and Gurnett, D. A.: A survey of upwelling ion event characteristics, J. Geophys. Res., 95, 18969–18980, https://doi.org/10.1029/JA095iA11p18969, 1990.

Rème, H., Aoustin, C., Bosqued, J. M., Dandouras, I., Lavraud, B., Sauvaud, J. A., Barthe, A., Bouyssou, J., Camus, Th., Coeur-Joly, O., Cros, A., Cuvilo, J., Ducay, F., Garbarowitz, Y., Medale, J. L., Penou, E., Perrier, H., Romefort, D., Rouzaud, J., Vallat, C.,

Alcaydé, D., Jacquey, C., Mazelle, C., d'Uston, C., Möbius, E., Kistler, L. M., Crocker, K., Granoff, M., Mouikis, C., Popecki, M., Vosbury, M., Klecker, B., Hovestadt, D., Kucharek, H., Kuenneth, E., Paschmann, G., Scholer, M., Sckopke, N., Seidenschwang, E., Carlson, C. W., Curtis, D. W., Ingraham, C., Lin, R. P., McFadden, J. P., Parks, G. K., Phan, T., Formisano, V., Amata, E., Bavassano-Cattaneo, M. B., Baldetti, P., Bruno, R., Chionchio, G., Di Lellis, A., Marcucci, M. F., Pallocchia, G., Korth, A., Daly, P. W., Graeve, B., Rosenbauer, H., Vasyliunas, V., McCarthy, M., Wilber, M., Eliasson, L., Lundin, R., Olsen, S., Shelley, E. G., Fuselier, S., Ghielmetti, A. G., Lennartsson, W., Escoubet, C. P., Balsiger, H., Friedel, R., Cao, J.-B., Kovrazhkin, R. A., Papamastorakis, I., Pellat, R., Scudder, J., and Sonnerup, B.: First multispacecraft ion measurements in and near the Earth's magnetosphere with the identical Cluster ion spectrometry (CIS) experiment, Ann. Geophys., 19, 1303–1354, https://doi.org/10.5194/angeo-19-1303-2001, 2001.

Ribas, S., Guinan, E. F., Güdel, M., and Audard, M.: Evolution of the solar activity over time and effects on planetary atmospheres. I. High-energy irradiances (1–1700 Å), Astrophys. J., 622, 680–694, https://doi.org/10.1086/427977, 2005.

Rosenqvist, L., Opgenoorth, H., Buchert, S., McCrea, I., Amm, O., and Lathuillere, C.: Extreme solar-terrestrial events of October 2003: High-latitude and Cluster observations of the large geomagnetic disturbances on 30 October, J. Geophys. Res., 110, A09S23, https://doi.org/10.1029/2004JA010927, 2005.

Shue, J.-H., Chao, J., Fu, H., Russell, C., Song, P., Khurana, K., and Singer, H.: A new functional form to study the solar wind control of the magnetopause size and shape, J. Geophys. Res., 102, 9497–9511, https://doi.org/10.1029/97JA00196, 1997.

Slapak, R., Nilsson, H., Waara, M., André, M., Stenberg, G., and Barghouthi, I. A.: O$^+$ heating associated with strong wave activity in the high altitude cusp and mantle, Ann. Geophys., 29, 931–944, https://doi.org/10.5194/angeo-29-931-2011, 2011.

Slapak, R., Nilsson, H., Westerberg, L. G., and Eriksson, A.: Observations of oxygen ions in the dayside magnetosheath associated with southward IMF, J. Geophys. Res., 117, A07218, https://doi.org/10.1029/2012JA017754, 2012.

Slapak, R., Nilsson, H., and Westerberg, L. G.: A statistical study on O$^+$ flux in the dayside magnetosheath, Ann. Geophys., 31, 1005–1010, https://doi.org/10.5194/angeo-31-1005-2013, 2013.

Slapak, R., Nilsson, H., Westerberg, L. G., and Larsson, R.: O$^+$ transport in the dayside magnetosheath and its dependence on the IMF direction, Ann. Geophys., 33, 301–307, https://doi.org/10.5194/angeo-33-301-2015, 2015.

Song, P. and Russell, C. T.: Model of the formation of the low-latitude boundary layer for strongly northward interplanetary magnetic field, J. Geophys. Res., 97, 1411–1420, https://doi.org/10.1029/91JA02377, 1992.

Waara, M., Slapak, R., Nilsson, H., Stenberg, G., André, M., and Barghouthi, I. A.: Statistical evidence for O+ energization and outflow caused by wave-particle interaction in the high altitude cusp and mantle, Ann. Geophys., 29, 945–954, https://doi.org/10.5194/angeo-29-945-2011, 2011.

Wood, B. E.: The solar wind and the Sun in the past, Space Sci. Rev., 126, 3–14, https://doi.org/10.1007/s11214-006-9006-0, 2006.

Yau, A. W. and André, M.: Sources of ion outflow in the high latitude ionosphere, Space Sci. Rev., 80, 1–25, https://doi.org/10.1023/A:1004947203046, 1997.

Yau, A. W., Peterson, W. K., and Shelley, E. G.: Quantitative parametrization of energetic ionospheric ion outflow, Geophys. Monogr. Ser., 44, 211–217, https://doi.org/10.1029/GM044p0211, 1988.

Young, D. T., Balsiger, H., and Geiss, J.: Correlations of magnetospheric ion composition with geomagnetic and solar activity, J. Geophys. Res., 87, 9077–9096, https://doi.org/10.1029/JA087iA11p09077, 1982.

Annales
Geophysicae

Corrigendum to

"Atmospheric loss from the dayside open polar region and its dependence on geomagnetic activity: implications for atmospheric escape on evolutionary timescales" published in Ann. Geophys., 35, 721–731, 2017

Rikard Slapak[1], **Audrey Schillings**[1,2], **Hans Nilsson**[1,2], **Masatoshi Yamauchi**[2], **Lars-Göran Westerberg**[3], **and Iannis Dandouras**[4,5]

[1]Division of Space Technology, Luleå University of Technology, Kiruna, Sweden
[2]Swedish Institute of Space Physics, Kiruna, Sweden
[3]Division of Fluid and Experimental Mechanics, Luleå University of Technology, Luleå, Sweden
[4]CNRS, Institut de Recherche en Astrophysique et Planétologie, Toulouse, France
[5]University of Toulouse, UPS-OMP, IRAP, Toulouse, France

Correspondence: Rikard Slapak (rikard.slapak@eiscat.se)

In the paper "Atmospheric loss from the dayside polar region and its dependence on geomagnetic activity: implications for atmospheric escape on evolutionary timescales" by Rikard Slapak et al., published in in Ann. Geophys., 35, 721–731, 2017, there is an error in the quantification of the O^+ escape rate (total flux) via the plasma mantle ($\Phi_{O^+}^{pm}$). The O^+ escape rate directly from the cusp into the dayside magnetosheath ($\Phi_{O^+}^{ms}$) is correct, however. The discovered error is due to a small mistake in relation to the considered outflow area when calculating the total flux, and $\Phi_{O^+}^{pm}$ should be a factor of about 2.1 larger than given in the paper. The error does not affect the found Kp dependence that was presented. Therefore, the correct expression for the plasma mantle O^+ escape rate as a function of Kp is

$$\Phi_{O^+}^{pm}(\text{Kp}) = 8.2 \times 10^{24} \exp(0.45\,\text{Kp}), \quad [\text{s}^{-1}].$$

Figure 7 in the paper should be updated accordingly and a correct figure is given in this corrigendum (Fig. 7). As can be seen, the corresponding upper and lower limits of the plasma mantle O^+ escape have also been adjusted in response to the calculation error. The average O^+ escape directly from the cusp into the dayside magnetosheath is approximately $\Phi_{O^+}^{ms} \approx \Phi_{O^+}^{pm}/6$, instead of $\Phi_{O^+}^{pm}/3$ as stated in the paper, and

the total escape ($\Phi_{O^+}^{ms} + \Phi_{O^+}^{pm}$) should therefore be a factor of 1.8 larger than stated in the paper.

This factor of 1.8 affects our estimations that follow in the discussion section; the total O^+ escape extrapolated to extreme geomagnetic conditions (Kp = 9) gives an escape rate of $5.5 \times 10^{26}\,\text{s}^{-1}$, instead of $3 \times 10^{26}\,\text{s}^{-1}$ as presented in the paper. Also, we made rough estimates of the total O^+ escape during the course of roughly 4 billion years. We used two different and simple assumptions on how the average Kp index has changed over time and estimated the total escape to be 0.4 and 1.3, respectively, of today's atmospheric oxygen content. These values are instead 0.7 and 2.3, respectively.

As far as we know results from the paper have been used or discussed in two newly published papers: Schillings et al. (2017), who studied O^+ escape during events of extreme geomagnetic conditions and compared their result with ours, and Yamauchi and Slapak (2018), who suggested magnetospheric O^+ outflow to mass-load incoming solar wind plasma causing field-aligned currents that connect the magnetosphere and ionosphere. The discussions and conclusions in these two papers are not affected by the error in the paper.
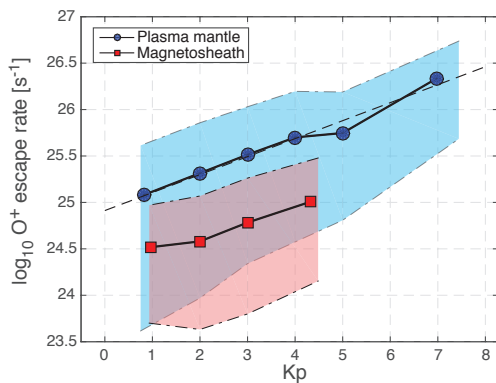
Figure 7. Corrected figure, where the lower, average and upper O$^+$ escape rate as a function of Kp has been corrected with a factor of 2.1. The corresponding O$^+$ escape rates directly from the cusp into the dayside magnetosheath are left unchanged.

References

Schillings, A., Nilsson, H., Slapak, R., Yamauchi, M., and Westerberg, L.-G.: Relative outflow enhancements during major geomagnetic storms – Cluster observations, Ann. Geophys., 35, 1341–1352, https://doi.org/10.5194/angeo-35-1341-2017, 2017.

Yamauchi, M. and Slapak, R.: Energy conversion through mass loading of escaping ionospheric ions for different Kp values, Ann. Geophys., 36, 1–12, https://doi.org/10.5194/angeo-36-1-2018, 2018.

Relative outflow enhancements during major geomagnetic storms - Cluster observations

Authors:
A. Schillings, H. Nilsson, R. Slapak, M. Yamauchi and L.-G. Westerberg

Annales
Geophysicae

Relative outflow enhancements during major geomagnetic storms – Cluster observations

Audrey Schillings[1,2]**, Hans Nilsson**[1,2]**, Rikard Slapak**[2]**, Masatoshi Yamauchi**[1]**, and Lars-Göran Westerberg**[3]

[1]Swedish Institute of Space Physics, Kiruna, Sweden
[2]Division of Space Technology, Luleå University of Technology, Kiruna, Sweden
[3]Division of Fluid and Experimental Mechanics, Luleå University of Technology, Luleå, Sweden

Correspondence: Audrey Schillings (audrey.schillings@irf.se)

Abstract. The rate of ion outflow from the polar ionosphere is known to vary by orders of magnitude, depending on the geomagnetic activity. However, the upper limit of the outflow rate during the largest geomagnetic storms is not well constrained due to poor spatial coverage during storm events. In this paper, we analyse six major geomagnetic storms between 2001 and 2004 using Cluster data. The six major storms fulfil the criteria of Dst < -100 nT or Kp $> 7+$. Since the shape of the magnetospheric regions (plasma mantle, lobe and inner magnetosphere) are distorted during large magnetic storms, we use both plasma beta (β) and ion characteristics to define a spatial box where the upward O^+ flux scaled to an ionospheric reference altitude for the extreme event is observed. The relative enhancement of the scaled outflow in the spatial boxes as compared to the data from the full year when the storm occurred is estimated. Only O^+ data were used because H^+ may have a solar wind origin. The storm time data for most cases showed up as a clearly distinguishable separate peak in the distribution toward the largest fluxes observed. The relative enhancement in the outflow region during storm time is 1 to 2 orders of magnitude higher compared to less disturbed time. The largest relative scaled outflow enhancement is 83 (7 November 2004) and the highest scaled O^+ outflow observed is 2×10^{14} m^{-2} s^{-1} (29 October 2003).

Keywords. Magnetospheric physics (storms and substorms; magnetosphere–ionosphere interactions; solar-wind–magnetosphere interactions)

1 Introduction

The young sun appears to have been much more active; flares were more frequent and the solar wind was more powerful and had stronger high-energy emissions (Ribas et al., 2005). Thus, current geomagnetic storms can be considered as a proxy for the normal conditions of the past (Krauss et al., 2012). Therefore, studies of outflow for extreme events have implications outside direct space weather effects. Indeed, the ion outflow under current major geomagnetic storms could have been the normal rate of ion outflow in the past (young sun), so ion outflow during storms may be especially important to understand atmospheric evolution on a geological timescale. Slapak et al. (2017) roughly estimated the escape rate in the past. The authors extrapolated their result on the O^+ escape rate in the plasma mantle and dayside magnetosheath to the past and obtained a total O^+ loss of about 40 % of today's total oxygen mass in the atmosphere. Ion outflow and escape from the polar ionosphere play a key role in magnetospheric dynamics and atmospherical evolution and have been the subject of numerous studies; see, e.g., Kronberg et al. (2014) and references therein. However, there is a lack of studies on escaping ions during extreme geomagnetic conditions. This study presents observations of outflowing ions during major geomagnetic storms and discusses them in terms of relative enhancements because there is not enough data to fully quantify the escape.

The regions of open magnetic field lines, which include the cusp, the polar cap and the plasma mantle, are the main pathways for ion outflow leading to escape (Nilsson et al., 2012). The cusp is the dayside region of recently opened magnetic field lines where the solar wind has the most direct entry to the magnetosphere. The plasma mantle is the high-

altitude region downstream of the cusp, dominated by solar wind ions that have been reflected by the mirror force of the earth's magnetic field, streaming outward and tailward. The polar cap is the whole region of open magnetic field lines mapping mainly to the magnetotail lobes. Ion outflow occurs from all of these regions, but the oxygen outflow from the cusp and mantle is most intense and also most likely to escape into interplanetary space (Nilsson et al., 2012; Slapak et al., 2013).

A dependency on magnetospheric conditions and interplanetary magnetic field (IMF) has been established for outflowing ions in the altitude range of 1.3 to 2.0 R_E (Yau et al., 1988). Yau et al. (1988) showed that upflow increase exponentially with geomagnetic activity as measured by the Kp index. A Kp increased from 0 to 6 led to a factor of 20 increase in O^+ outflow and a factor of 4 increase in H^+ outflow in their covered energy range of 0.01 to 17 keV. What the fate of these outflowing ions will be and where they will end up is not clear because of the relatively low altitude of these observations. Slapak et al. (2017) carried out a similar study of Kp dependence based on high-altitude Cluster spacecraft data, trying to estimate the total atmospheric escape by looking at the plasma mantle and the magnetosheath. The authors estimate the contribution from the plasma mantle as $3.9 \times 10^{24} \exp(0.45 \, \text{Kp}) \, \text{s}^{-1}$. They could not obtain a direct escape estimation for the most extreme geomagnetic conditions because of a lack of statistics.

Their study only concerned O^+, as it is more challenging to distinguish the ionospheric origin of H^+ from solar wind in the plasma mantle. The same is true of our study, and we will therefore only discuss O^+ outflow.

During geomagnetic storms, the solar wind speed and density are higher than usual. The solar wind is mainly composed of H^+ and thus most of the oxygen ions observed in the magnetosphere originate from the ionosphere (Shelley et al., 1982; Chappell et al., 1987). As discussed above, the outflow of both O^+ and H^+ increases with geomagnetic activity.

Kistler et al. (2010) showed that the density of the oxygen ions in the cusp increases by a factor of 10 before or during the early main phase of a storm. This result was corroborated by Liao et al. (2010), who found that the occurrence frequency of O^+ observations in the lobes increases during the storm main phase. Liao et al. (2015) discussed the influence of the geomagnetic activity on the velocity increase in O^+ as it is transported from the cusp to the tail lobe. The authors found that from the cusp to the polar cap and to the tail lobes, the acceleration of oxygen ions is not significant. However, during storm time, accelerated O^+ was observed in the cusp. Nilsson et al. (2012) showed consistent results with a little acceleration in the polar cap and lobes but significant heating and subsequent acceleration in the cusp and plasma mantle. They did however not divide their data according to geomagnetic activity.

Plasma in the tail lobes typically ends up in the plasma sheet. An enhancement of the oxygen ions density and pressure in the plasma sheet has been observed for disturbed geomagnetic conditions (Kistler et al., 2006, 2010). Li et al. (2012) investigated the sources for magnetospheric cold ions and the change in the outflow rate during geomagnetic disturbances (Dst < -20 nT). They found that cold-ion outflow was higher during disturbed magnetospheric conditions, consistent with the findings of Haaland et al. (2012). They also showed that the polar cap area is extended for disturbed times. These studies show how outflow is increased and also show the transport to the plasma sheet. The question is how much of these flowing ions will escape into interplanetary space during geomagnetic storms. Haaland et al. (2015) studied the cold ions during two geomagnetic storms. The authors calculated the characteristic outflow parameters, and they found that the density and bulk outflow velocity vary with the storm intensity. They estimated the cold-ion outflow rate to vary by 1 order of magnitude between disturbed and quiet magnetospheric conditions.

Without taking geomagnetic activity into account, the amount of escaping ions has been discussed in a number of studies. Seki et al. (2001) discussed outflow and return flow in the plasma sheet. They observed less and less O^+ outflow with tail distance, covering distances from 0 to 210 R_E and suggested that this was because of transport to the plasma sheet. The authors mentioned two transport processes leading to ion escape through the plasma sheet: a plasmoid that is formed by a tailward injection of a helical magnetic field structure and the transport of ions coming from the lobe or plasma mantle region to the distant neutral line. Other studies have shown that ion heating and acceleration in the cusp and mantle instead lead to escape into the magnetosheath for these ions (Nilsson et al., 2006, 2012; Nilsson, 2011; Slapak et al., 2013). A statistical study on O^+ flux from Slapak et al. (2013) estimated the total escape flux observed in the dayside magnetosheath to be $\sim 7 \times 10^{24} \, \text{s}^{-1}$. Nilsson (2011) similarly estimated the escaping flux in the cusp and plasma mantle to be of the order of $10^{25} \, \text{s}^{-1}$. Low-energy ions which flow out from the polar cap are called polar wind and were first discussed by Axford (1968). Moore et al. (1997) studied polar wind at high altitude, and, with POLAR spacecraft, they observed the acceleration of the polar wind through the lobes supplying the plasma sheet. They also found that supersonic ionospheric outflow travelling along the local magnetic field lines fills the lobe region, which was believed to be empty of plasma. Studies by Engwall et al. (2006) and Haaland et al. (2012) studied cold plasma and found that around $10^{25} \, \text{ions s}^{-1}$ of the outflowing cold ions are lost to the solar wind. A study by Nilsson et al. (2010) indicated that these cold ions are made up of protons and not oxygen. Moreover, geomagnetic disturbances lead to significant enhancement of the outflow but also strong convection towards the plasma sheet (Haaland et al., 2012, 2015).

This paper studies the relative outflow enhancement of O^+ for six case studies of major geomagnetic storms between 2001 and 2004. In Sect. 2, a brief description of the Clus-

ter mission and the instruments used is given. Section 3 describes the methodology and how the data set was chosen. Thereafter, the observations on the oxygen ion outflow during the six storms are presented in Sect. 4. Finally, in Sects. 5 and 6, we discuss the results and summarize the paper.

2   Instrument and data analysis

The Cluster mission (Escoubet et al., 2001) consists of four identical spacecraft flying in tetrahedral formation in an elliptical polar orbit. In this study, data from the Cluster Ion Spectrometer (CIS) instrument are used. The COmposition DIstribution Function (CODIF) is part of the CIS instrument and uses a time-of-flight technique that enables us to distinguish between H$^+$, He^{2+}, He$^+$ and O$^+$ in terms of mass per charge (see Rème et al., 2001). During major events, intense H$^+$ fluxes may contaminate other mass channels. To remove such data, a method described by Nilsson et al. (2006) is applied. Finally, the fluxgate magnetometer (FGM) provides the magnetic field data (see Balogh et al., 2001).

3   Data set and methodology

The data set consists of Cluster data from 2001 to 2004. During these years, several geomagnetic storms occurred, of which six were major geomagnetic storms. Our major geomagnetic storms are defined by Dst ≤ -100 nT or Kp $\geq 7+$ according to Zhang et al. (2007). Furthermore, the six chosen storms occurred during months which have a higher occurrence rate for geomagnetic storms, namely April–May and October–November (Zhang et al., 2007; Kamide et al., 1998). In the following sections, we define outflow as local flux with a net outward flux. In order to study changes in the outflow from the ionosphere, we use the upward O$^+$ flux scaled to an ionospheric altitude to compensate for altitude dependencies and magnetospheric compressions. We will in the following text term this "scaled outflow". The local flux can be mapped to an ionospheric altitude by considering an ionospheric magnetic field strength of 50 000 nT and assuming the total flux to be conserved along a magnetic flux tube. For each event, the scaled oxygen ion outflow is investigated and compared to the average scaled outflow during 1 year (the year of the storm). During these events, we do not have data from all the spacecraft and the available data are not necessarily crossing the regions of main ion outflow so that the spatial coverage of the extreme storm events is poor. We try to overcome this by looking at the relative change in the scaled outflow in the region where suitable Cluster observations were made.

Spectrograms and the magnetic fields related to the extreme storms are plotted to define the duration of the event and remove regions of closed magnetic field lines. Spectrograms and magnetic field are investigated for spacecraft 1 (SC1), SC3 and SC4 to identify the spacecraft with the best

data set for each storm and see if O$^+$ fluxes are visible during the storms (more detail in Sect. 3.1). Once the duration of the event has been determined, we define a spatial region corresponding to the storm event. This spatial region corresponding to the storm event is defined as a box which covers the spacecraft trajectory during the duration of our event. Our observations were made in the high-altitude polar cap and plasma mantle, where the plasma beta (β) value, i.e. the ratio of the plasma pressure over the magnetic pressure, varies. Thus, we investigate the plasma beta for our events, as it could represent outflow in different regions within the spatial boxes. The plasma beta in the polar cap is considerably smaller than in the magnetosheath ($\beta \approx 1$). In addition, inside the magnetosphere, the plasma beta helps to distinguish the cusp and plasma mantle ($\beta > 0.1$) from the polar cap ($\beta < 0.1$) regions. The spatial distribution of the plasma beta in our region of interests is shown and discussed in the next section where we use a sample case to illustrate the method in more details. Therefore, to identify the regions included in our spatial box, for each storm, the plasma beta, O$^+$ and H$^+$ fluxes along the trajectory of the selected spacecraft are investigated. In practice the plasma beta during the event was selected to be lower than $\beta < 0.1$, as there were very few data from the cusp and plasma mantle region ($\beta > 0.1$). We then check that the plasma beta of the event does not stand out from the plasma beta observed in the same box for all data obtained during the year of the storm. Finally, the scaled oxygen ion outflow in this spatial box is represented in histograms for 1 year of data and for the major storm itself. This is done for each extreme event separately. In the next section, one of the storms, the Halloween event on 29 October 2003, is used to illustrate the steps of the method in more detail.

3.1   Sample event

The steps of the method are described in more detail using the 29 October 2003 part of the Halloween storm as an example. The first step of the method is to look at the magnetic field and the energy and pitch-angle spectrograms of O$^+$ and H$^+$ respectively. Figure 1 shows the spectrograms for the Halloween event on 29 October 2003 between 08:30 and 20:00 UT. Panel **(a)** shows the magnetic field components. Panels **(b)** and **(c)** represent the energy spectrograms for O$^+$ and H$^+$ respectively and panels **(d)**, **(e)** (O$^+$) and **(f)** (H$^+$) the corresponding pitch-angle distributions for different energy ranges. First, we perform a visual inspection of the energy spectrograms to identify the presence of O$^+$ in the open field line region **(b)**. Then, we look at the pitch-angle data for the ion outflow at different energy ranges. We see from panel **(d)** that the O$^+$ pitch angle (0.3–30 keV) is close to 0° between 08:30 and 11:00 UT and from panel **(e)** that it is close to 180° between approximately 15:00 and 20:00 UT (0.03–0.3 keV). Note that part of the apparent O$^+$ fluxes seen during the inbound leg are due to the crosstalk from intense fluxes of protons. These periods are not included in our data set. In the po-
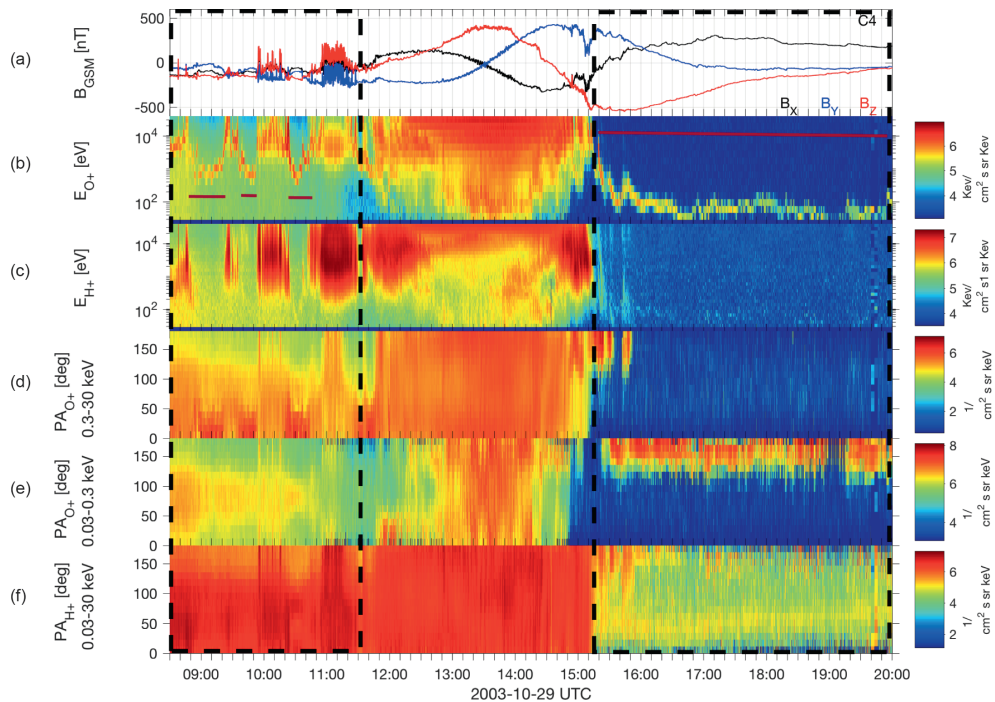
Figure 1. Magnetic field, energy and pitch-angle spectrograms for the Halloween event on 29 October 2003 between 08:30 and 20:00 UT with Cluster SC4. The panel **(a)** shows the three components of the magnetic field in nT during the storm. Panels **(b)** and **(c)** represent the energy spectrogram (eV) for O^+ and H^+ respectively. Panels **(d)**, **(e)** and **(f)** show the corresponding pitch angle (°) for different energy ranges. The black dashed rectangles show the regions identified as the open magnetic field line regions, and the red lines in the O^+ energy spectrogram show the regions included in the data (magnetosheath is excluded).

lar cap region, the pitch-angle spectra usually show less variability than in the magnetosheath or within the closed field line region. Moreover, narrow oxygen beams are included as well as a clear high-energy O^+ outflow that relates to a strong magnetic field (not shown; this does not apply to the Halloween event), for example $B \sim 200$ nT for 29–30 May 2003 in the Southern Hemisphere. Finally, to confirm the location of the outflow region; panel **(a)** shows that the magnetic field slowly varies and stronger in the inner magnetosphere; in the open field line regions, it is weaker and more strongly oscillating in the magnetosheath. The regions of open magnetic field lines (outflow regions) are thus identified between 08:30 and 11:30 UT for the Southern Hemisphere (SH) and between 15:15 and 20:00 UT for the Northern Hemisphere (NH) represented by the black dashed rectangles. To summarize, this identification is based on the pitch-angle data showing field-aligned flow and the presence of O^+ ions, the magnetic field being weak but quite stable and then also using the location of the spacecraft in the general polar cap–cusp–plasma mantle regions. In Fig. 1c, the first dashed black box

indicates a region in the SH where intense fluxes of H^+ at several kilo-electronvolts energy are observed. We interpret these data as magnetosheath data and the variation between high and low energies in H^+ as flapping motions of the magnetopause. Such magnetosheath data are removed by our algorithm, which removes O^+ data significantly contaminated by crosstalk from intense proton fluxes (see Nilsson et al., 2006, for more detail). The periods of data included in our data set are shown with red lines (panel **(b)**).

Figure 2 shows the second step of the method. As briefly mentioned at the beginning of Sect. 3, the plasma beta is used to distinguish between the different magnetospheric regions. Therefore, the plasma beta and the oxygen ion flux is computed along the entire spacecraft trajectory during the event. Fig. 2a shows the plasma beta along Cluster SC4 trajectory in the XZ_{GSM} and XY_{GSM} planes respectively. Fig. 2b shows the corresponding oxygen ion flux. The colour scales represent the logarithmic values of the plasma beta and the oxygen ion flux respectively. Black arrows illustrate the direction of the spacecraft motion, starting at 08:30 and ending
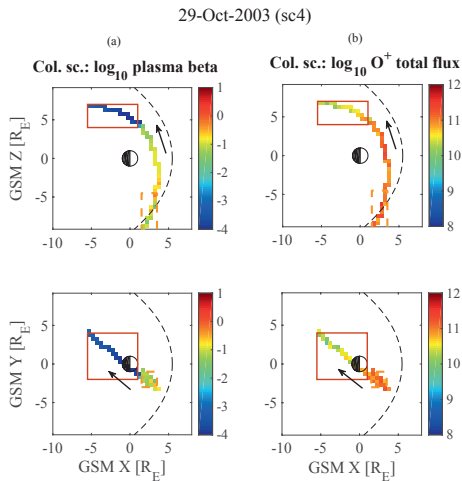
Figure 2. The plasma beta **(a)** and the O$^+$ flux **(b)** along the trajectory of Cluster SC4 on 29 October 2003 from 08:30 to 20:00 UT. The location of the magnetopause is a prediction obtained from the model of Shue et al. (1998) for the solar wind conditions at around 11:00 UT.

Figure 3. Average distribution of the plasma beta in cylindrical coordinates for 2003, storms included. The β is low for high-altitude regions, i.e. the polar cap, then increases again, which corresponds to the cusp and plasma mantle region with $\log_{10}(\beta) > 0.1$. The dashed line represents the prediction of the average magnetopause by Shue et al. (1998) during 2003.

at 20:00 UT. In addition, the magnetopause is represented by a dashed black line in all panels and is a prediction obtained from the model of Shue et al. (1998) for the solar conditions at around 11:00 UT. The entry and exit time (08:30 and 11:30 UT for the SH and 15:15 and 20:00 UT for the NH, defined in Fig. 1) in the region of interest is converted to spacecraft positions in geocentric solar magnetospheric (GSM) coordinates. These positions are plotted and give a spatial box for the region of outflow during the event. Then, we inspect whether the spatial box defined by the positions converted from the entry and exit time (Fig. 1) corresponds to plasma beta lower than 0.1 in Fig. 2. The final spatial box is sometimes slightly adjusted to give a plasma beta within the range < 0.1 along the trajectory. The spatial boxes for the Halloween event obtained in this way are illustrated by red and orange rectangles for the NH and SH respectively.

The third step is to perform statistics over 1 year of data in the spatial boxes defined by the storm. First, we check that, in terms of plasma beta, the geomagnetic storm does not stand out from the average for the year for the spatial region and that the plasma beta is in the same range (less than 0.1) in our spatial box during the year. Figure 3 illustrates the average distribution of β in cylindrical coordinates for 2003, storms included, and for the regions of the magnetosphere that we investigate in this study. The cylindrical coordinates are used so that Fig. 3 can be directly compared to that of Nilsson et al. (2012, their Fig. 1). In Fig. 3, we see that the plasma beta is low in the polar cap region and increases with altitude. The average magnetopause for 2003 is predicted from the model
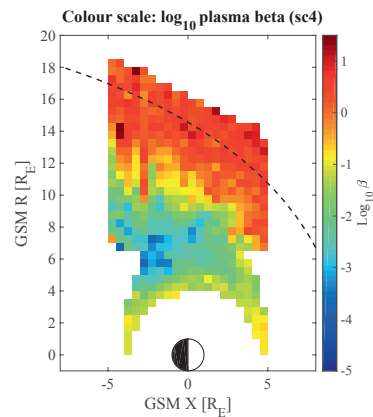
of Shue et al. (1998) and the red region or $\log_{10}(\beta) > 0.1$ corresponds to the cusp and plasma mantle. Comparing with the results of Nilsson et al. (2012, their Fig. 1), we see that the plasma beta increases with altitude, as does the scaled ionospheric flux. Note that in their Fig. 1, sampling is not along a given magnetic field line; therefore, the scaled ionospheric flux is not conserved with altitude. Thus, for this region of geospace, a region of similar β typically corresponds to similar outflow along a similar flight trajectory from the source (cusp or polar cap). This can be further investigated using Fig. 4, where we present the distribution of the scaled oxygen ion outflow for each interval of plasma beta during 2003 (storm included) in **(a)**. The colour scale represents the percentage of the scaled O$^+$ outflow for each interval of β. The columns are normalized so that the sum of all data in a column equals 100 %, and the colour scale is in per cent. Figure 4 shows a linear relation between the scaled O$^+$ outflow and the plasma beta, where lower β corresponds to the polar cap and higher β (above 0.1) to the plasma mantle and cusp. Spatial boxes with a similar plasma beta range thus corresponds to a region with, on average, comparable outflow from the ionosphere. Furthermore, the linear relationship means that if the scaled outflow for the extreme event stands out significantly from the year's average but β does not, then we can say with confidence that the enhanced scaled outflow is not because we are sampling an entirely different region. The plasma beta can be expected to increase to some extent for the extreme event because the plasma density and temperature are higher than on average. Note that β is calculated at the observation point, so the scaling of the ion flux to
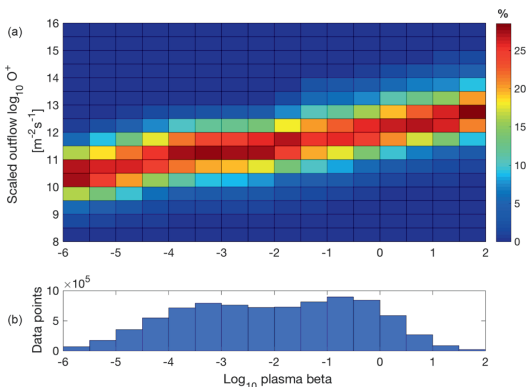
Figure 4. (a) Distribution of scaled oxygen ion outflow (m^{-2}s^{-1}) for each interval of plasma beta during 2003, including storms events. The colour scale represents the percentage of scaled O$^+$ outflow for each interval of plasma beta. Each column is normalized so that the sum of the data equals 100 % and the colour scale is in per cent. **(b)** Number of data points contributing to each column.

Figure 5. Spatial boxes are defined for each major geomagnetic storm. This figure shows all the individual spatial boxes that defined the location of the open magnetic field line region during each storm. The events are divided into the April–May storms and October–November storms. For the April–May storms, the scaled outflow regions in Northern and Southern Hemispheres are represented in dark green and in light green respectively. In the same way, orange corresponds to the outflow region in the north of the October–November storms and red to the outflow region in the south. Finally, each storm in these two groups is distinguished by different lines (dot–dashed, dashed and full). The numbers from 1 to 6 refer to Table 1, which identifies the storms.

ionospheric altitude does not affect the plasma beta calculation. This particular relation between plasma beta and scaled oxygen ion outflow is valid for our Cluster data set in our sampling region; it is not necessarily true for the magnetosphere as a whole. Panel **(b)** shows the number of data points contributing to the corresponding column in **(a)**.

After verifying the plasma beta range (less than 0.1, so corresponding to the polar cap for all our cases) within the box for the extreme event and during the year, the average oxygen ion outflow during the year 2003 (including the storm) is computed and projected in 2-D (not shown). We check whether the major geomagnetic storm stands out from the less disturbed conditions and if there is an enhancement in O$^+$. Finally, to visualize and estimate the enhancement, the oxygen ion outflow, scaled to an ionospheric reference level, is plotted using histograms separating the O$^+$ storm population from the entire O$^+$ population during the year of the storm. This final step is shown in more detail in Sect. 4 together with the other major storms considered in this study.

4   Observations

The relative enhancement of oxygen ion is investigated during six separate intense geomagnetic storms between 2001 and 2004. Three storms were observed around April–May, months with a high occurrence rate for geomagnetic storms (Zhang et al., 2007): 29–31 March and 11–12 April 2001 and 29–30 May 2003. Moreover, October and November have a higher storm occurrence rate (Zhang et al., 2007) and are months when three other storms were investigated: the Halloween event or 28–30 October 2003 as well as 7–8 and 9–11
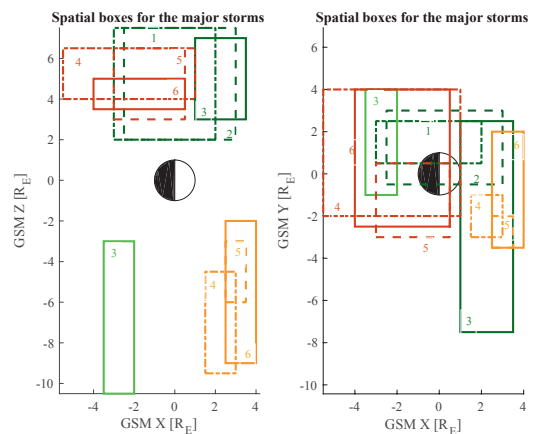
November 2004. With an orbit period of 57 h, Cluster crossed the polar caps and the plasma mantle and cusp only for a few hours during the storms; therefore, the amount of data for each individual event is limited.

These six major storms and different aspects of them have been studied and presented in a large number of papers, e.g. Baker et al. (2002), Wang et al. (2003), Hanuise et al. (2006), Rosenqvist et al. (2005), Tsurutani et al. (2008), Foster et al. (2002), Zhang et al. (2007), Echer et al. (2010) and Yermolaev et al. (2008). The storm conditions are summarized in Table 1. The six storms are listed in chronological order, numbered 1 to 6. We determine the storm dates according to the position of the Cluster spacecraft at the dayside. The duration of each passage and the spacecraft used are given by the second and third row respectively. The Dst and Kp indices are two different indices, which describe the intensity of a geomagnetic storm and the magnetospheric conditions respectively. However, Dst is an hourly index while Kp is a 3 h index. The PC index gives the enhancement in the polar cap. Table 1 gives the minimum Dst index, the highest Kp, the PC index, and the solar wind speed and density for the corresponding day. Finally, the average values for the event and the year as well as the mean ratio event / year of the solar radio flux at the wavelength of 10.7 cm (or F10.7 index;

this index is a proxy for solar extreme ultraviolet flux) are calculated.

Section 3 describes how the outflow regions are defined, and in Fig. 5, we present the spatial boxes corresponding to all events in this study. Axes are in R_E in the GSM coordinates system and the Earth is represented in the middle of the panels. The numbers 1 to 6 and the associated boxes in Fig. 5 correspond to the numbering of the events in Table 1. The dark and light green rectangles correspond to the April–May storms, where each storm is shown as dot–dashed, dashed or solid lines, numbered 1 to 3, whereas the red and orange rectangles correspond to the October–November storms, also defined by dot–dashed, dashed or solid lines and numbered 4 to 6. Therefore, lines, numbers and colours together define one particular outflow region (in NH or SH) for one of the six geomagnetic storms.

The scaled oxygen ion outflow during the extreme events is estimated in the spatial boxes (see Fig. 5). Figure 6 shows histograms of 1 year of scaled O$^+$ outflow in these boxes for each considered storm event in the Northern Hemisphere. The x and y axes correspond to the logarithmic values of the oxygen ion outflow scaled to the ionosphere and the number of data points respectively. The data covering the whole year of the storm are represented by blue bars, while the yellow bars correspond to the storm itself. In November 2004, several geomagnetic storms occurred in a short period. Hence, the middle and right panels in row **(b)** display two storms: 7 November (in yellow) and 10 November 2004 (in white and red). A common feature of all the events is an enhancement in the scaled oxygen ion outflow during the storms compared to the background data. In the same way, the scaled O$^+$ outflow is shown for the SH in Fig. 7, where enhancements in the scaled O$^+$ outflow for the storm are clearly visible as a separate peak in the distribution toward the largest fluxes observed.

The relative scaled O$^+$ outflow enhancements during the storms compared to less disturbed conditions can readily be obtained from Figs. 6 and 7 and are presented in Table 1. The median and mean taken from the histograms in Figs. 6 and 7 are listed as well as the ratio between the *event* mean/median and the *year* mean/median, which gives the relative enhancement. The median and mean values are expressed in m^{-2} s^{-1}. Due to different boxes used for different events, the estimated scaled O$^+$ outflow during the same year is not identical for different events. The last row displays the highest scaled O$^+$ outflow for each extreme event, with a minimum of 10 data points in the bin (Figs. 6 and 7).

5 Discussion

5.1 Geomagnetic activity

The main purpose of this study is to quantify the relative enhancement of the scaled O$^+$ outflow during major geomag-

netic storms. Figures 6 and 7 present the upward O$^+$ flux scaled to an ionospheric altitude for six major geomagnetic storms and the year when they occurred. This scaled O$^+$ outflow is calculated in a spatial box which is defined by the spacecraft trajectory (position) during the storm. Note that we also observe plasma-sheet-like earthward return flux for two cases. Our boxes therefore contain a small fraction of plasma observed on closed field magnetic lines, for example due to tail flapping. These data are removed from our data set since we are only considering outflow.

The magnetosphere may be compressed during storms, so that observations during storms may be closer to the magnetopause. On the other hand, the cusp and plasma mantle also moves equatorward (Newell et al., 1989; Newell and Meng, 1994), and therefore our observations are in the polar cap further from the storm main outflow region. As a consequence, during storm time, the polar cap area is extended 2 or 3 times more than during quiet conditions (Li et al., 2012). Consequently, the spatial box might represent another region during the year when the storm occurred rather than the outflow region defined for the storm. This issue was dealt with in two ways. We demanded that the local plasma beta range was similar for the extreme event and the average for the whole year. We also compared the scaled ionospheric flux, thus compensating for any effect of a direct local compression of the magnetic field, which would enhance the local flux. This combined with the fact that the ionospheric source region, the polar cap, is much larger during a storm strongly indicates that the enhanced scaled flux during the storm corresponds to increased scaled outflow in the spatial box we study.

To look at this in more detail, we refer again to Figs. 3 and 4. These figures show how the scaled O$^+$ outflow changes for different plasma beta, where $\beta < 0.1$ usually corresponds to the polar cap regions while higher β represents typically the cusp and plasma mantle. The scaled O$^+$ outflow as a function of the plasma beta parameter displays roughly a linear relation (Fig. 4), showing that when averaged over all conditions, we have a rather smooth variation of scaled outflow as function of plasma beta and more scaled outflow in the cusp and mantle as known from previous studies, e.g. Nilsson et al. (2012). If the magnetosphere was strongly compressed so that the spatial box was located in the polar cap for the average conditions (year) but in the plasma mantle and cusp for the extreme event, then we could expect that the plasma beta of the extreme event would stand out compared to the average conditions during the year in a similar way that the scaled O$^+$ outflow for the extreme event stands out. If instead the expansion of the polar cap is more important, then the extreme event is located further into the polar cap, away from the main outflow channel, the cusp and plasma mantle. In such a case we may not see a strong difference in the plasma beta, but the scaled outflow enhancement observed would be even more significant and our observations would be an underestimation of the actual enhancement. For exam-
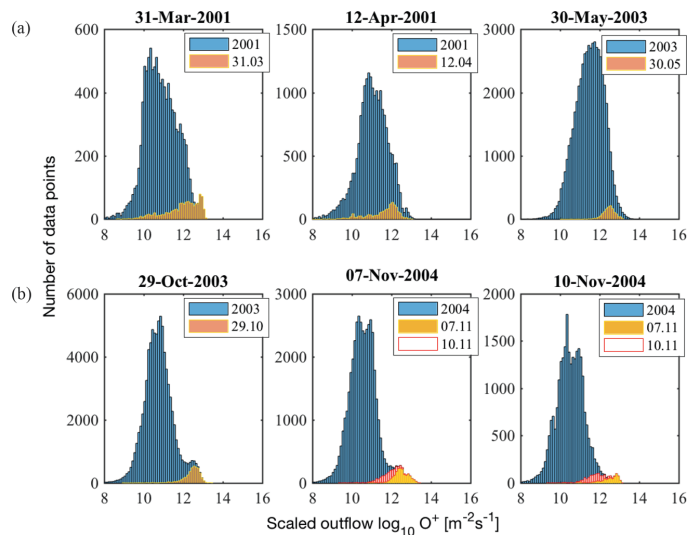
Figure 6. Histograms of the scaled O⁺ outflow in logarithmic scale for the outflow region in the Northern Hemisphere. Each panel shows 1 year of data and one of the six geomagnetic storms. The three top panels **(a)** are the April–May storms, and the October–November storms are shown in the bottom panels **(b)**. The blue bars correspond to 1 year of data (year of the storm) with all the storms during that year included, and the yellow bars represent the storms themselves. Each histogram is computed with the spatial box related to the extreme event.
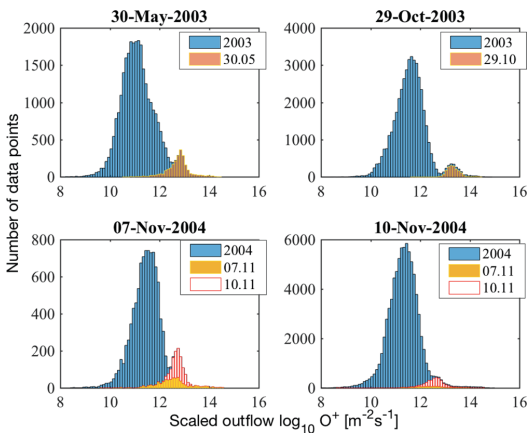

Figure 7. Same as Fig. 6 but for the outflow region in the Southern Hemisphere. However, only four storms have data during Cluster perigee.

ple, the year of our most extreme geomagnetic storm, the Halloween storm, has a scaled O⁺ outflow of approximately 10^{11} m⁻² s⁻¹ (see Table 1), typical for the polar cap (see also Nilsson et al., 2013, for typical fluxes in different regions). There was an insignificant amount of data points in the cusp and plasma mantle ($\beta > 0.1$) also for the storms; therefore,

the amount of data that could be located outside the intended magnetospheric region does not affect the statistics.

In Table 1, the scaled O⁺ outflow during geomagnetic storms ranges between 3.5×10^{11} and 2.1×10^{13} m⁻² s⁻¹, which is related to the intensity of the storm and subsequently with the Kp and F10.7 index (discussed below). We have estimated the average scaled O⁺ outflow in the open field line region to be 10^{12} m⁻² s⁻¹ during storm time. Our results are consistent with previous observations made by Kitamura et al. (2010), who determined the average of cold oxygen ion fluxes in the polar cap during two major geomagnetic storms (30 March and 17 April 1990). They obtained 2.1×10^{13} m⁻² s⁻¹ for the first event and between $4 \times 10^{12} - 4 \times 10^{13}$ m⁻² s⁻¹ for 17 April 1990. However, the scaled O⁺ outflow that we estimate is not considerably higher than during less disturbed conditions. Indeed, Nilsson et al. (2012) found that the oxygen ion flux at a high cusp altitude is 5×10^{12} m⁻² s⁻¹, and Lennartsson et al. (2004) observed O⁺ flux in the cusp regions of approximately 10^{12} m⁻² s⁻¹ above 65° invariant latitude. However, we observe significant relative scaled outflow enhancements from a factor of 3 to 83 (or 0.5 to approximately 2 orders of magnitude) in Figs. 6 and 7. This considerable difference is associated with the geomagnetic indices Kp given in Table 1. The mean ratio of the F10.7 index between the event and the corresponding year is up to about 2 times larger than usual for geomagnetic storms with Kp > 8. The index has no discernible trend on a 1-year scale, so that the ratios vary

Table 1. Features of the six major geomagnetic storms. Each column corresponds to one storm, while each row corresponds to one feature. The storms are given in chronological order, with one number assigned for each storm. The duration (in UT) is the time taken to study the storm during Cluster passage at the dayside. The second row gives the spacecraft used for each event. Dst, Kp, the PC index, and solar wind (SW) speed and density are the highest values taking during the corresponding day. The average values for the event and the year and the mean ratio event / year of the F10.7 index are calculated. The year / event mean or median are calculated from the histograms shown in Figs. 6 and 7 respectively in the Northern and Southern Hemispheres (NH and SH). The mean and median are expressed in m^{-2}s^{-1}.

	1	2	3	4	5	6
Dates	31 Mar 2001	12 Apr 2001	29–30 May 2003	29 Oct 2003	07 Nov 2004	09–10 Nov 2004
Duration (UT)	06:00–14:00	02:00–19:00	22:00–16:00	08:30–20:00	14:00-22:00	20:00–10:00
Spacecraft	1	3	1	4	4	4
Dst index (nT)	−387	−271	−144	−350	−117	−259
Kp index	9−	7+	7+	9	8	9−
PC index	12.7	6.4	4.8	12.8	12	11.7
SW speed (km s^{-1})	723	722	813	−	696	794
SW density (N cm^3)	37.9	4.4	52.2	−	90.2	18.0
Average F10.7 (event)	245.3	149.8	121.56	275.4	127.2	110.21
Average F10.7 (year)	181.1	181.1	128.45	128.45	106.53	106.53
Mean ratio F10.7	1.3545	0.8272	0.9465	2.1440	1.1941	1.0346
Year mean value (m^{-2} s^{-1})	NH 7.9×10^{10} —	NH 1.1×10^{11} —	NH 3.1×10^{11} SH 1.5×10^{11}	NH 5.9×10^{10} SH 4.1×10^{11}	NH 4×10^{10} SH 3.6×10^{11}	NH 3.5×10^{10} SH 2.2×10^{11}
Year median value (m^{-2} s^{-1})	NH 6.6×10^{10} —	NH 1.1×10^{11} —	NH 3.4×10^{11} SH 1.3×10^{11}	NH 5.3×10^{10} SH 4×10^{11}	NH 3.6×10^{10} SH 3.4×10^{11}	NH 3.2×10^{10} SH 2.2×10^{11}
Event mean value (m^{-2} s^{-1})	NH 8.7×10^{11} —	NH 3.5×10^{11} —	NH 3×10^{12} SH 5.6×10^{12}	NH 2.6×10^{12} SH 2.1×10^{13}	NH 2.8×10^{12} SH 3.3×10^{12}	NH 5.6×10^{11} SH 3.8×10^{12}
Event median value (m^{-2} s^{-1})	NH 1.3×10^{12} —	NH 6.5×10^{11} —	NH 3.1×10^{12} SH 6.2×10^{12}	NH 3.2×10^{12} SH 2×10^{13}	NH 3×10^{12} SH 3.4×10^{12}	NH 5.8×10^{11} SH 4×10^{12}
Mean ratio (event / year)	NH 11 —	NH 3 —	NH 10 SH 37	NH 44 SH 51	NH 70 SH 9	NH 16 SH 17
Median ratio (event / year)	NH 20 —	NH 6 —	NH 9 SH 47	NH 60 SH 50	NH 83 SH 10	NH 18 SH 18
Highest scaled O$^+$ outflow (event) (m^{-2} s^{-1})	NH 1.3×10^{13} —	NH 6.3×10^{12} —	NH 1.6×10^{13} SH 1.6×10^{14}	NH 1.6×10^{13} SH 2×10^{14}	NH 2×10^{13} SH 8×10^{13}	NH 4×10^{12} SH 3.2×10^{13}

in a small range. Therefore, it appears that the varying solar cycle trend over the year does not affect our results. One of the strongest storms, the Halloween event (number 4 in Table 1), has the highest scaled O$^+$ outflow (SH), Kp and F10.7 index. This strongest enhancement in scaled O$^+$ outflow for the storm is approximately 2 orders of magnitude higher than during less disturbed magnetospheric conditions. In addition, the Halloween storm occurred near the solar maximum where increased oxygen flux has been observed in the past (Yau and Andre, 1997). This result is consistent with Yau et al. (1988), who showed a Kp dependence on the O$^+$ flux at lower altitudes, and with Slapak et al. (2017), who studied the oxygen ion escape from the plasma mantle and cusp and its dependence on the geomagnetic activity. Slapak et al. (2017) found that in the plasma mantle and the dayside magnetosheath, the scaled O$^+$ outflow increases exponentially as exp(0.45Kp). In the plasma mantle, they observed an increase of 1.5 orders of magnitude for the scaled oxygen ion outflow between average conditions (Kp ≈ 3) and highest geomagnetic activities. In comparison with Slapak et al. (2017, their Fig. 4), who show the distribution of O$^+$ observations over Kp for the plasma mantle and the dayside mag-

netosheath, we estimate a lower scaled O$^+$ outflow, which is reasonable because our region of observations is in the polar cap. We also note that due to the Cluster orbit, suitable data are not always obtained from the period of highest geomagnetic activity for each storm. Similar enhancements in the O$^+$ density with geomagnetic activity in the near-Earth tail plasma sheet have been reported by Lennartsson and Shelley (1986), Mouikis et al. (2010), and Maggiolo and Kistler (2014).

Unfortunately, we were not able to confirm that this scaled outflow enhancement is escaping because our observations are made in the polar cap and the average velocities do not confirm a clear O$^+$ escape tendency. However, this result of a scaled outflow enhancement during major geomagnetic storms shows that there is a strong relative enhancement in the regions where we have Cluster observations. Slapak et al. (2017) used the Halloween event Kp index as a reference to estimate the total O$^+$ loss over 4 billion years. Their result gives a total O$^+$ loss 1.3 times the total oxygen mass in the present atmosphere. Our patchy observations from parts of the magnetosphere are consistent with the escape value extrapolated from their data.

5.2 Most extreme case

During geomagnetic storms, the polar cap is moving equatorward, and subsequently the main outflow region moves as well compared to the average outflow region. In this paper, we are mostly not in the main outflow region of the storm. During the six events (see Table 1) in the NH and SH, we calculate the highest scaled O$^+$ outflow. There is a 1 order of magnitude difference between the SH and NH, which could be explained by the different relative location of the spatial boxes and the geomagnetic activity. A similar trend has been observed by Luo et al. (2017), who studied the energetic ion distributions in the dayside magnetosphere and the plasma sheet. The authors found that there is a strong correlation between the dawn–dusk asymmetry and the IMF direction, with a higher asymmetry in the Southern Hemisphere. The highest scaled O$^+$ outflow value for the six events is $2 \times 10^{14} \, \mathrm{m}^{-2} \, \mathrm{s}^{-1}$ observed in the 29 October SH spatial box. This result is 2 orders of magnitude higher than what is observed during average conditions (Kp ≈ 3) (Nilsson et al., 2012); therefore, the upper limit of scaled O$^+$ outflow during the storm peak is probably more intense. The scaled O$^+$ outflow is lower in the NH than in the SH, and the upper limit in the NH is $2 \times 10^{13} \, \mathrm{m}^{-2} \, \mathrm{s}^{-1}$ (event number 5) for our cases.

6 Conclusions

Using Cluster CODIF data between 2001 and 2004, we have calculated the upward O$^+$ flux scaled to an ionospheric reference altitude for six major geomagnetic storms (Dst ≤ -100 nT or Kp $\geq 7+$). The scaled O$^+$ outflow is estimated for the storms themselves and for 1 year of data (the year when the storm occurred) in the region corresponding to the storm observations in the Northern and Southern Hemispheres. The main result is a clear relative enhancement in the scaled O$^+$ outflow by a factor of 3 to 83 during storm times, indicating that the entire magnetospheric circulation increases significantly during extreme events. The upper limit for the scaled O$^+$ outflow was found in the Southern Hemisphere for 29 October 2003, with $2 \times 10^{14} \, \mathrm{m}^{-2} \, \mathrm{s}^{-1}$ (Halloween event). Cluster was not located in the main outflow region (the cusp and plasma mantle) during any of the investigated storms. Therefore, we are not able to estimate the total escape. However, the scaled O$^+$ outflow for the extreme events stood out from the general distribution as a bump in the tail of the distribution. Thus, there is an extreme enhancement of the scaled outflow in the regions investigated. Furthermore, the relative scaled outflow enhancements vary with the Kp index in a way that is consistent with Slapak et al. (2017), who show the Kp dependence on escaping O$^+$ scaled outflow in the plasma mantle. Our results show a general increase in the magnetospheric scaled O$^+$ outflow of 2 orders of magnitude for the most intense geomagnetic storms

and thus support the estimation of Slapak et al. (2017) of a 2 orders of magnitude increase in the total escape for highest geomagnetic activity (Kp ≥ 8). Thus, the escape during extreme events which occur only rarely can still have a significant effect on the total outflow, in particularly for ancient solar conditions when such events are expected to have been more common. Our main results can be summarized as follows:

1. we observe a clear relative scaled outflow enhancement by a factor of 3 to 83 during the major geomagnetic storms in the polar cap region;

2. the upper limit of the scaled outflow during these storms is estimated to be $2 \times 10^{14} \, \mathrm{m}^{-2} \, \mathrm{s}^{-1}$ (during the Halloween event SH);

3. the general increase in the magnetospheric scaled O$^+$ outflow supports the estimation of Slapak et al. (2017) of a 2 orders of magnitude increase for the total escape during extreme geomagnetic activity.

References

Axford, W. I.: The polar wind and the terrestrial helium budget, J. Geophys. Res., 73, 6855–6859, https://doi.org/10.1029/JA073i021p06855, 1968.

Baker, D. N., Ergun, R. E., Burch, J. L., Jahn, J.-M., Daly, P. W., Friedel, R., Reeves, G. D., Fritz, T. A., and Mitchell,

D. G.: A telescopic and microscopic view of a magnetospheric substorm on 31 March 2001, Geophys. Res. Lett., 29, 1862, https://doi.org/10.1029/2001GL014491, 2002.

Balogh, A., Carr, C. M., Acuña, M. H., Dunlop, M. W., Beek, T. J., Brown, P., Fornacon, K.-H., Georgescu, E., Glassmeier, K.-H., Harris, J., Musmann, G., Oddy, T., and Schwingenschuh, K.: The Cluster Magnetic Field Investigation: overview of in-flight performance and initial results, Ann. Geophys., 19, 1207–1217, https://doi.org/10.5194/angeo-19-1207-2001, 2001.

Chappell, C. R., Moore, T. E., and Waite, Jr., J. H.: The ionosphere as a fully adequate source of plasma for the earth's magnetosphere, J. Geophys. Res., 92, 5896–5910, https://doi.org/10.1029/JA092iA06p05896, 1987.

Echer, E., Tsurutani, B. T., and Guarnieri, F. L.: Interplanetary origins of November 2004 superstorms, J. Atmos. Sol.-Terr. Phy., 72, 280–284, https://doi.org/10.1016/j.jastp.2009.02.009, 2010.

Engwall, E., Eriksson, A. I., André, M., Dandouras, I., Paschmann, G., Quinn, J., and Torkar, K.: Low-energy (order 10 eV) ion flow in the magnetotail lobes inferred from spacecraft wake observations, Geophys. Res. Lett., 33, L06110, https://doi.org/10.1029/2005GL025179, 2006.

Escoubet, C. P., Fehringer, M., and Goldstein, M.: *Introduction* The Cluster mission, Ann. Geophys., 19, 1197–1200, https://doi.org/10.5194/angeo-19-1197-2001, 2001.

Foster, J. C., Erickson, P. J., Coster, A. J., Goldstein, J., and Rich, F. J.: Ionospheric signatures of plasmaspheric tails, Geophys. Res. Lett., 29, 1623, https://doi.org/10.1029/2002GL015067, 2002.

Haaland, S., Eriksson, A., Engwall, E., Lybekk, B., Nilsson, H., Pedersen, A., Svenes, K., André, M., Förster, M., Li, K., Johnsen, C., and Østgaard, N.: Estimating the capture and loss of cold plasma from ionospheric outflow, J. Geophys. Res.-Space, 117, A07311, https://doi.org/10.1029/2012JA017679, 2012.

Haaland, S., Eriksson, A., André, M., Maes, L., Baddeley, L., Barakat, A., Chappell, R., Eccles, V., Johnsen, C., Lybekk, B., Li, K., Pedersen, A., Schunk, R., and Welling, D.: Estimation of cold plasma outflow during geomagnetic storms, J. Geophys. Res.-Space, 120, 10622–10639, https://doi.org/10.1002/2015JA021810, 2015.

Hanuise, C., Cerisier, J. C., Auchère, F., Bocchialini, K., Bruinsma, S., Cornilleau-Wehrlin, N., Jakowski, N., Lathuillère, C., Menvielle, M., Valette, J.-J., Vilmer, N., Watermann, J., and Yaya, P.: From the Sun to the Earth: impact of the 27–28 May 2003 solar events on the magnetosphere, ionosphere and thermosphere, Ann. Geophys., 24, 129–151, https://doi.org/10.5194/angeo-24-129-2006, 2006.

Kamide, Y., Baumjohann, W., Daglis, I. A., Gonzalez, W. D., Grande, M., Joselyn, J. A., McPherron, R. L., Phillips, J. L., Reeves, E. G. D., Rostoker, G., Sharma, A. S., Singer, H. J., Tsurutani, B. T., and Vasyliunas, V. M.: Current understanding of magnetic storms: Storm-substorm relationships, J. Geophys. Res., 103, 17705–17728, https://doi.org/10.1029/98JA01426, 1998.

Kistler, L. M., Mouikis, C. G., Cao, X., Frey, H., Klecker, B., Dandouras, I., Korth, A., Marcucci, M. F., Lundin, R., McCarthy, M., Friedel, R., and Lucek, E.: Ion composition and pressure changes in storm time and nonstorm substorms in the vicinity of the near-Earth neutral line, J. Geophys. Res.-Space, 111, A11222, https://doi.org/10.1029/2006JA011939, 2006.

Kistler, L. M., Mouikis, C. G., Klecker, B., and Dandouras, I.: Cusp as a source for oxygen in the plasma sheet during geomagnetic storms, J. Geophys. Res.-Space, 115, A03209, https://doi.org/10.1029/2009JA014838, 2010.

Kitamura, N., Nishimura, Y., Ono, T., Ebihara, Y., Terada, N., Shinbori, A., Kumamoto, A., Abe, T., Yamada, M., Watanabe, S., Matsuoka, A., and Yau, A. W.: Observations of very-low-energy (<10 eV) ion outflows dominated by O$^+$ ions in the region of enhanced electron density in the polar cap magnetosphere during geomagnetic storms, J. Geophys. Res.-Space, 115, A00J06, https://doi.org/10.1029/2010JA015601, 2010.

Krauss, S., Fichtinger, B., Lammer, H., Hausleitner, W., Kulikov, Yu. N., Ribas, I., Shematovich, V. I., Bisikalo, D., Lichtenegger, H. I. M., Zaqarashvili, T. V., Khodachenko, M. L., and Hanslmeier, A.: Solar flares as proxy for the young Sun: satellite observed thermosphere response to an X17.2 flare of Earth's upper atmosphere, Ann. Geophys., 30, 1129–1141, https://doi.org/10.5194/angeo-30-1129-2012, 2012.

Kronberg, E. A., Ashour-Abdalla, M., Dandouras, I., Delcourt, D. C., Grigorenko, E. E., Kistler, L. M., Kuzichev, I. V., Liao, J., Maggiolo, R., Malova, H. V., Orlova, K. G., Peroomian, V., Shklyar, D. R., Shprits, Y. Y., Welling, D. T., and Zelenyi, L. M.: Circulation of Heavy Ions and Their Dynamical Effects in the Magnetosphere: Recent Observations and Models, Space Sci. Rev., 184, 173–235, https://doi.org/10.1007/s11214-014-0104-0, 2014.

Lennartsson, O. W., Collin, H. L., and Peterson, W. K.: Solar wind control of Earth's H^+ and O^+ outflow rates in the 15-eV to 33-keV energy range, J. Geophys. Res.-Space, 109, A12212, https://doi.org/10.1029/2004JA010690, 2004.

Lennartsson, W. and Shelley, E. G.: Survey of 0.1- to 16-keV/e plasma sheet ion composition, J. Geophys. Res., 91, 3061–3076, https://doi.org/10.1029/JA091iA03p03061, 1986.

Li, K., Haaland, S., Eriksson, A., André, M., Engwall, E., Wei, Y., Kronberg, E. A., Fränz, M., Daly, P. W., Zhao, H., and Ren, Q. Y.: On the ionospheric source region of cold ion outflow, Geophys. Res. Lett., 39, L18102, https://doi.org/10.1029/2012GL053297, 2012.

Liao, J., Kistler, L. M., Mouikis, C. G., Klecker, B., Dandouras, I., and Zhang, J.-C.: Statistical study of O$^+$ transport from the cusp to the lobes with Cluster CODIF data, J. Geophys. Res.-Space, 115, A00J15, https://doi.org/10.1029/2010JA015613, 2010.

Liao, J., Kistler, L. M., Mouikis, C. G., Klecker, B., and Dandouras, I.: Acceleration of O$^+$ from the cusp to the plasma sheet, J. Geophys. Res.-Space, 120, 1022–1034, https://doi.org/10.1002/2014JA020341, 2015.

Luo, H., Kronberg, E. A., Nykyri, K., Trattner, K. J., Daly, P. W., Chen, G. X., Du, A. M., and Ge, Y. S.: IMF dependence of energetic oxygen and hydrogen ion distributions in the near-Earth magnetosphere, J. Geophys. Res.-Space, 122, 5168–5180, https://doi.org/10.1002/2016JA023471, 2017.

Maggiolo, R. and Kistler, L. M.: Spatial variation in the plasma sheet composition: Dependence on geomagnetic and solar activity, J. Geophys. Res.-Space, 119, 2836–2857, https://doi.org/10.1002/2013JA019517, 2014.

Moore, T. E., Chappell, C. R., Chandler, M. O., Craven, P. D., Giles, B. L., Pollock, C. J., Burch, J. L., Young, D. T., Waite, Jr., J. H., Nordholt, J. E., Thomsen, M. F., McComas, D. J., Berthelier, J. J., Williamson, W. S., Robson, R., and Mozer, F. S.: High-

altitude observations of the polar wind., Science, 277, 349–351, https://doi.org/10.1126/science.277.5324.349, 1997.

Mouikis, C. G., Kistler, L. M., Liu, Y. H., Klecker, B., Korth, A., and Dandouras, I.: H$^+$ and O$^+$ content of the plasma sheet at 15-19 Re as a function of geomagnetic and solar activity, J. Geophys. Res.-Space, 115, A00J16, https://doi.org/10.1029/2010JA015978, 2010.

Newell, P. T. and Meng, C.-I.: Ionospheric projections of magnetospheric regions under low and high solar wind pressure conditions, J. Geophys. Res.-Space, 99, 273–286, https://doi.org/10.1029/93JA02273, 1994.

Newell, P. T., Meng, C.-I., Sibeck, D. G., and Lepping, R.: Some low-altitude cusp dependencies on the interplanetary magnetic field, J. Geophys. Res.-Space, 94, 8921–8927, https://doi.org/10.1029/JA094iA07p08921, 1989.

Nilsson, H.: Heavy Ion Energization, Transport, and Loss in the Earth's Magnetosphere, Springer Netherlands, Dordrecht, 315–327, https://doi.org/10.1007/978-94-007-0501-2_17, 2011.

Nilsson, H., Waara, M., Arvelius, S., Marghitu, O., Bouhram, M., Hobara, Y., Yamauchi, M., Lundin, R., Rème, H., Sauvaud, J.-A., Dandouras, I., Balogh, A., Kistler, L. M., Klecker, B., Carlson, C. W., Bavassano-Cattaneo, M. B., and Korth, A.: Characteristics of high altitude oxygen ion energization and outflow as observed by Cluster: a statistical study, Ann. Geophys., 24, 1099–1112, https://doi.org/10.5194/angeo-24-1099-2006, 2006.

Nilsson, H., Engwall, E., Eriksson, A., Puhl-Quinn, P. A., and Arvelius, S.: Centrifugal acceleration in the magnetotail lobes, Ann. Geophys., 28, 569–576, https://doi.org/10.5194/angeo-28-569-2010, 2010.

Nilsson, H., Barghouthi, I. A., Slapak, R., Eriksson, A. I., and André, M.: Hot and cold ion outflow: Spatial distribution of ion heating, J. Geophys. Res.-Space, 117, A11201, https://doi.org/10.1029/2012JA017974, 2012.

Nilsson, H., Barghouthi, I. A., Slapak, R., Eriksson, A. I., and André, M.: Hot and cold ion outflow: Observations and implications for numerical models, J. Geophys. Res.-Space, 118, 105–117, https://doi.org/10.1029/2012JA017975, 2013.

Rème, H., Aoustin, C., Bosqued, J. M., Dandouras, I., Lavraud, B., Sauvaud, J. A., Barthe, A., Bouyssou, J., Camus, Th., Coeur-Joly, O., Cros, A., Cuvilo, J., Ducay, F., Garbarowitz, Y., Medale, J. L., Penou, E., Perrier, H., Romefort, D., Rouzaud, J., Vallat, C., Alcaydé, D., Jacquey, C., Mazelle, C., d'Uston, C., Möbius, E., Kistler, L. M., Crocker, K., Granoff, M., Mouikis, C., Popecki, M., Vosbury, M., Klecker, B., Hovestadt, D., Kucharek, H., Kuenneth, E., Paschmann, G., Scholer, M., Sckopke, N., Seidenschwang, E., Carlson, C. W., Curtis, D. W., Ingraham, C., Lin, R. P., McFadden, J. P., Parks, G. K., Phan, T., Formisano, V., Amata, E., Bavassano-Cattaneo, M. B., Baldetti, P., Bruno, R., Chionchio, G., Di Lellis, A., Marcucci, M. F., Pallocchia, G., Korth, A., Daly, P. W., Graeve, B., Rosenbauer, H., Vasyliunas, V., McCarthy, M., Wilber, M., Eliasson, L., Lundin, R., Olsen, S., Shelley, E. G., Fuselier, S., Ghielmetti, A. G., Lennartsson, W., Escoubet, C. P., Balsiger, H., Friedel, R., Cao, J.-B., Kovrazhkin, R. A., Papamastorakis, I., Pellat, R., Scudder, J., and Sonnerup, B.: First multispacecraft ion measurements in and near the Earth's magnetosphere with the identical Cluster ion spectrometry (CIS) experiment, Ann. Geophys., 19, 1303–1354, https://doi.org/10.5194/angeo-19-1303-2001, 2001.

Ribas, I., Guinan, E. F., Güdel, M., and Audard, M.: Evolution of the Solar Activity over Time and Effects on Planetary Atmospheres. I. High-Energy Irradiances (1-1700 Å), Astrophys. J., 622, 680–694, https://doi.org/10.1086/427977, 2005.

Rosenqvist, L., Opgenoorth, H., Buchert, S., McCrea, I., Amm, O., and Lathuillere, C.: Extreme solar-terrestrial events of October 2003: High-latitude and Cluster observations of the large geomagnetic disturbances on 30 October, J. Geophys. Res.-Space, 110, A09S23, https://doi.org/10.1029/2004JA010927, 2005.

Seki, K., Elphic, R. C., Hirahara, M., Terasawa, T., and Mukai, T.: On Atmospheric Loss of Oxygen Ions from Earth Through Magnetospheric Processes, AGU Spring Meeting Abstracts, 2001.

Shelley, E. G., Peterson, W. K., Ghielmetti, A. G., and Geiss, J.: The polar ionosphere as a source of energetic magnetospheric plasma, Geophys. Res. Lett., 9, 941–944, https://doi.org/10.1029/GL009i009p00941, 1982.

Shue, J.-H., Song, P., Russell, C. T., Steinberg, J. T., Chao, J. K., Zastenker, G., Vaisberg, O. L., Kokubun, S., Singer, H. J., Detman, T. R., and Kawano, H.: Magnetopause location under extreme solar wind conditions, J. Geophys. Res., 103, 17691–17700, https://doi.org/10.1029/98JA01103, 1998.

Slapak, R., Nilsson, H., and Westerberg, L. G.: A statistical study on O+ flux in the dayside magnetosheath, Ann. Geophys., 31, 1005–1010, https://doi.org/10.5194/angeo-31-1005-2013, 2013.

Slapak, R., Schillings, A., Nilsson, H., Yamauchi, M., Westerberg, L.-G., and Dandouras, I.: Atmospheric loss from the dayside open polar region and its dependence on geomagnetic activity: implications for atmospheric escape on evolutionary timescales, Ann. Geophys., 35, 721–731, https://doi.org/10.5194/angeo-35-721-2017, 2017.

Tsurutani, B. T., Echer, E., Guarnieri, F. L., and Kozyra, J. U.: CAWSES November 7–8, 2004, superstorm: Complex solar and interplanetary features in the post-solar maximum phase, Geophys. Res. Lett., 35, L06S05, https://doi.org/10.1029/2007GL031473, 2008.

Wang, Y. M., Ye, P. Z., and Wang, S.: Multiple magnetic clouds: Several examples during March-April 2001, J. Geophys. Res.-Space, 108, 1370, https://doi.org/10.1029/2003JA009850, 2003.

Yau, A. W. and Andre, M.: Sources of Ion Outflow in the High Latitude Ionosphere, Space Sci. Rev., 80, 1–25, https://doi.org/10.1023/A:1004947203046, 1997.

Yau, A. W., Peterson, W. K., and Shelley, E. G.: Quantitative parametrization of energetic ionospheric ion outflow, Washington DC American Geophysical Union Geophysical Monograph Series, 44, 211–217, https://doi.org/10.1029/GM044p0211, 1988.

Yermolaev, Y. I., Zelenyi, L. M., Kuznetsov, V. D., Chertok, I. M., Panasyuk, M. I., Myagkova, I. N., Zhitnik, I. A., Kuzin, S. V., Eselevich, V. G., Bogod, V. M., Arkhangelskaja, I. V., Arkhangelsky, A. I., and Kotov, Y. D.: Magnetic storm of November, 2004: Solar, interplanetary, and magnetospheric disturbances, J. Atmos. Sol.-Terr. Phy., 70, 334–341, https://doi.org/10.1016/j.jastp.2007.08.020, 2008.

Zhang, J., Richardson, I. G., Webb, D. F., Gopalswamy, N., Huttunen, E., Kasper, J. C., Nitta, N. V., Poomvises, W., Thompson, B. J., Wu, C.-C., Yashiro, S., and Zhukov, A. N.: Solar and interplanetary sources of major geomagnetic storms (Dst $\leq$ -100 nT) during 1996–2005, J. Geophys. Res.-Space, 112, A10102, https://doi.org/10.1029/2007JA012321, 2007.

O$^+$ escape during the extreme space weather event of 4–10 September, 2017

Authors:
A. Schillings, H. Nilsson, R. Slapak, P. Wintoft, M. Yamauchi, M. Wik, I. Dandouras and C.M. Carr

Space Weather

Key Points:
- Multiple X-flares and three CMEs occurred in 4-10 September 2017, CMEs are the driver of the storm, whereas the X-flares might have preheated the ionosphere
- The O^+ outflow in the polar cap and cusp is estimated to be 10^{13} $m^{-2} s^{-1}$ during the main phase of the geomagnetic storm
- The entire magnetosphere is affected by space weather event, and the O^+ enhancement in the cusp might be a good indicator for satellite drag fluctuations

Correspondence to:
A. Schillings,
audrey.schillings@irf.se

O^+ Escape During the Extreme Space Weather Event of 4–10 September 2017

Audrey Schillings[1,2] [ID], Hans Nilsson[1,2] [ID], Rikard Slapak[3], Peter Wintoft[4] [ID], Masatoshi Yamauchi[1] [ID], Magnus Wik[4] [ID], Iannis Dandouras[5] [ID], and Chris M. Carr[6] [ID]

[1]Swedish Institute of Space Physics, Kiruna, Sweden, [2]Division of Space Technology, Luleå University of Technology, Kiruna, Sweden, [3]EISCAT Scientific Association, Kiruna, Sweden, [4]Swedish Institute of Space Physics, Lund, Sweden, [5]IRAP, Université de Toulouse, CNRS, UPS, CNES, France , [6]Department of Physics, Imperial College London, London, UK

Abstract We have investigated the consequences of extreme space weather on ion outflow from the polar ionosphere by analyzing the solar storm that occurred early September 2017, causing a severe geomagnetic storm. Several X-flares and coronal mass ejections were observed between 4 and 10 September. The first shock—likely associated with a coronal mass ejection—hit the Earth late on 6 September, produced a storm sudden commencement, and began the initial phase of the storm. It was followed by a second shock, approximately 24 hr later, that initiated the main phase and simultaneously the Dst index dropped to Dst = −142 nT and Kp index reached Kp = 8. Using COmposition DIstribution Function data on board Cluster satellite 4, we estimated the ionospheric O^+ outflow before and after the second shock. We found an enhancement in the polar cap by a factor of 3 for an unusually high ionospheric O^+ outflow (mapped to an ionospheric reference altitude) of 10^{13} $m^{-2} s^{-1}$. We suggest that this high ionospheric O^+ outflow is due to a preheating of the ionosphere by the multiple X-flares. Finally, we briefly discuss the space weather consequences on the magnetosphere as a whole and the enhanced O^+ outflow in connection with enhanced satellite drag.

1. Introduction

Solar storms with associated flares, coronal mass ejections (CMEs), and radio bursts may be hazardous to Earth, potentially affecting satellite operations through enhanced satellite drag, causing electric power distribution failures due to extraordinary ground-induced currents, disturbing radio communications, and causing radio blackouts due to higher ionization rates in the lower ionosphere. Balch et al. (2004) report occurrence rates of such events; extreme and severe radio blackouts occur approximately 1 day and 8 days per solar cycle, respectively. Similarly, the planetary Kp index (Bartels et al., 1939; Mayaud, 1980), widely used as a general indicator of geomagnetic disturbances for midlatitude regions and as a general geomagnetic alert and hazard scale, reaches extreme (Kp = 9) and severe (Kp = 8) levels, respectively 4 and 100 days per solar cycle, (Balch et al., 2004).

In solar cycle 23, there were more than 100 X-flares, the strongest occurring in November 2003 (X28.0) and in April 2001 (X20.0). However, for these events the solar active regions (ARs) were close to the solar limb; therefore, no severe or extreme geomagnetic storms were observed (Zhang et al., 2007). The third strongest was an X17.2 flare detected on 28 October 2003 and due to a strong interplanetary coronal mass ejection (ICME) an extreme geomagnetic storm—also known as the Halloween storm—took place (e.g ; Gopalswamy et al., 2005; Rosenqvist et al., 2005; Yamauchi et al., 2006). It produced disturbances around the world (Balch et al., 2004). In the same solar cycle, on 20 January, 2005 an outstanding solar flare occurred (X7.1), followed by an ICME, which was detected in the near-Earth space on 21 January. This ICME arrival resulted in an extreme magnetospheric compression (Dandouras et al., 2009). In solar cycle 24, in September 2017, several X-flares occurred of which the most intense was an X9.0-flare (the largest observed since December 2006), which with strong CMEs produced an extreme geomagnetic storm. These extreme events caused a strong response in the ionosphere and magnetosphere, for example, variations in the total electron content and enhanced magnetospheric convection. An additional effect is the strongly enhanced ion outflow from the polar ionosphere (Schillings et al., 2017).

Ion outflow from the ionosphere has been widely studied, that is, by Shelley et al. (1982), Chappell et al. (1987), Moore et al. (1997), Lennartsson et al. (2004), Kronberg et al. (2014), Maes et al. (2015), and references therein. The most profound magnetospheric ion outflow is usually observed in the open magnetic field line regions: the polar caps, cusps, and plasma mantle (Nilsson et al., 2012). The mirror force plays a key role in the acceleration of outflowing ions, with perpendicular energy converted into parallel energy as the ions move into higher altitudes and weaker magnetic fields. Therefore, perpendicular heating of ions causes subsequent outward acceleration. Wave-particle interaction can cause such transverse ion heating, and these processes and their effects have been investigated at different altitudes (e.g., Andre et al., 1990; Bouhram et al., 2005; Moore & Horwitz, 2007; Nilsson et al., 2012; 2006; Norqvist et al., 1996; Slapak et al., 2011; Waara et al., 2011). If the heating is effective enough, the ions will gain sufficient velocities to escape into the solar wind downstream in the tail (Nilsson et al., 2012) or even directly from the cusp (Slapak et al., 2013).

Ion outflow has been studied for different solar wind and geomagnetic conditions. Cully et al. (2003) identified four factors that influence the ion outflow: the solar radio flux at 10.7 cm (F10.7), the interplanetary magnetic field (IMF), the solar wind electric field, and the solar wind dynamic pressure. Using data in an altitude range of 1.3 to 2.0 R_E, Yau et al. (1988) found that ion outflow depends on the geomagnetic condition such that it increases exponentially with Kp. Similarly, Slapak et al. (2017) made a statistical study using high-altitude plasma mantle and magnetosheath Cluster data in order to quantify the total O^+ escape as a function of Kp. Complementary to that study, Schillings et al. (2017) presented that the escape rate during extreme geomagnetic storms could be higher than what a linear extrapolation of the results of Slapak et al. (2017) would predict. As the whole magnetosphere is affected by disturbed magnetospheric conditions, the O^+ outflow that does not escape into the solar wind is transported to the lobes through the polar cap. Through reconnection in the plasma sheet, O^+ coming from the lobe is heated and feeds both the distant and near-Earth plasma sheet (Kistler et al., 2006; Mouikis et al., 2010).

The consequence of space weather on ion outflow has not been well studied. Therefore, it is not clear what parameter is most influential with what timescale. In this paper, we first investigate the space weather during 4 to 10 September 2017, from solar storm to geomagnetic storm. Thereafter, we examine the effects on magnetosphere-ionosphere coupling, in particular, ion outflow. The goal is primarily to see the space weather effects on ion outflow for this well-studied storm. Despite that ion outflow in itself not causing hazardous to human activity, the enhanced ion outflow and resulting escape are mainly observed in the cusp, which has an important role in some hazards as discussed in section 5.3.

2. Instrumentation and Data

2.1. Cluster Mission

The Cluster mission (Escoubet et al., 2001) was launched in 2000 and consists of four spacecraft flying in tetrahedral formation in an elliptical polar orbit. Only spacecraft 4 (SC4) was used in this study, because in 2017 the COmposition DIstribution Function (CODIF) part of the Cluster Ion Spectrometer (Rème et al., 2001) on board the other spacecraft are no longer functional. The particle detection efficiency of CODIF on board spacecraft 4 has also been degraded (Kistler et al., 2013); this degradation is taken into account by the instrument in-flight calibration files. The CODIF instrument measures the 3-D distributions of H^+, He^{2+}, He^+, and O^+ using a time-of-flight technique. When CODIF is subject to intense proton fluxes, the heavier ion channels may be contaminated with false counts. If so, the ratio of the O^+ to H^+ perpendicular bulk velocity will have a local peak at 1/4, and these unreliable O^+ data can be removed (Nilsson et al., 2006). The magnetic field data are provided by the FluxGate Magnetometer (Balogh et al., 2001), which has a normal mode sample frequency of 22.4 Hz. In this study we are interested in the background magnetic field and use the field averaged over the spacecraft spin period of 4 s.

2.2. Solar and Solar Wind Data

We utilized a range of observations and derived data from the Sun to the solar wind. The Solar Dynamics Observatory (Pesnell et al., 2012) is especially targeted at producing observations of the solar drivers in order to understand and predict space weather. Images from the photosphere and photospheric magnetic fields, and up through the corona, are produced at high resolution and high cadence. Solar ARs are summarized and collected on a daily basis in the Solar Region Summary by National Oceanic and Atmospheric Administration (NOAA)/Space Weather Prediction Center (SWPC). SWPC also provides full-disk X-ray observations from the GOES spacecraft. CMEs are observed by the ESA/NASA SOHO and the NASA STEREO (currently, only one
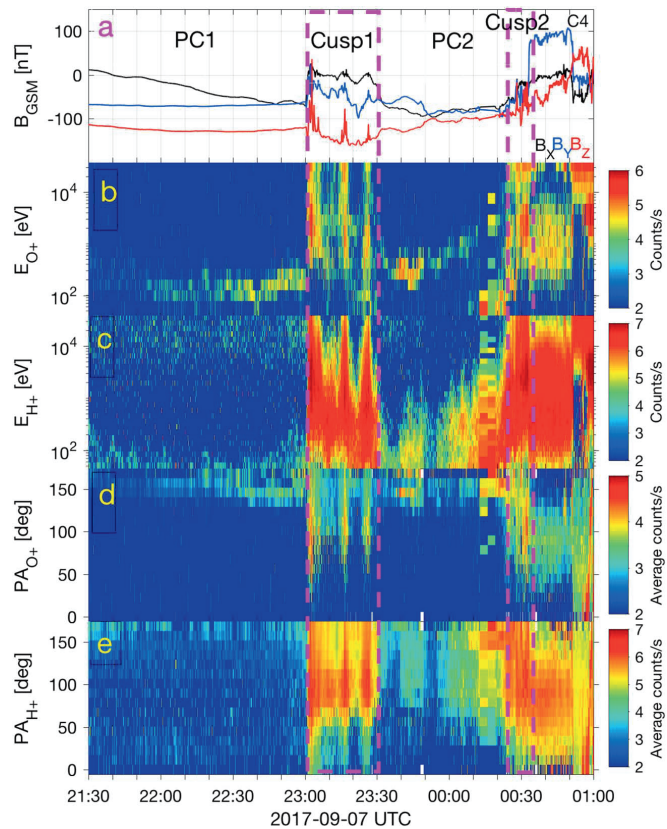
Figure 1. Geomagnetic storm on 7–8 September 2017. (a) The local magnetic field in the Northern Hemisphere for the polar caps (PC1 and PC2) and the cusps (Cusp 1 and Cusp 2). (b–e) The energy and PA spectrograms for the O^+ and H^+, respectively. PC = polar cap; PA = pitch angle; GSM = geocentric solar magnetospheric.

spacecraft is operational). From coronal images, the SIDC automatically detects and estimates CME parameters, producing a catalog of CMEs. Finally, solar wind plasma and magnetic fields are measured by the DSCOVR spacecraft; data are provided by NOAA/SWPC.

3. Method

This section describes how we analyzed the September 2017 storm from the solar point of view to the O^+ outflow in the polar regions at Earth. We study the complete chain of events from the Sun, through the solar wind, geomagnetic indices, and ion outflow, in particular, the ionospheric O^+ ions. The O^+ ions mainly originate from the ionosphere whereas the distinction between the ionospheric and solar origin of the H^+ is more complex. We first looked and analyzed the solar data such as X-flares and CMEs from the beginning of September. Afterward, we checked the solar wind parameters from 4 to 10 September to identify the arrival time of the shocks at Earth and finally compare them with Cluster observations.

At Earth, a geomagnetic storm is characterized by three phases—the initial, main, and recovery phase—which can be identified by the behavior of the Dst index. The Dst index is a 1-hr index estimated from the deviations of the horizontal component of the magnetic field at low-latitude magnetometer stations. In principle, it is a measure of the equatorial ring current strength. The Kp index is a 3-hr index estimated from local disturbances in the horizontal magnetic field component and relates to geomagnetic activity over
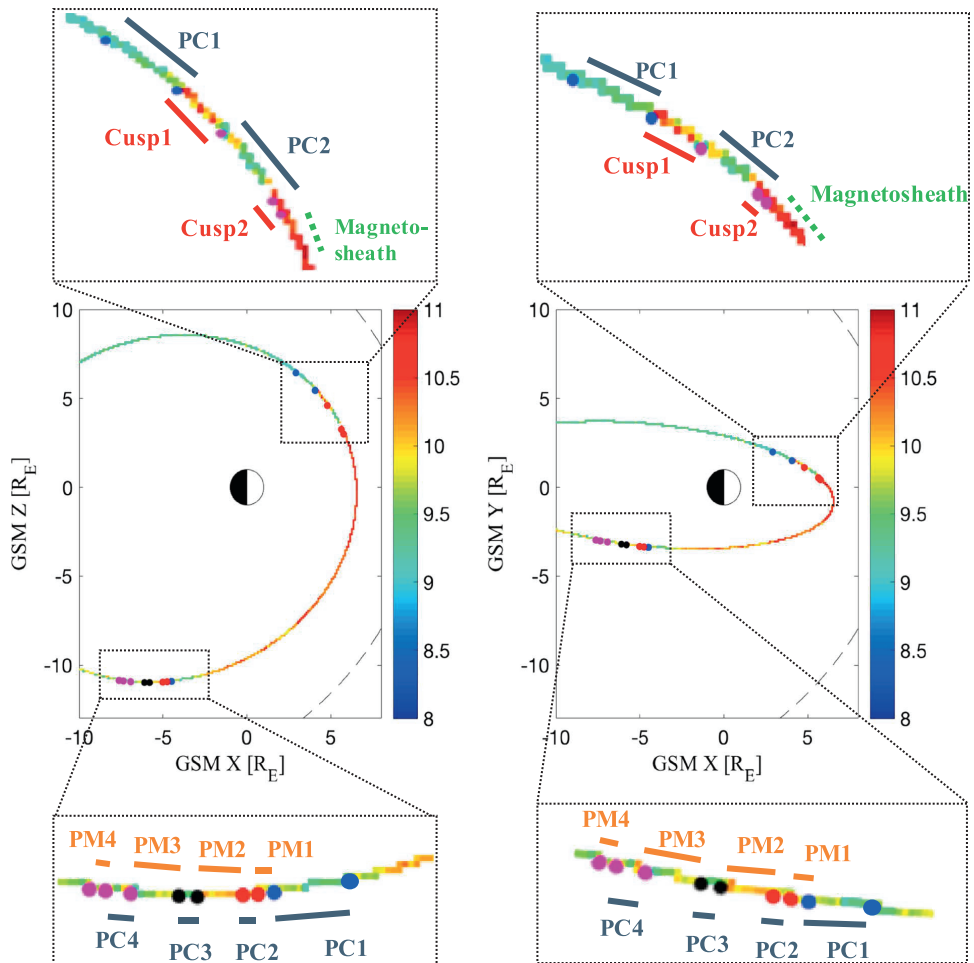

Figure 2. The middle panels show Cluster orbit in the planes XZ_{GSM} and XY_{GSM}. The color bar represents the O^+ flux ($\log_{10}$ m^{-2}s^{-1}) along this orbit. The top panels correspond to a zoom of the northern outflowing regions, namely, polar cap and cup, whereas the bottom panels correspond to a zoom of the southern outflowing regions, polar cap and plasma mantle. The regions (PC, Cusp, and PM) are marked out with color dots. PC = polar cap; PM = plasma mantle; GSM = geocentric solar magnetospheric.

a global scale. A combination of these two magnetic indices provides magnetospheric information on the geomagnetic storm. The initial phase of a geomagnetic storm is typically characterized by a positive disturbance in the Dst index, which could also be associated with an storm sudden commencement (SSC). When the positive perturbation drops drastically to negative values, the main phase of the storm starts and lasts a few hours—typically 2 to 10 hr—and is followed by the recovery phase that can last hours to a few days.

In order to estimate the O^+ outflow during the geomagnetic storm, we first looked at the O^+ and H^+ energy and pitch angle (PA) spectrograms and the magnetic field for SC4. Figure 1a shows that the local magnetic field varied slowly and was weaker in the regions marked as polar cap (PC1 and PC2), while it was stronger and variable in the cusp (Cusp 1 and Cusp 2). Figures 1b–1e correspond to O^+ and H^+ energy and PA spectrograms, respectively (for more details see Schillings et al., 2017). The color bar represents counts per second, which is proportional to the particle differential energy flux, and the dashed (pink) rectangles distinguish the polar
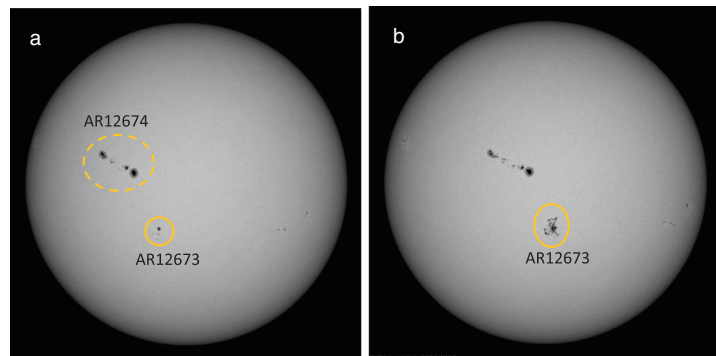
Figure 3. Continuum images from the Sun taken by the HMI on board Solar Dynamics Observatory. Courtesy of NASA/SDO and the HMI science teams (a) We highlight the solar active regions (AR) 12674 in yellow dashed circle and the AR12673 in yellow solid circle in the morning of 3 September. Similarly, (b) shows the same regions in the evening of 3 September.

caps from the cusps. From Figure 1, we visually identified the outflowing regions in the Northern Hemisphere. In the polar cap, we observed an oxygen ion beam at lower energies than in the cusp, see Figure 1b. Furthermore, the magnetic field in the polar cap is more stable as opposed to the cusp, which is characterized by more variability. The PA spectrograms, displayed in Figures 1d and 1e, clearly show outflowing ions (PA $\simeq 180°$, Northern Hemisphere) for O^+ and H^+ in the polar cap regions. In the cusp, outflowing ions (PA $\simeq 180°$) are visible and also ion populations with most energy perpendicular to the magnetic field (PA $\simeq 90°$).

The identified outflowing regions are confirmed from the observations by inspecting the Cluster orbit. We first used the Orbit Visualization Tool (Y. Khotyaintsev, https://ovt.irfu.se) for a 3-D view of the SC4 orbit with the location of the magnetopause and the bow shock. Second, we plotted the O^+ flux along the orbit for these time periods (Figure 2). In Figure 2, the outflowing regions are represented by the zoomed plots (top for the north and bottom for the south) on the orbit planes XZ_{GSM} and XY_{GSM}. The color bars correspond to the O^+ flux along the Cluster trajectory, and the points mark the identified regions. In the north, we observed polar cap and cusp regions, while in the south we identified polar cap and plasma mantle regions. During each time period, which corresponds to the polar cap, the cusp, or the plasma mantle, we made histograms of the scaled O^+ outflow. The scaled O^+ outflow is defined as the net outward flux scaled to an ionospheric reference altitude and given by the formula $F_{map} = \frac{F_{O^+} * B_{iono}}{B_{local}}$. We mapped the fluxes ($F_{O^+}$) to an ionospheric reference altitude with a magnetic field strength of $B_{iono} = 50,000$ nT. The local outward flux can be mapped assuming conservation of particle flux along the corresponding magnetic flux tube (B_{local}). This scaled net outward flux is thus independent of the altitude and any magnetic compression giving an estimate of the original ionospheric outflow.

4. Observations

This section presents the September storm from the solar storm to the ion escape during the extreme geomagnetic storm. The solar regions where the flares and CMEs were produced are described, and we estimate the terrestrial magnetospheric O^+ outflow during the main phase of the geomagnetic storm.

4.1. Solar Storm

Multiple X-type flares and Earth-directed CMEs were observed during 4–10 September 2017. On 1 September, the solar AR 12673 was a small unipolar spot just south of the solar equator (magnetic type α). At the same time AR12674 (Figure 3a, yellow dashed circle) on the Northern Hemisphere was much larger and more complex ($\beta - \gamma$). However, during 3–4 September AR12673 grew dramatically both in size (more than 10 times in area, see Figures 3a and 3b, yellow solid circle) and complexity ($\beta - \gamma - \delta$) and thus became a highly interesting region. The region stayed large and magnetically complex during its passage over the solar disk until it went around the west limb during 10 September.
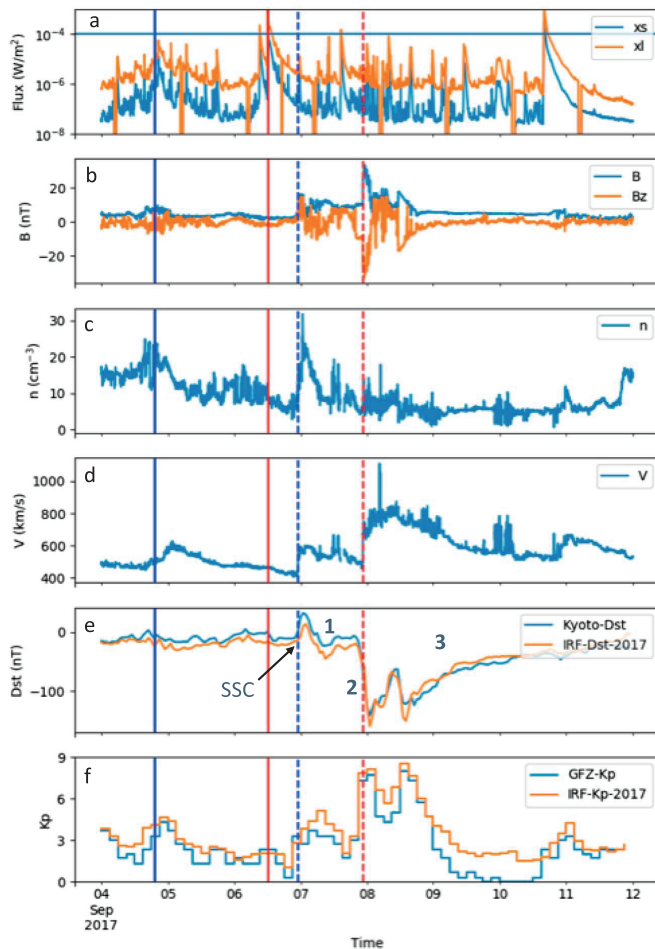
Figure 4. Solar wind parameters for 4 to 12 September 2017. (a) The short (xs, 0.05–0.4 nm, orange line) and long wavelength (xl, 0.1–0.8 nm, blue line) of the solar flux from Solar X-ray Imager/Solar Dynamics Observatory, (b–d) interplanetary magnetic field, solar wind density and velocity, respectively, and (e and f) the Dst and Kp indices, respectively. The vertical solid blue and red lines correspond to respectively the first and second CME, whereas the dashed blue and red lines display the associated shock at Earth. The tree phases of the geomagnetic storm and the storm sudden commencement are illustrated on panel (e) where 1 is the initial phase, 2 is the main phase and 3 is the recovery phase. GFZ = Deutsches GeoForschungsZentrum; SSC = storm sudden commencement; IRF = Swedish Institute of Space Physics.

AR12673 produced numerous flares and CMEs from 4 to 10 September. Most notable was a CME in the evening of 4 September and another on midday 6 September. The Solar Influences Data Centre identified speeds in both events close to 2,000 km/s with onset times at 4 September 2017 19:12 UT and 6 September 2017 12:12 UT, respectively (Robbrecht et al., 2009). Another fast CME was launched on 10 September, but at that time AR12673 was on the western limb and the CME was not Earth directed.

Two X-flares occurred on 6 September, one on 7 September, and another on 10 September. The X-flares were observed by GOES-13 for short and long wavelengths with 1-min resolution X-ray flux, XS (0.05–0.4 nm) and XL (0.1–0.8 nm) as presented in Figure 4a. The horizontal solid blue line in Figure 4a corresponds to the lower
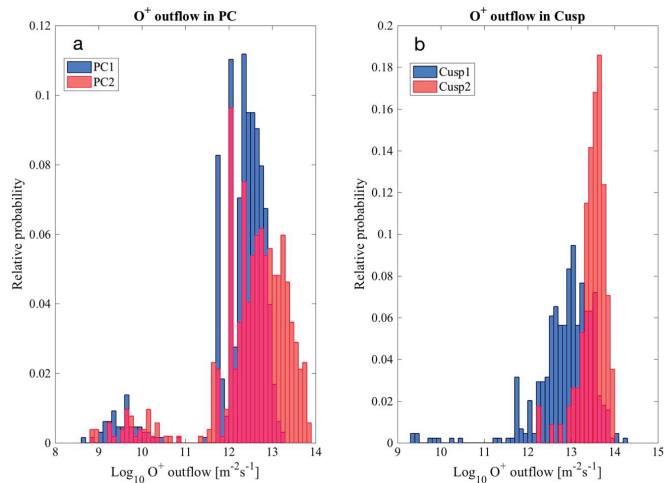
Figure 5. Distribution of the scaled O$^+$ outflow (log$_{10}$m^{-2} s^{-1}) in the polar cap (PC 1, 7 September 22:11-23:00 UT; PC2, 7–8 September 23:35–00:24 UT) and in the cusp (Cusp 1, 7 September 23:00–23:35 UT; PC2, 8 September 00:24–00:33 UT) in the Northern Hemisphere.

limit for an X-type flare. The onset of the first CME on 4 September and the likely associated shock in the solar wind are indicated by the vertical solid and dashed blue lines, respectively. The latter is clearly seen in the IMF (Figure 4b), solar wind density (Figure 4c), and velocity (Figure 4d) 1-min resolution data taken from DSCOVR. Finally, the vertical solid and dashed red lines indicate the onset and the likely associated shock, respectively, of the second CME. Figures 4e and 4f display the Dst and Kp index values from Kyoto, World Data Center for Geomagnetism (blue line, panel (e)), and Deutsches GeoForschungsZentrum, Potsdam (blue line panel (f)), and estimated by the Swedish Institute of Space Physics, Sweden (orange line; Wintoft et al., 2017).

4.2. Geomagnetic Storm

Late on 6 September 2017, a shock associated with a CME was detected just before midnight in the IMF, density, and velocity. This first shock (Figure 4, dashed blue line) initiated the initial phase of the geomagnetic storm with a positive increase in the Dst index (Figure 4e) and in the z component of the local magnetic field, causing a SSC. After this abrupt change, the IMF turned and stayed northward for a few hours (Figure 4b, Bz in orange) and with a compressed magnetopause and stronger currents as a consequence. During the SSC, Cluster spacecraft 4 was located in the tail region, and therefore, the O$^+$ outflow cannot be estimated. This first shock probably caused a small geomagnetic storm. However, approximately 24 hr later a second CME (Figure 4, dashed red line) reached the Earth. The IMF was strong and southward this time, and with the earlier compression of the magnetosphere by the first CME (number 1 in Figure 4e), the second CME shock enhanced the incoming energy from the solar wind into the magnetosphere and directly initiated the main phase (number 2 in Figure 4e). The solar wind density (Figure 4c) was lower as compared to the first shock, the velocity (Figure 4d) increased from approximately 200 km/s, the Kp index increased to Kp = 8 (Figure 4f), and the Dst index dropped significantly to −142 nT. This negative drop is a signature of the storm main phase, which continued for approximately 5 hr (20:00–01:00 UT). During the main phase of the storm, Cluster was in the Northern Hemisphere (see Figure 2, and top panels for zooms).

The arrival of the second shock was coincident with an abrupt equatorward motion of the cusp, at 23:00 UT on 7 September (Figures 1b and 1c) in the Cluster data. When hitting the Earth, the shock again compressed the magnetopause, causing higher convection in the magnetosphere. Simultaneously, the southward IMF opened up the dayside geomagnetic field lines, such that the footprints of the cusp are at lower latitudes. Newell and Meng (1994) and Newell et al. (1989) described how the polar cap and plasma mantle move equatorward for disturbed magnetospheric conditions, and we observed such a motion of the cusp. After the second shock, Cluster was located in the cusp for about 50 min, before the cusp moved equatorward such that

Table 1
Parameters for Escaping O$^+$ Ions

Region	T_{perp} (eV)	T_{par} (eV)	v_{perp} (km/s)	v_{par} (km/s)
PC 1	11.02	86.97	14.51	37.26
Cusp 1	1,546.7	1,553.8	46.19	46.31
PC 2	38.07	94.63	20.63	50.76
Cusp 2	3,115.6	1,755.1	47.01	40.2

Cluster was again located in the polar cap for approximately 40 min (see Figure 1). Afterward, Cluster entered the cusp a second time, where the spacecraft stayed for a few minutes before ending up in the magnetosheath (see Figure 2, top panels).

Following the main phase, the recovery phase (number 3 in Figure 4e) was longer and in the meantime Cluster was at the nightside in the Southern Hemisphere (8 September around noon). In Figure 2, the bottom panels show the encountered regions in the south. We visually identified the polar cap and plasma mantle as Cluster was on the flank of the magnetosphere and in the nightside. Cluster encountered four polar cap/plasma mantle crossings.

4.3. O$^+$ Outflow During the Geomagnetic Storm
4.3.1. Northern Hemisphere
We estimated the scaled O$^+$ outflow in the different regions before and after the second shock signature, from 7 September 22:11 UT to 8 September 00:33 UT, while Cluster was located in the polar cap and in the cusp. Figure 5 displays the distribution of the scaled O$^+$ outflow in the polar cap (Figure 5a) and the cusp (Figure 5b). Polar cap 1 and Cusp 1 (blue) correspond to the first Cluster passage of those regions and Polar cap 2 and Cusp 2 (red) to the second passage. The *transitional* color corresponds to the superposition of the two distributions. The scaled O$^+$ outflow, given in per square meter per second in logarithmic scale, is shown on the *x* axis, while the *y* axis gives the relative probability from the number of data points in each bin compared to the total data points from the distribution.

The scaled O$^+$ outflow of the polar cap has clearly increased after the passage of the second shock. The average scaled O$^+$ outflow in the Polar cap 1 and Cusp 1 are 3.5×10^{12} and 1.6×10^{13} m^{-2} s^{-1}, respectively, and increase by a factor of 3 (polar cap) and 2 (cusp) after the shock signature. The highest value, with a minimum of 1% of the data in the bin, is 6.3×10^{13} m^{-2} s^{-1} for the polar cap and 1×10^{14} m^{-2} s^{-1} for the cusp.

To determine if the scaled O$^+$ outflow is escaping into the solar wind, we study the O$^+$ perpendicular and parallel temperatures, as well as the perpendicular and parallel velocities. Table 1 gives the four parameters we took into account to estimate the fate of the O$^+$ ions. In the polar cap regions, the parallel to perpendicular temperature ratio is high due to the high parallel component; therefore, the transverse heating is not efficient; this is as expected (significant transverse heating is usually observed only in the cusp due to the wave-particle interactions; Strangeway et al., 2005; Slapak et al., 2013). The ions in the polar cap are mostly accelerated through the centrifugal acceleration (Nilsson et al., 2012). Furthermore, the parallel velocity is twice the perpendicular velocity (in the polar cap), so that the ions follow the magnetic field upward with their fate in the plasma sheet tailward of the X-line (neutral line in the magnetotail) at about 20–30 R_E. Note that the X-line can be pushed earthward around 10 R_E for a severe geomagnetic storm (Tsyganenko & Sitnov, 2005). In the cusp region, the components of the temperature are similar before the shock, whereas the perpendicular temperature is about twice the parallel component. This indicates a transverse heating effect. However, the perpendicular velocities are very high (>40 km/s) compared to the average convection velocity of 7.5 km/s in the lobes (Haaland et al., 2012), and it leads to a strong convection in the cusp region. The cusp field lines will convect through the polar cap (lobes) before they reach the plasma sheet, and thus, we should use the perpendicular velocity in the polar cap for our calculations of where the ions reach the plasma sheet. A considerable amount of flux is therefore transported tailward and toward the plasma sheet, despite this strong convection, the ions have enough energy to escape directly downtail.

Figure 6 shows the relative probability of $\log_{10} T_\perp(O^+)$ (eV) in the northern polar cap and cusp before the shock signature (blue) and after (red). Note that the *transitional* color corresponds to the superposition of the two distributions. The dashed blue (Cut 1) and red (Cut 2) lines roughly mark the separation between the polar cap and the cusp. In the cusp, we observed a higher perpendicular temperature than in the polar cap as expected because the ions are more heated. The perpendicular energy is converted into parallel energy by the mirror force for outflowing ions, thus accelerating the ions upward. Slapak et al. (2011) showed that O$^+$ is effectively heated transversely through wave-particle interactions in the cusp. By the high perpendicular temperatures in the cusp combined with a parallel velocity $v_\parallel(O^+) > 30$ km/s (not shown), we can conclude that the observed O$^+$ in the cusp will eventually escaping into the solar wind (Nilsson, 2011).
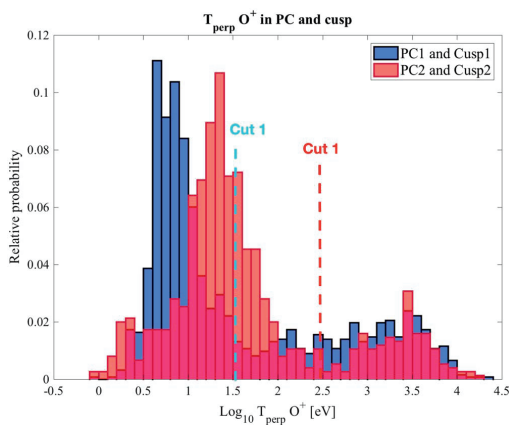
Figure 6. Distribution of the perpendicular temperature for the scaled O^+ outflow ($\log_{10}$ m^{-2} s^{-1}) in the polar and cusp regions in the Northern Hemisphere for 7–8 September 22:11–00:33 UT.

4.3.2. Southern Hemisphere

Cluster was located in the Southern Hemisphere during the recovery phase (number 3 in Figure 4e) of the geomagnetic storm. Thus, we checked which regions it encountered where O^+ outflow might be observed. We identified four crossings from polar cap to plasma mantle (see Figure 2, bottom panels) where the scaled O^+ outflow has been estimated. The four identified polar cap and plasma mantle observations are numbered from 1 to 4 according to the passage on the Cluster orbit (color points in Figure 2); that is, number 1 equals to the first polar cap/plasma mantle crossing in time along Cluster orbit. In plasma mantle regions from 1 to 4, the scaled O^+ outflow is roughly the same $\sim 3 \times 10^{12}$ m^{-2} s^{-1}. Similarly to the Northern Hemisphere, we looked at the perpendicular and parallel components of the temperature and velocities in the plasma mantle regions. The parallel temperatures are unexpectedly high (about twice the perpendicular component) for the four plasma mantle passages, which means that a local heating is observed in these regions; otherwise, the velocity filter effect would have decreased the parallel component of the temperature. Additionally, the perpendicular component of the velocity is not negligible; we thus have a significant convection. This strong convection implies a considerable magnetic flux transport that must be released through reconnection if it is not to accumulate in the magnetotail. The reconnection rate must then be correspondingly high, and the X-line might move earthward. Thus, due to the high parallel component of the temperature and the perpendicular velocity, the fate of the ions is less predictable than for the Northern Hemisphere. They might end up in the plasma sheet and feed the ring current with O^+ or tailward of the X-line and be lost in the magnetotail.

4.3.3. O^+ Flux in the Plasma Sheet

We also looked at the O^+ flux in the first plasma sheet crossing after the storm. The plasma sheet is identified around $X_{GSM} \simeq -15$ R_E, and the net O^+ flux is small. Following the method of Slapak et al. (2017) — dividing the flow between tailward and earthward flux — we estimated an average O^+ flux of $\sim 1.1 \times 10^9$ m^{-2} s^{-1} in both directions. This estimation is in agreement with the average O^+ flux calculated in the central plasma sheet by Slapak et al. (2017). In addition, Cluster was in the plasma sheet in the end of the recovery phase (9 September, about 00:00 to 16:00 UT) and our estimation shows that the average O^+ return flux was the same as during quiet magnetospheric conditions. This result is consistent with the results of Kistler et al. (2010), who showed that the O^+ density is reduced during the recovery phase.

5. Discussion

5.1. Solar Drivers for O^+ Escape During Geomagnetic Storm

Extreme geomagnetic storms are caused by ICMEs, while smaller storms could be caused by corotating interaction regions. On 4 and 6 September 2017, two CMEs were detected at the Sun and on 6 and 7 September, three X-flares (X2.2; X9.3 [6 September] and X1.3 [7 September]) were observed. The CMEs produced a severe geomagnetic storm recorded with Kp = 8 and Dst $\simeq -140$ nT. The first CME, which arrived late 6 September, had northward IMF with 600-km/s velocity, whereas the second that arrived late 7 September had southward IMF with 800-km/s velocity. These features are most likely the causes of higher-scaled O^+ outflow because both velocity and IMF are expected to influence O^+ outflow (Lennartsson et al., 2004; Yamauchi & Slapak, 2018). Lennartsson et al. (2004) showed that negative IMF Bz has a higher influence on the total O^+ outflow by approximately a factor 3. Considering also the timing of enhanced O^+ compared to arrival timing of CMEs and enhanced extreme ultraviolet (EUV) flux, the solar driver that influences O^+ outflow during a geomagnetic storm is probably CMEs, despite that the X-flares with long wavelength (0.1–0.08 nm) ionize the neutral atmosphere all the way down to approximately 95 km (Rees, 1989; Tsurutani et al., 2005). In comparison, the Halloween event that occurred 28–30 October 2003 had stronger X-flares (X17.2 [28 October] and X10.0 [29 October]) and Kp = 9_+, and Schillings et al. (2017) estimated a higher polar cap O^+ outflow than is observed for the September 2017 storm. Consequently, the ionization in the polar cap was higher and the X-flares could have influenced the ionization process (Tsurutani et al., 2005) such as a preheating of the ionosphere before

the CME hit the Earth. Yamauchi et al. (2018) wrote an overview of the ionospheric response to this storm with the European Incoherent Scatter radars. The authors showed that the electron density and temperature were enhanced after the detection of the X-flares. They also suggested that the increased ion temperature due to ion heating creates a precondition for O^+ upflow (upflow means that the ions are still gravitationally bound). This suggestion is strengthened by the increased F10.7 solar radio flux, which can be taken as a proxy of EUV flux, before and during the magnetic storm. In addition, Yau et al. (1988) found a clear correlation between O^+ outflow and Kp and F10.7. For low solar activity (F10.7 between 70 and 100 sfu) Yau et al. (1988) estimated the O^+ outflow to be a factor 4 lower than during high solar activity (F10.7 between 150 and 250 sfu). Cully et al. (2003) found a correlation between the total O^+ outflow and F10.7; higher O^+ outflow is observed for increasing F10.7. Despite that we do not have suitable Cluster data when the X-flares occurred, we conclude that the primary solar driver for O^+ outflow is probably ICMEs due to the clear influence seen in the Cluster data but X-flares might have a significant contribution in the heating process of the ionosphere (Yamauchi et al., 2018) and in causing additional ionization.

5.2. Escaping O^+ During the 7–8 September 2017 Geomagnetic Storm

We estimated the scaled O^+ outflow in the northern polar cap and cusp region during the main phase of the storm. Figure 5 shows the polar cap and cusps before and after the second CME shock (see section 4). We observed an enhancement of a factor 3 for the polar cap and a factor 2 for the cusp after the shock signature. This weak enhancement is comparable with the lowest relative scaled O^+ outflow enhancement for intense geomagnetic storms presented by Schillings et al. (2017), who found that the scaled O^+ outflow increases by 1 to 2 orders of magnitude during intense storm conditions compared to quiet magnetospheric conditions. However, the absolute value of the scaled O^+ outflow ($\sim 10^{13}$ m^{-2} s^{-1}) is quite high compared to similar storms studied in Schillings et al. (2017). We suggest that this unusual high-scaled O^+ outflow is due to the already compressed magnetosphere as a consequence of the first shock approximately 24 hr earlier. Moreover, before the second shock signature (7 September, 23:30 UT) the predicted Kp index was 3 and after the shock, Kp = 8, thus according to Slapak et al. (2017) and their Figure 5, the increase in the scaled O^+ should be around 1 order of magnitude. Our lower result could be explained by the difference in the studied regions (polar cap compared to plasma mantle/magnetosheath for Slapak et al., 2017). This increase in the unusually high O^+ outflow was observed within roughly 40 min, which is fast for a magnetospheric response. The quick response and lower relative enhancement in the O^+ outflow could be explained by the first shock, which already initiated a geomagnetic storm.

Schillings et al. (2017) could not confirm that the enhanced scaled O^+ outflow in the polar cap during the storm was escaping and lost into the interplanetary space. However, for the September 2017 storm, we studied and could compare the scaled O^+ outflow in two regions, the polar cap and the cusp. For these two regions, we looked at the perpendicular and parallel component of the temperature and the outflow parallel and perpendicular bulk velocity. Figure 6 shows that before the second CME shock, the perpendicular temperature in the polar cap 1 (blue, left side of Cut 1) is lower than after polar cap 2 (red, left side of Cut 2). This means that the ions in the polar cap have been heated and accelerated (Nilsson et al., 2006) after the shock passage. In both cusp regions, the perpendicular temperature remains more or less the same but is higher than in the polar cap. Consequently, despite a significantly high perpendicular bulk velocity, we observed ions with higher energy and parallel bulk velocity (not shown) in the cusp with sufficient energy to escape into the solar wind. This result confirms what Schillings et al. (2017) expected but could not claim.

In the Southern Hemisphere, the perpendicular temperature and the scaled O^+ outflow in the four identified polar cap and plasma mantle regions (1–4) are constant, despite that the parallel velocity is decreasing as Cluster moves tailward. This result suggests that an enhancement is still observed during the recovery phase, and in addition the local heating of O^+ is still significant as indicated by the unexpectedly high parallel temperature. Furthermore, the perpendicular bulk velocity is not negligible and the strong convection might drive the ions to the plasma sheet earthward of the X-line. In opposite, some ions experience enough heating/acceleration to end up behind the X-line and therefore be lost in the tail. The fate of these O^+ ions is less predictable than in the Northern Hemisphere. Finally, during the first 3 hr of the recovery phase, the Kp index was 5; hence, these observations also confirm the dependence of O^+ outflow on Kp (Slapak et al., 2017).

5.3. How Does Outflowing O^+ Relate to Space Weather Effects?

The space weather affects not only the O^+ outflow but the magnetosphere as a whole. Space weather influences the occurrence of substorms, the lifetime of the ring current, the density of the plasma sheet, and the

occurrence of bursty bulk flows (BBFs) and finally the energy conversion through mass loading in the cusp. Substorms do not always happen during geomagnetic storms, and therefore, a storm does not necessarily include substorms (Hori, 2006; Kamide et al., 1998). At a substorm onset, Nosé et al. (2005) found that the O^+/H^+ energy density ratio increases. During substorm growth phase, energetic O^+ (tens of kiloelectron volts), which mainly originate from the dayside polar region (Nakayama et al., 2017), play an important role in feeding the ring current. The lifetime of the ring current is therefore prolonged by the addition of energy by dominant O^+ under disturbed magnetospheric conditions, which have also lower charge-exchange cross sections than the H^+ ions, resulting in a slower loss (Denton et al., 2017; Hori, 2006).

Another aspect is the transport of O^+ into the plasma sheet. Mouikis et al. (2010) looked at the ion composition changes in the plasma sheet associated with geomagnetic and solar activity and found a strong influence on O^+ density. Under strong geomagnetic activity, part of the O^+ outflow is transported through the magnetotail and fed to the plasma sheet (Kistler et al., 2010). These ions can be seen in BBFs. However, Nilsson et al. (2016) showed that O^+ is less accelerated during BBFs than the dominating protons. Finally, high O^+ escape into the inflow solar wind plasma leads to a high mass loading rate and high extraction rate of the solar wind kinetic energy to the ionosphere in a limited and small region at high latitudes (Yamauchi & Slapak, 2018). Therefore, we expect ground-induced currents at much higher latitudes than normal. Since human activity is expanding to the polar region, such as arctic sea routes, this can become important.

The O^+ escape itself is not hazardous to human activity. However, enhanced O^+ escape rate can be observed at the same time as other space weather effects for example satellite drag. The expansion of the neutral atmosphere in the thermosphere and extreme enhancements of the ion escape can be linked because both occur when there is stronger energy input into the atmosphere during extreme geomagnetic storms. When Kp and EUV flux vary, the neutral temperature above the thermopause fluctuates (Chandra & Krishnamurthy, 1967). The variation of EUV flux heats the upper atmosphere through ion-neutral collisions, which tend to expand the thermosphere (Rees, 1989) and thus increase the atmospheric density at higher altitudes. Therefore, high EUV flux (or the proxy F10.7 cm flux > 250 solar units flux) and Kp (>6) values result in extreme short-term increases in satellite drag, particularly for satellites on low Earth orbit. These parameters are used in satellite drag models (Bowman et al., 2008; Storz et al., 2005). Tsurutani et al. (2007) reported, for the Halloween event, ion-neutral drag due to quick upward motion of O^+ that causes upward neutral oxygen (O) at equatorial latitudes. Similarly, Lakhina and Tsurutani (2017) generalized the ion-neutral drag for oxygen for 1859-type (Carrington) superstorms. The O^+ outflow (higher latitudes) could have an impact on this ion-neutral drag.

The cusp plays a significant role in the ion outflow as well as for the satellite drag (Lühr et al., 2004). Lühr et al. (2004) studied the enhancement of the air density for moderate geomagnetic activity (~Kp 3) over the cusp with the CHAMP satellite. They concluded that these enhancements of air density are accompanied by small-scale structures such as field-aligned currents filaments and suggested the Joule heating as the primary source for the upward movement of the air. This air upwelling over the cusp at low altitude become mostly, due to several chemical reactions, O^+ ions in the F region of the ionosphere. Furthermore, Masutti (2017) studied the thermosphere during this storm with the QB50 mission (CubeSats) and observed an orbit decay of roughly 2 km during the September storm. Thus, the size or area, the current system, or its equatorward motion under extreme conditions is important for the accuracy of satellite drag models. This speculative approach needs further investigations that were beyond the scope of this study. However, we do believe that stronger O^+ escape indicates an expansion of the thermosphere and could be strongly connected to increased satellite drag.

6. Conclusions

In this paper, we studied the consequences of the space weather on the O^+ outflow at Earth. We investigated the 4–9 September 2017 storm from the Sun down to the ionosphere. At the beginning of September, several X-flares and two CMEs were detected, which produced a severe geomagnetic storm (Kp $\simeq$ 8 and Dst = −142 nT). The first CME carried northward IMF, and the associated shock initiated a SSC at Earth followed by the initial phase of a geomagnetic storm. A second shock, driven by a CME with southward IMF, hit the magnetosphere 24 hr later and caused an equatorward motion of the cusp, which was observed by Cluster satellite 4 in the Northern Hemisphere. The ionospheric O^+ outflow was estimated in the polar cap and cusp before and after the second shock, which initiated the main phase of the storm. The ionospheric O^+ outflow increased after the passage of the second shock by a factor 3 in the polar cap and a factor 2 in the

cusp. However, the relative enhancement of the O^+ outflow was lower than expected compared to Schillings et al. (2017); nevertheless, the initial value of O^+ outflow (before the shock) for the regions of observation was high $\sim 10^{13}$ m^{-2} s^{-1}. The unusually high ionospheric O^+ outflow was probably due to an enhancement after the first shock and a preheating of the ionosphere by the EUV flux due to the X-flares in the previous days (Yamauchi et al., 2018). Therefore, the second shock did not increase O^+ outflow during the main phase as much as previous studies would have led us to believe (Schillings et al., 2017), but the heated O^+ had enough velocity to escape directly into the solar wind. On 8 September, the magnetosphere started to recover from the massive injection of energy from the solar wind. During this phase, Cluster was moving tailward in the Southern Hemisphere and we observed local heating of the ionospheric O^+ outflow indicated by high parallel temperature and strong convection as seen in the perpendicular component of the velocity. The fate of the O^+ is therefore less predictable. Furthermore, observations were made in the plasma sheet on 9 September; the O^+ flux estimated is consistent with the average flux calculated by Slapak et al. (2017).

The observation of escaping O^+ during geomagnetic storms caused by CMEs and X-flares also shows that the neutral atmosphere could be ionized sufficiently to expand the neutral thermosphere and lead to significant satellite drag effects. Satellite drag models take into account the geomagnetic activity and the EUV flux (Bowman et al., 2008; Storz et al., 2005), and the higher these parameters are, the more impact they have on satellite drag. A similar Kp and EUV flux relation was also observed with O^+ escape (Cully et al., 2003; Slapak et al., 2017; Yau et al., 1988), and therefore, we suggest that higher O^+ outflow indirectly indicates stronger satellite drag. Our finding can be summarized as follows:

1. In the polar cap and cusp, we observed an increase in the ionospheric O^+ outflow by a factor 3 and 2, respectively, after the passage of a shock associated with the second CME. These ions will eventually escape into interplanetary space.
2. The increase in the O^+ outflow is not extremely high; however, the magnetosphere response to the second CME is fast ($\sim$40 min).
3. During the recovery phase, local heating and strong convection are observed in the plasma mantle as seen, respectively, in extremely high parallel component of the temperature and high perpendicular velocity.
4. The upper limit of the ionospheric O^+ outflow (Northern Hemisphere) is 6.3×10^{13} and 1×10^{14} m^{-2} s^{-1} in the polar cap and cusp, respectively.
5. The solar drivers for O^+ outflow seem to be mostly ICMEs, whereas X-flares might have a significant contribution in the earlier preheating (Yamauchi et al., 2018) and ionization of the neutral atmosphere.

References

Andre, M., Crew, G. B., Peterson, W. K., Persoon, A. M., & Pollock, C. J. (1990). Ion heating by broadband low-frequency waves in the cusp/cleft. *Journal of Geophysical Research*, 95, 20,809–20,823. https://doi.org/10.1029/JA095iA12p20809

Balch, C., Murtagh, B., Zezula, D., Combs, L., Nelson, G., Tegnell, K., et al. (2004). *Service assessment: Intense space weather storms October 19–November 07, 2003* (Tech. Rep.). U.S. Department of Commerce: NOAA.

Balogh, A., Carr, C. M., Acuña, M. H., Dunlop, M. W., Beek, T. J., Brown, P., et al. (2001). The Cluster magnetic field investigation: Overview of in-flight performance and initial results. *Annales Geophysicae*, 19, 1207–1217. https://doi.org/10.5194/angeo-19-1207-2001

Bartels, J., Heck, N. H., & Johnston, H. F. (1939). The three-hour-range index measuring geomagnetic activity. *Terrestrial Magnetism and Atmospheric Electricity*, 44(4), 411–454. https://doi.org/10.1029/TE044i004p00411

Bouhram, M., Klecker, B., Paschmann, G., Haaland, S., Hasegawa, H., Blagau, A., et al. (2005). Survey of energetic O^+ ions near the dayside mid-latitude magnetopause with Cluster. *Annales Geophysicae*, 23, 1281–1294. https://doi.org/10.5194/angeo-23-1281-2005

Bowman, B., Tobiska, W. K., Marcos, F., Huang, C., Lin, C., & Burke, W. (2008). A new empirical thermospheric density model JB2008 using new solar and geomagnetic indices. In *American Institute of Aeronautics and Astronautics, Astrodynamics Specialist Conference 18-21 August 2008, Honolulu, Hawaii*. https://doi.org/10.2514/6.2008-6438

Chandra, S., & Krishnamurthy, B. V. (1967). The response of the upper atmospheric temperature to changes in solar EUV radiation and geomagnetic activity (Tech. Rep. 19680000890). Greenbelt, MD: NASA Goddard Space Flight Center.

Chappell, C. R., Moore, T. E., & Waite, J. H. Jr. (1987). The ionosphere as a fully adequate source of plasma for the Earth's magnetosphere. *Journal of Geophysical Research*, 92, 5896–5910. https://doi.org/10.1029/JA092iA06p05896

Cully, C. M., Donovan, E. F., Yau, A. W., & Arkos, G. G. (2003). Akebono/Suprathermal Mass Spectrometer observations of low-energy ion outflow: Dependence on magnetic activity and solar wind conditions. *Journal of Geophysical Research*, 108, 1093. https://doi.org/10.1029/2001JA009200

Dandouras, I. S., Rème, H., Cao, J., & Escoubet, P. (2009). Magnetosphere response to the 2005 and 2006 extreme solar events as observed by the Cluster and Double Star spacecraft. *Advances in Space Research*, 43(4), 618–623. https://doi.org/10.1016/j.asr.2008.10.015

Denton, M. H., Thomsen, M. F., Reeves, G. D., Larsen, B. A., Henderson, M. G., Jordanova, V. K., et al. (2017). The evolution of the plasma sheet ion composition: Storms and recoveries. *Journal of Geophysical Research: Space Physics*, 122, 12,040–12,054. https://doi.org/10.1002/2017JA024475

Escoubet, C. P., Fehringer, M., & Goldstein, M. (2001). Introduction: The Cluster mission. *Annales Geophysicae*, 19, 1197–1200. https://doi.org/10.5194/angeo-19-1197-2001

Gopalswamy, N., Barbieri, L., Cliver, E. W., Lu, G., Plunkett, S. P., & Skoug, R. M. (2005). Introduction to violent Sun-Earth connection events of October–November 2003. *Journal of Geophysical Research*, 110, A09S00. https://doi.org/10.1029/2005JA011268

Haaland, S., Eriksson, A., Engwall, E., Lybekk, B., Nilsson, H., et al. (2012). N. Østgaard Estimating the capture and loss of cold plasma from ionospheric outflow. *Journal of Geophysical Research*, 117, A07311. https://doi.org/10.1029/2012JA017679

Hori, T. (2006). Storm-substorm relationship: Controversies and recent development, solar terrestrial (ST). *Advances in Geosciences*, 8, 47–67.

Kamide, Y., Baumjohann, W., Daglis, I. A., Gonzalez, W. D., Grande, M., Joselyn, J. A., et al. (1998). Current understanding of magnetic storms: Storm-substorm relationships. *Journal of Geophysical Research*, 103, 17,705–17,728. https://doi.org/10.1029/98JA01426

Kistler, L. M., Mouikis, C. G., Cao, X., Frey, H., Klecker, B., Dandouras, I., et al. (2006). Ion composition and pressure changes in storm time and nonstorm substorms in the vicinity of the near-Earth neutral line. *Journal of Geophysical Research*, 111, A11222. https://doi.org/10.1029/2006JA011939

Kistler, L. M., Mouikis, C. G., & Genestreti, K. J. (2013). In-flight calibration of the Cluster/CODIF sensor, geoscientific instrumentation. *Methods and Data Systems*, 2(2), 225–235. https://doi.org/10.5194/gi-2-225-2013

Kistler, L. M., Mouikis, C. G., Klecker, B., & Dandouras, I. (2010). Cusp as a source for oxygen in the plasma sheet during geomagnetic storms. *Journal of Geophysical Research*, 115, A03209. https://doi.org/10.1029/2009JA014838

Kronberg, E. A., Ashour-Abdalla, M., Dandouras, I., Delcourt, D. C., Grigorenko, E. E., Kistler, L. M., et al. (2014). Circulation of heavy ions and their dynamical effects in the magnetosphere: Recent observations and models. *Space Science Reviews*, 184, 173–235. https://doi.org/10.1007/s11214-014-0104-0

Lakhina, G. S., & Tsurutani, B. T. (2017). Satellite drag effects due to uplifted oxygen neutrals during super magnetic storms. *Nonlinear Processes in Geophysics*, 24(4), 745–750. https://doi.org/10.5194/npg-24-745-2017

Lennartsson, O. W., Collin, H. L., & Peterson, W. K. (2004). Solar wind control of Earth's H^+ and O^+ outflow rates in the 15-eV to 33-keV energy range. *Journal of Geophysical Research*, 109, A12212. https://doi.org/10.1029/2004JA010690

Lühr, H., Rother, M., Köhler, W., Ritter, P., & Grunwaldt, L. (2004). Thermospheric up-welling in the cusp region: Evidence from CHAMP observations. *Geophysical Research Letters*, 31, L06805. https://doi.org/10.1029/2003GL019314

Maes, L., Maggiolo, R., De Keyser, J., Dandouras, I., Fear, R. C., Fontaine, D., & Haaland, S. (2015). Solar illumination control of ionospheric outflow above polar cap arcs. *Geophysical Research Letters*, 42, 1304–1311. https://doi.org/10.1002/2014GL062972

Masutti, D. (2017). *Lessons learned from the first educational CubeSat Constellation Presentation at ESWW14*. Belgium: Oostende.

Mayaud, P. N. (1980). *Derivation, meaning, and use of geomagnetic indices, Geophysical Monograph Series* (Vol. 22). Washington DC: American Geophysical Union. https://doi.org/10.1029/GM022

Moore, T. E., Chappell, C. R., Chandler, M. O., Craven, P. D., Giles, B. L., Pollock, C. J., et al. (1997). High-altitude observations of the polar wind. *Science*, 277, 349–351. https://doi.org/10.1126/science.277.5324.349

Moore, T. E., & Horwitz, J. L. (2007). Stellar ablation of planetary atmospheres. *Reviews of Geophysics*, 45, RG3002. https://doi.org/10.1029/2005RG000194

Mouikis, C. G., Kistler, L. M., Liu, Y. H., Klecker, B., Korth, A., & Dandouras, I. (2010). H^+ and O^+ content of the plasma sheet at 15–19 Re as a function of geomagnetic and solar activity. *Journal of Geophysical Research*, 115, A00J16. https://doi.org/10.1029/2010JA015978

Nakayama, Y., Ebihara, Y., Fok, M. C., & Tanaka, T. (2017). Impact of substorm time O^+ outflow on ring current enhancement. *Journal of Geophysical Research: Space Physics*, 122, 6304–6317. https://doi.org/10.1002/2016JA023766

Newell, P. T., & Meng, C.-I. (1994). Ionospheric projections of magnetospheric regions under low and high solar wind pressure conditions. *Journal of Geophysical Research*, 99, 273–286. https://doi.org/10.1029/93JA02273

Newell, P. T., Meng, C.-I., Sibeck, D. G., & Lepping, R. (1989). Some low-altitude cusp dependencies on the interplanetary magnetic field. *Journal of Geophysical Research*, 94, 8921–8927. https://doi.org/10.1029/JA094iA07p08921

Nilsson, H. (2011). *Heavy ion energization, transport, and loss in the Earth's magnetosphere* (pp. 315–327). Dordrecht, Netherlands: Springer.

Nilsson, H., Barghouthi, I. A., Slapak, R., Eriksson, A. I., & André, M. (2012). Hot and cold ion outflow: Spatial distribution of ion heating. *Journal of Geophysical Research*, 117, A11201. https://doi.org/10.1029/2012JA017974

Nilsson, H., Hamrin, M., Pitkänen, T., Karlsson, T., Slapak, R., Andersson, L., et al. (2016). Oxygen ion response to proton bursty bulk flows. *Journal of Geophysical Research: Space Physics*, 121, 7535–7546. https://doi.org/10.1002/2016JA022498

Nilsson, H., Waara, M., Arvelius, S., Marghitu, O., Bouhram, M., Hobara, Y., et al. (2006). Characteristics of high altitude oxygen ion energization and outflow as observed by Cluster: A statistical study. *Annales Geophysicae*, 24, 1099–1112. https://doi.org/10.5194/angeo-24-1099-2006

Norqvist, P., André, M., Eliasson, L., Eriksson, A. I., Blomberg, L., Lühr, H., et al. (1996). Ion cyclotron heating in the dayside magnetosphere. *Journal of Geophysical Research*, 101, 13,179–13,194. https://doi.org/10.1029/95JA03596

Nosé, M, Taguchi, S., Hosokawa, K., Christon, S. P., McEntire, R. W., Moore, T. E., et al. (2005). Overwhelming O^+ contribution to the plasma sheet energy density during the October 2003 superstorm: Geotail/EPIC and IMAGE/LENA observations. *Journal of Geophysical Research*, 110, a09S24. https://doi.org/10.1029/2004JA010930

Pesnell, W. D., Thompson, B. J., & Chamberlin, P. C. (2012). The Solar Dynamics Observatory (SDO). *Solar Physics*, 275(1), 3–15. https://doi.org/10.1007/s11207-011-9841-3

Rees, M. H (1989). *Physics and Chemistry of the Upper Atmosphere (Cambridge Atmospheric and Space Science Series)*. Cambridge: Cambridge University Press. https://doi.org/10.1017/CBO9780511573118

Rème, H., Aoustin, C., Bosqued, J. M., Dandouras, I., Lavraud, B., Sauvaud, J. A., et al. (2001). First multispacecraft ion measurements in and near the Earth's magnetosphere with the identical Cluster ion spectrometry (CIS) experiment. *Annales Geophysicae*, 19, 1303–1354. https://doi.org/10.5194/angeo-19-1303-2001

Robbrecht, E., Berghmans, D., & Van der Linden, R. A. M. (2009). Automated LASCO CME catalog for solar cycle 23: Are CMEs scale invariant? *Astrophysical Journal*, 691, 1222–1234. https://doi.org/10.1088/0004-637X/691/2/1222

Rosenqvist, L., Opgenoorth, H., Buchert, S., McCrea, I., Amm, O., & Lathuillere, C. (2005). Extreme solar-terrestrial events of October 2003: High-latitude and Cluster observations of the large geomagnetic disturbances on 30 October. *Journal of Geophysical Research*, 110, A09S23. https://doi.org/10.1029/2004JA010927

Schillings, A., Nilsson, H., Slapak, R., Yamauchi, M., & Westerberg, L.-G. (2017). Relative outflow enhancements during major geomagnetic storms—Cluster observations. *Annales Geophysicae*, 35(6), 1341–1352. https://doi.org/10.5194/angeo-35-1341-2017

Shelley, E. G., Peterson, W. K., Ghielmetti, A. G., & Geiss, J. (1982). The polar ionosphere as a source of energetic magnetospheric plasma. *Geophysical Research Letters*, 9, 941–944. https://doi.org/10.1029/GL009i009p00941

Slapak, R., Hamrin, M., Pitkänen, T., Yamauchi, M., Nilsson, H., Karlsson, T., et al. (2017). Quantification of the total ion transport in the near-Earth plasma sheet. *Annales Geophysicae*, 35(4), 869–877. https://doi.org/10.5194/angeo-35-869-2017

Slapak, R., Nilsson, H., Waara, M., André, M., Stenberg, G., & Barghouthi, I. A. (2011). O^+ heating associated with strong wave activity in the high altitude cusp and mantle. *Annales Geophysicae*, 29, 931–944. https://doi.org/10.5194/angeo-29-931-2011

Slapak, R., Nilsson, H., & Westerberg, L. G. (2013). A statistical study on O^+ flux in the dayside magnetosheath. *Annales Geophysicae*, 31, 1005–1010. https://doi.org/10.5194/angeo-31-1005-2013

Slapak, R., Schillings, A., Nilsson, H., Yamauchi, M., Westerberg, L.-G., & Dandouras, I. (2017). Atmospheric loss from the dayside open polar region and its dependence on geomagnetic activity: Implications for atmospheric escape on evolutionary timescales. *Annales Geophysicae*, *35*, 721–731.

Storz, M. F., Bowman, B. R., Branson, M. J. I., Casali, S. J., & Tobiska, W. K. (2005). High Accuracy Satellite Drag Model (HASDM). *Advances in Space Research*, *36*(12), 2497–2505. https://doi.org/10.1016/j.asr.2004.02.020

Strangeway, R. J., Ergun, R. E., Su, Y., Carlson, C. W., & Elphic, R. C. (2005). Factors controlling ionospheric outflows as observed at intermediate altitudes. *Journal of Geophysical Research*, *110*, A03221. https://doi.org/10.1029/2004JA010829

Tsurutani, B. T., Judge, D. L., Guarnieri, F. L., Gangopadhyay, P., Jones, A. R., Nuttall, J., et al. (2005). The October 28, 2003 extreme EUV solar flare and resultant extreme ionospheric effects: Comparison to other halloween events and the bastille day event. *Geophysical Research Letters*, *32*, L03S09. https://doi.org/10.1029/2004GL021475

Tsurutani, B. T., Verkhoglyadova, O. P., Mannucci, A. J., Araki, T., Sato, A., Tsuda, T., et al. (2007). Oxygen ion uplift and satellite drag effects during the 30 October 2003 daytime superfountain event. *Annales Geophysicae*, *25*(3), 569–574. https://doi.org/10.5194/angeo-25-569-2007

Tsyganenko, N. A., & Sitnov, M. I. (2005). Modeling the dynamics of the inner magnetosphere during strong geomagnetic storms. *Journal of Geophysical Research*, *110*, A03208. https://doi.org/10.1029/2004JA010798

Waara, M., Slapak, R., Nilsson, H., Stenberg, G., André, M., & Barghouthi, I. A. (2011). Statistical evidence for O^+ energization and outflow caused by wave-particle interaction in the high altitude cusp and mantle. *Annales Geophysicae*, *29*, 945–954. https://doi.org/10.5194/angeo-29-945-2011

Wintoft, P., Wik, M., Matzka, J., & Shprits, Y. (2017). Forecasting Kp from solar wind data: Input parameter study using 3-hour averages and 3-hour range values. *Journal Space Weather Space Climate*, *7*, A29. https://doi.org/10.1051/swsc/2017027

Yamauchi, M., Iyemori, T., Frey, H., & Henderson, M. (2006). Unusually quick development of a 4000 nt substorm during the initial 10 min of the 29 October 2003 magnetic storm. *Journal of Geophysical Research*, *111*, a04217. https://doi.org/10.1029/2005JA011285

Yamauchi, M., Sergienko, T., Enell, C. F., Schillings, A., Slapak, R., Johnsen, M. G., et al. (2018). Ionospheric response observed by EISCAT during the September 6–8, 2017 space weather event: Overview. *Space Weather*, *16*. https://doi.org/10.1029/2018SW001937

Yamauchi, M., & Slapak, R. (2018). Energy conversion through mass loading of escaping ionospheric ions for different Kp values. *Annales Geophysicae*, *36*(1), 1–12. https://doi.org/10.5194/angeo-36-1-2018

Yau, A. W., Peterson, W. K., & Shelley, E. G. (1988). *Quantitative parametrization of energetic ionospheric ion outflow*, *Geophysical Monograph Series* (Vol. 44, pp. 211–217). Washington DC: American Geophysical Union. https://doi.org/10.1029/GM044p0211

Zhang, J., Richardson, I. G., Webb, D. F., Gopalswamy, N., Huttunen, E., Kasper, J. C., et al. (2007). Solar and interplanetary sources of major geomagnetic storms (Dst ≤ -100 nT) during 1996–2005. *Journal of Geophysical Research*, *112*, A10102. https://doi.org/10.1029/2007JA012321

PAPER IV

Earth atmospheric loss through the plasma mantle and its dependence on solar wind parameters

Authors:
A. Schillings, R. Slapak, H. Nilsson, M. Yamauchi, I. Dandouras and L.-G. Westerberg

○ Earth, Planets and Space

FULL PAPER

Earth atmospheric loss through the plasma mantle and its dependence on solar wind parameters

Audrey Schillings[1,2]* ○, Rikard Slapak[3], Hans Nilsson[1,2], Masatoshi Yamauchi[1], Iannis Dandouras[4] and Lars-Göran Westerberg[5]

Abstract

Atmospheric loss and ion outflow play an important role in the magnetospheric dynamics and in the evolution of the atmosphere on geological timescales—an evolution which is also dependent on the solar activity. In this paper, we investigate the total O^+ outflow $[s^{-1}]$ through the plasma mantle and its dependency on several solar wind parameters. The oxygen ion data come from the CODIF instrument on board the spacecraft Cluster 4 and solar wind data from the OMNIWeb database for a period of 5 years (2001–2005). We study the distribution of the dynamic pressure and the interplanetary magnetic field for time periods with available O^+ observations in the plasma mantle. We then divided the data into suitably sized intervals. Additionally, we analyse the extreme ultraviolet radiation (EUV) data from the TIMED mission. We estimate the O^+ escape rate [ions/s] as a function of the solar wind dynamic pressure, the interplanetary magnetic field (IMF) and EUV. Our analysis shows that the O^+ escape rate in the plasma mantle increases with increased solar wind dynamic pressure. Consistently, it was found that the southward IMF also plays an important role in the O^+ escape rate in contrast to the EUV flux which does not have a significant influence for the plasma mantle region. Finally, the relation between the O^+ escape rate and the solar wind energy transferred into the magnetosphere shows a nonlinear response. The O^+ escape rate starts increasing with an energy input of approximately 10^{11}W.

Keywords: O^+ outflow/escape, Plasma mantle, Solar wind, Interplanetary magnetic field (IMF), Extreme ultraviolet (EUV), Coupling functions

Introduction

The Sun plays an important role in terrestrial atmospheric loss. It is believed that billions of years ago, the Sun was more active than today. Enhanced particle fluxes and solar radiation affected the planetary environment and may have led to significant atmospheric losses (Güdel 2007). Thus, the Earth's atmospheric loss is an important phenomenon which may affect the evolution of the atmosphere on geological timescales. This terrestrial phenomenon is driven, at lower altitudes (∼ 2 Earth radius [Re]), by atmospheric ions energised to a few eV and photoelectrons called the

polar wind (Axford 1968; Nagai et al. 1984; Green and Waite 1985; Chappell et al. 1987; Chandler et al. 1991; Yau et al. 2007). At higher altitudes (> 2Re), highly energised—up to a few keV—heavy ions, such as oxygen ions (O^+), are flowing upward (Shelley et al. 1982). Those O^+ ions are heated through different processes, such as field-aligned currents (Maggiolo et al. 2006) at lower altitudes or perpendicular heating via wave–particle interactions (Bouhram et al. 2004b; Slapak et al. 2011; Waara et al. 2011; Nilsson et al. 2012) at higher altitudes. Once the upward moving ions have sufficient energy to escape the gravity, they become ion outflow. The latter are further accelerated under the curvature of the magnetic field lines, called centrifugal acceleration (Nilsson et al. 2008, 2010). The main regions where we observe outflowing ions are the open magnetic

---

*Correspondence: audrey.schillings@irf.se
[1] Swedish Institute of Space Physics, Kiruna, Sweden
Full list of author information is available at the end of the article

Schillings *et al. Earth, Planets and Space* (2019) 71:70

Page 2 of 13

field line regions: the polar cap, cusp and plasma mantle. The polar cap represents the mapping of the open field lines to the ionosphere, whereas the cusp is a funnel between the dayside closed magnetic field lines and the open magnetic field lines. This funnel provides a direct entry for magnetosheath plasma into the magnetosphere. The plasma mantle located downstream of the cusp has a mixed plasma population of ionospheric and magnetosheath ions. It is, however, dominated by solar wind ions conducted by the mirror force. In the part of the magnetotail, Wang et al. (2014b) found that the plasma mantle is characterised by similar temperature as in the magnetosheath and lower density, namely ~ 0.05–0.2 keV and ~ 0.1–1 cm^{-3}. The area and size of the three regions are influenced by strong solar wind conditions, and it results in fluctuations of the penetrating solar wind. Several studies have been conducted in different magnetospheric regions to determine how the solar wind affects the O$^+$ outflow (e.g Palmroth et al. 2001; Abe et al. 1996; Denton and Taylor 2008; Gou et al. 2016).

The global low-energy ion outflow (dominated by H$^+$, not O$^+$) has been studied under one solar cycle by André et al. (2015). The authors found that during one solar cycle, the increasing extreme ultraviolet (EUV) radiations (F$_{10.7}$ a proxy for EUV flux) increase the outflow by a factor 2. They explained this enhancement by a higher density in the outflowing population and concluded that the available ionospheric ion density limits the outflow mechanism. Those low-energy ions can gain energy through solar illumination which changes the ionospheric scale height (Maes et al. 2015). However, according to Li et al. (2018) the energy transfer efficiency of the solar wind is 6–7 orders of magnitude higher than the energy originating from the solar illumination. Solar illumination of the polar cap is much affected by the tilt of the geomagnetic dipole. In another study, Li et al. (2017) studied this aspect combined with the F$_{10.7}$ flux and found that the cold ion outflow is strongly influenced by the dipole tilt angle and the EUV flux. In a similar way, Engwall et al. (2009) showed an increase in the cold ion outflow (up to 60 eV) with F$_{10.7}$ and concluded that EUV radiation mainly controls the low-energised ion density.

Some cold ions are further energised to become a hot plasma population observed in the cusp, and they are either accelerated further to the plasma mantle and escape directly into the magnetosheath (Slapak et al. 2013) or transported to the plasma sheet (Kronberg et al. 2014; Liao et al. 2015). The density of those energetic O$^+$ ions observed in the plasma sheet is strongly influenced by the geomagnetic (Kp) and solar (EUV) activity

(Mouikis et al. 2010; Maggiolo and Kistler 2014; Kistler and Mouikis 2016).

The O$^+$ outflow dependence on the interplanetary magnetic field (IMF) has been observed in the dayside magnetosheath and magnetopause regions (Slapak et al. 2012; Marcucci et al. 2004). However, in the high-altitude polar cap, Elliott et al. (2001) did not found any correlation between IMF and O$^+$ density in contrast to Lennartsson et al. (2004) who considered the same region but for O$^+$ outflow. The latter found that the total O$^+$ outflow rate was approximately three times higher for southward IMF (B$_z$ < 0) than for northward IMF. Despite all these studies on different solar wind parameters related to O$^+$ outflow, the plasma mantle has not been well analysed. The plasma mantle was well sampled by the Cluster mission and is suitable to study ions that are likely to escape from the magnetosphere. Thus, this study aims to answer how the O$^+$ escape rate from the plasma mantle depends on the solar wind dynamic pressure, IMF, EUV and solar wind energy input.

Instrumentation and data
For our data analysis, we used oxygen ion data provided by the Cluster mission (see "Cluster data" section) and solar wind data (see "Solar wind data" and "TIMED data" sections) in order to establish the correlation between O$^+$ flux and the solar wind.

Cluster data
The Cluster mission (Escoubet et al. 2001) was launched in 2000 and has collected magnetospheric data for more than 18 years. Four spacecrafts are flying in tetrahedral formation on a polar elliptical orbit and carry 11 identical instruments each. One of the instruments is the COmposition DIstribution Function (CODIF) included in the Cluster Ion Spectrometer (CIS) (Rème et al. 2001) that provides a 3-D distributions of ion data, with mass discrimination through a time-of-flight section. With this technique, it can measure H$^+$, He^{2+}, He$^+$ and O$^+$. CODIF has a 360° field of view, an energy coverage from 25 eV/q (per charge) up to 40 keV/q and an energy resolution of $\Delta E/E \sim 0.16$.

The magnetic field data were taken from the FluxGate Magnetometer (FGM) (Balogh et al. 2001). The instrument has a normal mode sample frequency of 22.4 Hz and operative ranges for different magnetic intensities from a few nT to several thousand of nT. However, we only used the averaged magnetic field over the spacecraft spin (4 sec).

Solar wind data
The solar wind data, such as velocity, density and interplanetary magnetic field (IMF), were retrieved from the

OMNIWeb online database. This NOAA/SWPC database is a collection of solar data from several satellites with various scientific objectives at diverse positions. The plasma parameters and IMF are provided by IMP8, Wind, Geotail and ACE. In our study, we used the high-resolution data, 5 min and 1 min, time-shifted to the Earth's bow shock.

TIMED data

The extreme ultraviolet (EUV) data are taken from the SEE instrument on board TIMED (Thermosphere, Ionosphere, Mesosphere Energetics and Dynamics) mission (Kusnierkiewicz 2003). TIMED was launched in December 2001 and has so far collected 17 years of data. It has a circular orbit with an inclination of $74.1°$ and an orbital period of 97 min and carries four sensors. One of these is the Solar EUV Experiment (SEE) (Woods et al. 2000) designed to measure and determine the rates of energy deposition, dissociation and ionisation of solar FUV (Far Ultraviolet), EUV and soft X-ray irradiance from 1 to 195 nm and with a 0.5-nm spectral resolution. The Sun is observed a few minutes (~ 3 min) during each orbit and an average value is determined, which gives 14–15 measurements per day.

Data set criteria

Our data set consists of 5 years of solar wind and Cluster data (from 2001 to 2005) and 4 years (as the mission started 1 year later) of EUV data (2002–2005). Our reason not to include more data is to focus on the oxygen data dependency on solar wind parameters without including a potential solar cycle dependency. The resolutions of the data for Cluster, solar wind and EUV are approximately 4 s, 1 min and 97 min, respectively, as well as a 0.5-nm spectral resolution for the wavelength of EUV irradiance.

In the Cluster data set, some of the O^+ counts might be false due to high flux proton contamination. Those ions typically originate from the intense magnetosheath fluxes, and they occur as a background in the O^+ mass channel. Such contamination typically leads to underestimated O^+ velocity moments. The false counts have a similar energy distribution as the protons, so for only false counts, the O^+ perpendicular bulk velocity will be 1/4 smaller than the proton velocity, and this can be used to identify cases with significant contamination; see Nilsson et al. (2006) for more details about the method. About 20% of data with significant background counts are removed from our data set. However, these data correspond mainly to magnetosheath data (which we do not want in our data set), and even if the percentage of removed data is high, this does not affect our O^+ occurrence rate in the plasma mantle (see "Method" section).

In order to analyse O^+ data from the plasma mantle, some conditions are consequently implemented to remove magnetosheath, cusp and polar cap data. The polar cap is usually associated with low-energy ions in contrast to the plasma mantle composed mainly of energetic solar particles, meaning these two regions can be distinguished by the ratio between the thermal pressure and the magnetic pressure called the plasma β. In the polar cap, plasma β is typically around 0.05 and consequently our constraint is $\beta > 0.1$ to avoid polar cap data (see e.g. Liao et al. 2010, 2015; Haaland et al. 2017). Moreover, several studies, such as Nilsson et al. (2006), Kistler et al. (2006), Slapak et al. (2017), have shown that the plasma sheet and plasma mantle populations have similar plasma β but can be distinguished by their density and temperature. Thus, we excluded the plasma sheet population by setting the proton perpendicular temperature to $T_\perp(H^+) < 1750$ eV. The density constraints are $n(H^+) > 10^{-3}$ cm^{-3} and $10^{-3} < n(O^+) < 100$ cm^{-3} to guarantee reliable bulk velocity estimates. The inner magnetosphere is removed by an arbitrary spatial constraint that still has a significant latitudinal and dawn–dusk coverage and defined in cylindrical coordinates as $R_{\text{GSM}} = \sqrt{Y_{\text{GSM}}^2 + Z_{\text{GSM}}^2} > 6 \, R_e$ and $-5 < X_{\text{GSM}} < 8 \, R_e$. To avoid cusp data, we set $v_\parallel(H^+) > 0$ because most of the proton outward flux is observed in the plasma mantle. In practice, $v_\parallel(H^+)$ is mostly positive, and thus, only a few observations are removed by this conditions. Magnetosheath data are removed by the cross-talk condition (false background counts). These conditions lead to a data set containing only plasma mantle data. Finally, we define the O^+ outflow in the plasma mantle as the local flux with an outward flux and therefore $v_\parallel(O^+) > 0$ km/s.

Data from some major geomagnetic storms are removed from our data set since they turn out to correspond to other magnetospheric regions than the plasma mantle (Schillings et al. 2017). Those events are 29 Oct 2003 (full day), 7 and 9 Nov 2004 (full days), 4 Dec 2003 (from 20:00 to 00:00 UT) and 13 Sep 2004 (from 20:00 to 00:00 UT).

Interpolation

The solar wind data provided by the OMNIWeb online database have 1-min resolution while Cluster data have 4 s. Therefore, two interpolations have been done on the solar wind data: The first one removes the values set at 999.999 in the database corresponding to *no measured values*, and the second one interpolates the solar wind data to the Cluster data points. The interpolations use a nearest neighbour interpolation
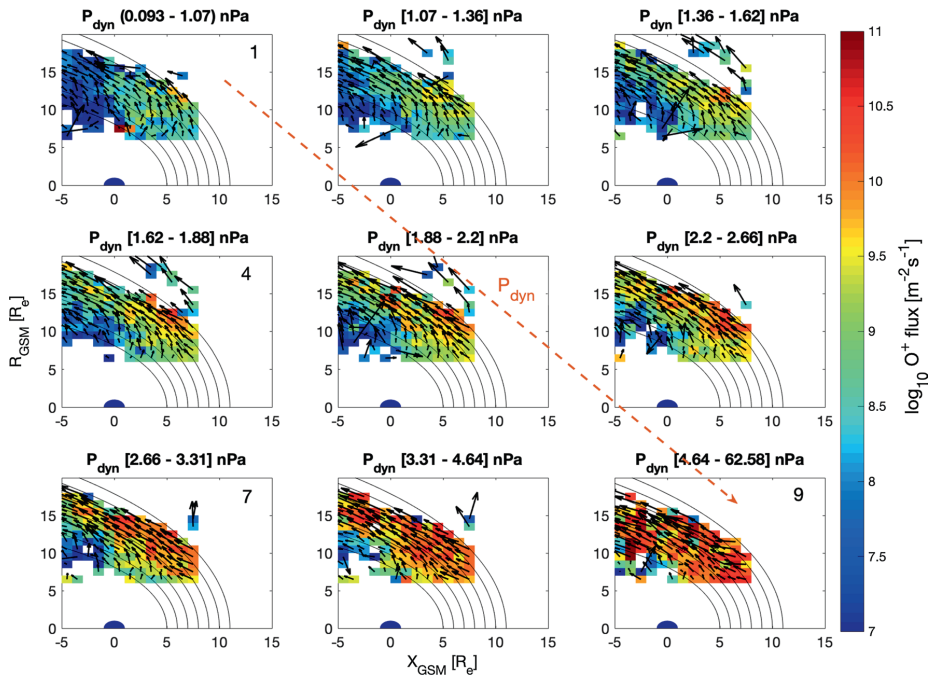
Fig. 1 Solar wind dynamic pressure subsets. O^+ flux (colour bar in $\log_{10} \mathrm{m}^{-2}\mathrm{s}^{-1}$) in the plasma mantle for 9 different solar wind dynamic pressure conditions numbered from 1 to 9 or, respectively, from the lowest to the highest dynamic pressure

technique. The same procedure is applied to the TIMED data for EUV.

Method

This section describes how we analysed the total O^+ escape $[\mathrm{s}^{-1}]$ from the plasma mantle under different solar wind conditions.

Solar wind dynamic pressure and interplanetary magnetic field

Based on previous studies of ion escape at Mars by Ramstad et al. (2015, 2017), we first looked at the solar wind velocity and density distributions. We divided these distributions into 9 solar wind subsets, with approximately the same amount of observations in each. The O^+ outflow (net outward flux) is calculated for the 9 subsets. However, analysis of these 9 subsets indicated that we could use the dynamic pressure instead. We therefore chose to not use exactly the same method as used for Mars, even though this was our original intention. It appears that the parameters and conditions to determine outflow at Earth or at Mars differ.

The solar wind dynamic pressure in Pa is given by

$$P_{\mathrm{dyn}} = m_{\mathrm{SW}} \cdot n_{\mathrm{SW}} \cdot v_{\mathrm{SW}}^2 \qquad (1)$$

where $m_{\mathrm{SW}} \cdot n_{\mathrm{SW}}$ is the solar wind mass density in $\mathrm{kg/m}^3$ and v_{SW} the solar wind velocity in m/s. We then divided P_{dyn} equally (approximately same amount of data points) in an increasing order to obtain 9 new solar wind subsets. Following the same method as Slapak et al. (2013, 2017), we estimated the O^+ flux (in the plasma mantle) for these 9 subsets shown in Fig. 1. In Fig. 1, the average O^+ fluxes is represented in 1 Re × 1 Re bins by the colour bar showing the O^+ flux in logarithmic scale. Note that the bins are only a representation of our data and are not used in the O^+ flux calculations (see Eq. 2 below). The small black arrows associated with the O^+ flux correspond to the average bulk velocity direction in each bin. The six black curves, referred to as *layer* hereafter, are magnetopause-like curves based on the Shue model (Shue et al. 1998) and are used to divide the plasma mantle region into layers. They contribute to the total escape flux estimate (see explanation below). Furthermore, the 9 subplots display the 9 P_{dyn} subsets from the lowest values (top left, number 1) to the highest P_{dyn} values (bottom right, number 9), also illustrated with an orange dashed arrow. The P_{dyn}

Schillings *et al. Earth, Planets and Space* (2019) 71:70

Page 5 of 13

intervals for each subset are given in the title of the subplots in nPa.

Afterwards, the total O^+ escape was calculated for the 9 P_{dyn} subsets. These steps are described below and summarised by Eq. 2.

First, for each layer i (or between two magnetopause-like segments), we defined the total escape flux $f_{esc,i}(O^+)$ $[s^{-1}]$ as the average O^+ flux $f_{mean,i}(O^+)$ $[m^{-2} s^{-1}]$ estimated in the layer times the layer area A_i. The area is given by $A_i = 0.59 \cdot \pi \cdot (r_{i+1}^2 - r_i^2)$ [Re] taken from Slapak et al. (2013) where the factor 0.59 comes from a 106° wide angle in the ZY_{GSE} plane containing most of the O^+ observations. Additionally, the first magnetopause-like segment is plotted at $r_1 = 5$ Re, so that $r_i = 4 + i$ [Re].

For the second step, we considered how often O^+ is observed in the layer ($N_i(O^+)$) compared to the total number of observations in the layer ($N_{tot,i}$). This parameter is called the occurrence rate and defined as $N_i(O^+)/N_{tot,i}$. The second step gave us the total escape O^+ flux for each layer $F_{esc,i}(O^+)$.

Finally, the third step was an addition of the layers as shown in the last line of Eq. 2 to obtain the total O^+ escape flux $F_{tot}(O^+)$ from the plasma mantle. Thus, we get $F_{tot}(O^+)$ for the 9 subplots corresponding to different solar wind dynamic pressure conditions.

$$\text{step 1: } f_{esc,i}(O^+) \quad [s^{-1}] = f_{mean,i}(O^+) \cdot A_i \quad (2a)$$

$$\text{step 2: } F_{esc,i}(O^+) \quad [s^{-1}] = f_{esc,i}(O^+) \cdot \frac{N_i(O^+)}{N_{tot,i}} \quad (2b)$$

$$\text{step 3: } F_{tot}(O^+) \quad [s^{-1}] = \sum_i F_{esc,i}(O^+) \quad (2c)$$

We also investigated the relation between the total O^+ escape rate and IMF through the clock angle given by $\theta = \arctan(|B_{Y,IMF}|/|B_{Z,IMF}|)$. A similar method was applied: division of the parameter in an increasing order and estimate of the total O^+ escape flux for the 9 subsets through the tree steps described above.

Solar wind coupling functions

Since the solar wind dynamic pressure contains only density and velocity and not IMF, we looked at solar wind coupling functions such as the epsilon or Akasofu parameter (Akasofu 1981) and a derivative of the epsilon parameter, the Vasyliunas et al. formula (Vasyliunas et al. 1982). Koskinen and Tanskanen (2002) give a physical review in a modern context and clarifications how to use the Akasofu parameter with correct units. They described ϵ as a rate of solar wind energy that empowers the magnetosphere. The Koskinen formula of the epsilon parameter in SI units reads

$$\epsilon \ [W] = \frac{4\pi}{\mu_0} \cdot v_{SW} \cdot B_T^2 \cdot \sin^4(\theta/2) \cdot l_0^2 \quad (3)$$

where $\mu_0 = 4\pi \times 10^{-7}$ [kg m/A^2 s^2] is the vacuum permeability, v_{SW} [m/s] is the solar wind velocity, $B_T = \sqrt{B_Y^2 + B_Z^2}$ [T] is the transverse IMF, θ [rad] is the clock angle and $l_0^2 = 49$ [R_e^2] is the effective area of the solar wind–magnetosphere interaction (Akasofu 1981). However, the epsilon parameter is usually used for geomagnetic storms and a few hours, not years of data (Finch and Lockwood 2007; Tenfjord and Østgaard 2013; Wang et al. 2014a).

Thus, we also implemented three variations of the Vasyliunas et al. formula. The original formula (Vasyliunas et al. 1982) describing the rate of solar wind energy that enters the magnetosphere is given by

$$\begin{aligned} P_\alpha \ [W] = M_E^{2/3} \cdot \mu_0^{(1/3-\alpha)} \cdot m_{SW}^{(2/3-\alpha)} \\ \cdot n_{SW}^{(2/3-\alpha)} \cdot v_{SW}^{(7/3-2\alpha)} |B|^{2\alpha} F(\theta) \end{aligned} \quad (4)$$

where $M_E = 8.06 \times 10^{22}$ [A/m^2] is the Earth's magnetic dipole moment, μ_0 the vacuum permeability, $m_{SW} \cdot n_{SW}$ [kg/m^3] the mass density, v_{SW} [m/s] the velocity, $|B|$ the IMF [T], $F(\theta)$ a function of the clock angle and finally α, a coupling function that can be found empirically. The function $F(\theta)$ is commonly defined as sinus of the clock angle and α has different values within the literature, e.g. Murayama (1982), Stamper et al. (1999), Finch and Lockwood (2007), Tenfjord and Østgaard (2013), Wang et al. (2014a). In our study, one variation of the Vasyliunas et al. formula is the original one (Eq. 4) with the coupling coefficient $\alpha = 0.3$ from Finch and Lockwood (2007). Note that we did not use the author's formula but only their α value (see Additional file 1 for more details). For the second variation, we used a coupling coefficient $\alpha = 0.5$ from Tenfjord and Østgaard (2013). The authors defined energy coupling functions for storms and long time series. In our study, we took their long time series formula (see Additional file 1: Eq. 1 for more details). The third variation was taken from Wang et al. (2014a), who made 240 simulations and found $\alpha = 0.43$ and $F(\theta) = \sin(\theta/2)^{2.7} + 0.25$. We also used the original authors equation (see Additional file 1: Eq. 3 for more details). As before, the coupling functions were divided in 9 approximately equal subsets (same amount of data points in each division) where we estimated the total O^+ escape rate. The four coupling functions and how O^+ escape depends on them were then investigated; see "Observations and results" section.

Extreme ultraviolet radiation

The EUV irradiance is provided by the SEE instrument on board TIMED (see "Instrumentation and data" section for more details). In this study, we used the observational average that consists of about 15 measurements

Schillings *et al. Earth, Planets and Space* (2019) 71:70

Page 6 of 13

per day. In these measurements, only the wavelengths absorbed by O^+ ($\lambda = 10–90$ nm) are of interests. The total EUV intensity I_{tot} including these wavelengths $I(\lambda)$ is calculated as

$$I_{tot} = \int I(\lambda)d\lambda \simeq \sum_{n=\lambda}^{\lambda_{end}} I(\lambda)\Delta\lambda \tag{5}$$

where $\Delta\lambda = 1$ [nm] is the bin of the wavelength. Afterwards, the total EUV intensity was interpolated on the Cluster data for the years 2002–2005. In order to look at the correlation between EUV and the total O^+ escape flux, the EUV intensity values were also sorted in increasing order and equally distributed in 9 subsets. Furthermore, the EUV intensity was divided in *Low EUV* and *High EUV* according to its mean value 0.0035 W/m^2.

Another way to express the EUV correlation with the total O^+ escape flux is to estimate the photoionisation flux (see "Discussion" section). The latter is defined by the EUV intensity $I(\lambda)$ divided by the photon energy E_γ as

$$F(\lambda) = \frac{I(\lambda)}{E_\gamma(\lambda)} \quad \text{with} \quad E_\gamma(\lambda) = \frac{hc}{\lambda}$$
$$F_{tot} = \int F(\lambda)d\lambda \simeq \sum_{n=\lambda}^{\lambda_{end}} F(\lambda)\Delta\lambda \tag{6}$$

where h and c are the Planck constant and speed of light, respectively. Like all others parameters, the photoionisation flux was equally distributed in 9 subsets for which we calculated the total O^+ escape flux.

Observations and results

We hereby present the correlation between the total O^+ escape flux and the solar wind parameters described in "Method" section.

Solar wind dynamic pressure and IMF

The solar wind density and velocity were first investigated individually; however, these two parameters can be coupled by taking the solar wind dynamic pressure P_{dyn} (see Eq. 1). After dividing P_{dyn} into 9 ascending subsets, Fig. 1 shows the O^+ outflow for each subset. An enhancement of approximately 1.5 order of magnitude is observed for the O^+ flux between the subsets of lowest and highest solar wind dynamic pressure. The O^+ outflow for the lowest P_{dyn}, first subset (Fig. 1, subplot nb. 1 top left) has an upper limit of 2.78×10^9 m^{-2} s^{-1} (with a minimum of 5% observations in the bin), whereas for the higher P_{dyn}, last subset (Fig. 1, subplot nb. 9 bottom right) we already see visually an enhancement of the O^+ outflow. The latter has an upper limit of 8.84×10^{10} m^{-2} s^{-1} (with a
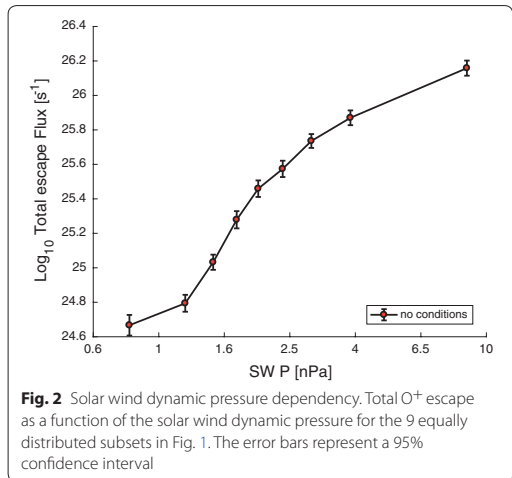

Fig. 2 Solar wind dynamic pressure dependency. Total O^+ escape as a function of the solar wind dynamic pressure for the 9 equally distributed subsets in Fig. 1. The error bars represent a 95% confidence interval

minimum of 5% observations in the bin). Afterwards, the total O^+ escape flux was estimated for the 9 P_{dyn} subsets and the tendency clearly shows a correlation between the O^+ outflow and P_{dyn} (Fig. 2). The error bars correspond to 95% confidence intervals and are estimated, for each subset (represented as black dots filled in red), from the average O^+ outflow per layer. As an example, the first dot representing the lowest P_{dyn} at $10^{24.6}$ s^{-1} in Fig. 2 contains the average O^+ outflow observations from the layers shown in Fig. 1, subplot 1. Thus, the 95% confidence interval for this subset is given by CI (95%) $= \sqrt{CI_{layer1}^2 + CI_{layer2}^2 + \cdots + CI_{layerN}^2}$, where $CI_{layer} = \frac{\sigma * 1.96}{\sqrt{N}}$ with σ the standard deviation of $\log_{10}$ (O^+ total flux) in the layer and N the number of O^+ observations in the layer. The same method is applied for the 8 P_{dyn} subsets left. As shown in Fig. 2, the total O^+ escape reaches 1.36×10^{26} s^{-1} for a dynamic pressure of 8.4 nPa. The enhancement of the total O^+ escape rate is about two orders of magnitude meaning that the larger the solar wind dynamic pressure is, the more ions would escape from the plasma mantle.

Furthermore, it is likely that the IMF direction will affect the ion outflow, possibly independent of the geomagnetic activity level (see Additional file 1: Fig. 1). Thus, we investigated O^+ escape for different IMF configurations represented by the clock angle (CA) θ for different dynamic pressure subsets as shown in Fig. 3a. The three dashed curves above the main black curve (labelled no conditions) are for southward IMF or CA $> 90°$. We observed that the more IMF turned southward (CA $> 150°$), the more ions are escaping (see dashed light blue curve). On the contrary, for strong northward
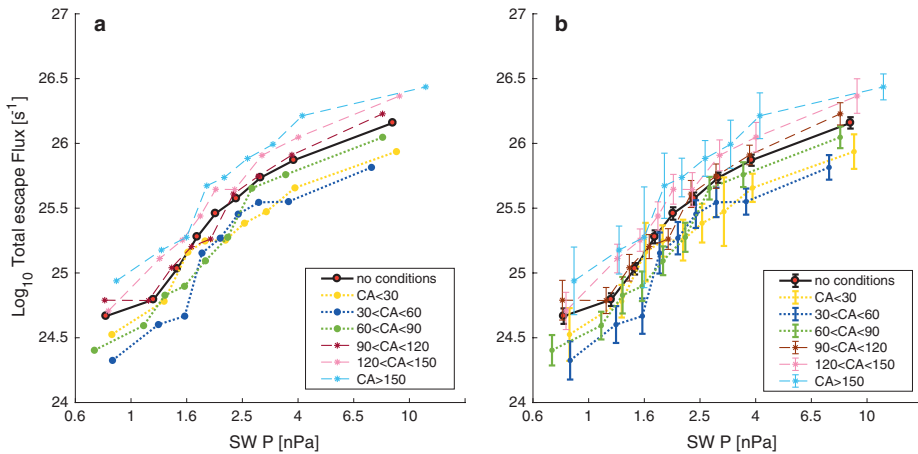
Schillings *et al. Earth, Planets and Space* (2019) 71:70

Page 7 of 13

Fig. 3 Interplanetary magnetic field dependency. **a** Total O$^+$ escape as a function of the solar wind dynamic pressure for the 9 equally distributed subsets with different IMF configurations (clock angle θ—CA). **b** Same plot as plot (**a**) including a 95% confidence interval

IMF (CA < 30°) or dotted yellow curve, the total O$^+$ escape is smaller. The difference between strong northward and strong southward IMF is about 1 order of magnitude. Intermediary curves show the configuration for slightly northward and southward IMF. The dotted dark blue and green curves correspond to northward IMF for 30° < CA < 60° and 60° < CA < 90°, respectively, and the dashed red and pink curves to southward IMF for 90° < CA < 120° and 120° < CA < 150°, respectively. Figure 3b displays the same curves as described but with 95% confidence intervals described above.

Coupling functions
After the solar wind dynamic pressure, we investigated the solar wind coupling functions because it includes the three previous parameters (n, v and θ) analysed in section Observations. The first coupling function is the Akasofu (or epsilon) parameter, which was initially used to study storms and substorms (Akasofu 1981). As the epsilon parameter is intended for a short period of time, we also estimated three variant formulae of Vasyliunas et al. (1982) for statistics. The four coupling functions investigated for this study are shown in Fig. 4a. This figure gives the total O$^+$ escape as a function of the coupling functions [W]. The dashed blue curve corresponds to the epsilon parameter, the dotted green one to the Vasyliunas et al. formula with $P_{input(\alpha=0.5)}$, $F(\theta) = \sin^4(\theta/2)$ (Eq. 2 in the Additional file 1: Tenfjord and Østgaard 2013), the dashed–dotted violet one $P_{\alpha=0.3}$, $F(\theta) = \sin^4(\theta/2)$ (Eq. 1 in the Additional file 1: Finch and Lockwood 2007) and

finally the solid orange to the Vasyliunas et al. formula E_{input} with $\alpha = 0.43$ and $F(\theta) = \sin^{2.7}(\theta/2) + 0.25$ (Eq. 3 in the Additional file 1: Wang et al. 2014a). Figure 4b shows the same coupling functions as described above but with error bars corresponding to a 95% confidence interval (see more details in "Solar wind dynamic pressure and IMF" section).

Similarly to P_{dyn}, the four functions are equally divided into 9 subsets (with the average subsets shown using circles, diamonds, crosses and points on the curves); the first subset corresponds to the average lowest energy input ($\sim 10^7$ W for epsilon and between 10^8 and 10^{11} W for the Vasyliunas et al. formulae) and the last subset to the largest energy input, $\sim 10^{12}$ W. For weak to moderate solar wind energy input or roughly the 5 first subsets, three functions (ϵ, P_α and P_{input}) show a small decrease producing a reduction of O$^+$ escape flux. For stronger solar wind energy input into the magnetosphere, we observe in the four functions a strong increase in the total O$^+$ flux (see Fig. 5, zoom of Fig. 4 for higher energy input). However, the 95% confidence intervals of the Akasofu parameter overlap except for the last subset. Consequently, no clear correlation between this parameter and the O$^+$ escape can be claimed.

Extreme ultraviolet flux
As a complement to the coupling functions, we compare the EUV intensity and EUV flux from the TIMED data with the oxygen data from Cluster. Figure 6a displays the total O$^+$ escape as a function of the solar wind dynamic pressure for different EUV (intensity, see
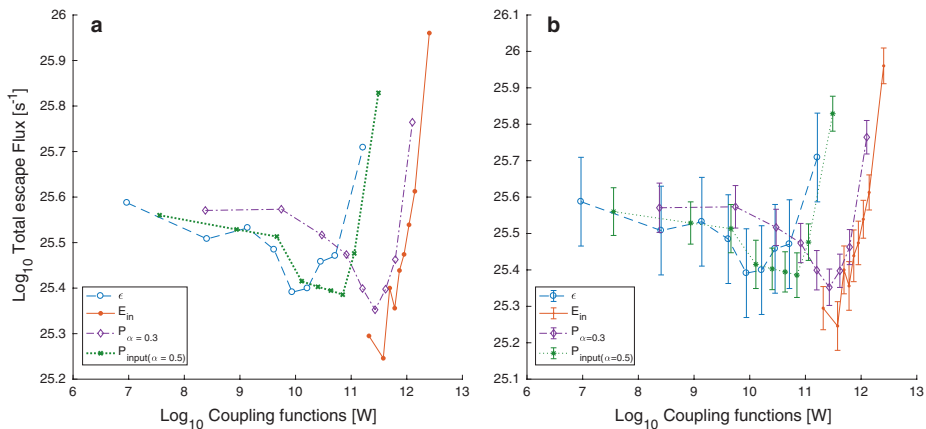
Fig. 4 Coupling functions for O$^+$ in the plasma mantle. **a** Total O$^+$ escape from the plasma mantle as a function of the solar wind coupling functions. The different curves represent the Akasofu parameter (dashed blue) and three variations of the Vasyliunas et al. formula (solid orange, doted green and dashed–dot violet). **b** Same plot as in plot (**a**) including a 95% confidence interval
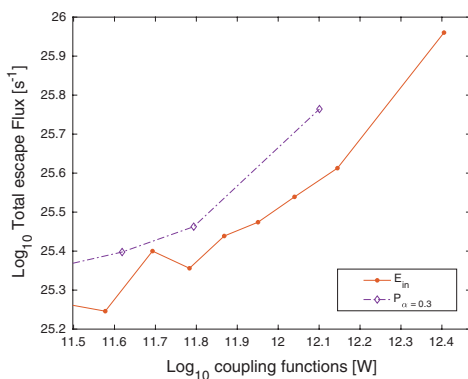

Fig. 5 Zoom of two coupling functions for O$^+$ in the plasma mantle. Zoom of two functions E$_{in}$ and P$_{\alpha=0.3}$ from Fig. 4. The increase of O$^+$ escape rate after the threshold is almost linear

Eq. 5) conditions, namely low EUV (dashed blue curve) and high EUV (dotted green curve). Note that the limit between low and high EUV is given by its mean at 0.0035 W/m^2 and the solid dark curve has no EUV conditions (same as in Fig. 2). Figure 6b is identical to Fig. 6a with error bars corresponding to a 95% confidence interval. Our observations show that EUV has a very limited influence, if any, on the total O$^+$ escape in the plasma mantle.

Discussion

Compression of the magnetosphere and solar dynamic pressure

The magnetospheric dynamics is strongly influenced by changing solar wind conditions. During solar storms or long periods of southward IMF, the magnetosphere is compressed. This magnetospheric compression can be observed in Fig. 1 for high dynamic pressure (subplot 9). The O$^+$ average bins represented in this figure do not fill up the last layer between 10 Re and 11 Re ($\sim$ 50% less observations than for 8 others subplots). Thus, we interpret a compression of the magnetopause located near 10 Re. On the other hand, for quiet conditions, the average O$^+$ bins outside the layers (see Fig. 1, subplots 3, 4, 5 for example), which physically means O$^+$ ions in the magnetosheath (because the magnetopause in quiet conditions is estimated around 10 Re to 11 Re), are discarded in the estimation of the total O$^+$ escape rate. Thus, in the total O$^+$ estimation, the escaping area of the filled layers in Fig. 1 includes this compression effect.

We believe that most of the O$^+$ outflow from the plasma mantle is escaping and lost into the solar wind. Therefore, in this study we replace the total O$^+$ *outflow* by total O$^+$ *escape rate*. This statement can be discussed using the ion convection towards the plasma sheet (perpendicular bulk velocity) and the parallel bulk velocity of the ions. Slapak and Nilsson (2018) calculated a convection speed in the plasma mantle of 35 km/s during extreme geomagnetic storms and a corresponding typical parallel ion speed of
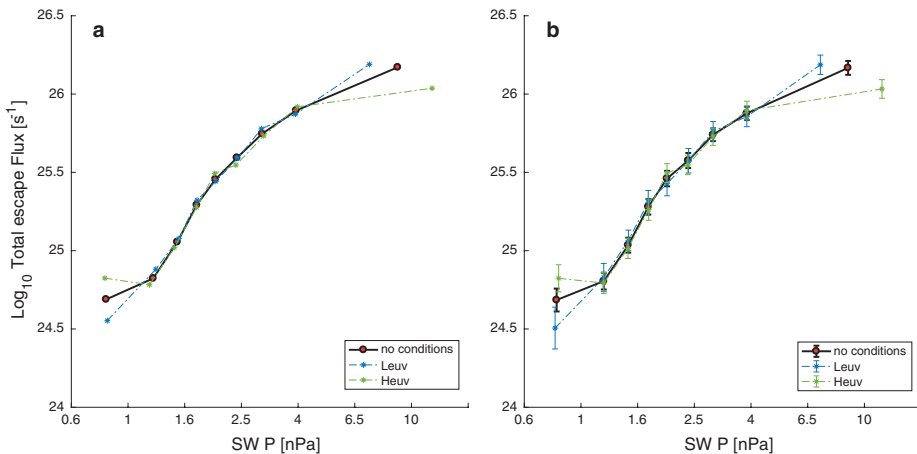
Schillings *et al. Earth, Planets and Space* (2019) 71:70

Page 9 of 13

Fig. 6 EUV intensity dependency. **a** Extreme ultraviolet dependency on the total O^+ escape as a function of the dynamic pressure. Those radiations do not have a strong influence on the escape flux. **b** Same plot as in plot (**a**) including the 95% confidence interval

115 km/s, such that these ions reach the plasma sheet ($Z_{GSM} = 0$) at around 50 Re downtail. Under disturbed conditions, those ions are then tailward of the near-Earth neutral sheet X-line (Nagai et al. 1994, 1998) and the O^+ ions will be lost in the distant magnetotail. For more general conditions, Nilsson (2011) found that the average parallel velocity in the mantle was 70 km/s, with a perpendicular temperature of 1 keV. Our ion trajectories for the plasma mantle pass $X_{GSM} = 0$ at an altitude typically above 12 Re, and an average convection velocity towards the plasma sheet for southward IMF is 10 km/s (Haaland et al. 2008). A simple estimate of the transport time from 12 Re to the centre of the plasma sheet would thus be $(12 \times 6371)/10 \simeq 7600$ s, yielding a tailward field-aligned transport of 70 km/s $\times$ 7600 s $\approx$ 80 Re. Here we did not take into account the mirror force acting on the 1 keV average perpendicular temperature, any further ion heating nor any centrifugal acceleration. We thus confirm the conclusions of Nilsson (2011); Nilsson et al. (2012) that most of the cusp/plasma mantle ion outflow will escape.

Our result in Fig. 2 shows a clear correlation between the O^+ escape rate and the solar wind dynamic pressure. A similar trend has been observed by Elliott et al. (2001), who found that in the high-altitude polar cap, the O^+ density and parallel flux increases with solar dynamic pressure. Another aspect influencing the O^+ escape is the IMF direction [here studied through several clock angles (CA)] shown in Fig. 3. Our estimation shows that the O^+ escape rate is higher by a factor of 3 for southward IMF than for northward IMF. Despite that Elliott et al. (2001) did not see any influence of the IMF direction on the O^+

density and parallel flow at high altitudes, this trend was observed by Marcucci et al. (2004) for magnetosheath O^+ ions having higher velocities during southward IMF. Finally, the cusp area increases (Newell and Meng 1994) and moves towards lower latitudes (Palmroth et al. 2001) under larger solar wind pressure and IMF B_z, which also contributes to a higher O^+ escape rate. So, our results are in line with what we expected for O^+ ions in the plasma mantle.

The coupling functions

The coupling functions are defined by the epsilon parameters and the Vasyliunas et al. formula. They are employed for quantifying the energy transferred from the solar wind through the magnetosphere (for further details see Akasofu 1981; Koskinen and Tanskanen 2002 and references therein). In this study, we chose to implement the Akasofu parameter and three variations of the Vasyliunas et al. formula (Eq. 4) with different coupling coefficient α. Note that more details about the three varied equations are given in the Additional file 1.

For a transferred power into the magnetosphere of approximately 10^{10} W, we estimated an O^+ escape rate of 9.13×10^{25} s^{-1} for the Vasyliunas et al. formulae and 5.11×10^{25} s^{-1} for the Akasofu parameter. In comparison, Li et al. (2017) analysed the epsilon parameter for cold ion outflow. The authors used 10 years of Cluster data and estimated the Akasofu parameter under several solar wind parameters. They found that the total cold ion flux is increasing for higher ϵ (up to 10^{11} W). This result (Li et al. 2017) is in agreement with ours as our

Schillings *et al. Earth, Planets and Space* (2019) 71:70

Page 10 of 13

epsilon values is estimated in average to 3.05×10^{10} W (see dashed blue curve in Fig. 4) and goes up to 10^{12} W for a few values (see Fig. 5). According to Akasofu (1981), a transferred power of 10^{12} W or higher corresponds to a magnetic storm. From our observations, this statement implies that for geomagnetic storms the O^+ escape rate increases, which is in good agreement with the results found by Schillings et al. (2017, 2018). In addition, we observe a slightly higher solar energy transfer into the magnetosphere during strong southward IMF (up to -30 nT, not shown); meanwhile, the cusp is expanding and moving equatorward (Newell et al. 1989; Palmroth et al. 2001; Li et al. 2012). Therefore, during more intense southward IMF, the interaction area for the penetrating solar wind expands and powers significantly the magnetospheric dynamics.

The most striking feature with all the different coupling functions is that the energy input must reach a certain threshold before any significant change of the O^+ escape rate is seen. After that, there is a strong correlation between any of the coupling functions and the O^+ escape rate. At lower energy input, there is no or even a negative correlation. A possible interpretation is that for low to intermediate energy input, the initial upflow is mainly determined by the solar wind precipitation into the upper atmosphere (Nilsson et al. 1996; Ogawa et al. 2009). As energy input increases, the O^+ escape rate increases and may be due to an expansion of the polar

cap and ion circulation to lower latitudes, which results in denser plasma from lower latitude moving towards higher latitudes into the cusp. With the available data we have, this is only a speculation, but it can be tested using ground-based data such as incoherent scatter radars.

Extreme ultraviolet

The low-energy O^+ density and outflow in the polar cap, cusp and lobes have been observed to be dependent of EUV radiation ($F_{10.7}$) (Young et al. 1982; Yau et al. 1988; Cully et al. 2003; André et al. 2015). Despite this, we observe no correlation between the EUV intensity and the O^+ escape rate in the plasma mantle (see Fig. 6). As an extra caution, we tested the EUV dependence for polar cap data using our code and obtained a similar result to the papers cited above (not shown). EUV radiations have an impact in the ionosphere between roughly 80 and 600 km, the ionisation of atomic oxygen to O^+ ions increases at those altitudes, and the O^+ density extends in altitude. On the other hand, all those newly formed ions are not transversely heated and accelerated enough to reach the plasma mantle. One portion will remain bound by gravity, and another portion will become outflow and end up in the plasma sheet. It seems that the amount that reaches the plasma mantle is not strongly dependent on this initial production of ions. This may be because the O^+ in the plasma mantle mainly originates from the ionospheric cusp, where there is also significant soft electron
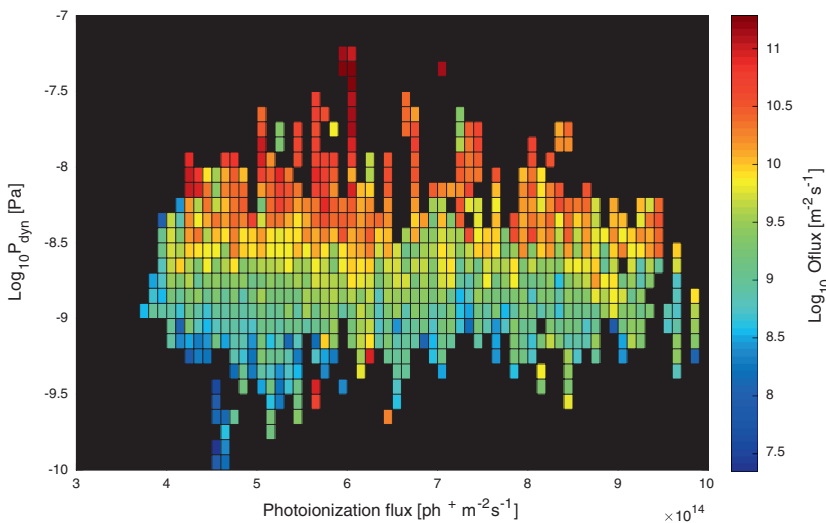

Fig. 7 Photoionisation flux. O^+ outflow in the plasma mantle (colour bar) for different solar wind dynamic pressure and different photoionisation fluxes

precipitation to heat and ionise the ionospheric F-region, leading to the initial upflow (Nilsson et al. 1996; Ogawa et al. 2009); see also statistical maps of electron precipitation (Newell et al. 2009). To strengthen this result, we implemented the O^+ flux as a function of both EUV flux (see Eq. 6) and dynamic pressure (see Fig. 7). We see that, in the plasma mantle, the O^+ escape rate definitely depends on the solar wind dynamic pressure and not on the photoionisation flux (neither does the Kp index see Additional file 1: Fig. 1).

Conclusions

Previous work has reported O^+ outflow dependency with solar wind parameters such as IMF (Slapak et al. 2015), EUV (Yau et al. 1988; Cully et al. 2003; Mouikis et al. 2010) or among other parameters e.g. Abe et al. (1996), Elliott et al. (2001), Lennartsson et al. (2004). However, those results do not cover the plasma mantle region. In this study, we analysed the O^+ escape rate in the plasma mantle for different solar wind parameters, namely the dynamic pressure P_{dyn}, IMF through the clock angle and the EUV flux. We found that

1. The O^+ that will eventually escape from the plasma mantle increase with the solar wind dynamic pressure by about 2 orders of magnitude between the lowest to highest dynamic pressure conditions.
2. The IMF has a clear influence on the O^+ escape with an increase by a factor 3 between northward and southward IMF,
3. The photoionisation flux (EUV flux) does not influence the O^+ escape rate in the plasma mantle.

Our results imply that the higher the O^+ escape rate is, the higher solar wind flux and energy penetrates into the magnetosphere. Therefore, atmospheric loss through the plasma mantle strongly depends on solar wind conditions but not solar radiation. When using a solar wind coupling function, the response is nonlinear and starts to increase only after some threshold is reached. Thus, if we consider higher solar energy input as extreme solar wind conditions, we suggest as a possible explanation that the O^+ escape rate increases significantly due to an increased polar cap size and increased convection of fresh plasma into the ionospheric upflow region. Finally, considering that the young Sun had stronger solar wind, we await that O^+ escape driven by solar wind conditions has a crucial influence on the evolution of the Earth's atmosphere. Therefore, questions remain open and could be addressed in future studies regarding how does the intrinsic magnetic field protect the Earth from significant solar wind penetration and our atmosphere from atmospheric loss.

Additional file

Additional file 1. The first paragraph of the Additional file 1 provides more details on the calculations of the Vasyliunas et al. formula used in Figs. 4 and 5. The equations are fully described. The second part provides additional information on the geomagnetic activity (Kp) compared with the solar wind dynamic pressure and the photoionisation flux.

Author details
[1] Swedish Institute of Space Physics, Kiruna, Sweden. [2] Division of Space Technology, Luleå University of Technology, Kiruna, Sweden. [3] EISCAT Scientific Association, Kiruna, Sweden. [4] IRAP, Université de Toulouse, CNRS, UPS, CNES, Toulouse, France. [5] Division of Fluid and Experimental Mechanics, Luleå University of Technology, Luleå, Sweden.

References
Abe T, Watanabe S, Whalen BA, Yau AW, Sagawa E (1996) Observations of polar wind and thermal ion outflow by Akebono/SMS. J Geomagn Geoelectr 48(3):319–325. https://doi.org/10.5636/jgg.48.319
Akasofu S-I (1981) Energy coupling between the solar wind and the magnetosphere. Space Sci Rev 28(2):121–190. https://doi.org/10.1007/BF00218810
André M, Li K, Eriksson AI (2015) Outflow of low-energy ions and the solar cycle. J Geophys Res Space Phys 120(2):1072–1085. https://doi.org/10.1002/2014JA020714
Axford WI (1968) The polar wind and the terrestrial helium budget. J Geophys Res 73:6855–6859. https://doi.org/10.1029/JA073i021p06855
Balogh A, Carr CM, Acuña MH, Dunlop MW, Beek TJ, Brown P, Fornaçon K-H, Georgescu E, Glassmeier K-H, Harris J, Musmann G, Oddy T, Schwingenschuh K (2001) The Cluster magnetic field investigation: overview of in-flight performance and initial results. Ann Geophys 19:1207–1217. https://doi.org/10.5194/angeo-19-1207-2001
Bouhram M, Klecker B, Miyake W, Rème H, Sauvaud J-A, Malingre M, Kistler L, Blăgău A (2004b) On the altitude dependence of transversely heated O^+ distributions in the cusp/cleft. Ann Geophys 22(5):1787–1798. https://doi.org/10.5194/angeo-22-1787-2004

Schillings *et al. Earth, Planets and Space* (2019) 71:70

Page 12 of 13

Chandler MO, Waite JH, Moore TE (1991) Observations of polar ion outflows. J Geophys Res Space Phys 96(A2):1421–1428. https://doi.org/10.1029/90JA02180

Chappell CR, Moore TE, Waite JH Jr (1987) The ionosphere as a fully adequate source of plasma for the Earth's magnetosphere. J Geophys Res 92:5896–5910. https://doi.org/10.1029/JA092iA06p05896

Cully CM, Donovan EF, Yau AW, Arkos GG (2003) Akebono/Suprathermal Mass Spectrometer observations of low-energy ion outflow: dependence on magnetic activity and solar wind conditions. J Geophys Res Space Phys 108:1093. https://doi.org/10.1029/2001JA009200

Denton MH, Taylor MGGT (2008) Solar wind dependence of ion parameters in the Earth's magnetospheric region calculated from cluster observations. Ann Geophys 26(3):387–394. https://doi.org/10.5194/angeo-26-387-2008

Elliott HA, Comfort RH, Craven PD, Chandler MO, Moore TE (2001) Solar wind influence on the oxygen content of ion outflow in the high-altitude polar cap during solar wind minimum conditions. J Geophys Res Space Phys 106(A4):6067–6084. https://doi.org/10.1029/2000JA003022

Engwall E, Eriksson AI, Cully CM, André M, Puhl-Quinn PA, Vaith H, Torbert R (2009) Survey of cold ionospheric outflows in the magnetotail. Ann Geophys 27(8):3185–3201. https://doi.org/10.5194/angeo-27-3185-2009

Escoubet CP, Fehringer M, Goldstein M (2001) Introduction the Cluster mission. Ann Geophys 19:1197–1200. https://doi.org/10.5194/angeo-19-1197-2001

Finch I, Lockwood M (2007) Solar wind-magnetosphere coupling functions on timescales of 1 day to 1 year. Ann Geophys 25(2):495–506

Gou XC, Shi QQ, Tian AM, Sun WJ, Dunlop MW, Fu SY, Zong QG, Facskó G, Nowada M, Pu ZY, Mailyan B, Xiao T, Shen XC (2016) Solar wind plasma entry observed by cluster in the high-latitude magnetospheric lobes. J Geophys Res Space Phys 121(5):4135–4144. https://doi.org/10.1002/2015JA021578

Green JL, Waite JH Jr (1985) On the origin of polar ion streams. Geophys Res Lett 12:149–152. https://doi.org/10.1029/GL012i003p00149

Güdel M (2007) The sun in time: activity and environment. Living Rev Sol Phys 4:3. https://doi.org/10.12942/lrsp-2007-3. arXiv:0712.1763

Haaland S, Paschmann G, Förster M, Quinn J, Torbert R, Vaith H, Puhl-Quinn P, Kletzing C (2008) Plasma convection in the magnetotail lobes: statistical results from cluster edi measurements. Ann Geophys 26(8):2371–2382. https://doi.org/10.5194/angeo-26-2371-2008

Haaland S, Lybekk B, Maes L, Laundal K, Pedersen A, Tenfjord P, Ohma A, Østgaard N, Reistad J, Snekvik K (2017) North–south asymmetries in cold plasma density in the magnetotail lobes: Cluster observations. J Geophys Res Space Phys 122(1):136–149. https://doi.org/10.1002/2016JA023404

Kistler LM, Mouikis CG (2016) The inner magnetosphere ion composition and local time distribution over a solar cycle. J Geophys Res Space Phys 121(3):2009–2032. https://doi.org/10.1002/2015JA021883

Kistler LM, Mouikis CG, Cao X, Frey H, Klecker B, Dandouras I, Korth A, Marcucci MF, Lundin R, McCarthy M, Friedel R, Lucek E (2006) Ion composition and pressure changes in storm time and nonstorm substorms in the vicinity of the near-Earth neutral line. J Geophys Res Space Phys 111(A10):11222. https://doi.org/10.1029/2006JA011939

Koskinen HEJ, Tanskanen EI (2002) Magnetospheric energy budget and the epsilon parameter. J Geophys Res Space Phys 107(A11):42–14210. https://doi.org/10.1029/2002JA009283

Kronberg EA, Ashour-Abdalla M, Dandouras I, Delcourt DC, Grigorenko EE, Kistler LM, Kuzichev IV, Liao J, Maggiolo R, Malova HV, Orlova KG, Peroomian V, Shklyar DR, Shprits YY, Welling DT, Zelenyi LM (2014) Circulation of heavy ions and their dynamical effects in the magnetosphere: recent observations and models. Space Sci Rev 184:173–235. https://doi.org/10.1007/s11214-014-0104-0

Kusnierkiewicz DY (2003) An overview of the timed spacecraft. Technical Report 2, JHU/APL Technical Digest

Lennartsson OW, Collin HL, Peterson WK (2004) Solar wind control of Earth's H^+ and O^+ outflow rates in the 15-eV to 33-keV energy range. J Geophys Res Space Phys 109(A18):12212. https://doi.org/10.1029/2004JA010690

Li K, Haaland S, Eriksson A, André M, Engwall E, Wei Y, Kronberg EA, Fränz M, Daly PW, Zhao H, Ren QY (2012) On the ionospheric source region of cold ion outflow. Geophys Res Lett 39:18102. https://doi.org/10.1029/2012GL053297

Li K, Wei Y, André M, Eriksson A, Haaland S, Kronberg EA, Nilsson H, Maes L, Rong ZJ, Wan WX (2017) Cold ion outflow modulated by the solar wind energy input and tilt of the geomagnetic dipole. J Geophys Res Space Phys 122(10):10658–10668. https://doi.org/10.1002/2017JA024642

Li K, Wei Y, Haaland S, Kronberg EA, Rong ZJ, Maes L, Maggiolo R, André M, Nilsson H, Grigorenko E (2018) Estimating the kinetic energy budget of the polar wind outflow. J Geophys Res Space Phys 123(9):7917–7929. https://doi.org/10.1029/2018JA02581

Liao J, Kistler LM, Mouikis CG, Klecker B, Dandouras I, Zhang J-C (2010) Statistical study of O^+ transport from the cusp to the lobes with Cluster CODIF data. J Geophys Res Space Phys 115:00–15. https://doi.org/10.1029/2010JA015613

Liao J, Kistler LM, Mouikis CG, Klecker B, Dandouras I (2015) Acceleration of O^+ from the cusp to the plasma sheet. J Geophys Res Space Phys 120:1022–1034. https://doi.org/10.1002/2014JA020341

Maes L, Maggiolo R, De Keyser J, Dandouras I, Fear RC, Fontaine D, Haaland S (2015) Solar illumination control of ionospheric outflow above polar cap arcs. Geophys Res Lett 42(5):1304–1311. https://doi.org/10.1002/2014GL062972.2014GL062972

Maggiolo R, Kistler LM (2014) Spatial variation in the plasma sheet composition: dependence on geomagnetic and solar activity. J Geophys Res Space Phys 119:2836–2857. https://doi.org/10.1002/2013JA019517

Maggiolo R, Sauvaud J-A, Fontaine D, Teste A, Grigorenko E, Balogh A, Fazakerley A, Paschmann G, Delcourt D, Rème H (2006) A multi-satellite study of accelerated ion beams above the polar cap. Ann Geophys 24(6):1665–1684. https://doi.org/10.5194/angeo-24-1665-2006

Marcucci MF, Bavassano Cattaneo MB, Pallocchia G, Amata E, Bruno R, Di Lellis AM, Formisano V, Rème H, Bosqued JM, Dandouras I, Sauvaud J-A, Kistler LM, Moebius E, Klecker B, Carlson CW, Parks GK, McCarthy M, Korth A, Lundin R, Balogh A (2004) Energetic magnetospheric oxygen in the magnetosheath and its response to IMF orientation: Cluster observations. J Geophys Res Space Phys. https://doi.org/10.1029/2003JA010312

Mouikis CG, Kistler LM, Liu YH, Klecker B, Korth A, Dandouras I (2010) H^+ and O^+ content of the plasma sheet at 15–19 Re as a function of geomagnetic and solar activity. J Geophys Res Space Phys 115:00–16. https://doi.org/10.1029/2010JA015978

Murayama T (1982) Coupling function between solar wind parameters and geomagnetic indices. Rev Geophys 20(3):623–629. https://doi.org/10.1029/RG020i003p00623

Nagai T, Waite JH, Green JL, Chappell CR, Olsen RC, Comfort RH (1984) First measurements of supersonic polar wind in the polar magnetosphere. Geophys Res Lett 11(7):669–672. https://doi.org/10.1029/GL011i007p00669

Nagai T, Takahashi K, Kawano H, Yamamoto T, Kokubun S, Nishida A (1994) Initial geotail survey of magnetic substorm signatures in the magnetotail. Geophys Res Lett 21(25):2991–2994. https://doi.org/10.1029/94GL01420

Nagai T, Fujimoto M, Nakamura R, Saito Y, Mukai T, Yamamoto T, Nishida A, Kokubun S, Reeves GD, Lepping RP (1998) Geotail observations of a fast tailward flow at × gsm = −15 Re. J Geophys Res Space Phys 103(A10):23543–23550. https://doi.org/10.1029/98JA02246

Newell PT, Meng C-I (1994) Ionospheric projections of magnetospheric regions under low and high solar wind pressure conditions. J Geophys Res Space Phys 99:273–286. https://doi.org/10.1029/93JA02273

Newell PT, Sotirelis T, Wing S (2009) Diffuse, monoenergetic, and broadband aurora: the global precipitation budget. J Geophys Res Space Phys. https://doi.org/10.1029/2009JA014326

Newell PT, Meng C-I, Sibeck DG, Lepping R (1989) Some low-altitude cusp dependencies on the interplanetary magnetic field. J Geophys Res Space Phys 94:8921–8927. https://doi.org/10.1029/JA094iA07p08921

Nilsson H, Waara M, Arvelius S, Marghitu O, Bouhram M, Hobara Y, Yamauchi M, Lundin R, Rème H, Sauvaud J-A, Dandouras I, Balogh A, Kistler LM, Klecker B, Carlson CW, Bavassano-Cattaneo MB, Korth A (2006) Characteristics of high altitude oxygen ion energization and outflow as observed by Cluster: a statistical study. Ann Geophys 24:1099–1112. https://doi.org/10.5194/angeo-24-1099-2006

Nilsson H, Waara M, Marghitu O, Yamauchi M, Lundin R, Rème H, Sauvaud J-A, Dandouras I, Lucek E, Kistler LM, Klecker B, Carlson CW, Bavassano-Cattaneo MB, Korth A (2008) An assessment of the role of the centrifugal acceleration mechanism in high altitude polar cap oxygen ion outflow. Ann Geophys 26:145–157. https://doi.org/10.5194/angeo-26-145-2008

Nilsson H, Engwall E, Eriksson A, Puhl-Quinn PA, Arvelius S (2010) Centrifugal acceleration in the magnetotail lobes. Ann Geophys 28:569–576. https://doi.org/10.5194/angeo-28-569-2010

Schillings *et al. Earth, Planets and Space* (2019) 71:70

Page 13 of 13

Nilsson H, Barghouthi IA, Slapak R, Eriksson AI, André M (2012) Hot and cold ion outflow: spatial distribution of ion heating. J Geophys Res Space Phys 117(A16):11201. https://doi.org/10.1029/2012JA017974

Nilsson H (2011) In: Liu W, Fujimoto M (ed) Heavy ion energization, transport, and loss in the Earth's magnetosphere. Springer, Dordrecht, pp 315–327

Nilsson H, Kirkwood S, Bjørnå N (1996) Bistatic measurements of incoherent scatter plasma lines. J Atmos Terr Phys 58(1):175–187. https://doi.org/10.1016/0021-9169(95)00028-3 (**Selected papers from the sixth international Eiscat Workshop**)

Ogawa Y, Buchert SC, Fujii R, Nozawa S, van Eyken AP (2009) Characteristics of ion upflow and downflow observed with the european incoherent scatter svalbard radar. J Geophys Res Space Phys. https://doi.org/10.1029/2008JA013817

Palmroth M, Laakso H, Pulkkinen TI (2001) Location of high-altitude cusp during steady solar wind conditions. J Geophys Res Space Phys 106(A10):21109–21122. https://doi.org/10.1029/2001JA900073

Ramstad R, Barabash S, Futaana Y, Nilsson H, Wang X-D, Holmström M (2015) The Martian atmospheric ion escape rate dependence on solar wind and solar EUV conditions: 1. Seven years of Mars Express observations. J Geophys Res Planets 120(7):1298–1309. https://doi.org/10.1002/2015JE004816

Ramstad R, Barabash S, Futaana Y, Nilsson H, Holmström M (2017) Global mars-solar wind coupling and ion escape. J Geophys Res Space Phys 122(8):8051–8062. https://doi.org/10.1002/2017JA024306

Rème H, Aoustin C, Bosqued JM, Dandouras I, Lavraud B, Sauvaud JA, Barthe A, Bouyssou J, Camus T, Coeur-Joly O, Cros A, Cuvilo J, Ducay F, Garbarowitz Y, Medale JL, Penou E, Perrier H, Romefort D, Rouzaud J, Vallat C, Alcaydé D, Jacquey C, Mazelle C, D'Uston C, Möbius E, Kistler LM, Crocker K, Granoff M, Mouikis C, Popecki M, Vosbury M, Klecker B, Hovestadt D, Kucharek H, Kuenneth E, Paschmann G, Scholer M, Sckopke N, Seidenschwang E, Carlson CW, Curtis DW, Ingraham C, Lin RP, McFadden JP, Parks GK, Phan T, Formisano V, Amata E, Bavassano-Cattaneo MB, Baldetti P, Bruno R, Chionchio G, di Lellis A, Marcucci MF, Pallocchia G, Korth A, Daly PW, Graeve B, Rosenbauer H, Vasyliunas V, McCarthy M, Wilber M, Eliasson L, Lundin R, Olsen S, Shelley EG, Fuselier S, Ghielmetti AG, Lennartsson W, Escoubet CP, Balsiger H, Friedel R, Cao J-B, Kovrazhkin RA, Papamastorakis I, Pellat R, Scudder J, Sonnerup B (2001) First multispacecraft ion measurements in and near the Earth's magnetosphere with the identical Cluster ion spectrometry (CIS) experiment. Ann Geophys 19:1303–1354. https://doi.org/10.5194/angeo-19-1303-2001

Schillings A, Nilsson H, Slapak R, Yamauchi M, Westerberg L-G (2017) Relative outflow enhancements during major geomagnetic storms—Cluster observations. Ann Geophys 35(6):1341–1352. https://doi.org/10.5194/angeo-35-1341-2017

Schillings A, Nilsson H, Slapak R, Wintoft P, Yamauchi M, Wik M, Dandouras I, Carr CM (2018) O$^+$ escape during the extreme space weather event of 4–10 September 2017. Space Weather 16(9):1363–1376. https://doi.org/10.1029/2018SW001881

Shelley EG, Peterson WK, Ghielmetti AG, Geiss J (1982) The polar ionosphere as a source of energetic magnetospheric plasma. Geophys Res Lett 9:941–944. https://doi.org/10.1029/GL009i009p00941

Shue J-H, Song P, Russell CT, Steinberg JT, Chao JK, Zastenker G, Vaisberg OL, Kokubun S, Singer HJ, Detman TR, Kawano H (1998) Magnetopause location under extreme solar wind conditions. J Geophys Res 103:17691–17700. https://doi.org/10.1029/98JA01103

Slapak R, Nilsson H (2018) The oxygen ion circulation in the outer terrestrial magnetosphere and its dependence on geomagnetic activity. Geophys Res Lett 45:12669–12676

Slapak R, Nilsson H, Westerberg LG (2013) A statistical study on O$^+$ flux in the dayside magnetosheath. Ann Geophys 31:1005–1010. https://doi.org/10.5194/angeo-31-1005-2013

Slapak R, Nilsson H, Waara M, André M, Stenberg G, Barghouthi IA (2011) O$^+$ heating associated with strong wave activity in the high altitude cusp and mantle. Ann Geophys 29:931–944. https://doi.org/10.5194/angeo-29-931-2011

Slapak R, Nilsson H, Westerberg LG, Eriksson A (2012) Observations of oxygen ions in the dayside magnetosheath associated with southward IMF. J Geophys Res Space Phys 117:07218. https://doi.org/10.1029/2012JA017754

Slapak R, Nilsson H, Westerberg LG, Larsson R (2015) O$^+$ transport in the dayside magnetosheath and its dependence on the IMF direction. Ann Geophys 33(3):301–307. https://doi.org/10.5194/angeo-33-301-2015

Slapak R, Schillings A, Nilsson H, Yamauchi M, Westerberg L-G, Dandouras I (2017) Atmospheric loss from the dayside open polar region and its dependence on geomagnetic activity: implications for atmospheric escape on evolutionary timescales. Ann Geophys 35:721–731

Stamper R, Lockwood M, Wild MN, Clark TDG (1999) Solar causes of the long-term increase in geomagnetic activity. J Geophys Res Space Phys 104(A12):28325–28342. https://doi.org/10.1029/1999JA900311

Tenfjord P, Østgaard N (2013) Energy transfer and flow in the solar wind–magnetosphere–ionosphere system: a new coupling function. J Geophys Res Space Phys 118(9):5659–5672. https://doi.org/10.1002/jgra.50545

Vasyliunas VM, Kan JR, Siscoe GL, Akasofu S-I (1982) Scaling relations governing magnetospheric energy transfer. Planet Space Sci 30(4):359–365. https://doi.org/10.1016/0032-0633(82)90041-1

Waara M, Slapak R, Nilsson H, Stenberg G, André M, Barghouthi IA (2011) Statistical evidence for O$^+$ energization and outflow caused by wave-particle interaction in the high altitude cusp and mantle. Ann Geophys 29:945–954. https://doi.org/10.5194/angeo-29-945-2011

Wang C, Han JP, Li H, Peng Z, Richardson JD (2014a) Solar wind–magnetosphere energy coupling function fitting: results from a global MHD simulation. J Geophys Res Space Phys 119(8):6199–6212. https://doi.org/10.1002/2014JA019834

Wang CP, Lyons LR, Angelopoulos V (2014b) Properties of low-latitude mantle plasma in the Earth's magnetotail: ARTEMIS observations and global MHD predictions. J Geophys Res Space Phys 119(9):7264–7280. https://doi.org/10.1002/2014JA020060

Woods TN, Bailey S, Eparvier F, Lawrence G, Lean J, McClintock B, Roble R, Rottman GJ, Solomon SC, Tobiska WK, White OR (2000) Timed solar EUV experiment. Phys Chem Earth Part C Solar Terr Planet Sci 25(5):393–396. https://doi.org/10.1016/S1464-1917(00)00040-4

Yau AW, Peterson WK, Shelley EG (1988) Quantitative parametrization of energetic ionospheric ion outflow. In: Moore TE, Waite Jr JH, Moorehead TW, Hansin WB (eds) Modeling magnetospheric plasma. Geophysical Monograph Series, vol 44. American Geophysical Union, Washington, DC, pp 211–217. https://doi.org/10.1029/GM044p0211

Yau AW, Abe T, Peterson WK (2007) The polar wind: recent observations. J Atmos Solar Terr Phys 69(16):1936–1983. https://doi.org/10.1016/j.jastp.2007.08.010 (**Recent Advances in the Polar Wind Theories and Observations**)

Young DT, Balsiger H, Geiss J (1982) Correlations of magnetospheric ion composition with geomagnetic and solar activity. J Geophys Res Space Phys 87(A11):9077–9096. https://doi.org/10.1029/JA087iA11p09077

Publisher's Note

The fate of O$^+$ ions observed in the plasma mantle and cusp: particle tracing modelling and Cluster observations

Authors:
Schillings, A., H. Gunell, H. Nilsson, A. De Spiegeleer, Y. Ebihara, L.-G. Westerberg, M. Yamauchi, and R. Slapak

The fate of O^+ ions observed in the plasma mantle and cusp: particle tracing modelling and Cluster observations

Audrey Schillings[1,2], Herbert Gunell[3,4], Hans Nilsson[1,2], Alexandre De Spiegeleer[3], Yusuke Ebihara[5], Lars G. Westerberg[6], Masatoshi Yamauchi[1], and Rikard Slapak[7]

[1]Swedish Institute of Space Physics, Kiruna, Sweden
[2]Division of Space Technology, Luleå University of Technology, Kiruna, Sweden
[3]Department of Physics, Umeå University, Umeå, Sweden
[4]Belgian Institute for Space Aeronomy, Brussels, Belgium
[7]EISCAT Scientific Association, Kiruna, Sweden
[6]Division of Fluid- and Experimental Mechanics, Luleå University of Technology, Luleå, Sweden
[5]Research Institute for Sustainable Humanosphere, Kyoto University, Japan, 611-0011, Gokasho, Uji, Kyoto

Correspondence: Audrey Schillings (audrey.schillings@irf.se)

Abstract. Ion escape is of particular interest for studying the evolution of the atmosphere on geological time scales. Previously, using Cluster-CODIF data, we investigated the oxygen ion outflow from the plasma mantle for different solar wind conditions and geomagnetic activity. We found significant correlations between solar wind parameters, geomagnetic activity (Kp index) and the O^+ outflow. From these studies, we suggested that O^+ ions observed in the plasma mantle and cusp have enough energy and velocity to escape the magnetosphere and be lost into the solar wind or in the distant magnetotail. Thus, this study aims to investigate where do the ions observed in the plasma mantle end up. In order to answer this question, we numerically calculate the trajectories of O^+ ions using a tracing code to further test this assumption and determine the fate of the observed ions. Our code consists of a magnetic field model (Tsyganenko T96) and an ionospheric potential model (Weimer 2001) in which particles initiated in the plasma mantle and cusp regions are launched and traced forward in time. We analysed 136 observations of plasma mantle or cusp events in Cluster data between 2001 and 2007, and for each event 200 O^+ particles were launched with an initial parallel and perpendicular velocity corresponding to the bulk velocity observed by Cluster. From the observations, our results show that 93% of the events have an initial parallel velocity component twice the initial perpendicular velocity. After the tracing, we found that 96% of the particles are lost into the solar wind or in the distant tail. Out of these 96%, 20% escape into the dayside magnetosphere.

1 Introduction

Before the 1970's, it was believed that the solar wind was the primary source of magnetospheric plasma. However, this conception became obsolete a few years later with the studies of Shelley et al. (1976); Sharp et al. (1977) who observed ionospheric O^+ ions with high velocities in the high-latitude ionosphere. A few decades later, it is now well known that ion upflow from the ionosphere is a significant source for the magnetosphere (Hoffman, 1968; Chappell et al., 1987; Abe et al., 1993) and it is accelerated through several processes to reach the high altitude cusp and plasma mantle. A part of this ion upflow is also known

as the polar wind in analogy with the solar wind (Axford, 1968). The polar wind is composed of H^+, He^+, O^+ and electrons with an energy of a few eV and commonly observed between $1000 \, \mathrm{km}$ and roughly $50\,000 \, \mathrm{km}$. Polar wind observations have been reviewed by Yau et al. (2007). At higher altitudes the terminology changes, and the term ionospheric outflow is used instead of polar wind, as it is complicated to distinguish solar wind H^+ from ionospheric H^+. Furthermore, the ion outflow is
25 then divided into two distinct populations, cold ions (up to a few tens eV) and hot ions (up to a few tens keV). The cold ions – detected with the spacecraft wake technique (Engwall et al., 2009) – are believed to be dominant for the magnetospheric plasma (André and Cully, 2012). These ions have been observed in the lobes (Haaland et al., 2009; Haaland et al., 2012; Liao et al., 2010) and have low enough parallel velocity so that convection dominates, and therefore will likely end up in the plasma sheet during strong solar wind conditions and southward interplanetary magnetic field (IMF) (Haaland et al., 2012). Under
30 northward IMF the convection is more stable and weaker Haaland et al. (2012), meaning this cold population will escape in the distant tail and be lost into the solar wind. The energetic ions are frequently heated transversely to the magnetic field due to wave-particles interactions in the cusp (Norqvist et al., 1998; Strangeway et al., 2005; Slapak et al., 2011; Waara et al., 2011; Nilsson et al., 2012) and parallel to the magnetic field due to centrifugal acceleration (Nilsson et al., 2008; Nilsson, 2011). Arvelius et al. (2005) showed that O^+ ions are accelerated from less than $0.1 \, \mathrm{keV}$ to more than $1 \, \mathrm{keV}$ between 8 and 12 Re.
35 The authors suggested that wave-particle interaction play the main role in the ion heating and subsequent acceleration. These energetic ions form the ion outflow at higher altitudes and several studies demonstrate the correlation between energetic ion outflow and solar and solar wind conditions (e.g., Peterson et al., 2001; Kistler et al., 2006; Li et al., 2012; Kistler and Mouikis, 2016; Schillings et al., 2019). It is the presence of a cusp and a polar cap that makes magnetised planets have atmospheric escape rates at least as high as planets without intrinsic magnetic fields (Gunell et al., 2018).

40 The main route of outflowing/escaping energetic ions is along open magnetic field lines, which include the polar cap, cusp and plasma mantle. The polar cap is defined as the footprint of the open magnetic field lines and the cusp as the entry of the solar wind into the magnetosphere. The plasma mantle is the region downstream of the cusp formed by reflected particles from the cusp, which are then convected toward the tail (Rosenbauer et al., 1975). Slapak et al. (2017) studied the O^+ outflow in the plasma mantle and dayside high-latitude magnetosheath for different geomagnetic conditions using the Kp index. They
45 found that the O^+ escape rate increases by 1.5 orders of magnitude during very disturbed magnetospheric conditions (> Kp=6) compared to quiet conditions ($\sim$ Kp=0-2). Despite 5 years of data, Slapak et al. (2017) did not have enough statistics for extreme disturbances, and therefore Schillings et al. (2017, 2018) performed case studies of major geomagnetic storms (> Kp=7+) in order to complement the study of Slapak et al. (2017). The authors found a 2 orders of magnitude enhancement in the O^+ outflow for the major storms as compared to the average O^+ flux for the same year of each storm. They also suggested
50 that the O^+ ions have been heated enough when they reach the plasma mantle to eventually escape the magnetosphere. During major geomagnetic storms Slapak and Nilsson (2018) estimated a perpendicular velocity of the plasma mantle O^+ to $35 \, \mathrm{km/s}$ and a parallel velocity of $115 \, \mathrm{km/s}$, thus for their particular example the ions would reach the plasma sheet around -50 Re. As the near-Earth X-line is pushed towards Earth during disturbed conditions, these ions are expected to escape in to distant tail.

Models and simulations have been extensively employed to investigate polar wind and ionospheric outflow. Schunk and
55 Sojka (1989) simulated the polar wind behaviour using a combination of a low-altitude ionosphere-atmosphere and a high-

altitude hydrodynamic model in a simulated region from 120 km to 9000 km. They discovered the complexity of the polar wind density structures in different altitude ranges as well as for geomagnetic variations. Polar wind behaviour during one idealised geomagnetic storm has been investigated by Schunk and Sojka (1997), who updated their model to an altitude coverage of 90 km to 9000 km for latitudes higher than 50°. They investigated the seasonal and solar cycle variations for four idealised
60   geomagnetic storms (winter and summer solstices and solar minimum and maximum). They found that O^+ upflow increases over the polar cap during the storms, while O^+ is the dominant ion species at all polar latitudes. These results are similar to the ones by Barakat and Schunk (2006) who studied the generalised behaviour of the polar wind, also during an idealised geomagnetic storm using a macroscopic PIC (particle-in-cell) model. Their results agreed with satellite observations. At an intermediate lower altitude of 4000 km, Horwitz et al. (1994) determined the bulk velocity and temperature profiles of O^+
65   and H^+ in the polar wind using a semi-kinetic outflow model. They found that centrifugal forces increase the outflowing O^+ flux with 2 orders of magnitude when the convection electric field is enhanced from 0 mV/m to 100 mV/m. A similar result has been shown by Abudayyeh et al. (2015), who used a Monte Carlo simulation based on the Tsyganenko T96 model and included the effects of the ambipolar electric field as well as gravitational and mirror forces. Additionally, Abudayyeh et al. (2015) observed higher bulk velocities and densities (H^+ and O^+) in the cusp than in the polar cap.
70   At an altitude range of 1.2 Re to 15.2 Re, Barghouthi et al. (2016) employed the same 1-D Monte Carlo model used by Abudayyeh et al. (2015) to investigate energetic H^+ and O^+ outflows along two trajectories (from the polar cap to the cusp) and compared them with Cluster data. Considering the centrifugal acceleration, the ambipolar electric field and the wave-particle interaction, they concluded that the latter was the most important mechanism especially at higher altitudes (cusp). Finally, a statistical model of the fate of energetic ions showed that these ions are highly dependent on the magnetic field
75   configuration. Therefore, for quiet magnetic field, more ions escape directly through the magnetopause, whereas for active magnetic field, the ions are convected towards the tail and reach the distant tail at 50 Re (Ebihara et al., 2006). Ebihara et al. (2006) also showed that under strong convection most of the ions in their model end up in the ring current.

   Previous studies demonstrate that several models already exist to determine the behaviour of polar wind and/or ion outflow at different altitudes including the heating processes the ions are subject to. Ebihara et al. (2006) discussed the fates of the
80   ions launched at different magnetic local time (MLT) and at 1 Re. Furthermore, Krcelic et al. (2019) estimated the fate of ions using the Tsyganenko T96 model and observations of ion velocities observed by Cluster satellites. They suggested that 69% of the ions escape the magnetosphere with 50% in the distant tail. Despite all those interesting studies, the fate of ions observed in the plasma mantle has not yet been well defined. This study aims to clarify if O^+ ion outflows observed in the plasma mantle will escape the magnetosphere and be lost into the solar wind as suggested previously from observations (Slapak et al.,
85   2017; Slapak and Nilsson, 2018; Schillings et al., 2018). For a more accurate estimate of the fate of ions, the starting point should be high-altitude, so that much of the transverse heating and centrifugal acceleration are already included. In order to answer this question, we traced particles in a combination of the Tsyganenko T96 (Tsyganenko, 1995) and the Weimer 2001 (Weimer, 2001) models. About 25 000 O^+ particles were launched from the plasma mantle with initial parameters taken from Cluster observations. This model thus incorporates the effect of the mirror force on the launched ions, centrifugal acceleration

90 and $\boldsymbol{E} \times \boldsymbol{B}$ drift. It does not include any further wave particle interaction than what the ions had experienced prior to the observation point.

This paper is organised as follows: Section 2 describes the instrumentation and data set we used, followed by the method and a description of our code in Section 3. Section 4 and 5 present and discusses our results respectively. Finally, the final section, Section 6, summarises our study.

2 Instrument and data

2.1 Cluster and solar wind data

The Cluster mission (Escoubet et al., 2001) consists of four identical spacecraft flying in a tetrahedral formation with an apogee and perigee of approximately 19 Re and 4 Re respectively. On board the spacecraft, the Cluster Ion spectrometer (CIS) is composed of two instruments; the Hot Ion Analyser (HIA) and the COmposition and DIstribution Function analyser (CODIF)
100 (Rème et al., 2001). The latter provides 3-D distributions of ions with an energy resolution of $\Delta E/E \sim 0.16$, an energy per charge range between $25\,\mathrm{eV/q}$ and $40\,\mathrm{keV/q}$ and a $360°$ field of view. The resolution of the data is usually $4\,\mathrm{s}$, however, it can go up to $16\,\mathrm{s}$. Those features enable observations of O^+ in different magnetospheric plasma regions. Additionally, Cluster has a FluxGate Magnetometer (FGM) (Balogh et al., 2001) with a mode sample frequency of $22.4\,\mathrm{Hz}$. In our study, we use the magnetic field averaged over the spacecraft spin period ($4\,\mathrm{s}$).
105 The solar wind data were retrieved from the OMNIWeb database. This database consists of data from several satellites at diverse positions around Earth. In our simulations (see Section 3.2), we utilise the solar wind dynamic pressure and velocity, the IMF By and Bz components in high-resolution ($5\,\mathrm{min}$) as well as the magnetic Dst index ($1\,\mathrm{h}$).

2.2 Plasma mantle and cusp dataset

Our dataset consists of plasma mantle and cusp events observed by the Cluster spacecraft 4 between 2001 and 2007. In order
110 to only retrieve plasma mantle and cusp data, we apply several constraints on the observational data. Firstly, the CODIF O^+ counts are contaminated when strong proton fluxes from the magnetosheath are recorded at the same energy level as the O^+ ions (Nilsson et al., 2006). These false O^+ counts usually originate from the magnetosheath and lead to an underestimate of the O^+ velocity moment. The technique to remove these false counts is based on the $\boldsymbol{E} \times \boldsymbol{B}$ drift, because the drift is neither mass nor charge dependent. Consequently, using the kinetic energy equation, the cross talk signal is seen as an O^+ perpendicular
115 bulk velocity that is 1/4 of the corresponding perpendicular proton velocity, and typically the O^+ density is higher than $2\,\mathrm{cm}^{-3}$ (for more details, we refer the reader to Nilsson et al. (2006)). We avoid these contaminated data (and therefore magnetosheath data) using the method described by Nilsson et al. (2006). However, we slightly changed the threshold defined by Nilsson et al. (2006) because over the years the quality of the Cluster data devolved and so did the threshold. The new thresholds are given by $\frac{v_{tot(O^+)}}{v_{tot(H^+)}} < 0.2$ and $\frac{v_{tot(O^+)}}{v_{tot(H^+)}} > 0.5$ as well as $\frac{N_{O^+}}{N_{H^+}} > 0.25$.

To pick out only cusp and plasma mantle observations we implement different conditions for the high latitude regions. In these regions, the plasma beta β (O^+ and H^+) is typically higher than 0.05, whereas it is lower than 0.05 in the polar cap (Liao et al., 2010, 2015; Haaland et al., 2017). We use a threshold value of $\beta > 0.1$ for high latitude regions. Additionally, the perpendicular temperature of the protons should be lower than 1750 eV in order to distinguish plasma sheet from plasma mantle data (Nilsson et al., 2006; Kistler et al., 2006; Slapak et al., 2017). As partly mentioned above, the O^+ and H^+ densities are restricted to n(H^+) > 10^{-3} cm^{-3} and 10^{-3} cm^{-3} < n(O^+) < 2 cm^{-3} to keep only reliable velocity estimates. In order to study the fate of ions, we take O^+ data with an outward flow ($v_\parallel > 0$ or $v_\parallel < 0$ in the southern and northern hemispheres respectively). Finally, we use a spatial coverage restriction to remove the inner magnetosphere, which is defined by -5 Re < X_{GSM} < 8 Re and $R_{GSM} = \sqrt{Y_{GSM}^2 + Z_{GSM}^2}$ > 6 Re (see also Slapak et al. (2017)). Major geomagnetic storms data are removed to exclude other magnetospheric regions than the cusp and plasma mantle (Schillings et al., 2017).

When all the above conditions are met, we define one event by 60 data points or more in a row. Between 2001 and 2007, our automatic routine detected 136 events that met the region criteria and the model restrictions (see Section 3.1).

3 Methodology

The section aims at briefly describing how our model works and its inputs and outputs.

3.1 Particle tracing simulations

We use a test particle simulation code (Gunell et al., 2019) to compute ion trajectories in the magnetic fields given by the Tsyganenko T96 model (Tsyganenko, 1995) and electric fields derived from the ionospheric potential given by the Weimer 2001 model (Weimer, 2001). The electric field is defined on a grid, and during the test particle trajectory calculation the electric field at the particle position is found by interpolation. Before the trajectory calculation starts, we define the electrostatic potential V on a three-dimensional grid with a cell size of $1200\,\mathrm{km} \times 1200\,\mathrm{km} \times 1200\,\mathrm{km}$ in the region $-60 < X < 10$ Re, $|Y| < 19$ Re and $|Z| < 19$ Re by tracing the magnetic field lines from each cell down to the ionosphere, where we retrieve the potential from the Weimer model. The electric field is then found from the relationship $\mathbf{E} = -\nabla V$. Figure 1 illustrates the magnetic field lines in light grey and the electric field grid in brown. This illustration represents the magnetosphere based on T96 and the grid for the interpolation of the electric field. Due to the limits of the Tsyganenko model, the electric field grid goes to -60 Re in the tail and 10 Re in the dayside (Tsyganenko, 1995). In the nort–south, Z, and dawn–dusk, Y, directions, the limit of the grid are at $\pm 19\,\mathrm{Re}$. Note that the illustration is not to scale.

To launch a particle, its initial ion velocity is calculated using the following equation

$$v_{tot} = v_\parallel \frac{\boldsymbol{B}}{B} + v_{\boldsymbol{E} \times \boldsymbol{B}} + v_\perp \frac{\boldsymbol{E}}{E}, \tag{1}$$

where $v_\parallel$ and $v_\perp$ are the parallel and perpendicular velocities of the O^+ ion respectively (see Section 3.2 for more details), B the magnetic field, E the electric field and $v_{\boldsymbol{E} \times \boldsymbol{B}}$ the $\boldsymbol{E} \times \boldsymbol{B}$ drift velocity in the model. Then, using the magnetic field line at
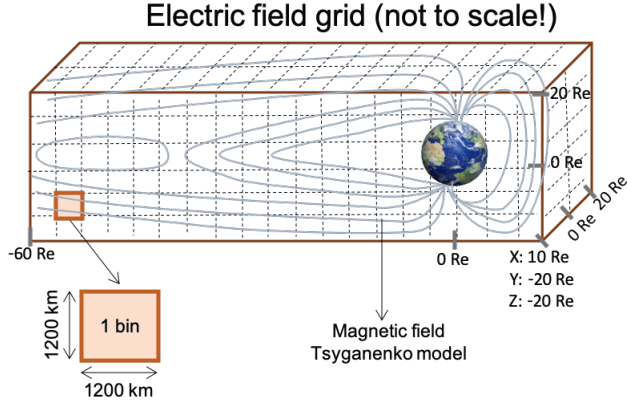
Figure 1. Schematic representation of the modelling of the Earth's environment. The Earth magnetosphere is represented in light grey and the brown grid displays the electric field grid. Note that the illustration is not to scale.

150   the position where the O$^+$ ion is launched, we interpolate the electric field in the corresponding electric cell. Finally, from the interpolated electric field, a new velocity is calculated with the Boris algorithm (e.g. Birdsall and Langdon, 1991).

      The last step is repeated as far as the limitations of the code allows it. The tracing uses a time step based on the gyro-period, so that our time step is $dt = 2\pi/20\omega_c$ whereas the maximum number of iterations is limited to 10000. In 99,5% of the cases, the particle stops because they reach the limit of our model (electric field grid), whereas for the 0.5% remaining the maximum

155   number of the iterations have been completed.

      The grid that defined the limit of our model is sufficient for our study because it includes the whole magnetosphere around Earth (magnetopause is defined around X = 10 Re in the dayside and about $|Y| = 13\,\mathrm{Re}$ and $|Z| = 13\,\mathrm{Re}$). Further in the magnetotail, the magnetopause expands into a "cone shape" in the Y and Z direction and beyond 200 Re in the X direction. Our grid stops at $X = -60\,\mathrm{Re}$ in the tail due to Tsyganenko model limits, moreover most of the particles reaching that distance will

160   most likely be lost (see Sections 4 and 5 for more details). Concerning constraints, the Weimer model imposes no constraints on solar wind parameters, while Tsyganenko T96 does. Therefore, when an observation meet the criteria described above it also has to match with Tsyganenko T96 constraints, which concerns the Dst index (-100 nT < Dst < 20 nT), the dynamic pressure (0.5 nPa < P_{dyn} < 10 nPa) and IMF B_z and B_y ($-10\,\mathrm{nT} < B_z, B_y < 10\,\mathrm{nT}$).

3.2   Inputs and outputs of the model

165   The inputs of the models are (a) solar wind parameters as required by the Tsyganenko- and Weimer models, (b) the positions, $v_\parallel$ and $v_\perp$ based on Cluster observations. The solar wind parameters (see Section 2.1) are taken for each corresponding event. The 136 plasma mantle- and cusp events are automatically detected by a routine scanning Cluster data (see Section 2.2). During

6

these events, we calculate the bulk parallel and perpendicular velocities and retrieve the spacecraft positions. These parameters are then used to create the initial positions, $v_\parallel$ and $v_\perp$ of 200 O^+ ions (per event) that we trace forward in time. Note that the perpendicular component of the velocity corresponds to the general variability of the data set. Instead, the thermal velocity could have been used, which would mostly lead to a larger range of perpendicular velocities, and in turn the mirror force would give even higher parallel velocities along most of the trajectories.

Figure 2 shows the bulk parallel- and perpendicular velocities from Cluster data from a sample event in the northern hemisphere. This plasma mantle event occurred on 11th of June 2001 between 01:24 UT and 01:29 UT. The solid black line shows the weighted mean defined by $\sum v_{\parallel,i} n_i / \sum n_i$ (where i denote the observations, typically one 4 s measurement for CODIF), whereas the dashed red lines display the standard deviations. For this event, the mean $v_\parallel(O^+)$ is -109.01 $\pm$ 44.54 km/s and the $v_\perp(O^+)$ is 61.63 $\pm$ 36.71 km/s. A uniform standard distribution of random values in these intervals $v_\parallel$ = [-64.47;-153.55] km/s and $v_\perp$ = [24.92;98.34] km/s give the initial $v_\parallel$ and $v_\perp$ utilised as inputs for the forward traced particles. In a similar way, the initial positions of the 200 traced O^+ particles are randomly chosen in the interval x = [2.046;2.061], y = [-8.643;-8.558], z = [8.885;8.886], which are the minimum and maximum positions of Cluster during the event (11.06.2001 - approximately 5 min).

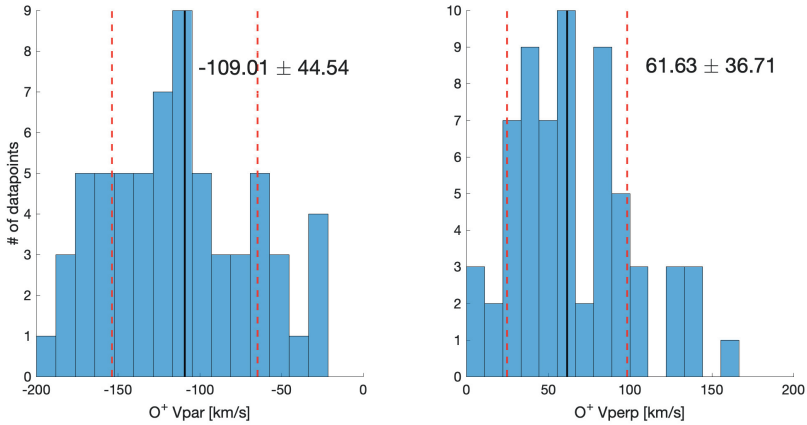**Figure 2.** Cluster SC4 observations: Parallel and perpendicular components of the O^+ velocity on 11.06.2001 between 01:24 UT and 01:29 UT. The solid black line represents the mean and the dashed red lines show the standard deviations.

The output of the model give us the final positions of O^+ in the magnetosphere as well as the travelling times of the particles in the magnetosphere.

4 Observations and Results

We analysed 136 event based on Cluster observations between 2001 and 2007. For each event, we launched 200 O^+ ions with various perpendicular and parallel velocities. Therefore, the statistics presented in this section are based on 27200 O^+ ions starting in the high altitude regions. Their ending positions are spread within the magnetosphere but a significant amount end up at the limit of our model. An example of 40 O^+ trajectories (out of the 200 computed) is shown in Fig. 3. This event occurred on 06.11.2001 during approximately 5 minutes (01:24 UT - 01:29 UT), the Dst index was -10 nT with a slightly southward IMF (Bz = -0.486 nT) and negative By (-1.16 nT). The solar wind velocity was around 550 km/s and the dynamic pressure 1.74 nPa. The top panel in Fig.3 displays the trajectories in the XZ plane, while the middle and bottom panels display the YZ and XY planes respectively. The different colours represent various trajectories, the crosses show the initial positions (noted by starting positions), whereas the asterisks show the final positions. This event clearly shows that ions from similar positions but with different velocities (see Fig. 2 for velocity range) can have very distinct trajectories. Part of the O^+ ions follow the magnetic field lines and stop at -60 Re in the distant tail (limit of the model), others are mirroring a few times before being lost on the flank (see bottom panel). Finally, a few ions are mirroring back and forth around Earth and end up in the cusp, the polar cap or simply in the plasma sheet. In this event (Fig. 3), 196 trajectories out of the 200 computed are considered to be long (more than 2000 iteration steps, see next paragraph for more details). In other events, we observed ions following magnetic field lines into the distant tail that eventually reach the plasma sheet around X = -50 Re and turn back toward Earth (not shown). Those particles are return flow (earthward flow), and we discuss their fate in the Discussion (see Section 5).

Since the plasma mantle is close to the magnetopause, some events have very short trajectories (approximately 8 min). Indeed, the O^+ ions that are launched at high altitudes in the plasma mantle typically follow the magnetic field lines and reach the magnetopause almost immediately. Those ions escape into the magnetosheath and will most likely never turn back to the magnetosphere. Fig. 4a shows the length of the 27200 trajectories in our sample, the mean trajectory is about 1030 iteration steps (or $10^{2.75}$ in the panel). We analysed the fate of the ions with short (lower than 200 steps, average time 8 min), middle (200 to 2000 steps, average time 25 min) and long (over 2000 steps, average time 130 min) trajectories and found that O^+ trajectories with less than 2000 steps (short and middle) escape mainly from the flank of the magnetosphere and represents 89% of our samples. Ions with longer trajectories represent 11% of the total sample. Within the ions with a long trajectory, 32% end up in the near-Earth plasma sheet (at geocentric distance lower than 10 Re). We defined the escaping limit by the geocentric distance of the final positions $R = \sqrt{X_{\text{fin}}^2 + Y_{\text{fin}}^2 + Z_{\text{fin}}^2}$ that equals 10 Re. This is justified by the fact that if the tracing does not end due to the limits of iterations, such ions have left the simulation domain (except for 0.5% of the trajectories, see Section 3.1). Note that the minimum geocentric distance where the O^+ ions are launched is 7.64 Re (not shown). Only 4 % of the total trajectories have their final positions below this limit (10 Re), hence 96 % of the ions are escaping the magnetosphere. The geocentric distance R of the 27200 final positions is represented in the middle panel (b) of Fig. 4. The O^+ average final position is $R = 23.5$ Re.

Furthermore, we determined the minimum distance in the X direction for each trajectory, see Fig. 4c. This parameter is important because some particles that interact with the plasma sheet in the distant tail might come back close to Earth.
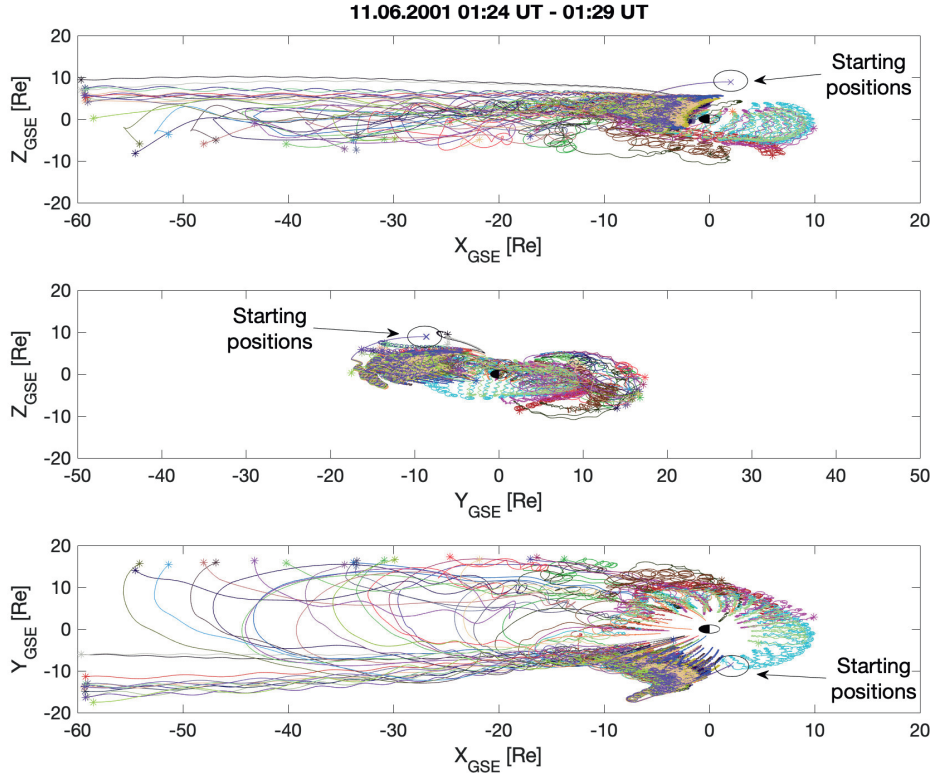
Figure 3. Example of 40 O$^+$ varied trajectories (different colours) from the plasma mantle on 11.06.2011 between 01:24 UT - 01:29 UT. The crosses denote the starting positions, whereas the asterisks denote the ending positions in the magnetosphere.

However, such cases are rare because for a total of 1751 trajectories having a X minimum distance beyond -50 Re only 79 trajectories finish their route close to Earth ($R < 10$ Re). The 1672 remaining are roughly equally spread between 10 Re and 66 Re. The average minimum X distance is around -10 Re, which corresponds to the plasma mantle region if |Z| > 5 Re (see also on Fig. 5).

Fig. 5 shows the start (left panel) and stop (right panel) positions of all trajectories in cylindrical coordinates ($R_{cyl} = \sqrt{Y^2 + Z^2}$). The colour bar represents the numbers of trajectories. In the left panel, we clearly see that particles are launched in the plasma mantle/cusp region, while on the right panel, the ending positions are spread at high R_{cyl}. O$^+$ ions from the plasma
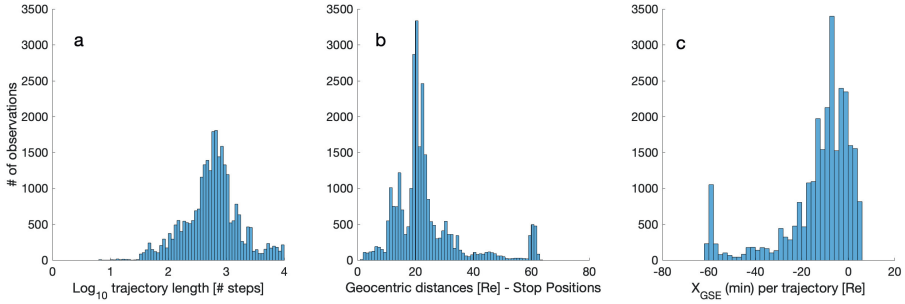
Figure 4. (a) Length of the 27200 O^+ trajectories in our sample. Note the logarithmic scale. (b) Final positions expressed in the geocentric distance R given in Re (see text for definition). (c) Minimum X distance for each trajectory.

225 mantle do not necessarily escape in the distant tail as we suggested in Slapak et al. (2017); Schillings et al. (2019), but they are escaping almost directly through the magnetopause because of their high velocities in these regions. The magnetopause is identified by abrupt changes in the tracing of the magnetic field lines, once the magnetopause is crossed, the field lines become straight and follow the IMF direction. Similarly, we observe 20% of the ions are escaping in the dayside (X > 0 Re). Note that the vertical line of ions at -60 Re have been stopped tracing due to the limit of our code.

230 The associated scaled O^+ flux (defined as the net outward flux mapped to an ionospheric reference altitude of 1000 km with a magnetic strength of 50 000 nT) is about 10^{13} m^{-2}s^{-1} in average (not shown). The highest O^+ scaled flux, 10^{14} m^{-2}s^{-1}, is observed around Earth (-3 Re < X < 3 Re) at R_{cyl} = 23 Re. In contrast, the lower scaled flux is observed below R_{cyl} = 10 Re and between 15 Re < R_{cyl} < 20 Re for X lower than -20 Re.

5 Discussion

235 In our 136 events based on Cluster-CODIF observations, the parallel and perpendicular components of the velocities during the events are taken as inputs to our forward tracing model (see Section 3.2 and Fig. 2). From these observations, we found that O^+ ions observed in the plasma mantle or higher altitude cusp have a parallel velocity which is twice the perpendicular component in 93% of the events. More precisely, the ratio between the velocity components ($|v_{\parallel}|/v_{\perp}$) is 2.06 ± 0.83. If we considered that perpendicular velocities measured by CODIF is mainly $\boldsymbol{E} \times \boldsymbol{B}$ drifts, these observations show that O^+ ions 240 at high altitude are not subject to a strong convective electric field anymore. However, Haaland et al. (2007) reported a high plasma convection strongly dependent on the IMF direction and magnitude. In the lobes and for southward IMF, the convection velocities towards the plasma sheet are around 10 km/s (Haaland et al., 2008). In contrast, the 7% of the our events with higher convection velocity have a corresponding Dst index between -5 nT and 5 nT and IMF B$_z$ component between -2 nT and 2 nT. The highest parallel to perpendicular ratios are found for strong southward IMF (53% of the cases) and strong geomagnetic 245 disturbances (46% for Dst < -20 nT) (not shown).
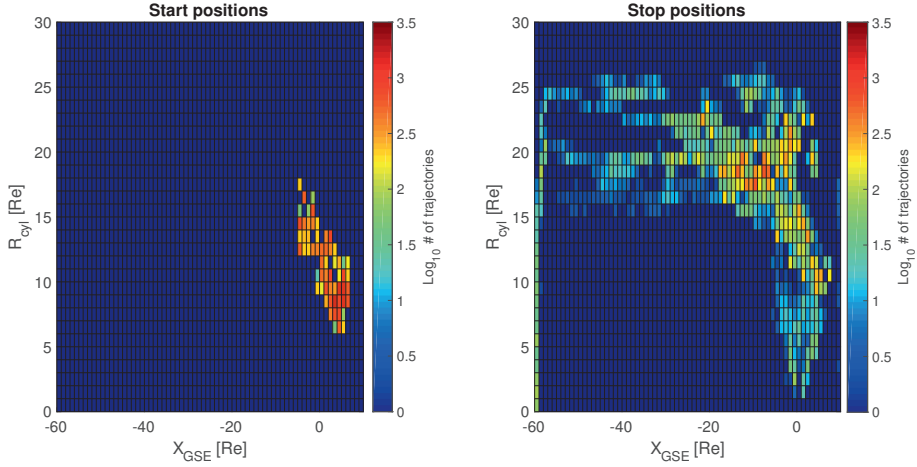
Figure 5. Cylindrical coordinates of the starting and ending positions of the launched O^+ ions. The colour bar represents the number of trajectories in each bin (1 Re x 1 Re).

We do not find any strong correlation between geomagnetic activity (Dst) and the final positions. For the IMF direction, we identify 47% of the events are associated with northward IMF and the final positions of these ions to be mainly spread between $R_{geoc} = 10$ Re and $R_{geoc} = 35$ Re (82% of the events with northward IMF). A similar trend is observed for the remaining 53% events associated with southward IMF. Thus, the direction of the IMF do not influence in which magnetospheric region the ions end up. However, if we consider only the ions with their ending positions in $R_{geoc} < 10$ Re, they occur during northward IMF (63%). This result can be compared to the cold ion outflow observed in the lobes during southward IMF. Haaland et al. (2012) found that for southward IMF the cold ion outflow is convected toward the plasma sheet due to strong convection, whereas for IMF directed northward convection is stagnant, so that cold ion outflow reach the far tail.

Slapak et al. (2012) suggested three main routes for ion outflow; (1) cold ion that will end up mainly in the plasma sheet (Mouikis et al., 2010; Haaland et al., 2012; Liao et al., 2015), (2) energised ions from the cusp to the plasma mantle (Liao et al., 2010; Slapak et al., 2017; Schillings et al., 2019), (3) energised ions from to cusp going directly to the magnetosheath (Slapak et al., 2017). Slapak et al. (2017); Slapak and Nilsson (2018); Schillings et al. (2019) suggested that ions observed in the plasma mantle have sufficient energy and velocity to escape in the distant tail. However, our results show that very few ions reach the distant tail but instead escape directly through the magnetopause after a few minutes (~ 22 min). These O^+ ions have short or middle length trajectories in our model (less than 2000 steps, see also Section 4) and represent 89% of our sample. Most (99.3%) of these O^+ ions reach a point where the tracing is stopped at a geocentric distance higher than 10 Re and escape the magnetosphere. For ions with trajectories longer than 2000 steps (11% of the total trajectories), 32% is earthward flow due to its interaction with the plasma sheet. Most of these ions do not return to the ionosphere. Some will

11

instead experience charge exchange, become neutral and be lost from the magnetosphere. This assumption is supported by Ebihara et al. (2006), who modelled O^+ trajectories and introduce a charge exchange process in their model. They estimated that 2% of the total outflow became neutral due to charge exchange with the hydrogen geocorona. Other particles will drift to the magnetopause (magnetopause shadowing) and be lost. We note that ion precipitation recorded by the DMSP spacecraft (Newell et al., 2007) indicates a total precipitation of ions (H^+ and O^+) of the order 10^{24} s^{-1}, which is most of the time dominated by cusp precipitation, not return flow precipitation. This is even less than the return flow estimated by Slapak and Nilsson (2018), indicating that most return flow indeed does not precipitate to the ionosphere. However, we do not study the fate of this earthward ions flow and therefore they are not considered as escaping ions in this study.

Under quiet magnetospheric conditions (Dst $\geq$ -20 nT), it was found that 6% of the final positions of the trajectories is within a geocentric distance of 10 Re (return flow), whereas during disturbed conditions we observe only 1.5% return flow. This result agrees with Ebihara et al. (2006), who found that under quiet time 4% to 7% of the outflowing ions return to Earth. Under disturbed conditions, the authors estimated a smaller return of 0.6% to 0.8%.

Finally, since O^+ ions are launched from the plasma mantle, the particles observed by CODIF already went through transverse heating and centrifugal acceleration. Thus this model includes most of the energisation and acceleration compared to other models. Moreover, the model does not include wave-particles interaction after the oxygen ion has been launched.

6 Summary and conclusions

Based on previous suggestions that O^+ ions from the plasma mantle are escaping (Slapak et al., 2017; Slapak and Nilsson, 2018; Schillings et al., 2019), we investigate the fate of ions by tracing the particles forward in time in the magnetospshere. The magnetospshere is represented by the Tsyganenko T96 model for the magnetic field and the Weimer 2001 model for the electric field (ionospheric potential). We analyse 136 plasma mantle and cusp events detected automatically in the Cluster data during 2001 and 2007. For each event, 200 O^+ ions with an initial parallel and perpendicular velocity are launched from the plasma mantle or high-latitude cusp. The initial velocities and positions are determined by Cluster observations and are used as inputs for the forward tracing. Our results are summarised in the following points:

1. The O^+ ions observed in the plasma mantle and high-latitude cusp have an initial parallel velocity that is twice the perpendicular velocity for 93% of the event. Thus, the parallel velocity dominates from the start, and through high perpendicular temperatures, the mirror force will increase the parallel velocity further downstream of the observation point.

2. The highest ratios between parallel and perpendicular velocities are found for southward IMF (53%) and strong geomagnetic disturbances (46% for Dst < -20 nT).

3. 96% of the final positions (out of 27200) are located beyond a geocentric distance of 10 Re. These particles escape and are lost into the solar wind. 20% of the ions escape directly through the high-latitude dayside magnetopause.

4. 3.5% of the total trajectories lead back towards earth, i.e. they constitute return flow. Some of these O^+ ions have interacted with the plasma sheet in the distant tail and eventually end up between the Earth and a geocentric distance of 10 Re.

5. Under disturbed magnetospheric conditions (Dst < -20 nT), we observe 1.5 % return flow, whereas during quiet time the return flow increases to 6%.

6. We do not find any correlation between the IMF direction, the geomagnetic disturbances and the final positions of O^+ in our tracing model. However, the ions ending up close to the Earth (geocentric distance smaller than 10 Re) are for 63% of the time associated with northward IMF.

Competing interests. The authors declare that they have no competing interests.

References

Abe, T., Whalen, B. A., Yau, A. W., Horita, R. E., Watanabe, S., and Sagawa, E.: EXOS D (Akebono) suprathermal mass spectrometer observations of the polar wind, Journal of Geophysical Research: Space Physics, 98, 11 191–11 203, https://doi.org/10.1029/92JA01971, 1993.

Abudayyeh, H. A., Barghouthi, I. A., Slapak, R., and Nilsson, H.: Centrifugal acceleration at high altitudes above the polar cap: A Monte Carlo simulation, Journal of Geophysical Research: Space Physics, 120, 6409–6426, https://doi.org/10.1002/2015JA021325, 2015.

André, M. and Cully, C. M.: Low-energy ions: A previously hidden solar system particle population, Geophysical Research Letters, 39, https://doi.org/10.1029/2011GL050242, 2012.

Arvelius, S., Yamauchi, M., Nilsson, H., Lundin, R., Hobara, Y., Rème, H., Bavassano-Cattaneo, M. B., Paschmann, G., Korth, A., Kistler, L. M., and Parks, G. K.: Statistics of high-altitude and high-latitude O^+ ion outflows observed by Cluster/CIS, Annales Geophysicae, 23, 1909–1916, https://doi.org/10.5194/angeo-23-1909-2005, https://www.ann-geophys.net/23/1909/2005/, 2005.

Axford, W. I.: The polar wind and the terrestrial helium budget, J. Geophys. Res., 73, 6855–6859, https://doi.org/10.1029/JA073i021p06855, 1968.

Balogh, A., Carr, C. M., Acuña, M. H., Dunlop, M. W., Beek, T. J., Brown, P., Fornaçon, K.-H., Georgescu, E., Glassmeier, K.-H., Harris, J., Musmann, G., Oddy, T., and Schwingenschuh, K.: The Cluster Magnetic Field Investigation: overview of in-flight performance and initial results, Annales Geophysicae, 19, 1207–1217, https://doi.org/10.5194/angeo-19-1207-2001, 2001.

Barakat, A. R. and Schunk, R. W.: A three-dimensional model of the generalized polar wind, Journal of Geophysical Research: Space Physics, 111, https://doi.org/10.1029/2006JA011662, 2006.

Barghouthi, I. A., Abudayyeh, H. A., Slapak, R., and Nilsson, H.: O+ and H+ above the polar cap: Observations and semikinetic simulations, Journal of Geophysical Research: Space Physics, 121, 459–474, https://doi.org/10.1002/2015JA021990, 2016.

Birdsall, C. K. and Langdon, A.: Plasma Physics via Computer Simulation, IOP Publishing Ltd, ISBN 0 7503 1025 1, 1991.

Chappell, C. R., Moore, T. E., and Waite, Jr., J. H.: The ionosphere as a fully adequate source of plasma for the earth's magnetosphere, J. Geophys. Res., 92, 5896–5910, https://doi.org/10.1029/JA092iA06p05896, 1987.

Ebihara, Y., Yamada, M., Watanabe, S., and Ejiri, M.: Fate of outflowing suprathermal oxygen ions that originate in the polar ionosphere, Journal of Geophysical Research: Space Physics, 111, https://doi.org/10.1029/2005JA011403, 2006.

Engwall, E., Eriksson, A. I., Cully, C. M., André, M., Puhl-Quinn, P. A., Vaith, H., and Torbert, R.: Survey of cold ionospheric outflows in the magnetotail, Annales Geophysicae, 27, 3185–3201, https://doi.org/10.5194/angeo-27-3185-2009, https://www.ann-geophys.net/27/3185/2009/, 2009.

Escoubet, C. P., Fehringer, M., and Goldstein, M.: IntroductionThe Cluster mission, Annales Geophysicae, 19, 1197–1200, https://doi.org/10.5194/angeo-19-1197-2001, 2001.

Gunell, H., Maggiolo, R., Nilsson, H., Stenberg Wieser, G., Slapak, R., Lindkvist, J., Hamrin, M., and De Keyser, J.: Why an intrinsic magnetic field does not protect a planet against atmospheric escape, Astronomy & Astrophysics, 614, L3, https://doi.org/10.1051/0004-6361/201832934, 2018.

Gunell, H., De Spiegeleer, A., and Schillings, A.: ham – a particle tracing code for Earth's magnetosphere, https://doi.org/10.5281/zenodo.3466771, 2019.

350 Haaland, S., Paschmann, G., Förster, M., Quinn, J., Torbert, R., Vaith, H., Puhl-Quinn, P., and Kletzing, C.: Plasma convection in the magne-
totail lobes: statistical results from Cluster EDI measurements, Annales Geophysicae, 26, 2371–2382, https://doi.org/10.5194/angeo-26-
2371-2008, https://www.ann-geophys.net/26/2371/2008/, 2008.

Haaland, S., Lybekk, B., Svenes, K., Pedersen, A., Förster, M., Vaith, H., and Torbert, R.: Plasma transport in the magnetotail lobes, Annales
Geophysicae, 27, 3577–3590, https://doi.org/10.5194/angeo-27-3577-2009, https://www.ann-geophys.net/27/3577/2009/, 2009.

355 Haaland, S., Eriksson, A., Engwall, E., Lybekk, B., Nilsson, H., Pedersen, A., Svenes, K., André, M., Förster, M., Li, K., Johnsen, C., and
Østgaard, N.: Estimating the capture and loss of cold plasma from ionospheric outflow, Journal of Geophysical Research (Space Physics),
117, A07311, https://doi.org/10.1029/2012JA017679, 2012.

Haaland, S., Lybekk, B., Maes, L., Laundal, K., Pedersen, A., Tenfjord, P., Ohma, A., Østgaard, N., Reistad, J., and Snekvik, K.: North-south
asymmetries in cold plasma density in the magnetotail lobes: Cluster observations, Journal of Geophysical Research: Space Physics, 122,
360 136–149, https://doi.org/10.1002/2016JA023404, 2017.

Haaland, S. E., Paschmann, G., Förster, M., Quinn, J. M., Torbert, R. B., McIlwain, C. E., Vaith, H., Puhl-Quinn, P. A., and Kletzing, C. A.:
High-latitude plasma convection from Cluster EDI measurements: method and IMF-dependence, Annales Geophysicae, 25, 239–253,
https://doi.org/10.5194/angeo-25-239-2007, https://www.ann-geophys.net/25/239/2007/, 2007.

Hoffman, J. H.: Ion composition measurements in the polar region from the Explorer 31 satellite, Trans. Am. Geophys. Union, 49, 1968.

365 Horwitz, J. L., Ho, C. W., Scarbro, H. D., Wilson, G. R., and Moore, T. E.: Centrifugal acceleration of the polar wind, Journal of Geophysical
Research: Space Physics, 99, 15 051–15 064, https://doi.org/10.1029/94JA00924, 1994.

Kistler, L. M. and Mouikis, C. G.: The inner magnetosphere ion composition and local time distribution over a solar cycle, Journal of
Geophysical Research: Space Physics, 121, 2009–2032, https://doi.org/10.1002/2015JA021883, 2016.

Kistler, L. M., Mouikis, C. G., Cao, X., Frey, H., Klecker, B., Dandouras, I., Korth, A., Marcucci, M. F., Lundin, R., McCarthy, M., Friedel,
370 R., and Lucek, E.: Ion composition and pressure changes in storm time and nonstorm substorms in the vicinity of the near-Earth neutral
line, Journal of Geophysical Research (Space Physics), 111, A11222, https://doi.org/10.1029/2006JA011939, 2006.

Krcelic, P., Haaland, S., Maes, L., Slapak, R., and Schillings, A.: Estimating the fate of oxygen ion outflow from the high altitude cusp.,
Submitted to Ann. Geophys., 2019.

Li, K., Haaland, S., Eriksson, A., André, M., Engwall, E., Wei, Y., Kronberg, E. A., Fränz, M., Daly, P. W., Zhao, H., and Ren, Q. Y.: On the
375 ionospheric source region of cold ion outflow, Geophys. Res. Lett., 39, L18102, https://doi.org/10.1029/2012GL053297, 2012.

Liao, J., Kistler, L. M., Mouikis, C. G., Klecker, B., Dandouras, I., and Zhang, J.-C.: Statistical study of O^+ transport from the cusp to the
lobes with Cluster CODIF data, Journal of Geophysical Research (Space Physics), 115, A00J15, https://doi.org/10.1029/2010JA015613,
2010.

Liao, J., Kistler, L. M., Mouikis, C. G., Klecker, B., and Dandouras, I.: Acceleration of O^+ from the cusp to the plasma sheet, Journal of
380 Geophysical Research (Space Physics), 120, 1022–1034, https://doi.org/10.1002/2014JA020341, 2015.

Mouikis, C. G., Kistler, L. M., Liu, Y. H., Klecker, B., Korth, A., and Dandouras, I.: H^+ and O^+ content of the plasma sheet
at 15-19 Re as a function of geomagnetic and solar activity, Journal of Geophysical Research (Space Physics), 115, A00J16,
https://doi.org/10.1029/2010JA015978, 2010.

Newell, P. T., Sotirelis, T., Liou, K., Meng, C.-I., and Rich, F. J.: A nearly universal solar wind-magnetosphere coupling function inferred
385 from 10 magnetospheric state variables, Journal of Geophysical Research: Space Physics, 112, https://doi.org/10.1029/2006JA012015,
2007.

Nilsson, H.: Heavy Ion Energization, Transport, and Loss in the Earth's Magnetosphere, in: The Dynamic Magnetosphere, edited by Liu, W. and Fujimoto, M., pp. 315–327, Springer Netherlands, Dordrecht, https://doi.org/10.1007/978-94-007-0501-2_17, 2011.

Nilsson, H., Waara, M., Arvelius, S., Marghitu, O., Bouhram, M., Hobara, Y., Yamauchi, M., Lundin, R., Rème, H., Sauvaud, J.-A., Dandouras, I., Balogh, A., Kistler, L. M., Klecker, B., Carlson, C. W., Bavassano-Cattaneo, M. B., and Korth, A.: Characteristics of high altitude oxygen ion energization and outflow as observed by Cluster: a statistical study, Annales Geophysicae, 24, 1099–1112, https://doi.org/10.5194/angeo-24-1099-2006, 2006.

Nilsson, H., Waara, M., Marghitu, O., Yamauchi, M., Lundin, R., Rème, H., Sauvaud, J.-A., Dandouras, I., Lucek, E., Kistler, L. M., Klecker, B., Carlson, C. W., Bavassano-Cattaneo, M. B., and Korth, A.: An assessment of the role of the centrifugal acceleration mechanism in high altitude polar cap oxygen ion outflow, Annales Geophysicae, 26, 145–157, https://doi.org/10.5194/angeo-26-145-2008, 2008.

Nilsson, H., Barghouthi, I. A., Slapak, R., Eriksson, A. I., and André, M.: Hot and cold ion outflow: Spatial distribution of ion heating, Journal of Geophysical Research (Space Physics), 117, A11201, https://doi.org/10.1029/2012JA017974, 2012.

Norqvist, P., André, M., and Tyrland, M.: A statistical study of ion energization mechanisms in the auroral region, Journal of Geophysical Research: Space Physics, 103, 23 459–23 473, https://doi.org/10.1029/98JA02076, 1998.

Peterson, W. K., Collin, H. L., Yau, A. W., and Lennartsson, O. W.: Polar/Toroidal Imaging Mass – Angle Spectrograph observations of suprathermal ion outflow during solar minimum conditions, Journal of Geophysical Research: Space Physics, 106, 6059–6066, https://doi.org/10.1029/2000JA003006, 2001.

Rème, H., Aoustin, C., Bosqued, J. M., Dandouras, I., Lavraud, B., Sauvaud, J. A., Barthe, A., Bouyssou, J., Camus, T., Coeur-Joly, O., Cros, A., Cuvilo, J., Ducay, F., Garbarowitz, Y., Medale, J. L., Penou, E., Perrier, H., Romefort, D., Rouzaud, J., Vallat, C., Alcaydé, D., Jacquey, C., Mazelle, C., D'Uston, C., Möbius, E., Kistler, L. M., Crocker, K., Granoff, M., Mouikis, C., Popecki, M., Vosbury, M., Klecker, B., Hovestadt, D., Kucharek, H., Kuenneth, E., Paschmann, G., Scholer, M., Sckopke, N., Seidenschwang, E., Carlson, C. W., Curtis, D. W., Ingraham, C., Lin, R. P., McFadden, J. P., Parks, G. K., Phan, T., Formisano, V., Amata, E., Bavassano-Cattaneo, M. B., Baldetti, P., Bruno, R., Chionchio, G., di Lellis, A., Marcucci, M. F., Pallocchia, G., Korth, A., Daly, P. W., Graeve, B., Rosenbauer, H., Vasyliunas, V., McCarthy, M., Wilber, M., Eliasson, L., Lundin, R., Olsen, S., Shelley, E. G., Fuselier, S., Ghielmetti, A. G., Lennartsson, W., Escoubet, C. P., Balsiger, H., Friedel, R., Cao, J.-B., Kovrazhkin, R. A., Papamastorakis, I., Pellat, R., Scudder, J., and Sonnerup, B.: First multispacecraft ion measurements in and near the Earth's magnetosphere with the identical Cluster ion spectrometry (CIS) experiment, Annales Geophysicae, 19, 1303–1354, https://doi.org/10.5194/angeo-19-1303-2001, 2001.

Rosenbauer, H., Grünwaldt, H., Montgomery, M. D., Paschmann, G., and Sckopke, N.: Heos 2 plasma observations in the distant polar magnetosphere: The plasma mantle, Journal of Geophysical Research (1896-1977), 80, 2723–2737, https://doi.org/10.1029/JA080i019p02723, 1975.

Schillings, A., Nilsson, H., Slapak, R., Yamauchi, M., and Westerberg, L.-G.: Relative outflow enhancements during major geomagnetic storms – Cluster observations, Annales Geophysicae, 35, 1341–1352, https://doi.org/10.5194/angeo-35-1341-2017, https://www.ann-geophys.net/35/1341/2017/, 2017.

Schillings, A., Nilsson, H., Slapak, R., Wintoft, P., Yamauchi, M., Wik, M., Dandouras, I., and Carr, C. M.: O+ Escape During the Extreme Space Weather Event of 4-10 September 2017, Space Weather, 16, 1363–1376, https://doi.org/10.1029/2018SW001881, 2018.

Schillings, A., Slapak, R., Nilsson, H., Yamauchi, M., Dandouras, I., and Westerberg, L.-G.: Earth atmospheric loss through the plasma mantle and its dependence on solar wind parameters, Earth, Planets and Space, 71, 70, https://doi.org/10.1186/s40623-019-1048-0, https://doi.org/10.1186/s40623-019-1048-0, 2019.

Schunk, R. W. and Sojka, J. J.: A three-dimensional time-dependent model of the polar wind, Journal of Geophysical Research: Space
Physics, 94, 8973–8991, https://doi.org/10.1029/JA094iA07p08973, 1989.

Schunk, R. W. and Sojka, J. J.: Global ionosphere-polar wind system during changing magnetic activity, Journal of Geophysical Research:
Space Physics, 102, 11 625–11 651, https://doi.org/10.1029/97JA00292, 1997.

Sharp, R. D., Johnson, R. G., and Shelley, E. G.: Observation of an ionospheric acceleration mechanism producing energetic
(keV) ions primarily normal to the geomagnetic field direction, Journal of Geophysical Research (1896-1977), 82, 3324–3328,
https://doi.org/10.1029/JA082i022p03324, https://agupubs.onlinelibrary.wiley.com/doi/abs/10.1029/JA082i022p03324, 1977.

Shelley, E. G., Sharp, R. D., and Johnson, R. G.: Satellite observations of an ionospheric acceleration mechanism, Geophysi-
cal Research Letters, 3, 654–656, https://doi.org/10.1029/GL003i011p00654, https://agupubs.onlinelibrary.wiley.com/doi/abs/10.1029/
GL003i011p00654, 1976.

Slapak, R. and Nilsson, H.: The Oxygen Ion Circulation in The Outer Terrestrial Magnetosphere and Its Dependence on Geomagnetic
Activity, Geophysical Research Letters, 45, 12,669–12,676, https://doi.org/10.1029/2018GL079816, 2018.

Slapak, R., Nilsson, H., Waara, M., André, M., Stenberg, G., and Barghouthi, I. A.: O^+ heating associated with strong wave activity in the
high altitude cusp and mantle, Annales Geophysicae, 29, 931–944, https://doi.org/10.5194/angeo-29-931-2011, 2011.

Slapak, R., Nilsson, H., Westerberg, L. G., and Eriksson, A.: Observations of oxygen ions in the dayside magnetosheath associated with
southward IMF, Journal of Geophysical Research (Space Physics), 117, A07218, https://doi.org/10.1029/2012JA017754, 2012.

Slapak, R., Schillings, A., Nilsson, H., Yamauchi, M., Westerberg, L.-G., and Dandouras, I.: Atmospheric loss from the dayside open polar
region and its dependence on geomagnetic activity: implications for atmospheric escape on evolutionary timescales, Annales Geophysicae,
35, 721–731, 2017.

Strangeway, R. J., Ergun, R. E., Su, Y., Carlson, C. W., and Elphic, R. C.: Factors controlling ionospheric outflows as observed at intermediate
altitudes, Journal of Geophysical Research: Space Physics, 110, https://doi.org/10.1029/2004JA010829, 2005.

Tsyganenko, N. A.: Modeling the Earth's magnetospheric magnetic field confined within a realistic magnetopause, Journal of Geophysical
Research: Space Physics, 100, 5599–5612, https://doi.org/10.1029/94JA03193, 1995.

Waara, M., Slapak, R., Nilsson, H., Stenberg, G., André, M., and Barghouthi, I. A.: Statistical evidence for O^+ energization
and outflow caused by wave-particle interaction in the high altitude cusp and mantle, Annales Geophysicae, 29, 945–954,
https://doi.org/10.5194/angeo-29-945-2011, 2011.

Weimer, D. R.: An improved model of ionospheric electric potentials including substorm perturbations and application to the
Geospace Environment Modeling November 24, 1996, event, Journal of Geophysical Research: Space Physics, 106, 407–416,
https://doi.org/10.1029/2000JA000604, 2001.

Yau, A. W., Abe, T., and Peterson, W.: The polar wind: Recent observations, Journal of Atmospheric and Solar-Terrestrial Physics, 69, 1936
– 1983, https://doi.org/10.1016/j.jastp.2007.08.010, recent Advances in the Polar Wind Theories and Observations, 2007.

425

430

435

440

445

450